

Constraining a relativistic mean field model using neutron star mass–radius measurements I: nucleonic models

Chun Huang,^{1,2,3}★ Geert Raaijmakers⁴, Anna L. Watts^{5,2}, Laura Tolos^{5,6,7} and Constança Providência⁸

¹Physics Department, Central China Normal University, Luoyu Road, 430030 Wuhan, China

²Anton Pannekoek Institute for Astronomy, University of Amsterdam, Science Park 904, 1090 GE Amsterdam, the Netherlands

³Physics Department, Washington University, One Brookings Drive, St. Louis, MO 63130, USA

⁴GRAPPA, University of Amsterdam, Science Park 904, 1098 XH Amsterdam, the Netherlands

⁵Institute of Space Sciences (ICE, CSIC), Campus UAB, Carrer de Can Magrans E-08193, Barcelona, Spain

⁶Institut d'Estudis Espacials de Catalunya (IEEC), E-08034, Barcelona, Spain

⁷Frankfurt Institute for Advanced Studies, Ruth-Moufang-Str 1, D-60438 Frankfurt am Main, Germany

⁸CFisUC, Department of Physics, University of Coimbra, P-3004-516 Coimbra, Portugal

Accepted 2024 March 21. Received 2024 March 20; in original form 2023 March 28

ABSTRACT

Measurements of neutron star mass and radius or tidal deformability deliver unique insight into the equation of state (EOS) of cold dense matter. EOS inference is very often done using generalized parametric or non-parametric models, which deliver no information on composition. In this paper, we consider a microscopic nuclear EOS model based on a field theoretical approach. We show that current measurements from NICER and gravitational wave observations constrain primarily the symmetric nuclear matter EOS. We then explore what could be delivered by measurements of mass and radius at the level anticipated for future large-area X-ray timing telescopes. These should be able to place very strong limits on the symmetric nuclear matter EOS, in addition to constraining the nuclear symmetry energy that determines the proton fraction inside the neutron star.

Key words: dense matter – equation of state – stars: neutron – X-rays: general.

1 INTRODUCTION

Neutron star observations, via electromagnetic radiation or gravitational waves (GWs), provide unique insight into the dense matter Equation of State (EOS), particularly at low temperatures (Lattimer 2012; Oertel et al. 2017; Baym et al. 2018; Tolos & Fabbietti 2020; Yang & Piekarewicz 2020; Burgio et al. 2021; Hebeler 2021). Measurements of the highest neutron star masses already restrict the range of dense matter possibilities (see, e.g. Özel et al. 2010; Cromartie et al. 2020). GW detectors are now providing constraints on tidal deformability from binary neutron star mergers (Abbott et al. 2018, 2019, 2020), and NASA’s Neutron Star Interior Composition Explorer (NICER; Gendreau et al. 2016) has reported its first results for the simultaneous inference of mass and radius (Miller et al. 2019; Riley et al. 2019; Miller et al. 2021; Riley et al. 2021; Salmi et al. 2022; Vinciguerra et al. 2024). These multimessenger results are now being combined, together with information from laboratory nuclear experiments, to constrain EOS models (for a selection of recent papers, see Legred et al. 2021; Li, Sedrakian & Alford 2021; Miller et al. 2021; Pang et al. 2021; Raaijmakers et al. 2021; Tang et al. 2021; Annala et al. 2022; Biswas 2022).

Given our lack of knowledge of the EOS relating to high densities and very asymmetric matter, or the appearance of exotic degrees of freedom, the community frequently uses meta-models that cover

the whole acceptable pressure-energy density or mass–radius (M–R) domains. Different methodologies have been used to implement this strategy, for example, through the parametrization of the EOS via polytropes (Read et al. 2009; Kurkela et al. 2014; Annala et al. 2018; Most et al. 2018), the speed of sound (Alford, Han & Prakash 2013; Bedaque & Steiner 2015; Tews et al. 2018; Greif et al. 2019; Annala et al. 2020), or spectral representations (Lindblom 2010; Abbott et al. 2018; Lindblom 2022) imposing, if necessary, causality. More recently, a non-parametric approach was also proposed through the introduction of Gaussian processes (Landry, Essick & Chatzioannou 2020; Essick et al. 2021; Legred et al. 2022).

While these approaches allow us to determine the EOS domain that satisfies the observational constraints, they deliver no information on composition, either the proton fraction or the existence of non-nucleonic degrees of freedom such as hyperons, delta-baryons, or deconfined quark matter. In the present study, the drawbacks of meta-models will be overcome by considering a microscopic model based on a relativistic field theoretical approach to determine the whole EOS space allowed by observations. This will be undertaken by changing the model parameters. Being defined in a relativistic framework, the model automatically incorporates causality. This approach has already been taken in Traversi, Char & Pagliara (2020), where the relativistic mean-field model (RMF) of Boguta & Bodmer (1977) was applied; and in Malik et al. (2022), who considered as their underlying model an RMF with density dependent couplings. The authors of Sun et al. (2023) have recently developed a Bayesian inference approach in the framework of several nuclear RMF, to

* E-mail: chun.h@wustl.edu

determine how GW and NICER measurements constrain the $\Lambda-\sigma$ and $\Lambda-\omega$ couplings, while fixing the Σ and Ξ couplings to reasonable values. A major advantage of this methodology is the possibility, once the inference is completed, to discuss the composition of matter, in particular, the proton fraction, or the nuclear matter properties. In the present study, we will base our approach on the framework that is behind the reasonably successful FSU2R nucleonic model (Tolos, Centelles & Ramos 2016, 2017).

The power of astrophysical observations to constrain microphysical models is also important to inform the design and observational strategy for future X-ray telescopes that will exploit the M–R inference technique used by NICER (Watts et al. 2016; Watts 2019). Large-area X-ray spectral timing telescope concepts like the enhanced X-ray Timing and Polarimetry mission (eXTP; Watts et al. 2019; Zhang et al. 2019) and the Spectroscopic Time-Resolving Observatory for Broadband Energy X-rays (STROBE-X; Ray et al. 2019) aim to measure mass and radius for not only faint rotation-powered millisecond pulsars (the sources being studied by NICER) but also accreting neutron stars. These sources are often transient, as are many of the other high-priority targets (such as black hole binaries) for these missions, and long observation times are required to build up sufficient photons to enable the analysis. Being able to make a well-informed decision on the potential scientific pay-off of observing a particular source is important, particularly if it comes at the expense of observing another potentially attractive target.

In this paper, we therefore consider not only the constraints arising from existing observations, but look at what might be delivered by future missions. Since we are particularly interested in determining the model space constrained by the astrophysical observations, we therefore impose only a minimal number of nuclear matter properties. A different approach was undertaken in Ghosh et al. (2022a); Ghosh, Chatterjee & Schaffner-Bielich (2022b), where, within a cut-off scheme applied to a prior already constrained by nuclear matter properties, constraints from chiral Effective Field Theory, Heavy Ion Collisions and astrophysics were imposed as filters.

In Section 2, we introduce the EOS model and our choice of priors. In Section 3, we describe the Bayesian inference procedure and the M–R scenarios that we consider in our analysis. Section 4 gives the results of inference using currently available M–R and tidal deformability constraints, while Section 5 considers what could be achieved by observations of M–R with future large-area X-ray telescopes. In Section 6, we discuss the implications of our findings, while we present our conclusions in Section 7.

2 EQUATION OF STATE MODELS

The EOS model we use for inference is the RMF of matter, where nucleons interact through the exchange of mesons and which provides a covariant description of the EOS and nuclear systems, using the parametrization denoted as FSU2R for nucleonic matter (Tolos et al. 2016, 2017). This model was developed from the nucleonic FSU2 model of Chen & Piekarewicz (2014), which was optimized to describe a set of properties of finite nuclei and of neutron stars. In particular, FSU2R has been developed to describe two solar mass stars and stellar radii below 13 km.

The well calibrated parameter set of the FSU2R model is chosen as the central value of our prior distributions (see Section 2.2). There are presently many parametrizations based on the same framework including Z272v (Horowitz & Piekarewicz 2001b; Pais & Providência 2016), FSU (Todd-Rutel & Piekarewicz 2005), IUFSU (Fattoyev et al. 2010; Cavagnoli, Menezes & Providência 2011), TM1 $\omega\rho$ (Providência & Rabhi 2013; Bao et al. 2014), TM1e (Shen

et al. 2020), TM1-2 $\omega\rho$ (Providência & Rabhi 2013), and Big Apple (Fattoyev et al. 2020).

The different models are based on distinct specific subsets of parameters chosen by different calibration methods. Thus, even though our inference is based on FSU2R, the power of the present inference approach extends far beyond this scheme, and could provide constraining and excluding evidence for numerous models that are based on the RMF description for nucleonic matter.

In the following subsection, we formulate the RMF framework (Serot & Walecka 1986; Glendenning 1996), then introduce our choice of priors for the full set of EOS parameters, which reproduce currently known nuclear physics quantities. For this last step, we consider the relations between the EOS parameters and nuclear matter properties (Chen & Piekarewicz 2014). In the last subsection, we calculate the M–R prior based on our set up. We then apply the model to the inference and Bayesian constraint process in Section 3.

2.1 Equation of state

The starting point of our theoretical framework is the Lagrangian density, which will be divided into three parts: nucleonic Lagrangian density N , lepton contribution l (e, μ), and meson field terms \mathcal{M} (σ, ω, ρ):

$$\mathcal{L} = \sum_N \mathcal{L}_N + \mathcal{L}_{\mathcal{M}} + \sum_l \mathcal{L}_l. \quad (1)$$

They can be separately expressed as

$$\begin{aligned} \sum_N \mathcal{L}_N &= \sum_N \bar{\Psi}_N (i\gamma_\mu \partial^\mu - m_N + g_\sigma \sigma \\ &\quad - g_\omega \gamma_\mu \omega^\mu - g_\rho \gamma_\mu \vec{I}_N \cdot \vec{\rho}^\mu) \Psi_N, \\ \sum_l \mathcal{L}_l &= \sum_l \bar{\psi}_l (i\gamma_\mu \partial^\mu - m_l) \psi_l, \\ \mathcal{L}_{\mathcal{M}} &= \frac{1}{2} \partial_\mu \sigma \partial^\mu \sigma - \frac{1}{2} m_\sigma^2 \sigma^2 - \frac{\kappa}{3!} (g_\sigma \sigma)^3 - \frac{\lambda_0}{4!} (g_\sigma \sigma)^4 \\ &\quad - \frac{1}{4} \Omega^{\mu\nu} \Omega_{\mu\nu} + \frac{1}{2} m_\omega^2 \omega_\mu \omega^\mu + \frac{\zeta}{4!} g_\omega^4 (\omega_\mu \omega^\mu)^2 \\ &\quad - \frac{1}{4} \vec{R}^{\mu\nu} \cdot \vec{R}_{\mu\nu} + \frac{1}{2} m_\rho^2 \vec{\rho}_\mu \cdot \vec{\rho}^\mu + \Lambda_\omega g_\rho^2 \vec{\rho}_\mu \cdot \vec{\rho}^\mu g_\omega^2 \omega_\mu \omega^\mu, \end{aligned} \quad (2)$$

where Ψ_N and ψ_l are the nucleon and lepton spinors, and \vec{I}_N is the nucleon isospin operator. The coupling of a meson to a nucleon is denoted by g , while the masses of the nucleons, mesons, and leptons are denoted by m . The parameters κ, λ_0, ζ , and Λ_ω plus the meson–nucleon coupling constants are coupling constants to be determined by the inference method.

By solving the Euler–Lagrange equations for nucleons and mesons in the RMF approach, we can obtain the Dirac equation for nucleons and the equations of motion for the expectation values of the mesons, as explained in Dutra et al. (2014). The EOS and composition of matter are then obtained by coupling those equations with global charge neutrality and β -equilibrium conditions, which relate the chemical potentials of the different species.

2.2 Choice of priors for model parameters

The free parameters in the EOS contain unique information on the field coupling strengths, meson mass, or interaction. The word ‘free’ indicates that their values have to be determined, and could vary within a reasonable range given by ground-based experiments. The parameters in the nucleonic EOS can be divided into three groups:

(i) scalar self-interaction coupling constants and mixed-interaction constants among mesons:

$$\kappa \quad \lambda_0 \quad \zeta \quad \Lambda_\omega. \quad (3)$$

The parameters κ and λ_0 are introduced to indicate the σ meson self-interaction (Boguta & Bodmer 1977); these two are constrained by reproducing the equilibrium properties of symmetric nuclear matter and finite nuclei. Both of them are responsible for producing the incompressibility K (Boguta & Bodmer 1977; Boguta & Stocker 1983; Müller & Serot 1996) in agreement with experiments on nuclear giant resonances and heavy ion collisions. The parameter ζ is the quartic self-coupling of the ω meson (Bodmer 1991) and heavily influences the high density behaviour of the EOS dominating the largest mass stars, as clearly discussed in Müller & Serot (1996), already in the nineties. Moreover, there is a mixed-interaction term, Λ_ω (Horowitz & Piekarewicz 2001b), between the ω and ρ meson. This term is responsible for modifying the density dependence of the nuclear symmetry energy, and influences the neutron-skin radius of heavy nuclei and the radii of neutron stars, first discussed in Horowitz & Piekarewicz (2001a,b), where it was shown that the larger Λ_ω , the smaller the radius of the canonical neutron star and the neutron radius of a heavy nucleus. The joint effect of both parameters on the neutron star properties is nicely illustrated in Fattoyev & Piekarewicz (2010a): ζ controls the maximum neutron star mass and Λ_ω has an effect on the radius of intermediate and high-mass stars¹ (for a similar discussion see Fattoyev & Piekarewicz 2010b). This last parameter defines the slope of the symmetry energy at saturation, L , as shown in Cavagnoli et al. (2011), where a correlation between L and the radius of 1.0 and 1.4 M_\odot stars was verified. However, in Alam et al. (2016), the authors show that this correlation is strong only for low-mass stars and becomes weaker as the mass increases. For masses above 1.4 M_\odot , the correlation of the radius with the nuclear matter incompressibility is stronger. A similar conclusion concerning the correlation between the slope L and the neutron star radius was drawn in Fortin et al. (2016) and Malik et al. (2018).

(ii) meson-nucleon coupling constants:

$$g_\sigma \quad g_\omega \quad g_\rho. \quad (4)$$

The parameters g_σ and g_ω are the couplings between the nucleon and the isoscalar σ and ω mesons, respectively. Those determine the energy per particle and density of the nuclear matter saturation point, thus becoming instrumental for the ground-state properties of finite nuclei. The g_ρ represents the coupling constant of the isovector ρ with the nucleon, which is responsible for producing a reasonable nuclear symmetry energy, impacting the properties of heavy neutron-rich nuclei and neutron stars.

(iii) meson mass

$$m_\sigma \quad m_\omega \quad m_\rho. \quad (5)$$

These are the masses of the σ , ω , and ρ meson, respectively. The values of m_ω and m_ρ are well determined (782.5 and 763 MeV, respectively), but m_σ is less well established, with a range from 495 to 510 MeV.

As discussed in Glendenning (1996), infinite nuclear matter described by the present model depends on the coupling constants and the meson masses only through the ratios g_i/m_i . We have confirmed that our results do not depend on the σ -meson mass and have set it to

¹In the following, we will refer to low, intermediate, and high-mass stars, as stars that have, respectively, a mass below 1.4 M_\odot , a mass in the range $1.4 \lesssim M/M_\odot \lesssim 2$, a mass $\gtrsim 2 M_\odot$.

Table 1. This is a summary for all the EOS parameters prior setting, where N stands for Gaussian distribution and \mathcal{U} means Uniform (Flat) distribution.

EOS parameter	Prior
κ (MeV)	$N(2.525, 1.525^2)$
λ_0	$N(0.0045, 0.0205^2)$
ζ	$\mathcal{U}(0, 0.04)$
Λ_ω	$\mathcal{U}(0, 0.045)$
g_σ^2	$N(107.5, 7.5^2)$
g_ω^2	$\mathcal{U}(150, 210)$
g_ρ^2	$\mathcal{U}(75, 210)$

a constant with a value of 497.479 MeV, consistent with the FSU2R model.

Taking into account all parameters, the nucleonic model space is a seven dimensional parameter space. However, each parameter can have its own distribution. Using some reasonable values of the parameter space based on nuclear experimental constraints, we make the following choices for the prior distributions.

We start with the parameter range for the scalar self-interaction coupling constants and mixed-interaction constants. The parameter κ is set as a Gaussian distribution, centred at 2.525 with $\sigma = 1.525$. The 1σ credible interval thus covers the range 1 to 4.05, denoted as $N(2.525, 1.525^2)$ (N for Gaussian distribution). The parameter λ_0 also has a Gaussian prior with $-0.016 \sim 0.025$ as the $\pm 1\sigma$ range, centred at 0.0045, denoted as $N(0.0045, 0.0205^2)$. The ζ parameter must be non-negative to prevent abnormal solutions of the vector field equation of motion. The parameter space where $\zeta > 0.04$ falls outside of the scope of our investigation, because it does not permit neutron stars with masses that reach $2 M_\odot$, so we set a flat prior $0 \sim 0.04$, denoted as $\mathcal{U}(0, 0.04)$ (\mathcal{U} for flat distribution, 0 and 0.04 are the lower and upper limit). The final Λ_ω parameter should be also non-negative, and we use a flat prior from 0 to 0.045, $\mathcal{U}(0, 0.045)$; outside this range the prior probability is set to zero.

As for the meson-nucleon couplings, the favoured value ranges are sometimes different depending on the experiment (Dutra et al. 2014). Due to this, wide ranges for these quantities are chosen and a hard cut off is never used for the distributions of the parameters. The g_σ^2 prior is a Gaussian distribution $N(107.5, 7.5^2)$. For g_ω^2 , we choose a flat prior, from 150 to 210, denoted as $\mathcal{U}(150, 210)$. The g_ρ^2 distribution is set as flat prior $\mathcal{U}(75, 210)$.

Together, these define a seven-dimensional prior space for the EOS (see Table 1), from which we can sample.

2.3 Nuclear matter saturation properties

All the parameters from the RMF model have a direct connection with the nuclear saturation properties. The relation between the parameters and the nuclear matter saturation properties can be found, for example, in the Appendix of Chen & Piekarewicz (2014).

As shown in that paper, given a set of isoscalar and isovector parameters, we can compute the nuclear saturation density (n_0), the energy per nucleon of symmetric matter at saturation density (E/A), the nucleon effective mass (M^*), and incompressibility of symmetric nuclear matter at saturation density (K), as well as the symmetry energy at saturation density (J) and its slope at that density (L). These nuclear matter saturation properties are reasonably well constrained by experiments, so that a plausible range is known for some of them (Dutra et al. 2014; Oertel et al. 2017; Margueron, Hoffmann Casali & Gulminelli 2018; Huth, Wellenhofer & Schwenk 2021). In particular, the nuclear saturation density n_0 ranges from

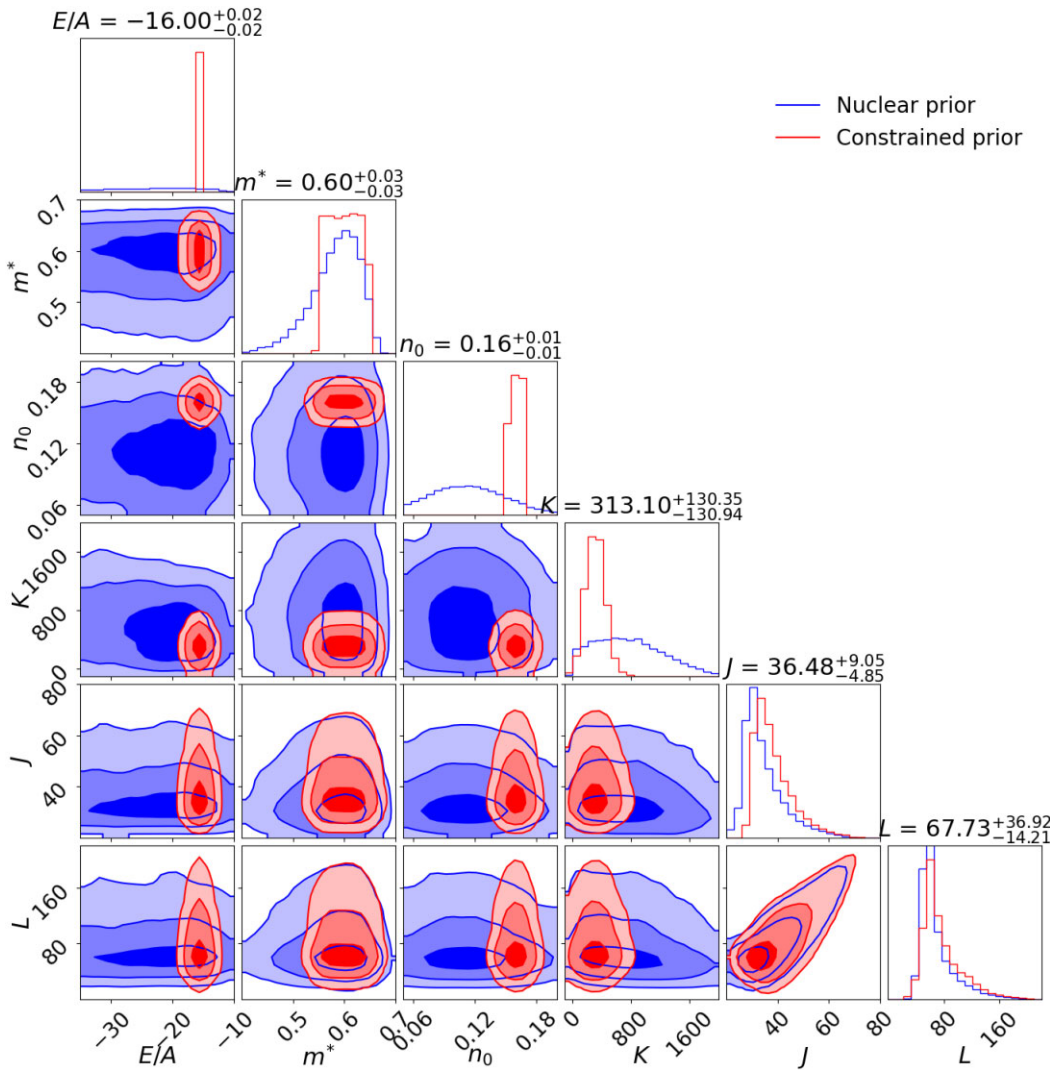


Figure 1. This corner plot illustrates the posterior distributions of the nuclear saturation properties after introducing constraints on E/A , m^* , n_0 , and the incompressibility of symmetric nuclear matter K (see Section 2.3) compared to the prior space on these properties established by the priors on the EOS parameters. K in particular would otherwise have a wide prior range that is much broader than all experimentally allowed values (note that formally, the full EOS parameter priors in Table 1 also admit values of K that are negative, but these are unphysical, so we do not show them in this plot). J is the symmetry energy at saturation density, and L is the slope of the symmetry energy at saturation density. The corner plot was produced by randomly sampling the EOS parameter space using 100 000 samples and then using the relationships between the EOS parameters and various nuclear matter properties to project the sampled points onto a five-dimensional space of nuclear quantities. In other words, the corner plot represents the distribution of nuclear quantities obtained by sampling the EOS parameter space and using the relevant relationships to compute the corresponding nuclear matter properties. The contour levels in the corner plot, going from deep to light colours, correspond to the 68, 84, and 98.9 per cent levels.

0.15 to 0.17 fm⁻³, the binding energy per particle E/A from 15.8 to 16.2 MeV, the incompressibility K from 175 to 315 MeV (Stone, Stone & Moszkowski 2014; Huth et al. 2021), the effective mass M^*/m goes from 0.55 to 0.65 (Hornick et al. 2018), and the range for the symmetry energy J lies between 25 and 38 MeV, whereas for the slope of the symmetry energy L , we have values between 30 and 86 MeV (Lattimer & Lim 2013; Oertel et al. 2017).

Note that a larger slope has been determined from the measurement of the skin thickness of ²⁰⁸Pb (Adhikari et al. 2021) in particular, $L = 106 \pm 37$ MeV was estimated in Reed et al. (2021). However, other studies (Essick et al. 2021; Reinhard, Roca-Maza & Nazarewicz 2021; Yue et al. 2022) have obtained smaller values of L . As has been discussed in Reinhard et al. (2021, 2022), Mondal & Gulminelli (2023), there is currently still some tension between experiment

and theory, and it is not clear whether the existing experimental uncertainties in the measured parity-violating asymmetry in PREX-II (Adhikari et al. 2021) make it an adequate observable to constrain theoretical models that have otherwise successfully described many other nuclear matter properties.

The values for the nuclear matter saturation properties that result from our choice of the parameter priors are spread over wider ranges than the values from nuclear experiments, especially for the incompressibility of symmetric nuclear matter K . We therefore impose some additional conditions: first, we fix E/A to be a Gaussian distribution centred on -16 MeV, with $\sigma = 0.02$, $N(-16, 0.02^2)$, and restrict m^* as $\mathcal{U}(0.55, 0.64)$ and n_0 as $\mathcal{U}(0.15, 0.17)$, as shown in Fig. 1. These quantities are needed to compute to K , J , and L . In order to include some minimal guidance for the parameter choices from

the known nuclear physics properties, but still keeping the initial objective of constraining the EOS primarily through astronomical observations, we also include a loose prior condition on K . We impose the condition that the incompressibility should satisfy $100 \lesssim K \lesssim 400$ MeV. To improve the convergence speed of the inference, we define a probability function as follows: $p(K) = -0.5 \times |250 - K^{10}/150^{10}|$, which is a super-Gaussian function. This is less extreme than a hard cut, but strongly disfavours values outside the nominal range. This condition still leaves enough freedom to explore the power of the astrophysical constraints, while avoiding extremely unreasonable nuclear matter properties.

The posterior distribution of nuclear quantities compared to the nuclear quantity prior generated from our defined EOS parameter prior is illustrated in Fig. 1. By applying these restrictions and utilizing the posterior of the EOS model parameters as new priors (referred to hereafter as *constrained priors*), it is possible to evaluate the constraining power of our observations while still maintaining the credibility of our inference from a nuclear physics perspective.

The restriction on K in particular has multiple effects on the different EOS model parameters due to the non-linear relationship between these parameters and nuclear matter properties. Some of the EOS parameter space of λ_0 has been excluded, as λ_0 exerts a significant influence on the radius of a $1.4 M_{\odot}$ star, and is therefore of interest in the context of our investigation. The cut off also has an impact on the parameter ζ , shifting it towards larger values. This is interesting as larger values of ζ may produce maximum mass stars below $2 M_{\odot}$, while smaller values are preferred for producing maximum mass stars above $2 M_{\odot}$. These opposing effects on ζ can lead to a strong constraint on the EOS parameters. This highlights the value of constraining these parameters using both nuclear physics and astrophysical methods. A similar shift can also be seen in the distributions of g_{ω} and g_{ρ} . The constrained priors (to be compared to the original priors in Table 1) can be seen in Fig. 4.

2.4 Mass–radius priors

Every point in EOS parameter space should be uniquely correlated to an EOS curve in the $P-\varepsilon$ plane. Then by varying central density, EOS points can be mapped to the M–R plane. Understanding the M–R prior that results from the EOS model choices is vital when trying to infer the M–R relation from e.g. astrophysical measurements of M–R (Greif et al. 2019).

The M–R relation is derived by solving the Tolman–Oppenheimer–Volkoff (TOV) equations (Oppenheimer & Volkoff 1939; Tolman 1939). The TOV equations for a static and spherically-symmetric system are

$$\begin{aligned} \frac{dP}{dr} &= -\frac{G}{r^2}(\varepsilon + P)(m + 4\pi r^3 P) \left(1 - \frac{2Gm}{r}\right)^{-1}, \\ \frac{dm}{dr} &= 4\pi r^2 \varepsilon, \end{aligned} \quad (6)$$

where m is the star mass for a given radial coordinate r (in spherical coordinates) and G is the gravitational constant. The TOV equations are solved by spanning the possible central densities of a neutron star. For a given central density, this set of equations gives a unique solution, that is, a point in the M–R diagram. By repeating this process for different central densities, we can map out the M–R relation. This extends to a maximum mass, beyond which solutions to the TOV equation are unstable, at which point the relation is truncated.

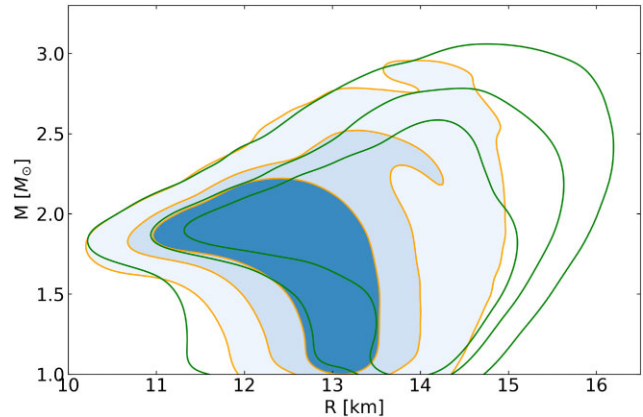


Figure 2. The M–R posterior after applying all four nuclear saturation property constraints (orange/blue), compared to the M–R prior resulting from the initial EOS model with the full EOS priors but after imposing priors on E/A , m^* , and n_0 (green), to demonstrate the effect of the additional constraint on K . The contour levels, from the innermost to the outermost, correspond to the 68, 84, and 100 per cent credible regions, 100 per cent being the point beyond which there are no more samples (for both the orange/blue and the green contours). After applying the K constraint, there are no samples with radii above 16 km. Note that the prominences on the high radius side in the post- K constraint contours are sampling artefacts.

To solve the TOV equations, we need to cover a wide range of densities. The RMF EOS introduced in Section 2.1 is taken to be the EOS in the neutron star core. We need to match this to an EOS for the neutron star crust and carefully treat the interface region. We use the BPS EOS (Baym, Pethick & Sutherland 1971) for the outer crust, the region where the energy density runs from $\varepsilon_{\min} = 1.0317 \times 10^4 \text{ g cm}^{-3}$ to $\varepsilon_{\text{outer}} = 4.3 \times 10^{11} \text{ g cm}^{-3}$. In the region between the core and the outer crust, $\varepsilon_{\text{outer}} < \varepsilon < \varepsilon_c$, where ε_c defines the crust–core transition, we use a polytropic EOS to avoid the complexity of the pasta structure (Carriere, Horowitz & Piekarewicz 2003; Piekarewicz, Fattoyev & Horowitz 2014). The complete EOS is then given by

$$P(\varepsilon) = \begin{cases} P_{\text{BPS}}(\varepsilon), & \text{for } \varepsilon_{\min} \leq \varepsilon \leq \varepsilon_{\text{outer}} \\ A + B\varepsilon^{4/3}, & \text{for } \varepsilon_{\text{outer}} < \varepsilon \leq \varepsilon_c \\ P_{\text{RMF}}(\varepsilon), & \text{for } \varepsilon_c < \varepsilon, \end{cases} \quad (7)$$

where P_{RMF} indicates the EOS computed from the RMF framework introduced previously. The parameters A and B are chosen to ensure matching at $\varepsilon_{\text{outer}}$ and ε_c . To improve the fitting accuracy and having as reference the FSU2R EOS, the inner crust is built in the following way: equation (7) is considered together with four points, one at the transition from the outer to the inner crust, $\varepsilon_{\text{outer}}$, and three other points from the unified FSU2R inner crust EOS obtained in Providêncio et al. (2019). The parameters A and B are chosen so that the inner crust EOS best fits the four points. The inner crust EOS is then matched to the core EOS at $\varepsilon_c \sim 2.14 \times 10^{14} \text{ g cm}^{-3}$ such that the pressure is an increasing function of the energy density.

The M–R prior can then be sampled by sampling the EOS parameter space and then solving the TOV equations for those parameters. The green contour lines in Fig. 2 show the M–R prior that results from the nucleonic seven-parameter priors defined in Table 1 together with the additional constraints on E/A , m^* , and n_0 . Our EOS model and prior choices favour radii in the range 13.5–14.5 km for a $1.4 M_{\odot}$ neutron star, and 11.5 to 14.5 km for a $2 M_{\odot}$ neutron star. Note that our choices do not admit any solutions for radii below

10 km in the prior space. They do, however, admit some solutions above 16 km (the maximum permissible radius is 16.18 km), which is slightly larger than the maximum of 16 km assumed in the NICER Pulse Profile Modelling analysis of Riley et al. (2019, 2021); Salmi et al. (2022).

After applying the K constraint, however, the maximum radius is under 15 km (see Fig. 2) so that the M–R space is now consistent with the priors assumed in these NICER analyses. The maximum mass is also smaller than in the case where the K constraint is not taken into account. This outcome is in line with expectations, since the K constraint generally favours larger values of ζ and smaller values of g_ω . This results in a generally softer EOS that favours a smaller maximum mass and a smaller maximum radius.

3 INFERENCE FRAMEWORK

We consider two types of inference scenarios in this work. First, we study the constraining power of current astronomical measurements: maximum masses derived from radio pulsar timing, GW measurements of tidal deformability, and M–R measurements from NICER. Secondly, we investigate the constraining power anticipated for M–R measurements made by future X-ray telescopes, like STROBE-X and eXTP. We will refer to these two scenarios as the *current constraints* and *future constraints* scenarios, respectively. Our goal with these analyses is to clarify both the constraining power we have now for fundamental nucleonic model parameters, and the prospects offered by more powerful X-ray telescopes.

The Bayesian inference methodology for the EOS parameters described here follows the framework developed and used in Greif et al. (2019), Raaijmakers et al. (2019, 2020, 2021). Bayes’ theorem states that the posterior distribution of θ and central energy densities ε is proportional to the product of the prior distribution of θ , ε , and the nuisance-marginalized likelihood function²

$$p(\theta, \varepsilon | \mathbf{d}, \mathcal{M}) \propto p(\theta | \mathcal{M})p(\varepsilon | \theta, \mathcal{M})p(\mathbf{d} | \theta, \mathcal{M}). \quad (8)$$

where θ is the seven-dimensional vector of the EOS model parameters (see Section 2.2), \mathcal{M} in this equation denotes the model, and \mathbf{d} is the data set. In this work, weighted sampling of the parameter vector θ is accomplished by the nested sampling Monte Carlo algorithm MLFriends (Buchner 2016, 2019) using the UltraNest³ package (Buchner 2021).⁴

For the *current constraints*, we consider the following astrophysical inputs: the most recent mass reported for the heavy pulsar PSR J0740+6620 derived from radio timing ($2.08 \pm 0.07 M_\odot$, Fonseca et al. 2021); the tidal deformabilities for the neutron star binary mergers GW170817 and GW190425 reported by the LIGO Scientific Collaboration (Abbott et al. 2017, 2020), and the masses and radii inferred from the NICER observations of PSR J0030+0451 and PSR J0740+6620 by Riley et al. (2019, 2021). Given that all of the measurements are independent, we can rewrite the likelihood

²For more discussion of nuisance parameters in this context, see Raaijmakers et al. (2019).

³<https://johannesbuchner.github.io/UltraNest/>

⁴3000–5000 live points were utilized, depending on the level of complexity of the obtained posterior samples. The Slice sampler in UltraNest was employed, which is well suited and efficient for high-dimensional sampling. It also ensures consistency in the convergence speed of the sampling process.

function:

$$\begin{aligned} p(\theta, \varepsilon | \mathbf{d}, \mathcal{M}) &\propto p(\theta | \mathcal{M})p(\varepsilon | \theta, \mathcal{M}) \\ &\times \prod_i p(\Lambda_{1,i}, \Lambda_{2,i}, M_{1,i}, M_{2,i} | d_{\text{GW},i} (\mathbf{d}_{\text{EM},i})) \\ &\times \prod_j p(M_j, R_j | d_{\text{NICER},j}) \\ &\times \prod_k p(M_k | \mathbf{d}_{\text{radio},k}). \end{aligned} \quad (9)$$

Note that we equate the nuisance-marginalized likelihoods to the nuisance-marginalized posterior distributions (for more details of this step and why it is justified see Section 2 of Raaijmakers et al. 2021).

When treating the GW events, we fix the chirp mass $M_c = (M_1 M_2)^{3/5} / (M_1 + M_2)^{1/5}$ to the median value $M_{c1} = 1.186 M_\odot$ for GW170817 and $M_{c2} = 1.44 M_\odot$ for GW190425. It was shown in Raaijmakers et al. (2021) that the small bandwidth of the chirp masses has almost no significant influence on the posterior distribution, contributing less than the sampling noise. We therefore fix the chirp mass, which is beneficial in also reducing the dimensionality of the parameter space and hence the computational cost. To speed up convergence of our inference process, we transform the GW posterior distributions to include the two tidal deformabilities, chirp mass and mass ratio q , simultaneously reweighing such that the prior distribution on these parameters is uniform. The posterior then becomes

$$\begin{aligned} p(\theta, \varepsilon | \mathbf{d}, \mathcal{M}) &\propto p(\theta | \mathcal{M})p(\varepsilon | \theta, \mathcal{M}) \\ &\times \prod_i p(\Lambda_{1,i}, \Lambda_{2,i}, q_i | M_c, \mathbf{d}_{\text{GW},i} (\mathbf{d}_{\text{EM},i})) \\ &\times \prod_j p(M_j, R_j | \mathbf{d}_{\text{NICER},j}) \\ &\times \prod_L p(M_L | \mathbf{d}_{\text{radio},L}), \end{aligned} \quad (10)$$

where $\Lambda_{2,i} = \Lambda_{2,i}(\theta; q_i)$ is the tidal deformability. We follow the same convention as in Abbott et al. (2018) and define $M_1 > M_2$, since the gravitational wave likelihood function is degenerate under exchange of the binary components.

For the *future constraints*, we consider the data set \mathbf{d} to be composed of M–R constraints of the quality that we anticipate from the next-generation X-ray telescopes (such as STROBE-X or eXTP). This is relatively straightforward to predict given that uncertainties in masses and radii should scale in a simple fashion with exposure time and telescope effective area (Lo et al. 2013; Psaltis, Özel & Chakrabarty 2014). While new GW measurements of tidal deformabilities are anticipated on a similar time-scale, it is hard to predict the quality of these given the dependence on source properties and the uncertainties in merger rates. It is also difficult to say with certainty whether we can expect an improved or increased maximum mass measurement from radio timing. We thus do not include any future GW or radio constraints in our *future constraints* simulations. It is also valuable to consider what can be achieved by a single technique for the purposes of independent cross-checks of different methods.

In this scenario, with only inferred masses and radii from X-ray pulse profile modelling, the likelihood function in equation (8) is given by:

$$\begin{aligned} p(\theta, \varepsilon | \mathbf{d}, \mathcal{M}) &\propto p(\theta | \mathcal{M})p(\varepsilon | \theta, \mathcal{M}) \\ &\times \prod_j p(M_j, R_j | d_{\text{Future/Future-X},j}). \end{aligned} \quad (11)$$

Table 2. This table shows the FSU2R, TM1- $2\omega\rho$, and BMPF260 parameter vectors (the latter two being used to generate simulated M–R measurements to test parameter recovery). The row labelled Posterior gives the median and 68 per cent credible intervals for the parameters as inferred from current observations, see Section 4.

Model	m_σ (MeV)	m_ω (MeV)	m_ρ (MeV)	g_σ^2	g_ω^2	g_ρ^2	κ	λ	ζ	Λ_ω
FSU2R	497.479	782.500	763.000	107.58	182.39	206.43	3.0911	-0.001680	0.024	0.045
TM1- $2\omega\rho$	511.198	783.000	770.000	99.97	156.34	127.75	3.5235	-0.004739	0.012	0.030
BMPF260	500.000	782.500	763.000	100.02	161.82	100.70	2.3030	-0.017016	0.002	0.038
Posterior	497.479	782.500	763.000	$108.22^{+7.49}_{-7.32}$	$175.67^{+21.42}_{-17.64}$	$140.05^{+47.15}_{-44.72}$	$2.47^{+1.34}_{-1.37}$	$0.0035^{+0.0095}_{-0.0092}$	$0.0228^{+0.0047}_{-0.0048}$	$0.0225^{+0.0153}_{-0.0154}$

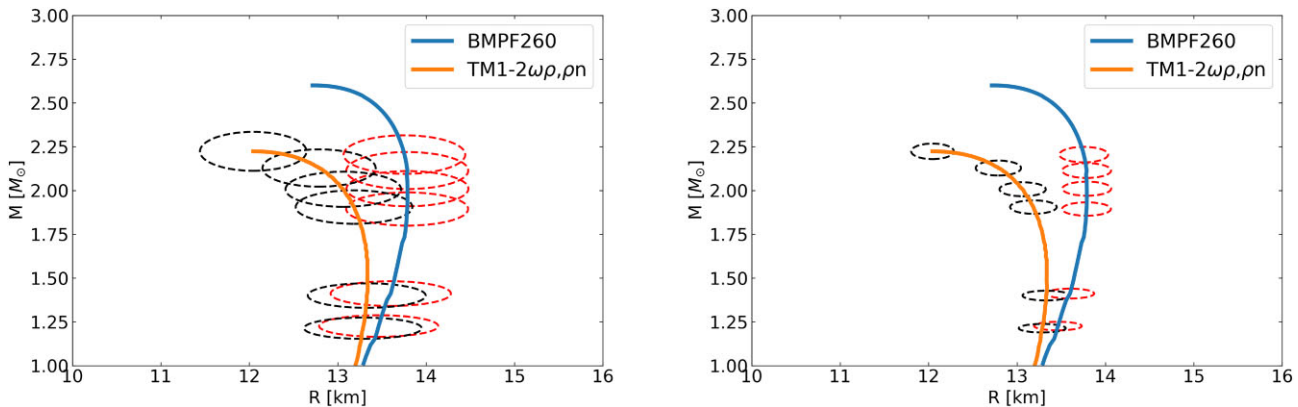


Figure 3. M–R curves for the TM1- $2\omega\rho$ EOS and BMPF260 EOS, which are two underlying scenarios (injected EOS parameter vectors), used to generate simulated mass–radius measurements for the *future constraints* scenario. The red dashed curves are the six simulated M–R posteriors, which are centred at $[1.2, 1.4, 1.9, 2.0, 2.1, 2.2] M_\odot$. Left-hand panel: corresponding to *Future* scenario with six 5 per cent uncertainty M–R observations. Right-hand panel: corresponding to *Future-X* scenario with six 2 per cent uncertainty M–R posteriors.

Based on studies of the capabilities of future telescopes (Watts et al. 2016; Watts 2019), we define two Future observation cases for study (similar to the scenarios considered in Rutherford et al. 2023). In our ‘Future’ set-up, somewhat beyond what is expected to be achievable with NICER, we assume that we will have six M–R measurements, which we model as bivariate Gaussians with 5 per cent uncertainty, distributed from ~ 1.2 to $\sim 2.2 M_\odot$, which are centred at $[1.2, 1.4, 1.9, 2.0, 2.1, 2.2] M_\odot$. These simulated measurements span a reasonable range compared to current observations and include three values corresponding to known masses for current NICER sources: PSR J0740+6620 ($2.1 M_\odot$, Cromartie et al. 2020; Fonseca et al. 2021), PSR J1614-2230 ($1.9 M_\odot$, Demorest et al. 2010), and PSR J0437-4715 ($1.4 M_\odot$, Reardon et al. 2016). In the ‘Future-X’ scenario, we upgrade our precision of the previous six measurements to the 2 per cent uncertainty level, distributed over the same mass range. This represents a ‘best case’ scenario for what we might be able to achieve with a telescope like STROBE-X or eXTP.

To assess parameter recovery, we now selected some specific EOS parameter vectors to test. Picking such a vector determines the M–R relation that is used to generate simulated M–R measurements (for the mass vector given in the previous paragraph). We choose the TM1- $2\omega\rho, pn$ EOS model (Providencia & Rabhi 2013), and the BMPF260 model (Malik et al. 2023), which are based on the same underlying model as FSU2R. Their parameter vectors are given in Table 2, with the parameters for FSU2R shown for comparison. The resulting M–R relations together with the simulated measurements are shown in Fig. 3. Note that in this study, due to computational constraints, we consider only two injected parameter vectors; while our results are still illustrative of the capabilities of future missions, follow-on studies should ideally examine parameter recovery for a broader range of injected models (and simulated M–R posteriors).

4 EOS CONSTRAINTS FROM CURRENT OBSERVATIONS

In this section, we investigate how well existing observations constrain both the EOS parameters and the corresponding nuclear matter saturation properties. We use the masses and radii inferred from NICER data by Riley et al. (2019) for the pulsar PSR J0030+0451 ($M = 1.34^{+0.15}_{-0.16} M_\odot$ and $R = 12.71^{+1.14}_{-1.19} \text{ km}$) and by Riley et al. (2021) for the heavy pulsar PSR J0740+6620 ($M = 2.07 \pm 0.07 M_\odot$ and $R = 12.39^{+1.30}_{-0.98} \text{ km}$), and the two GW tidal deformability measurements (Abbott et al. 2017, 2020), with GW170817 in particular favouring softer EOS.

In Fig. 4, we show the posterior distribution of the EOS parameters. The only parameters for which we see variation from the prior are ζ , g_ρ , and a very small shift in g_ω . This result is reasonable considering the precision of the current measurements; it is still not possible to extract strong constraints on all of the model parameters from the current M–R and tidal deformability measurements.

Significant constraints are achieved for ζ , a parameter that influences both the maximum mass, stellar mass, and radius simultaneously; both of them increase when ζ decreases. Extreme values are disfavoured, instead the data favour a middle value of ζ that allows a maximum mass compatible with PSR J0740+6620 and radii that are consistent with both the NICER and GW measurements. Fig. 5 illustrates the constraints that would have been delivered had we used only the mass measurement for PSR J0740+6620 from Fonseca et al. (2021), rather than the NICER M–R constraint for that source. The posterior on λ_0 shifts very slightly due to its sensitivity to the radius. However, the ζ parameter distribution becomes much sharper once the radius information is included, and values of $\zeta < 0.01$ become highly disfavoured. The parameters λ_0 and

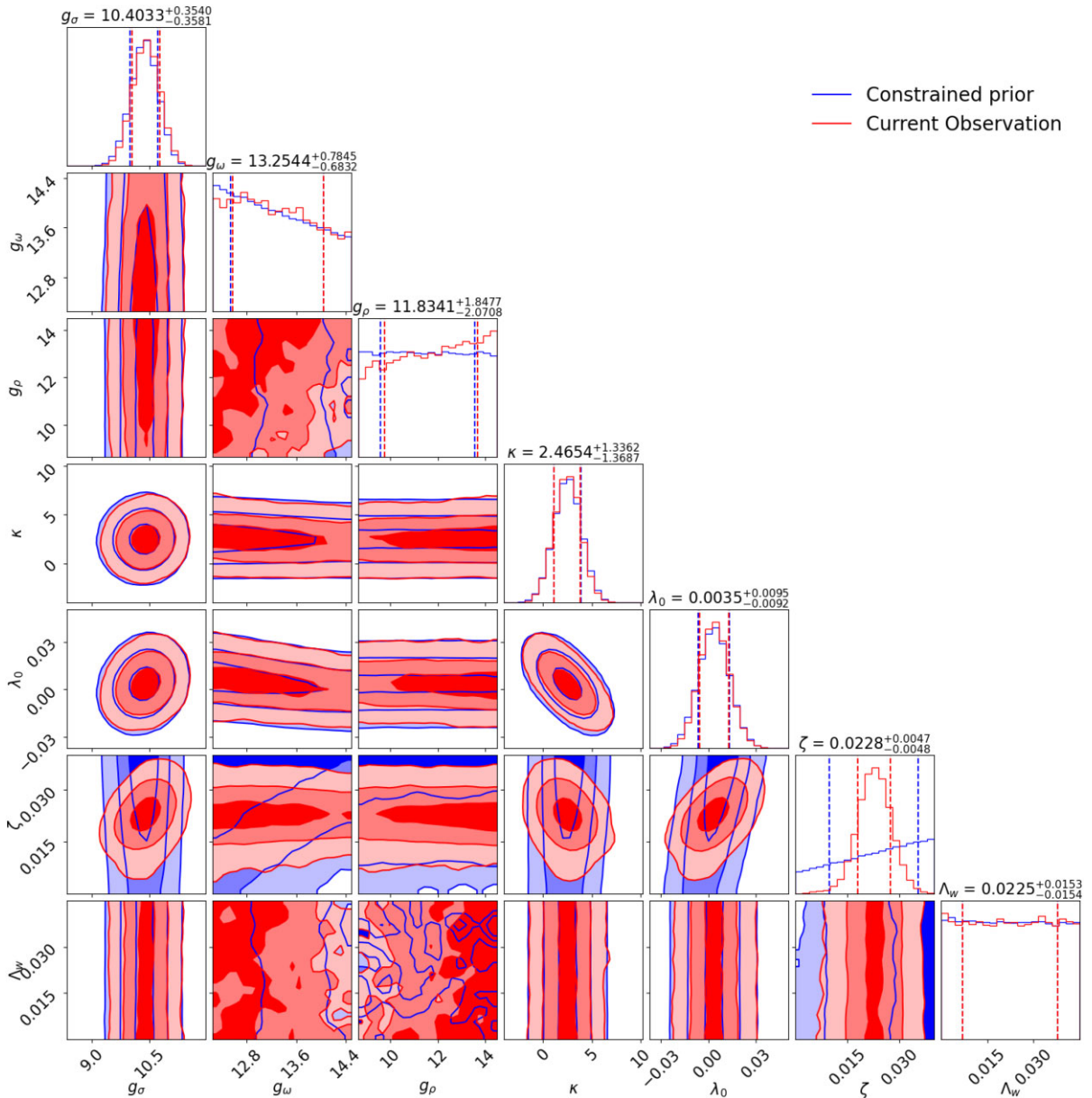


Figure 4. The posterior of the nucleonic EOS model parameters after applying constraints for all existing observations. Blue indicates the constrained priors, red the posteriors. The contour levels in the corner plot, going from deep to light colours, correspond to the 68, 84, and 98.9 per cent levels. The dashed line in the 1D corner plots represents the 68 per cent credible interval, and the title of that plot indicates the median value of the distribution as well as the range of 68 per cent credible interval. Here, κ is given in MeV.

ζ affect the symmetric nuclear matter properties, and therefore the incompressibility. K is the nuclear matter property most affected by *current observation* constraints, as seen in Fig. 6, where the posterior of all the nuclear quantities after applying constraints from current astrophysical observations are shown. Notice that in our analysis, the other symmetric nuclear matter properties (E/A , m^* , and n_0) are allowed to vary in a small range. The g_ρ shows a small increase, which results in a slight increase of the symmetry energy at saturation, however, these changes are not very significant (see Fig. 6).

One approach to evaluate the plausibility of the EOS models based on the same framework used in this work is to compute the Bayesian evidence for that model given current measurements. Table 3 gives the global log evidence ($\ln Z$) as returned by Ultranest for both individual EOS models with fixed parameters and our full RMF

model. For the fixed EOS parameter models, the only free parameters in the sampling process are the central densities of the stars for which astrophysical constraints are available. For the full RMF model, the EOS parameters are also free, and this affects the global evidence calculation due to the larger prior space. To illustrate this, we also give $\ln Z$ for a run where we fix the EOS parameters of the RMF model to those of the maximum posterior sample, so that only the central densities vary. As might be expected, the evidence improves by an amount that should be borne in mind when comparing to the other fixed parameter models.

In comparing the models, we use Bayes' factors. Kass & Raftery (1995) deem a model 'substantially preferred' if the Bayes' factor is more than 3.2 and 'strongly preferred' if more than 10. By this metric, the full RMF model is strongly preferred compared to IU-FSU, and

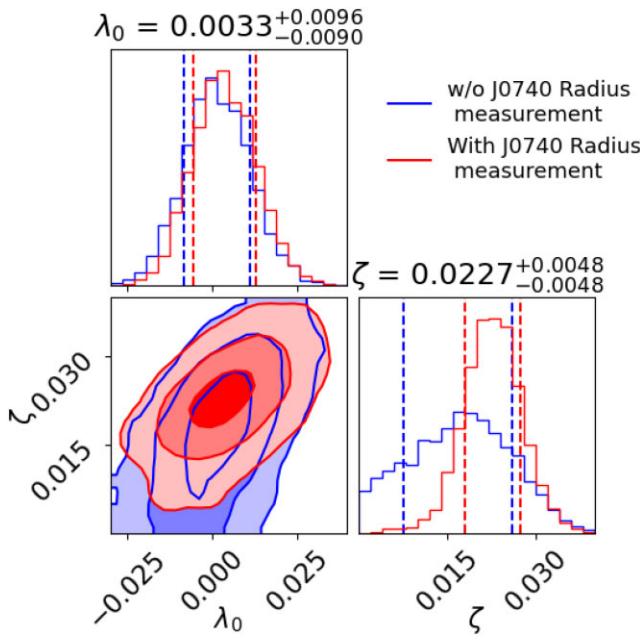


Figure 5. Comparison between the observational constraint with (red) and without (blue) the NICER PSR J0740+6620 radius measurement. The contour levels in the corner plot, going from deep to light colours, correspond to the 68, 84, and 98.9 per cent levels. The dashed line in the 1D corner plots represents the 68 per cent credible interval, and the title of each plot indicates the median value of the distribution as well as the range of 68 per cent credible interval.

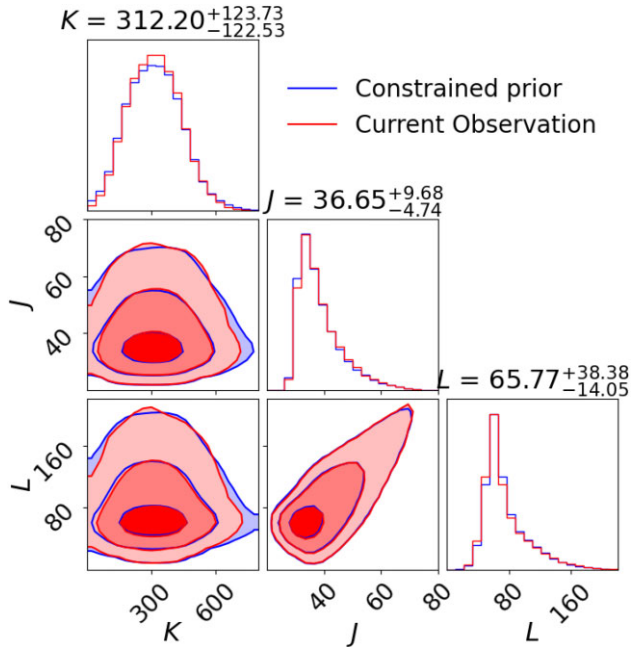


Figure 6. The posterior of all the nuclear quantities after applying constraints from current astrophysical observations. The contour levels in the corner plot, going from deep to light colours, correspond to the 68, 84, and 98.9 per cent levels. The dashed line in the 1D corner plots represents the 68 per cent range, and the title of that plot indicates the median value of the distribution as well as the range of 68 per cent credible interval.

Table 3. This table gives the global log evidence ($\ln Z$), as returned by Ultra-nest, for various different EOS models and current astrophysical constraints. For individual EOS models (above the line), the EOS model parameters are fixed, and the only free parameters in the sampling are the central densities of the stars, for which we have constraints. For our full parametrized RMF model (below the line), the EOS parameters are free as well; this affects the evidence computation since the prior space is larger. To illustrate this, we also give $\ln Z$ for the case where we fix the RMF EOS parameters to those of the maximum posterior sample in the full analysis; in this run, only the central densities vary. In this sense, it is more comparable to the other individual models.

Model	$\ln(Z)$	Bayes' factor ($Z/Z_{\text{Full RMF}}$)
FSUGarnet	-2.810	7.83
FSU2	-2.942	6.86
FSU2R	-2.967	6.69
TM1- $2\omega\rho$	-3.795	2.92
BigApple	-5.397	0.589
NL3	-6.986	0.120
IU-FSU	-7.356	0.083
RMF: Full model	-4.868	...
RMF: Max posterior	-2.753	8.29

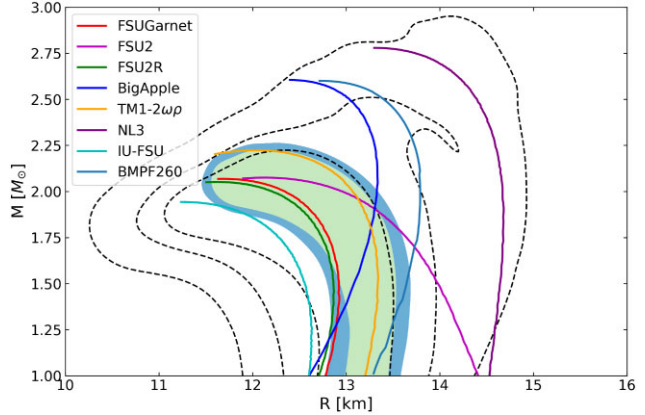


Figure 7. The posterior in M–R space once all current astrophysical constraints are taken into account, showing the 68 (light green) and 84 per cent (blue) credible regions. For comparison, we show M–R relations for various individual EOS models that map to specific individual parameter vectors within the broad prior space of our model. The outer black dashed line delineates the shape of our constrained M–R prior, delineating the 68, 84 per cent credible region, and 100 per cent credible regions (as in Fig. 2).

substantially preferred compared to NL3. FSUGarnet, FSU2, and FSU2R are substantially preferred compared to the full RMF model (but are statistically indistinguishable if one considers instead the Bayes' factor computed with reference to the Max Posterior RMF run).

In Fig. 7, we present the M–R posterior generated as a result of incorporating all current observational constraints. For the purpose of comparison, we have also plotted the EOS models that have been evaluated for evidence. From this figure, it is evident that the evidences of the EOS are correlated with their relative positioning to the inferred M–R posterior contour. The maximum posterior EOS set-up (denoted as ‘MAX’, detailed parametrization of this EOS in Table 2) has been plotted. It is seen that it does not fully traverse the region of maximum probability in the M–R space. This is understandable as the parameters utilized in this set-up essentially affect the high-density EOS. As a result, the MAX method is able to traverse a wide range of the highest-probability M–R posterior having

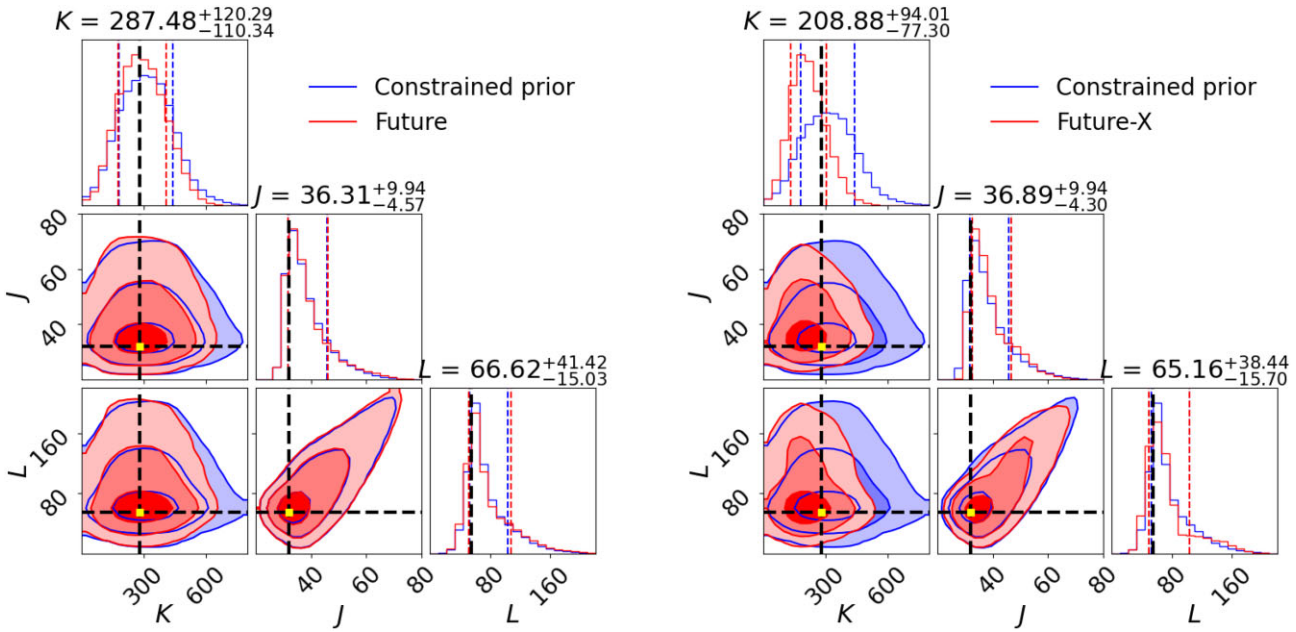


Figure 8. The posterior distributions of the nuclear quantities in the Future (left) and Future-X (right) scenarios for TM1-2 $\omega\rho$ as the injected model. In both panels, blue shows the constrained prior. The contour levels in the corner plots, going from deep to light colours, correspond to the 68, 84, and 98.9 per cent levels. The dashed line in the 1D corner plots represents the 68 per cent range, and the title of that plot indicates the median value of the distribution as well as the range of 68 per cent credible interval. The black dashed horizontal and vertical lines in the plot and yellow dots show the injected values used to generate the simulated M–R measurements.

high central energies, but is limited in its ability to traverse the low mass high posterior probability in the M–R space, approximately below $1.4 M_{\odot}$. This region is more closely influenced by the EOS of the inner crust. In future studies, it will be beneficial to utilize a universal EOS set-up that incorporates models for the core, inner crust, and outer crust in order to overcome this limitation. As is evident from the M–R contour presented, current observations, despite having ample room for improvement in terms of precision, are already capable of imposing a significant constraint on the EOS within the corresponding M–R space.

5 EOS CONSTRAINTS FROM FUTURE MASS–RADIUS MEASUREMENTS

In this section, we investigate the effectiveness of using simulated M–R measurements, of the type expected from future missions, to constrain the EOS. We do not consider any tidal deformability measurements, focusing purely on what can be delivered by pulse profile modelling. We consider two scenarios: six measurements with a 5 per cent uncertainty on the M–R of a single star, referred to as the Future scenario, and six measurements with a 2 per cent uncertainty on the M–R of a single star, the Future-X scenario. This section is organized as follows: results using TM1-2 $\omega\rho$ as the injected model are presented in Section 5.1 for the Future scenario and Section 5.2 for Future-X. We compare the two scenarios in Section 5.3. In Section 5.4, we repeat this analysis using a different injected model, BMPF260.

5.1 Constraints from the ‘Future’ scenario

In this section, we investigate the impact of the Future scenario on the constraints for the nucleonic model. The simulated M–R measurements are shown in the left-hand panel of Fig. 3. The

posterior of the EOS parameters is compared to the constrained priors in Fig. 9.

With the implementation of more stringent constraints, the posterior distribution of g_{ω} shifts a little towards lower values, serving as a potential screening tool for various EOS models that incorporate this parameter. The distributions of g_{ρ} and Λ_{ω} shift only very slightly to favour two extremities.

The parameters κ and λ_0 are constrained a little more tightly than the prior, with a slightly narrower range favoured by the inference. The parameter ζ is reshaped into a Gaussian-like distribution favouring a median value, with most of the prior space being excluded.

One notable observation is that even though we implemented more precise measurements compared to current observations, the exclusion of parameter space is only slightly better (comparing Figs 4 and 9). However, note that this is now delivered by M–R measurements alone, with no GW input – an important step to facilitating cross-comparisons of the different techniques and any potential systematic or modelling errors. The nuclear quantities resulting from the Future posterior are seen in left-hand panel of Fig. 8. Interestingly, the incompressibility K shows stronger constraints from the simulated measurements (Fig. 8), compared to the *current constraints* (Fig. 6). This underscores the importance of having radius measurements of high-mass stars.

5.2 Constraints from the ‘Future-X’ scenario

In this section, we explore the constraints arising from the Future-X scenario, in which the previous six simulated measurements now have 2 per cent M–R uncertainty. The simulated M–R measurements are shown in the right-hand panel of Fig. 3. In Fig. 9, the posterior distribution of the EOS parameters is compared to the prior.

The Future-X scenario, unlike the previous analyses, demonstrates the capability to extract robust constraints for almost all of the EOS

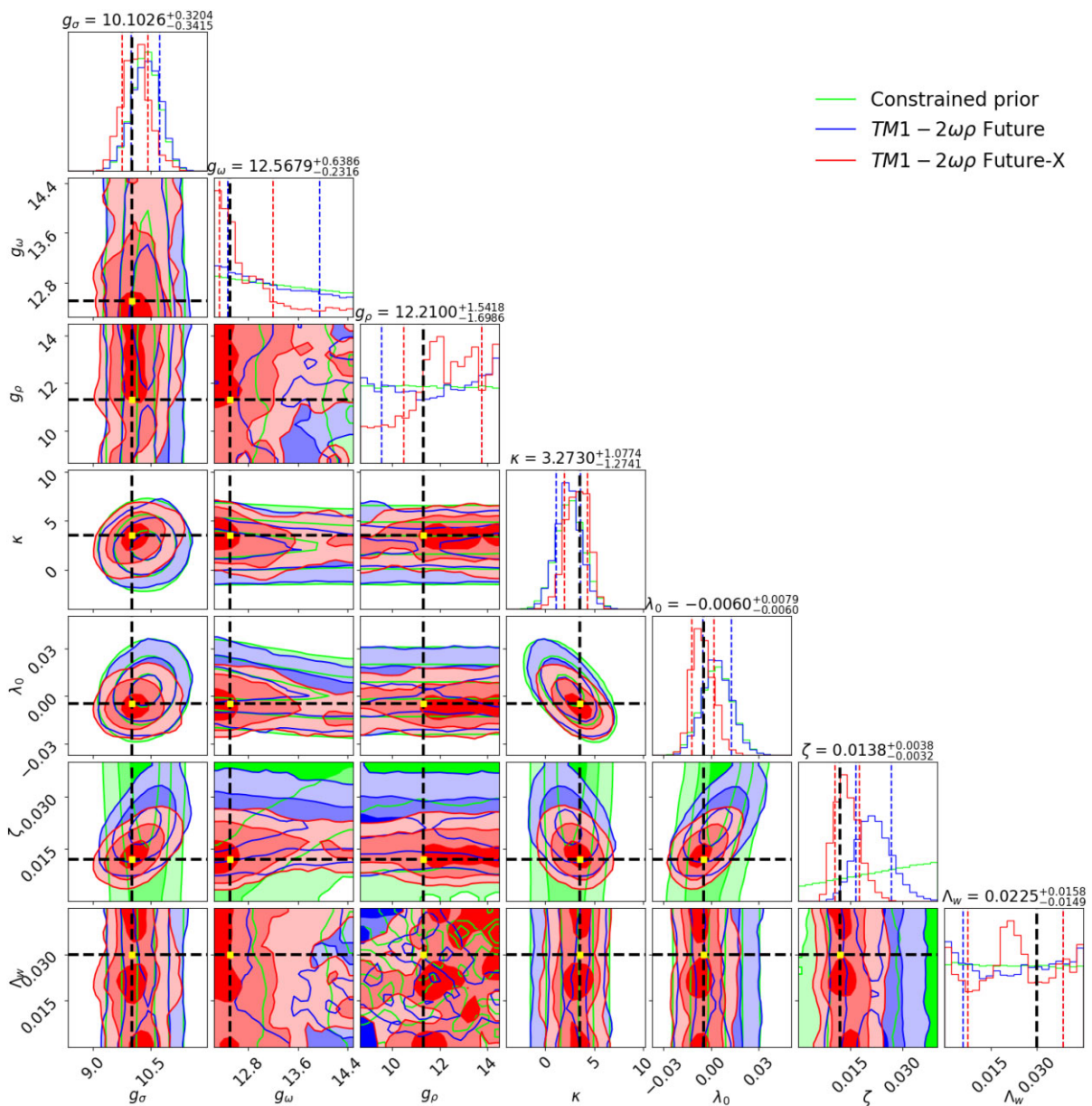


Figure 9. Comparison between the observational constraints from the Future and Future-X scenarios using TM1- $2\omega\rho$ as the injected EOS model used to generate the synthetic M-R posteriors. Lime green is the constrained prior, blue is the Future posterior, and Red the Future-X posterior. The contour levels in the corner plot, going from deep to light colours, correspond to the 68, 84, and 98.9 per cent levels. The dashed line in the 1D corner plots represents the 68 per cent range, and the title of that plot indicates the median value of the distribution as well as the range of 68 per cent credible interval. Here, κ in MeV. The black dashed horizontal and vertical lines in the plot and yellow dots show the injected values used to generate the simulated M-R measurements.

parameters. This results in a significant decoupling of the parameters from the prior distribution and reflects the fundamental properties of neutron stars. The parameters serve as a set of reliable indicators for distinguishing between numerous EOS, as demonstrated in Table 3. This provides stronger evidence for the exclusion or favouring of different models based on the posterior obtained from Future-X.

In Fig. 9, the constraint on ζ becomes even tighter than before. More than half of the g_ω prior space falls outside of the 68 per cent Future-X range, as the inference homes in on the input value. The inferred value of g_σ also shifts slightly: note that there is a link between g_σ and g_ω to reproduce the correct binding energy. The distribution of g_ρ generally favours a higher value, significantly reducing the 68 per cent credible interval. A shift in the distribution

of κ and λ_0 can also be observed. The behaviour of the posterior distribution of Λ_ω is particularly interesting. While no region of parameter space is excluded, we have seen the posterior distribution of this parameter starts to show some structure, meaning that it has been constrained. This trend was not observed in the Future scenario posterior. Note that Λ_ω is directly related to the symmetry energy, and it is expected that this parameter is mostly sensitive to observations that depend on the composition – in particular the proton fraction – such as cooling.

The nuclear quantities inferred from the Future-X posterior are depicted in the right-hand panel of Fig. 8. It is noteworthy that the posterior distribution of the incompressibility K has shifted significantly, and a considerable amount of parameter space has been

Table 4. This table shows the KL divergence comparison between current observations, Future and Future-X.

Parameters	Current constraints	Future	Future-X
g_σ	0.072620	0.099102	0.101921
g_ω	0.005315	0.039137	0.114267
g_ρ	0.022659	0.117450	0.223765
κ	0.001402	0.045308	0.054384
λ_0	0.038278	0.061046	0.095424
ζ	0.038472	0.073276	0.073910
Λ_ω	0.023653	0.034307	0.037426

excluded. However, this remains the only derived nuclear quantity that is strongly constrained by these simulated observations.

5.3 Comparing Future and Future-X

Although the range of parameter space excluded may not seem large, particularly for the Future scenario, the constraining power of the measurements in both future scenarios is an improvement over current constraints. To demonstrate this, we compute the Kullback–Leibler (KL) divergence, a measure of the parameter-by-parameter information gain of the posterior over – in this case – the constrained prior. If the KL divergence is zero, it implies no information gain; KL divergence is normalized (using the factor $1 - \exp(-D_{KL})$, where D_{KL} is the unnormalized KL divergence) such that the maximum value is 1. The KL divergence values for the seven parameters are given in Table 4, comparing the Future and Future-X with current observations. Every parameter shows an improvement as measured by the KL divergence value.

From this perspective, the Future and Future-X scenarios demonstrate stronger constraining power for some parameters. Our simulated observations constrain some of the parameters that define the symmetric nuclear matter EOS, but are not very sensitive to the symmetry energy, since the parameters g_ρ and Λ_ω are not affected as strongly as the other parameters.

Concerning the symmetric nuclear matter behaviour, g_σ and g_ω define the binding energy at saturation, g_ω , κ , and λ_0 are strongly related to the incompressibility, and ζ softens the EOS at large densities, allowing the reproduction of the mass and radius of the pulsar PSR J0740+6620. However, with the advancement in precision and an increase in the number of measurements, we have shown that the above limitations may be gradually overcome. As precision improves and new measurements are introduced, certain parameters will start to be constrained, decoupled from our prior set-up, as evidenced by a shift in posterior probability or exclusion of a certain parameter space.

The results shown in Fig. 9 demonstrate the increased constraining power of both Future and Future-X on the EOS parameters. It is observed that the parameter space of g_σ , g_ω , κ , λ_0 , and ζ has become narrower due to the improvement in precision of the simulated measurements. Furthermore, both g_ρ and Λ_ω exhibit a stronger preference for certain values. Upon comparing the contours of the posterior distribution with the position of the injected parameters used to generate the simulated M–R measurements (indicated by the black dashed lines in the plot), it is evident that an improvement in precision results in better recovery of the injected parameters. We note that, with the exception of Λ_ω , all of the injected parameters (yellow dots) fall within the 68 per cent credible regions. For Λ_ω , this is not unexpected, since this parameter is the least sensitive to M–R measurements and hence still strongly determined by our priors.

However, it is reasonable to anticipate that increasing the precision or the number of M–R measurements will eventually shape Λ_ω as a distribution peak at the injected value, thereby providing us with the potential to reproduce the full EOS from inference.

Overall, the goal of constraining the entire EOS parameter space has been achieved, as all parameters have deviated or are starting to deviate from the prior distributions, indicating that we would be entering the data-dominated rather than prior-dominated regime.

5.4 Comparing different injected parameter vectors

In this section, we explore the dependence of our results on the injected parameter vector being tested, and study the Future and Future-X scenarios for simulated M–R measurements based on the BMPF260 EOS (Malik et al. 2023). This particular EOS model allows for stars with a maximum mass of $2.5 M_\odot$ and produces larger radii than the TM1 – $2\omega\rho$, for stars with the same mass (see Fig. 3). By using the same fixed set of stellar masses [1.2, 1.4, 1.9, 2.0, 2.1, 2.2] M_\odot , we aim to isolate the influence of different radius measurements on the exclusion of parameter space.⁵ The results are shown in Fig. 10.

For this alternative injected model and this particular choice of injected masses, the data are less constraining: the only major improvement is in the constraint on ζ . Future-X performs better than Future (as we would expect), but even with Future-X, we do not recover the injected value of ζ within the 68 per cent credible interval.

This illustrates some important issues. First, it shows that a lower radius for the highest mass star in the data set is, for this model, more constraining. This can be understood from the M–R prior space shown in Fig. 2 and the influence of ζ . There is simply less prior space that allows lower radii at high mass. It also illustrates, however, that constraints will be weaker if we are not able to measure the full spread of masses allowed by the underlying EoS: the maximum mass star in our synthetic data set is well below the maximum allowed by the BMPF260 model. Constraints would be tighter if we had a higher mass star in the sample, and this is one motivation for trying to increase the sample size as much as possible for future instruments. A high mass measurement obtained from a complementary technique (radio pulsar timing or gravitational wave measurements if the compact object could be unequivocally identified as a neutron star) could also be incorporated.

6 ADDITIONAL PHYSICS OUTPUT FROM CURRENT CONSTRAINTS

In addition to the M–R information that can be used to constrain the EOS, more information can be extracted from these inferences. One particularly interesting piece of information is the constraint on the speed of sound from our model, which is computed from the derivative of the pressure with respect to the energy density. This information can be computed by resampling the posterior EOS parameter space. The result can be seen in Fig. 11, which shows the posterior distribution of c_s^2 after applying constraints from all available current observations. This figure also shows the constrained prior distribution, which allows us to conclude that the current observations have a constraining power on the speed of sound.

⁵Note that in this case, since the injected radius is larger, the absolute uncertainty in radius is higher than for the previous model for our two future scenarios.

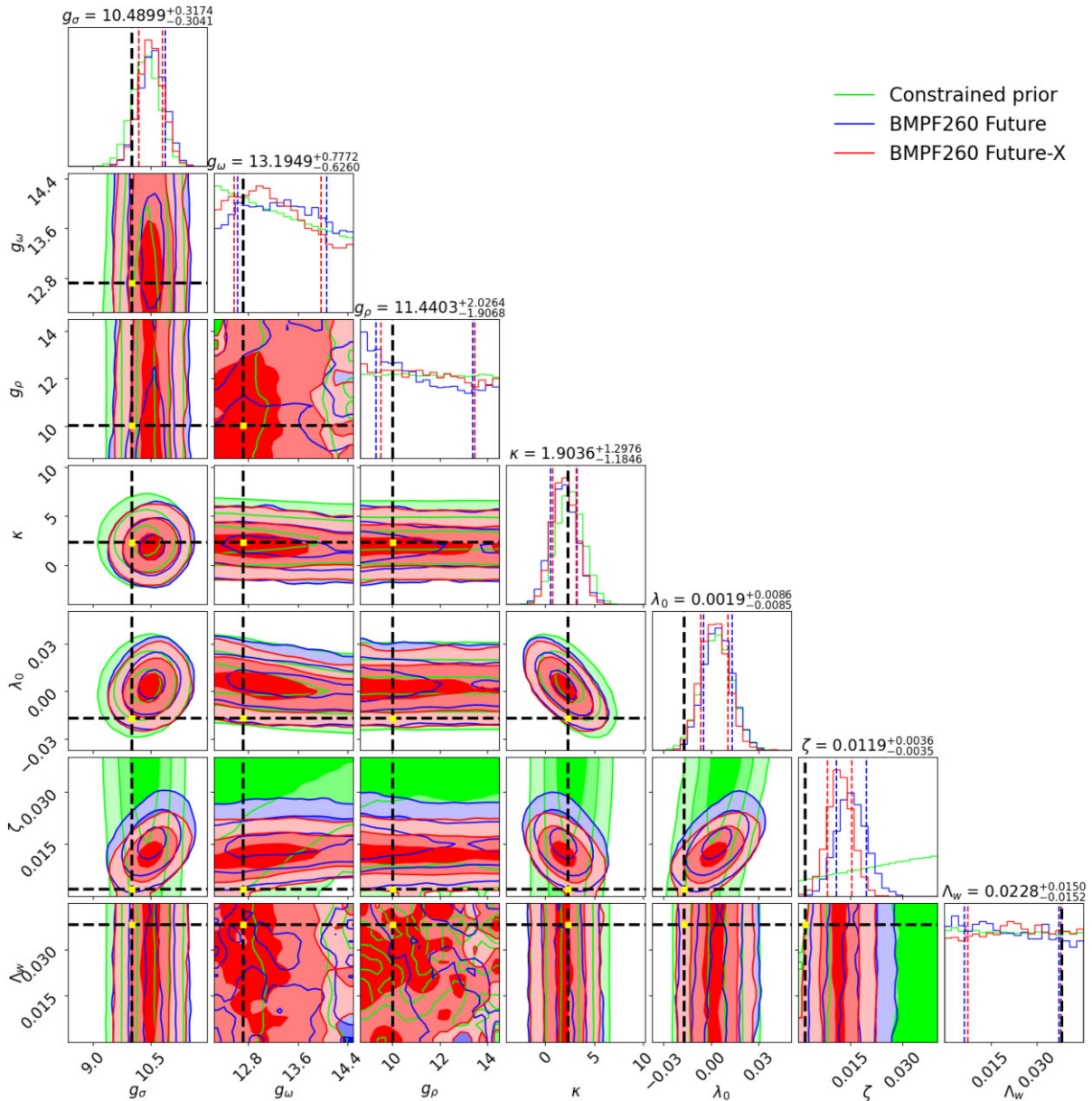


Figure 10. Comparison between the observational constraints from the Future and Future-X scenarios using BMPF260 as the injected EOS model used to generate the synthetic M–R posteriors. Lime green is the constrained prior, blue is the Future posterior, and red is the Future-X posterior. The contour levels in the corner plot, going from deep to light colours, correspond to the 68, 84, and 98.9 per cent levels. The dashed line in the 1D corner plots represents the 68 per cent range, and the title of that plot indicates the median value of the distribution as well as the range of 68 per cent credible interval. Here, κ in MeV. The black dashed horizontal and vertical lines in the plot and yellow dots show the injected values used to generate the simulated M–R measurements.

This reflects the constraining power previously identified on the isoscalar channel, in particular on the ζ coupling. As we are using a relativistic mean field theory framework, we expected causality to be automatically equipped as a relativistic model. Our result is surprising because the inferred speed of sound never exceeds $\sqrt{0.45}c$ at the 84 per cent level, and approaches a stable value after reaching a sufficiently high density. The speed of sound behaviour obtained in the present inference analysis is rather different (more restrictive, no turnover at an intermediate density, and no extension to values above $\sqrt{0.7}c$) compared to what has been obtained from previous speed of sound inferences using NICER and GW data (see, e.g. Legred et al. 2021; Raaijmakers et al. 2021; Altiparmak, Ecker & Rezzolla 2022; Annala et al. 2022, 2023; Gorda, Komoltsev & Kurkela 2023). In

Bedaque & Steiner (2015), the authors have shown that a speed of sound always below the conformal limit would be in tension with the observation of two solar mass neutron stars (see also Alford et al. 2013; Chamel et al. 2013). This conclusion was confirmed in Tews et al. (2018), where the authors with just nuclear matter constraints obtained an increasing speed of sound with density. In Tews et al. (2018), no peak was obtained around three times saturation density, as in studies where perturbative QCD constraints were also included (Annala et al. 2020; Altiparmak et al. 2022; Gorda et al. 2023). The behaviour of speed of sound in our analysis is partly due to the underlying framework used to generate the neutron stars EOS, which allows for different high density behaviours of the speed of sound, as discussed in Müller & Serot (1996). If the parameter ζ is

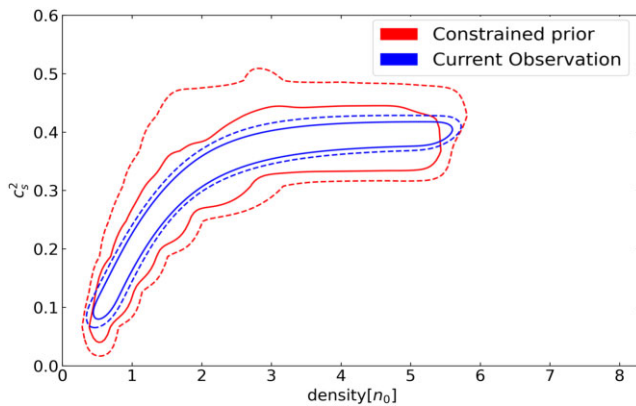


Figure 11. The posterior distribution of c_s^2 derived from current observations (blue solid line – 68 per cent credible interval, blue dashed line – 84 per cent credible interval), compared to the constrained prior distribution (same levels) in red.

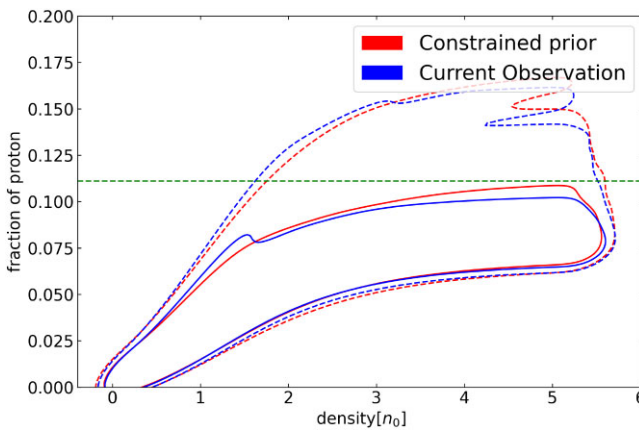


Figure 12. The posterior distribution of the proton fraction in neutron stars, derived from current observations (blue solid line – 68 per cent credible interval, blue dashed line – 84 per cent credible interval), compared to the constrained prior distribution (same levels) in red. The green horizontal line defines the nucleonic direct Urca onset when muons are not considered, $y_p = 1/9$. Note that the prominences at the boundaries of the contour levels are sampling artefacts.

large enough, the high density behaviour of the EOS changes from rising with the square of the density to increasing with a smaller power. The interesting result of our analysis is that observations favour large values of ζ , and therefore a speed of sound that saturates around $\sqrt{0.4}c$ instead of increasing to values close to c as in Tews et al. (2018). Besides in a recent work, it was shown that EOS with large values of ζ are compatible with the pQCD EOS (Malik et al. 2023). Our analysis of current observations requires a speed of sound larger than the conformal limit $c/\sqrt{3}$ in the interior of neutron stars, confirming the conclusions of Bedaque & Steiner (2015) and Tews et al. (2018), but not an increasing function of density as in Tews et al. (2018), nor with a sharp peak as in Gorda et al. (2023).

Performing inference using a real physics model framework gives some unique insights. One of these is the possible range of the total fraction of different particles in neutron stars. The proton fraction is of particular interest because it is directly related to the neutron star cooling process. As we are assuming beta equilibrium and electric neutrality, the proton fraction is equal to the sum of the electron and muon fractions. In Fig. 12, the posterior (blue lines) and constrained

prior contours (red lines) of the proton fraction are plotted as a function of the baryonic density. The horizontal line at $y_p = 1/9$ indicates the onset of the nucleonic direct Urca processes when muons are not included. Including muons, the nucleonic direct Urca sets in for $0.11 < y_p \lesssim 0.14$. We conclude that most of the models do not predict nucleonic direct Urca. However, after incorporating the constraints from current observations, the posterior distribution does not differ much from the constrained prior, suggesting that current astrophysical observations do not have much constraining power on this quantity. The conclusion is consistent with the one drawn earlier regarding the ability to constrain the couplings associated with the isovector channel, g_ρ and Λ_ω . The distributions indicate that the posterior predicts a lower proton fraction than the constrained prior distribution when considering the 68 per cent credible level, which disfavours the existence of the direct Urca process. Notice, however, that direct Urca processes may still occur if hyperons set in (Negreiros et al. 2018; Providênciá et al. 2019; Fortin et al. 2020). In Beznogov & Yakovlev (2015), it is predicted that according to observations, direct Urca should open in stars with masses 1.6 to $1.8 M_\odot$. A direct Urca constraint could easily be included in the analysis and will be considered in a future study.

7 CONCLUSIONS

In the present study, we have considered a microscopic nuclear model based on a field theoretical approach to span the whole meaningful neutron star M–R space. The model is based on a relativistic formulation and therefore has causality built-in. The parameters of the model have then been constrained by current neutron star observations, with only minimal guidance with respect to some nuclear matter properties: in particular, saturation density, binding energy at saturation, and incompressibility. This approach is in contrast to several commonly-used and more agnostic descriptions of the neutron star EOS, which do not contain information on the nuclear matter composition.

The model has been first constrained by current observations (radio, X-ray, and gravitational waves). In a second step, we have studied how effectively future X-ray observations could constrain the model parameters. We find that current observations mainly constrain the isoscalar channel of the EOS, i.e. the symmetric nuclear matter EOS. It is interesting to note that NICER’s radius measurement for the high mass pulsar PSR J0740+6620 has a visible effect on constraining parameters. This leads us to conclude that it is important to have simultaneous information from both low and high mass stars to more efficiently obtain information on the EOS.

The isovector channel on the other hand, in particular, the parameters that define the density dependence of the symmetry energy – turned out to be less sensitive to the current observations and to our ‘Future’ observational scenario (defined by M–R measurements at the ~ 5 per cent level). The reason could be simply a weakly constraining set of observations, since improved precision as simulated by our ‘Future-X’ scenario (M–R measurements at the ~ 2 per cent level) seems to put some constraints, or it could have a more fundamental nature, such as the fact that the observation of mass and radius does not give information on the composition of matter.

We have also shown that future M–R observations with low uncertainty, of the type that we expect to be able to achieve using future large area X-ray timing telescopes, should allow us to make measurements of the EOS using only pulse profile modelling. In the scenario that we considered, measurements at the ~ 2 per cent level were able to put strong constraints on most model parameters, in particular, on the parameters that determine the symmetric nuclear

matter EOS behaviour, and demonstrated robust recovery of the injected EOS model parameters. Although we considered only two test cases in this study, this is very encouraging. Again, it will be important to have both high and low-mass stars in the data set. Importantly, with the capabilities that we anticipate for future instruments, we will be able to cross-check EOS inference derived solely from pulse profile modelling against that derived solely from GW measurements, thus allowing us to test for modelling and systematic errors in both techniques.

Current observations also allow us to place constraints on the behaviour of both the speed of sound and the proton fraction. It was found that the speed of sound squared saturates around $0.4c^2$. This is an interesting result because the model allows a speed of sound that tends at sufficiently large densities to a value between the conformal limit $c/\sqrt{3}$ and the speed of light c , depending on the magnitude of the coupling ζ of the quartic isoscalar-vector self-interaction term. Observations seem to prefer larger values of ζ and, consequently, smaller speeds of sound and EOS that are compatible with the pQCD EOS. Finally, it has been shown that the proton fraction disfavours the nucleonic direct Urca, but it is important to stress that the isovector parameters are not very sensitive to the current observations used to extract the proton fraction, and therefore this result is not strongly binding.

ACKNOWLEDGEMENTS

CH acknowledges support from an Arts & Sciences Fellowship at Washington University in St. Louis, and would like to thank Yves Kini, Tuomo Salmi, Nathan Rutherford, Alex Chen, Serena Vinciguerra, Daniela Huppenkothen, Mark Alford, Alexander Haber, Liam Brodie, and the anonymous referee for helpful discussions and comments. GR is grateful for financial support from the Nederlandse Organisatie voor Wetenschappelijk Onderzoek (NWO) through the Projectruimte and VIDI grants (PI S. Nissanke). ALW acknowledges support from ERC Consolidator Grant (CoG) No. 865768 AEONS. Computations were carried out on the HELIOS cluster on dedicated nodes funded via this grant. ALW and GR would like to thank Jeannine de Kuijper, who did some preliminary work on this topic as part of her Bachelor and Masters degrees in Physics & Astronomy at the University of Amsterdam/Vrije Universiteit Amsterdam. LT acknowledges support from the CEX2020-001058-M project (Unidad de Excelencia ‘María de Maeztu’), PID2019-110165GB-I00 project financed by the Spanish MCIN/ AEI/10.13039/501100011033/, the EU STRONG-2020 project under the program H2020-INFRAIA-2018-1 grant agreement no. 824093, and from the Generalitat Valenciana under contract PROMETEO/2020/023. CP acknowledges support from FCT (Fundação para a Ciência e a Tecnologia, I.P., Portugal) under Projects UIDP/04564/2020, UIDB/04564/2020, and 2022.06460.PTDC.

DATA AVAILABILITY

The posterior samples and scripts to make the plots in this paper are available in a Zenodo repository (Huang et al. 2023).

REFERENCES

- Abbott B. P. et al., 2017, *Phys. Rev. Lett.*, 119, 161101
 Abbott B. P. et al., 2018, *Phys. Rev. Lett.*, 121, 161101
 Abbott B. P. et al., 2019, *Phys. Rev. X*, 9, 011001
 Abbott B. P. et al., 2020, *ApJ*, 892, L3
 Adhikari D. et al., 2021, *Phys. Rev. Lett.*, 126, 172502
 Alam N., Agrawal B. K., Fortin M., Pais H., Providência C., Raduta A. R., Sulaksono A., 2016, *Phys. Rev. C*, 94, 052801
 Alford M. G., Han S., Prakash M., 2013, *Phys. Rev. D*, 88, 083013
 Altiparmak S., Ecker C., Rezzolla L., 2022, *ApJ*, 939, L34
 Annala E., Gorda T., Kurkela A., Vuorinen A., 2018, *Phys. Rev. Lett.*, 120, 172703
 Annala E., Gorda T., Kurkela A., Näättilä J., Vuorinen A., 2020, *Nature Phys.*, 16, 907
 Annala E., Gorda T., Katerini E., Kurkela A., Näättilä J., Paschalidis V., Vuorinen A., 2022, *Phys. Rev. X*, 12, 011058
 Annala E., Gorda T., Hirvonen J., Komoltsev O., Kurkela A., Näättilä J., Vuorinen A., 2023, *Nat. Commun.*, 14, 8451
 Bao S. S., Hu J. N., Zhang Z. W., Shen H., 2014, *Phys. Rev. C*, 90, 045802
 Baym G., Pethick C., Sutherland P., 1971, *ApJ*, 170, 299
 Baym G., Hatsuda T., Kojo T., Powell P. D., Song Y., Takatsuka T., 2018, *Rep. Prog. Phys.*, 81, 056902
 Bedaque P., Steiner A. W., 2015, *Phys. Rev. Lett.*, 114, 031103
 Beznogov M. V., Yakovlev D. G., 2015, *MNRAS*, 452, 540
 Biswas B., 2022, *ApJ*, 926, 75
 Bodmer A., 1991, *Nucl. Phys. A*, 526, 703
 Boguta J., Bodmer A., 1977, *Nucl. Phys. A*, 292, 413
 Boguta J., Stocker H., 1983, *Phys. Lett. B*, 120, 289
 Buchner J., 2016, *Stat. Comput.*, 26, 383
 Buchner J., 2019, *PASP*, 131, 108005
 Buchner J., 2021, *J. Open Source Softw.*, 6, 3001
 Burgio G. F., Schulze H. J., Vidana I., Wei J. B., 2021, *Prog. Part. Nucl. Phys.*, 120, 103879
 Carriere J., Horowitz C. J., Piekarewicz J., 2003, *ApJ*, 593, 463
 Cavagnoli R., Menezes D. P., Providência C., 2011, *Phys. Rev. C*, 84, 065810
 Chamel N., Fantina A. F., Pearson J. M., Goriely S., 2013, *A&A*, 553, A22
 Chen W.-C., Piekarewicz J., 2014, *Phys. Rev. C*, 90, 044305
 Cromartie H. T. et al., 2020, *Nat. Astron.*, 4, 72
 Demorest P. B., Pennucci T., Ransom S. M., Roberts M. S. E., Hessels J. W. T., 2010, *Nature*, 467, 1081
 Dutra M. et al., 2014, *Phys. Rev. C*, 90, 055203
 Essick R., Tews I., Landry P., Schwenk A., 2021, *Phys. Rev. Lett.*, 127, 192701
 Fattoyev F. J., Piekarewicz J., 2010a, *Phys. Rev. C*, 82, 025805
 Fattoyev F. J., Piekarewicz J., 2010b, *Phys. Rev. C*, 82, 025810
 Fattoyev F. J., Horowitz C. J., Piekarewicz J., Shen G., 2010, *Phys. Rev. C*, 82, 055803
 Fattoyev F. J., Horowitz C. J., Piekarewicz J., Reed B., 2020, *Phys. Rev. C*, 102, 065805
 Fonseca E. et al., 2021, *ApJ*, 915, L12
 Fortin M., Providência C., Raduta A. R., Gulminelli F., Zdunik J. L., Haensel P., Beijer M., 2016, *Phys. Rev. C*, 94, 035804
 Fortin M., Raduta A. R., Avancini S., Providência C., 2020, *Phys. Rev. D*, 101, 034017
 Gendreau K. C. et al., 2016, in den Herder J.-W. A., Takahashi T., Bautz M., eds, SPIE Conf. Ser. Vol. 9905, Space Telescopes and Instrumentation 2016: Ultraviolet to Gamma Ray. SPIE, Bellingham, p. 99051H
 Ghosh S., Pradhan B. K., Chatterjee D., Schaffner-Bielich J., 2022a, *Front. Astron. Space Sci.*, 9, 864294
 Ghosh S., Chatterjee D., Schaffner-Bielich J., 2022b, *Eur. Phys. J. A*, 58, 37
 Glendenning N., 1996, Compact Stars. Nuclear Physics, Particle Physics and General Relativity. Springer-Verlag, New York
 Gorda T., Komoltsev O., Kurkela A., 2023, *ApJ*, 950, 107
 Greif S. K., Raaijmakers G., Hebeler K., Schwenk A., Watts A. L., 2019, *MNRAS*, 485, 5363
 Hebeler K., 2021, *Phys. Rep.*, 890, 1
 Hornick N., Tolos L., Zacchi A., Christian J.-E., Schaffner-Bielich J., 2018, *Phys. Rev. C*, 98, 065804
 Horowitz C. J., Piekarewicz J., 2001a, *Phys. Rev. C*, 64, 062802
 Horowitz C. J., Piekarewicz J., 2001b, *Phys. Rev. Lett.*, 86, 5647
 Huang C., Raaijmakers G., Watts A. L., Tolos L., Providência C., 2023, Constraining fundamental nuclear physics parameters using neutron star mass-radius measurements I: Nucleonic models,
 Huth S., Wellenhofer C., Schwenk A., 2021, *Phys. Rev. C*, 103, 025803

- Kass R. E., Raftery A. E., 1995, *J. Am. Stat. Assoc.*, 90, 773
- Kurkela A., Fraga E. S., Schaffner-Bielich J., Vuorinen A., 2014, *ApJ*, 789, 127
- Landry P., Essick R., Chatzioannou K., 2020, *Phys. Rev. D*, 101, 123007
- Lattimer J. M., 2012, *Annu. Rev. Nucl. Part. Sci.*, 62, 485
- Lattimer J. M., Lim Y., 2013, *ApJ*, 771, 51
- Legred I., Chatzioannou K., Essick R., Han S., Landry P., 2021, *Phys. Rev. D*, 104, 063003
- Legred I., Chatzioannou K., Essick R., Landry P., 2022, *Phys. Rev. D*, 105, 043016
- Li J. J., Sedrakian A., Alford M., 2021, *Phys. Rev. D*, 104, L121302
- Lindblom L., 2010, *Phys. Rev. D*, 82, 103011
- Lindblom L., 2022, *Phys. Rev. D*, 105, 063031
- Lo K. H., Miller M. C., Bhattacharyya S., Lamb F. K., 2013, *ApJ*, 776, 19
- Malik T., Alam N., Fortin M., Providência C., Agrawal B. K., Jha T. K., Kumar B., Patra S. K., 2018, *Phys. Rev. C*, 98, 035804
- Malik T., Ferreira M., Agrawal B. K., Providência C., 2022, *ApJ*, 930, 17
- Malik T., Ferreira M., Albino M. B., Providência C., 2023, *Phys. Rev. D*, 107, 103018
- Margueron J., Hoffmann Casali R., Gulminelli F., 2018, *Phys. Rev. C*, 97, 025805
- Miller M. C. et al., 2019, *ApJ*, 887, L24
- Miller M. C. et al., 2021, *ApJ*, 918, L28
- Mondal C., Gulminelli F., 2023, *Phys. Rev. C*, 107, 015801
- Most E. R., Weih L. R., Rezzolla L., Schaffner-Bielich J., 2018, *Phys. Rev. Lett.*, 120, 261103
- Müller H., Serot B. D., 1996, *Nucl. Phys. A*, 606, 508
- Negreiros R., Tolos L., Centelles M., Ramos A., Dexheimer V., 2018, *ApJ*, 863, 104
- Oertel M., Hempel M., Klähn T., Typel S., 2017, *Rev. Mod. Phys.*, 89, 015007
- Oppenheimer J. R., Volkoff G. M., 1939, *Phys. Rev.*, 55, 374
- Özel F., Psaltis D., Ransom S., Demorest P., Alford M., 2010, *ApJ*, 724, L199
- Pais H., Providência C., 2016, *Phys. Rev. C*, 94, 015808
- Pang P. T. H., Tews I., Coughlin M. W., Bulla M., Van Den Broeck C., Dietrich T., 2021, *ApJ*, 922, 14
- Piekarewicz J., Fattoyev F. J., Horowitz C. J., 2014, *Phys. Rev. C*, 90, 015803
- Providência C., Rabhi A., 2013, *Phys. Rev. C*, 87, 055801
- Providência C., Fortin M., Pais H., Rabhi A., 2019, *Front. Astron. Space Sci.*, 6, 13
- Psaltis D., Özel F., Chakrabarty D., 2014, *ApJ*, 787, 136
- Raaijmakers G. et al., 2019, *ApJ*, 887, L22
- Raaijmakers G. et al., 2020, *ApJ*, 893, L21
- Raaijmakers G. et al., 2021, *ApJ*, 918, L29
- Ray P. S. et al., 2019, preprint ([arXiv:1903.03035](https://arxiv.org/abs/1903.03035))
- Read J. S., Lackey B. D., Owen B. J., Friedman J. L., 2009, *Phys. Rev. D*, 79, 124032
- Reardon D. J. et al., 2016, *MNRAS*, 455, 1751
- Reed B. T., Fattoyev F. J., Horowitz C. J., Piekarewicz J., 2021, *Phys. Rev. Lett.*, 126, 172503
- Reinhard P.-G., Roca-Maza X., Nazarewicz W., 2021, *Phys. Rev. Lett.*, 127, 232501
- Reinhard P.-G., Roca-Maza X., Nazarewicz W., 2022, *Phys. Rev. Lett.*, 129, 232501
- Riley T. E. et al., 2019, *ApJ*, 887, L21
- Riley T. E. et al., 2021, *ApJ*, 918, L27
- Rutherford N., Raaijmakers G., Prescod-Weinstein C., Watts A., 2023, *Phys. Rev. D*, 107, 103051
- Salmi T. et al., 2022, *ApJ*, 941, 150
- Serot B. D., Walecka J. D., 1986, *Adv. Nucl. Phys.*, 16, 1
- Shen H., Ji F., Hu J., Sumiyoshi K., 2020, *ApJ*, 891, 148
- Stone J. R., Stone N. J., Moszkowski S. A., 2014, *Phys. Rev. C*, 89, 044316
- Sun X., Miao Z., Sun B., Li A., 2023, *ApJ*, 942, 55
- Tang S.-P., Jiang J.-L., Han M.-Z., Fan Y.-Z., Wei D.-M., 2021, *Phys. Rev. D*, 104, 063032
- Tews I., Carlson J., Gandolfi S., Reddy S., 2018, *ApJ*, 860, 149
- Todd-Rutel B. G., Piekarewicz J., 2005, *Phys. Rev. Lett.*, 95, 122501
- Tolman R. C., 1939, *Phys. Rev.*, 55, 364
- Tolos L., Fabbietti L., 2020, *Prog. Part. Nucl. Phys.*, 112, 103770
- Tolos L., Centelles M., Ramos A., 2016, *ApJ*, 834, 3
- Tolos L., Centelles M., Ramos A., 2017, *PASA*, 34, e065
- Traversi S., Char P., Pagliara G., 2020, *ApJ*, 897, 165
- Vinciguerra S. et al., 2024, *ApJ*, 961, 62
- Watts A. L., 2019, in Xiamen-CUSTIPEN Workshop on the Equation of State of Dense Neutron-Rich Matter in the Era of Gravitational Wave Astronomy. Vol. 2127, AIP Conference Proceedings, NY, USA, p. 020008
- Watts A. L. et al., 2016, *Rev. Mod. Phys.*, 88, 021001
- Watts A. L. et al., 2019, *Sci. China Phys. Mech. Astron.*, 62, 29503
- Yang J., Piekarewicz J., 2020, *Annu. Rev. Nucl. Part. Sci.*, 70, 21
- Yue T.-G., Chen L.-W., Zhang Z., Zhou Y., 2022, *Phys. Rev. Res.*, 4, L022054
- Zhang S. et al., 2019, *Sci. China Phys. Mech. Astron.*, 62, 29502

This paper has been typeset from a TeX/LaTeX file prepared by the author.

Constraining a relativistic mean field model using neutron star mass-radius measurements II: Hyperonic models

Chun Huang,^{1*} Laura Tolos,^{2,3,4} Constança Providênci,⁵ and Anna Watts⁶

¹Physics Department and McDonnell Center for the Space Sciences, Washington University in St. Louis; MO, 63130, USA

²Institute of Space Sciences (ICE, CSIC), Campus UAB, Carrer de Can Magrans, 08193, Barcelona, Spain

³Institut d'Estudis Espacials de Catalunya (IEEC), 08860 Castelldefels (Barcelona), Spain

⁴Frankfurt Institute for Advanced Studies, Ruth-Moufang-Str. 1, 60438, Frankfurt am Main, Germany

⁵CFisUC, Department of Physics, University of Coimbra, 3004-516 Coimbra, Portugal

⁶Anton Pannekoek Institute for Astronomy, University of Amsterdam, Science Park 904, 1090 GE Amsterdam, the Netherlands

Accepted XXX. Received YYY; in original form ZZZ

ABSTRACT

We investigate whether measurements of the neutron star mass and radius or the tidal deformability can provide information about the presence of hyperons inside a neutron star. This is achieved by considering two inference models, with and without hyperons, based on a field-theoretical approach. While current observations do not distinguish between the two scenarios, we have shown that data simulating expected observations from future large area X-ray timing telescopes could provide some information through Bayes factors. Inference using simulated data generated from an EOS containing hyperons decisively favours the hyperonic model over the nucleonic model. However, a 2% uncertainty in the mass and radius determination may not be sufficient to constrain the parameters of the model when only six neutron star mass-radius measurements are considered.

Key words: dense matter - equation of state - stars: neutron - X-rays: general

1 INTRODUCTION

If stable states of strange matter exist anywhere in the Universe, the most likely location is in the cores of neutron stars, where densities reach several times the nuclear saturation density (Chatterjee & Vidaña 2016; Tolos & Fabbietti 2020; Burgio et al. 2021). Strange matter could take various forms (deconfined quarks, mesons), but one possibility is that it is baryonic, in the form of *hyperons* (Ambartsumyan & Saakyan 1960).

The presence of hyperons would soften the dense matter Equation of State (EOS), affecting the overall structure of the star and the relationship between neutron star mass and radius/tidal deformability. The presence of hyperons can therefore in principle be explored using new observational techniques. Constraints on mass and tidal deformability can be derived from the properties of gravitational waves (GW) emitted during the final stages of neutron star binary inspiral (Abbott et al. 2018; Abbott et al. 2020a). And pulse profile modeling, using X-ray data from NICER (the Neutron Star Interior Composition Explorer, Gendreau et al. 2016), allows the inference of neutron star mass and radius (Riley et al. 2019; Miller et al. 2019; Riley et al. 2021; Miller et al. 2021; Salmi et al. 2022, 2023; Vinciguerra et al. 2024; Salmi et al.

2024a; Dittmann et al. 2024; Choudhury et al. 2024; Salmi et al. 2024b). Applying the latter technique to faint rotation-powered millisecond pulsars and accreting neutron stars is a key science driver for planned and proposed future X-ray telescopes (Barret et al. 2013; Watts et al. 2016, 2019; Ray et al. 2019).

These new observational constraints are already being applied to inform our understanding of dense matter (Miller et al. 2021; Raaijmakers et al. 2021; Annala et al. 2023; Takátsy et al. 2023; Pang et al. 2024; Koehn et al. 2024). Many of these studies use EOS meta-models (which may be parameterized or non-parameterized) that attempt to span all reasonable mass-radius parameter space, rather than being driven by microphysics (Kurkela et al. 2014; Annala et al. 2018; Tews et al. 2018; Annala et al. 2020; Landry et al. 2020; Essick et al. 2021; Legred et al. 2021; Altiparmak et al. 2022; Gorda et al. 2023; Rutherford et al. 2024). This means that they provide no direct insight into composition. In this study we will explore the constraints that current NICER and GW results pose for hyperonic models, using a microscopic model. We will also explore the prospects for improved constraints from the next generation of X-ray telescopes, which are expected to generate tighter mass-radius inferences via pulse profile modeling. We use a microscopic model based on a relativistic field theoretical approach for the EOS, which allows us to explore composition, and our sensitivity to the

* E-mail: chun.h@wustl.edu

possible presence of hyperons, directly. This study builds on earlier work using a purely nucleonic model (Huang et al. 2024b).

2 EQUATION OF STATE MODELS

We base our analysis on an EOS coming from a relativistic mean field (RMF) description of hadronic matter. In particular, the calibrated parameter set of the FSU2R EOS (Tolos et al. 2016, 2017) is chosen as the central value of our prior distributions for the nucleonic parameters, as done in our previous work (Huang et al. 2024b). This RMF scheme for nucleons was optimised to describe $2M_{\odot}$ stars and to satisfy the condition that the radius is less than 13 km, while reproducing the properties of nuclear matter and finite nuclei as well as certain restrictions on high-density matter deduced from heavy-ion collisions. In the present paper, we also take into account the effect of hyperons, thus taking a similar approach as the FSU2H parameterisation of Tolos et al. (2016, 2017). The hyperonic parameters are then calculated by fitting the experimental data available for hypernuclei, in particular, the possible values of the optical potential of hyperons extracted from these data. The parameters of the FSU2R and FSU2H are shown in the first two rows of Table 1. Note that there are many EOSs in the literature that are based on the same RMF framework, i.e. the same underlying Lagrangian density. Although our prior was defined with respect to a particular EOS, we could have started from any other EOS.

In the next subsection, we focus on how to introduce the hyperon sector on top of the nucleonic EOS model. We will not describe the nucleonic part of RMF theory in detail here, as we have done that in our previous work, see Huang et al. (2024b).

2.1 Hyperonic Equation of State

In order to discuss the role of hyperons inside neutron stars, we need to determine the interaction of hyperons with nuclear matter. So we start by recalling that the potential felt by hyperon i on the j particle matter at density n_j is given by

$$U_i^{(j)}(n_j) = -g_{\sigma i}\bar{\sigma}^{(j)} + g_{\omega i}\bar{\omega}^{(j)} + g_{\rho i}I_{3i}\bar{\rho}^{(j)} + g_{\phi i}\bar{\phi}^{(j)} \quad (1)$$

where $g_{\sigma i}$, $g_{\omega i}$, $g_{\rho i}$ and $g_{\phi i}$ are the couplings of the σ , ω , ρ and ϕ fields to hyperons, and $\bar{\sigma}^{(j)}$, $\bar{\omega}^{(j)}$, $\bar{\rho}^{(j)}$ and $\bar{\phi}^{(j)}$ are the meson mean-fields in the j -particle matter.

Flavor SU(3) symmetry, the vector dominance model and ideal mixing for the physical ω and ϕ mesons allows one to relate the couplings between the hyperons and the ω and ϕ mesons to the nucleon coupling $g_{\omega N}$ as in Schaffner & Mishustin (1996); Weissenborn et al. (2012); Providência & Rabhi (2013); Miyatsu et al. (2013); Banik et al. (2014); Tolos et al. (2016, 2017), that is,

$$\begin{aligned} g_{\omega \Lambda} : g_{\omega \Sigma} : g_{\omega \Xi} : g_{\omega N} &= \frac{2}{3} : \frac{2}{3} : \frac{1}{3} : 1 \\ g_{\phi \Lambda} : g_{\phi \Sigma} : g_{\phi \Xi} : g_{\phi N} &= -\frac{\sqrt{2}}{3} : -\frac{\sqrt{2}}{3} : -\frac{2\sqrt{2}}{3} : 1, \end{aligned} \quad (2)$$

where we note that $g_{\phi N} = 0$. The coupling of the Λ hyperon to the ϕ meson is however reduced by 20% so as to obtain a $\Lambda\Lambda$ bond energy in Λ matter at a density $n_{\Lambda} \simeq n_0/5$ of

$\Delta B_{\Lambda\Lambda}(n_0/5) = 0.67$ MeV, thus reproducing the value extracted from the ${}^6_{\Lambda\Lambda}\text{He}$ double Λ hypernucleus (Takahashi et al. 2001; Ahn et al. 2013). As for the couplings of hyperons to ρ we relate them to $g_{\rho N}$ according to

$$g_{\rho \Lambda} : g_{\rho \Sigma} : g_{\rho \Xi} : g_{\rho N} = 0 : 1 : 1 : 1.$$

We should indicate that the isospin operator I_{3i} appearing in the definition of the potentials in Eq. (1) implements the relative factor of 2 missing in the 1:1 relation between $g_{\rho \Sigma}$ and $g_{\rho N}$ displayed in Eq. (3) due to isospin, so that the effective coupling of the ρ meson to the Σ hyperon ($I_3 = -1, 0, +1$) is twice that to the nucleon ($I_3 = -1/2, +1/2$), as required by the isospin symmetry.

Then, the hyperon- σ coupling can be determined from Eq. (1) by reproducing the hyperon optical potential in symmetric nuclear matter at saturation density n_0 , as derived from hypernuclear data. For the Λ potential, the Woods-Saxon type potential of $U_{\Lambda}^{(N)}(n_0) \sim -28$ MeV reproduces the bulk of Λ hypernuclei binding energies (Millener et al. 1988). With regards to the Σ hyperon, a moderate repulsive potential could be extracted from (π^-, K^+) reactions off nuclei (Noumi et al. 2002) done in (Harada & Hirabayashi 2006; Kohno et al. 2006). Fits to Σ^- atomic data (Friedman & Gal 2007) also indicate a transition from an attractive Σ -nucleus potential at the surface to a repulsive one inside the nucleus, but the repulsion is not well determined. As for Ξ , the potential in symmetric nuclear matter is also quite uncertain. Whereas emulsion data shows attractive values of $U_{\Xi}^{(N)}(n_0) = -24 \pm 4$ MeV (Dover & Gal 1983), analyses of the (K^-, K^+) reaction on a ${}^{12}\text{C}$ target indicate a milder attraction (Fukuda et al. 1998; Khaustov et al. 2000). More recently, the value of $U_{\Xi} = -21.9 \pm 0.7$ MeV has been determined in Friedman & Gal (2021). This value was updated to -13.8 MeV by the same authors (Friedman & Gal 2023) using recent data obtained by experience E07 at J-PARC (Yoshimoto et al. 2021). Therefore, we take into account these experimental uncertainties so as to vary the hyperon potentials in symmetric nuclear matter as follows:

$$\begin{aligned} U_{\Lambda}^{(N)}(n_0) &= -25 \text{ to } -30 \text{ MeV} \\ U_{\Sigma}^{(N)}(n_0) &= 10 \text{ to } 40 \text{ MeV} \\ U_{\Xi}^{(N)}(n_0) &= -10 \text{ to } -25 \text{ MeV}. \end{aligned} \quad (3)$$

This range of values for the hyperon potentials at n_0 gives rise to the following range for the hyperon- σ couplings:

$$\begin{aligned} g_{\sigma \Lambda}/g_{\sigma N} &= 0.60475 - 0.61783 \\ g_{\sigma \Sigma}/g_{\sigma N} &= 0.43470 - 0.51319 \\ g_{\sigma \Xi}/g_{\sigma N} &= 0.29583 - 0.33507, \end{aligned} \quad (4)$$

where the lower values correspond to the most repulsive situation and the upper ones to the most attractive one.

Note that this way of proceeding is similar to the one discussed for the FSU2H parameterization in Tolos et al. (2016, 2017). The difference arises regarding the limiting allowed values for the hyperon potentials, as they are not well constrained for the case of Σ and Ξ .

To finalize this section, a word of caution is necessary when comparing the nucleonic model used in Huang et al. (2024b) and the present hyperonic model. The hyperonic couplings only measure the strength of the interaction of hyperons with nucleons. Thus, by switching off the hyperonic couplings, it

Model	m_σ (MeV)	m_ω (MeV)	m_ρ (MeV)	$g_{\sigma N}^2$	$g_{\omega N}^2$	$g_{\rho N}^2$	κ	λ	ζ	Λ_ω
FSU2R	497.479	782.500	763.000	107.5751	182.3949	206.4260	3.0911	-0.001680	0.024	0.045
FSU2H	497.479	782.500	763.000	102.7200	169.5315	197.2692	4.0014	-0.013298	0.008	0.045
TM1-2 $\omega\rho$	511.198	783.000	770.000	99.9661	156.3384	127.7469	3.5235	-0.004739	-0.012	0.030

Table 1. Parameters of the three EOS considered in the present work.

EOS parameter	Prior
κ (MeV)	$N(2.525, 1.525^2)$
λ_0	$N(0.0045, 0.0205^2)$
ζ	$\mathcal{U}(0, 0.04)$
Λ_ω	$\mathcal{U}(0, 0.045)$
g_σ^2	$N(107.5, 7.5^2)$
g_ω^2	$\mathcal{U}(150, 210)$
g_ρ^2	$\mathcal{U}(75, 210)$
$g_{\sigma\Lambda}/g_{\sigma N}$	$N(0.61129, 0.01308^2)$
$g_{\sigma\Sigma}/g_{\sigma N}$	$N(0.47395, 0.07849^2)$
$g_{\sigma\Xi}/g_{\sigma N}$	$N(0.31545, 0.03924^2)$
$g_{\phi\Lambda}/g_{\omega N}$	$N(0.87407, 0.10447^2)$

Table 2. The prior distributions assumed for the EOS parameters, where N is a Gaussian distribution and \mathcal{U} a Uniform (Flat) distribution.

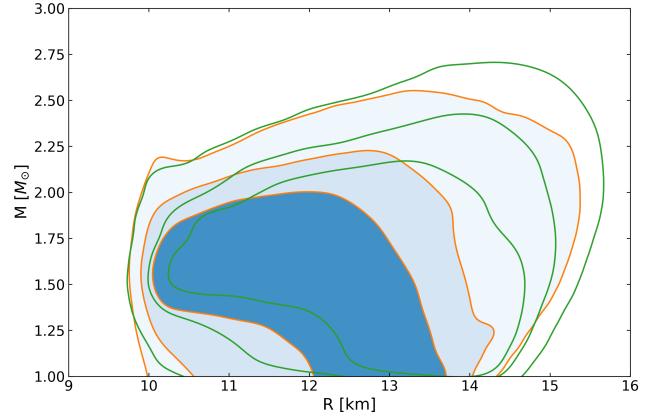
is not possible to recover the nucleonic model, since hyperons will be still present when β -equilibrium allows for it.

2.2 Choice of priors for model parameters

The choice of priors for the present analysis is given in Table 2. For the nucleonic parameters, g_σ , g_ω , g_ρ , which define, respectively, the strength of the coupling of the σ , ω and ρ mesons to the nucleons, and κ , λ_0 , ζ and Λ_ω which determine the strength of the meson self-interacting and mixed terms, we use the same central values and priors as in our previous work of Huang et al. (2024b) (see Eqs. (1) and (2) for the Lagrangian density in the former reference). For the newly introduced hyperonic degrees of freedom, the hyperon potentials at saturation density determine the range of the σ -hyperon couplings, while the Λ potential at saturation and the $\Lambda\Lambda$ bond at lower densities fix the value of the ϕ - Λ coupling, as discussed in Sec. 2.1.

It is critical for the inference method to have a prior distribution broad enough to encompass all possibilities. We therefore assume the $g_{\sigma\Lambda}/g_{\sigma N}$, $g_{\sigma\Sigma}/g_{\sigma N}$ and $g_{\sigma\Xi}/g_{\sigma N}$ priors to be Gaussian distributions whose 68% confidence intervals are within the limiting cases determined in Eq. (4). For the $g_{\phi\Lambda}/g_{\omega N}$ the 68% credible interval lies within $0.821 < g_{\phi\Lambda}/g_{\omega N} < 0.926$, which results from modifying the coupling of the Λ hyperon to the ϕ meson for a given $g_{\sigma\Lambda}/g_{\sigma N}$ so as to obtain the $\Lambda\Lambda$ bond energy.

Taking into account all the nucleonic and hyperonic parameters, the nucleonic model space will be a seven dimensional parameter space, while the consideration of the hyperon sector introduces another four dimensions, giving rise to an eleven dimensional parameter space.

**Figure 1.** The M-R posterior after applying the nuclear constraint (orange/blue), compared to the M-R prior resulting from the initial EOS model and priors (green). The contour levels, from the innermost to the outermost, correspond to the 68%, 84% and 100% credible regions, where 100% is the point beyond which there are no samples (for both the orange/blue and green contours).

2.3 Nuclear matter saturation properties

Following the method described in Chen & Piekarewicz (2014), the EOS parameters can be related to the saturation properties of nuclear matter. Without repeating all the derivations here, the quantity of particular interest to us is the incompressibility of symmetric nuclear matter K , since it has a much wider range of possible values than the experiments indicate. To control it, a minimal guidance from nuclear physics is included as in Huang et al. (2024b), imposing the probability function $p(K) = -0.5 \times |250 - K|^{10} / 150^{10}$ to be the prior filter that shapes the prior before we implement it in the inference. For the other nuclear quantities, we fix E/A to be a Gaussian distribution centred on -16 MeV, with $\sigma = 0.02$, $N(-16, 0.02^2)$, and restrict m^* to $\mathcal{U}(0.55, 0.64)$ and n_0 to $\mathcal{U}(0.15, 0.17)$, since they are sufficiently well constrained by nuclear experiments.

2.4 Mass-radius priors

The EOS can be mapped into the neutron star Mass-Radius (M-R) domain by solving the Tolman-Oppenheimer-Volkoff (TOV) equations (Tolman 1939; Oppenheimer & Volkoff 1939). The TOV equations for a static and spherically-

symmetric star are given by

$$\begin{aligned} \frac{dP}{dr} &= -\frac{G}{r^2}(\varepsilon + P)(m + 4\pi r^3 P) \left(1 - \frac{2Gm}{r}\right)^{-1}, \\ \frac{dm}{dr} &= 4\pi r^2 \varepsilon, \end{aligned} \quad (5)$$

where P , ε and m are the pressure, the energy density and the star mass, respectively, for a given radius r , the radial coordinate in spherical coordinates, and G is the gravitational constant.

In order to solve the TOV equations, the EOS for the whole neutron star is needed. The EOS described above by the RMF method only describes the core. For the crust, the BPS outer crust EOS (Baym et al. 1971) was applied for $\varepsilon < \varepsilon_{\text{outer}} = 4.30 \times 10^{11} \text{ g/cm}^3$. At the interface between the core and the outer crust, $\varepsilon_{\text{outer}} < \varepsilon < \varepsilon_c = 2.14 \times 10^{14} \text{ g/cm}^3$ region, we have implemented the same treatment as in Huang et al. (2024b), that is, a polytrope fitting that includes four additional points from the unified inner crust EOS obtained in Providéncia et al. (2019) to improve the fit. A detailed discussion of this method can be found in our previous work (Huang et al. 2024b).

We show in Figure 1 the hyperonic NS mass-radius prior, defined by the green contours, resulting from the eleven dimensional parameter prior space (nucleon + hyperon) given in Table 2. Our choice of priors does not include samples larger than 16 km, but does allow radii smaller than 10 km (the minimum allowed radius is 9.8 km). As a comparison, the full prior for the nucleonic model used in Huang et al. (2024b) (see Figure 2 of that paper)¹ allowed radii larger than 16 km, but the radius was limited by applying nuclear constraints (the minimum allowed radius for the constrained nucleonic model prior was 10.1 km, and the maximum 15.5 km). After filtering the initial hyperonic model prior with the nuclear constraints defined above for K , E/A , m^* and n_0 , the radius still extends to below 10 km (orange/blue contours in Figure 1), which matches expectations, as the introduction of hyperons will tend to soften the EOS.

The maximum mass is smaller once nuclear constraints are imposed. The presence of hyperons tends to soften the EOS, producing generally lower mass stars for the same central density. This effect is clearly seen by comparing the maximum mass star of the constrained hyperonic prior ($\sim 2.5 M_\odot$) with that of the constrained nucleonic prior ($\sim 3.0 M_\odot$).

3 INFERENCE FRAMEWORK

3.1 Inference method

The inference conducted here relies on the framework developed by the authors, namely the *CompactObject* (Huang et al. 2023) package. This is an open source full-scope package designed to implement Bayesian constraints on the neutron star EOS.

Two types of inference methods will be explored: i) current observations of neutron stars (maximum masses derived from radio pulsar timing, GW measurements of tidal deformability,

and M-R measurements from NICER), and ii) future mass-radius measurements simulated for future large-area X-ray telescopes. Our goal with these inferences is to test whether current observations can place any constraints on the parameters of the hyperonic model, and to investigate to what extent we can probe the existence of hyperons inside neutron stars using future X-ray telescopes.

The Bayesian inference methodology described here follows the same framework developed by Greif et al. (2019) and Raaijmakers et al. (2019, 2020, 2021). Bayes' theorem gives the nuisance-marginalized likelihood function as

$$p(\boldsymbol{\theta}, \varepsilon | \mathbf{d}, \mathcal{M}) \propto p(\boldsymbol{\theta} | \mathcal{M})p(\varepsilon | \boldsymbol{\theta}, \mathcal{M})p(\mathbf{d} | \boldsymbol{\theta}, \mathcal{M}), \quad (6)$$

where $p(\boldsymbol{\theta}, \varepsilon | \mathbf{d}, \mathcal{M})$ is the posterior distribution of $\boldsymbol{\theta}$ and central energy densities ε . For the nucleonic model, $\boldsymbol{\theta}$ is a 7-dimensional vector, whereas for the present hyperonic model this vector spans eleven dimensions (7-d nucleon + 4-d hyperon d.o.f). The variable \mathcal{M} indicates the model we use, and \mathbf{d} stands for the dataset.

3.2 Observational data sets

For current constraints, we can consider the following types of observations: measurements of high masses for radio pulsars; joint M-R measurements inferred from NICER data, and mass-tidal deformability measurements from GW events (see Section 4 for specifics of the observational data sets used). Since these measurements are independent, the likelihood function can be written as

$$\begin{aligned} p(\boldsymbol{\theta}, \varepsilon | \mathbf{d}, \mathcal{M}) &\propto p(\boldsymbol{\theta} | \mathcal{M})p(\varepsilon | \boldsymbol{\theta}, \mathcal{M}) \\ &\times \prod_i p(\Lambda_{1,i}, \Lambda_{2,i}, M_{1,i}, M_{2,i} | d_{\text{GW},i} (\mathbf{d}_{\text{EM},i})) \\ &\times \prod_j p(M_j, R_j | d_{\text{NICER},j}) \\ &\times \prod_k p(M_k | \mathbf{d}_{\text{radio},k}). \end{aligned} \quad (7)$$

We further modify the GW posterior distributions to include the two tidal deformabilities, the chirp mass and the mass ratio q , reweighting them simultaneously. The posterior formula then becomes

$$\begin{aligned} p(\boldsymbol{\theta}, \varepsilon | \mathbf{d}, \mathcal{M}) &\propto p(\boldsymbol{\theta} | \mathcal{M})p(\varepsilon | \boldsymbol{\theta}, \mathcal{M}) \\ &\times \prod_i p(\Lambda_{1,i}, \Lambda_{2,i}, q_i | \mathcal{M}_c, \mathbf{d}_{\text{GW},i} (\mathbf{d}_{\text{EM},i})) \\ &\times \prod_j p(M_j, R_j | \mathbf{d}_{\text{NICER},j}) \\ &\times \prod_L p(M_L | \mathbf{d}_{\text{radio},L}). \end{aligned} \quad (8)$$

Here $\Lambda_{2,i} = \Lambda_{2,i}(\boldsymbol{\theta}; q_i)$ is the tidal deformability. We follow the same convention as in Abbott et al. (2018) and assume $M_1 > M_2$, since the GW probability is symmetric when changing M_1 to M_2 or vice versa.

3.3 Simulated future observations

For future constraints, the data set \mathbf{d} defined here consists of simulated M-R measurements with the precision that we expect from the next generation of X-ray telescopes (M-R

¹ The nucleonic EOS prior we use here is still consistent with Huang et al. (2024b) (see Figure 1 of that paper).

credible regions should scale with exposure time and telescope effective area, see Lo et al. 2013; Psaltis et al. 2014). As in Huang et al. (2024b), we do not include future GW and radio constraints in our future constraint scenario simulations, since we are interested in what can be achieved from mass-radius measurements alone. The likelihood function in Eq. (6) is thus given by

$$p(\boldsymbol{\theta}, \varepsilon | \mathbf{d}, \mathcal{M}) \propto p(\boldsymbol{\theta} | \mathcal{M})p(\varepsilon | \boldsymbol{\theta}, \mathcal{M}) \\ \times \prod_j p(M_j, R_j | d_{\text{STROBEX/eXTP},j}). \quad (9)$$

First we need to generate simulated M-R measurements - injected data - assuming a "true" EOS of the neutron star such that the simulated measurements are based on an assumed M-R curve. We will consider a M-R curve from an EOS that contains only nucleonic degrees of freedom (with the associated simulated M-R measurements referred to as injected nucleonic data, or 'inject-nucl') and another from an EOS with nucleonic and hyperonic degrees of freedom (with the associated simulated M-R measurements referred to as injected hyperonic data or 'inject-hyp'). When doing inference on this simulated data, we use two different models based on a microscopic RMF description of hadronic matter, one including only nucleonic degrees of freedom, which we identify as the nucleonic model, and a second one including nucleonic and hyperonic degrees of freedom, which we identify as the hyperonic model. These two models will be used to model the injected data to test whether our inference could distinguish or obtain evidence about the composition of neutron stars (with/without hyperons). We will have to perform four different Bayesian analyses: inject-nucl data with the nucleonic and hyperonic models, and inject-hyp data with the nucleonic and hyperonic models.

Two different injected data sets are generated, with simulated M-R data constructed from the RMF TM1- $2\omega\rho n$ EOS and TM1- $2\omega\rho nH$ EOS. The parameters of TM1- $2\omega\rho$ are given in the last row of Table 1. The TM1- $2\omega\rho n$ EOS defines the 'inject-nucl' data and includes only nucleons (it was also used in our last paper, Huang et al. 2024b). The TM1- $2\omega\rho nH$ EOS defines the 'inject-hyp' data and includes hyperons and nucleons.

In this study, our focus will be exclusively on the presentation of the 'Future-X' scenario outlined in Huang et al. (2024b), i.e. considering 2% uncertainty M-R observational data. We proceed in this way in order to facilitate a comprehensive comparison between the two models under consideration, the nucleonic and the hyperonic models, for the two injected data sets, 'inject-nucl' and 'inject-hyp'.

Since the hyperonic injected data spans a smaller range of masses than in the nucleonic case, in the 'Future-X' hyperon scenario described by the 'inject-hyp' data we assume that we have six M-R measurements of neutron stars with 2% uncertainty, whose masses are centered at [1.40, 1.60, 1.70, 1.80, 1.90, 1.94] M_\odot . These simulated measurements span a sufficiently wide range of the simulated hyperonic M-R curve, with two values corresponding to known masses for current NICER sources: PSR J1614-2230 (1.9 M_\odot , Demorest et al. 2010) and PSR J0437-4715 (1.4 M_\odot , Reardon et al. 2016, 2024). The largest mass predicted in this injected data set is 1.94 M_\odot , a value that is still within the 95% credible interval of the most massive pulsar and NICER source PSR

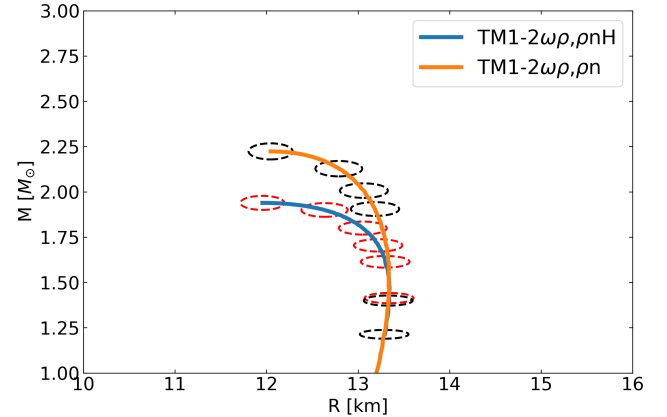


Figure 2. The M-R curves determined from the TM1- $2\omega\rho n$ EOS (without hyperons, orange line) and the TM1- $2\omega\rho nH$ EOS (with hyperons, blue line), which are the underlying EOS used to generate the simulated mass radius measurements for the 'Future-X' scenarios. The red dashed curves are the six simulated M-R inject-hyp data from the TM1- $2\omega\rho nH$ EOS, centered at [1.40, 1.60, 1.70, 1.80, 1.90, 1.94] M_\odot . The black dashed curves are the six simulated M-R inject-nucl data from the TM1- $2\omega\rho n$ EOS, centered at [1.20, 1.40, 1.90, 2.00, 2.10, 2.20] M_\odot corresponding to the 'Future-X' scenario with six 2% uncertainty M-R observations.

J0740+6620 (which has a reported mass of $2.08 \pm 0.07 M_\odot$, Cromartie et al. 2020; Fonseca et al. 2021). This 'Future-X' hyperon scenario is intended to illustrate the 'best case' that we might be able to obtain with future improved X-ray telescope missions. For the nucleonic injected data, as in Huang et al. (2024b), we choose six measurements whose masses are centered at [1.20, 1.40, 1.90, 2.00, 2.10, 2.20] M_\odot . Three of these values correspond to known NICER sources, PSR J0740+6620, PSR J1614-2230 and PSR J0437-4715, with the other three chosen to span a wide range of masses. Again we assume a 2% uncertainty. The two M-R curves, together with all simulated measurements, are shown in Figure 2.

The two different injected M-R datasets with (inject-hyp) and without hyperons (inject-nucl) will be fitted by the two different models (nucleonic and hyperonic). The cross-comparison of these four inferences will be performed to systematically test the ability of our future large area X-ray telescope data to discriminate the internal composition of neutron stars. We will compare model performance for the different sets of simulated observations using Bayes factors.

4 EOS CONSTRAINTS FROM CURRENT OBSERVATIONS

In this section we examine the constraints on EOS parameters and nuclear saturation quantities provided by all the current observations. Those are the M-R measurements derived from NICER observations for PSR J0030+0451 (Riley et al. 2019, $M = 1.34^{+0.15}_{-0.16} M_\odot$ and $R = 12.71^{+1.14}_{-1.19}$ km) and PSR J0740+6620 (Riley et al. 2021, $M = 2.07 \pm 0.07 M_\odot$ and $R = 12.39^{+1.30}_{-0.98}$ km). Note that there are now newer results available for PSR J0030+0451 (Vinciguerra et al. 2024) and PSR J0740+6620 (Salmi et al. 2024a) but since they are reasonably similar we do not update these.

We do not include any separate high mass measurements from radio pulsar timing since the current highest value - for PSR J0740+6620 - is included as a prior on the NICER M-R measurement for this source. We also include the two GW tidal deformability measurements GW170817 and GW190425 (Abbott et al. 2017; Abbott et al. 2020b). The chirp mass $M_c = (M_1 M_2)^{3/5} / (M_1 + M_2)^{1/5}$ is fixed to the median value $M_{c1} = 1.186 \text{ M}_\odot$ for GW170817 and $M_{c2} = 1.44 \text{ M}_\odot$ for GW190425.

In Figure 3, we illustrate the posterior distribution resulting from the nucleonic and hyperonic models, as determined from current observations, compared to the constrained hyperonic prior defined in section 2.2. We notice that after introducing the hyperonic part into the EOS to do the inference, the peak of ζ is shifted significantly to lower values. This is reasonable since the appearance of hyperons softens the EOS, but we still have to satisfy the observational constraints from the high-mass pulsar PSR J0740+6620. The inference naturally favours smaller values of ζ to stiffen the EOS, so as to predict stars with larger maximum masses and radii, as already seen in Huang et al. (2024b). The reduction of the ζ parameter results in an increase of radius of a 1.4 M_\odot star. However, the g_ω and λ_0 values slightly decrease when using the hyperonic model, thus compensating the increase of the radii, so that our results for the radius are still compatible with measurements from PSR J0740+6620 and PSR J0030+0451, together with the tidal deformability determination from GW170817.

The hyperonic parameters after inference using the current observations listed above are shown in Figure 4. It is clear that no significant constraint could be placed on the hyperonic parameters; current observations are still not sensitive to the neutron star composition and exotic degrees of freedom. This is in line with our conclusions in Huang et al. (2024b).

Figure 5 shows the posterior of certain nuclear quantities, such as the incompressibility K , symmetry energy J and slope of the symmetry energy L constrained by current observation data, resulting from the hyperonic model inference and the nucleonic model one compared with the constrained hyperonic prior. Inference using a hyperonic model as compared to a nucleonic model does not lead to any notable changes on the nuclear properties, except for a marginal reduction in the distribution width of K . This observation suggests that the current observational data are not yet sufficiently robust to induce significant shifts in the overall shape of the distributions, which is consistent with our previous analysis of the EOS parameters. In Figure 6 we show the M-R posterior of the hyperonic EOS inference with all the current observational constraints. We also show the M-R constrained hyperonic prior. It is clear that the area of the allowed region has shrunk significantly after the current observational constraint when hyperons are considered. Compared with the M-R posterior of the nucleonic EOS inference in (Huang et al. 2024b), the posteriors have a similar area in the mass-radius plane, but the hyperonic M-R posterior is slightly wider. It is interesting to see that a consequence of including hyperons and imposing observational constraints, in particular from PSR J0740+6620, is a shift in the probability distributions towards larger radii for all neutron star masses. Similar conclusions were drawn in (Malik & Providência 2022; Malik et al. 2023). This reflects the fact that the symmetric nuclear

matter EOS has to be much harder to meet the high mass constraint.

The constraining power of astrophysical observations on hyperon-meson couplings has also been the subject of discussion in (Sun et al. 2023). In this study, the authors constrained the couplings of the σ and ω mesons to the Λ hyperon within a Bayesian inference procedure, imposing separate astrophysical and hypernuclear constraints and considering a fixed set of nuclear EOS. They start from a uniform distribution for the ratios $R_{\sigma\Lambda} = g_{\sigma\Lambda}/g_{\sigma N}$ and $R_{\omega\Lambda} = g_{\omega\Lambda}/g_{\omega N}$, assuming that they should be less than 1. They verify that the hypernuclear data are the most constraining. This is consistent with our results showing that astrophysical observations do not constrain the hyperon-meson couplings, beyond the information we already have from hypernuclei.

4.1 Constraint from PSR J0437-4715

Recently Choudhury et al. (2024) reported the results of pulse-profile modeling using NICER data of PSR J0437-4715 (J0437), the closest and brightest rotation-powered millisecond pulsar. Using a mass prior from radio timing (Reardon et al. 2024) they reported a mass of $M = 1.418 \pm 0.037 \text{ M}_\odot$ and a radius of $R = 11.36^{+0.95}_{-0.63} \text{ km}$ (68% credible intervals). This source has a mass very close to that inferred for PSR J0030+0451, while the radius is slightly different. It could therefore be a very good source for constraining a phase transition or the onset of a new degree of freedom such as hyperons.

In Figure 7 we compare the posteriors with and without the J0437 constraint. The inclusion of the new data favors the upper end of the prior for g_ω , while λ_0 shows a narrower 68% interval shifted towards smaller values and the credible interval on the ζ parameter also narrows. The behaviour obtained for λ_0 is consistent with our expectation that a smaller value corresponds to a smaller radius of the 1.4 M_\odot star. The reduction of λ_0 comes with an increase of g_ω and a reduction of ζ to make the model stiff enough to also describe the two solar mass pulsar PSR J0740+6620. It is interesting to note that the parameter Λ_ω begins to take a shape different from the prior distribution, highlighting the increased constraining power of the new data.

Regarding the hyperonic parameters, the current precision of this new result still does not allow us to draw any obvious constraints. In Figure 8, we present the constrained nuclear quantities, comparing scenarios with and without J0437. There is no clear difference, leading to the conclusion that even with this new observation, we cannot constrain nuclear quantities in this hyperonic model.

5 EOS CONSTRAINTS FROM FUTURE OBSERVATIONS

In this section, we explore the extent to which future telescopes will be able to detect the composition of neutron stars. We do this by computing the evidence for each inference run, thereby allowing model comparison based on the same injected data. Our overall goal is to see whether we can accurately recover the models that generated the injected data and whether we can discriminate between the different models. Specifically, we want to determine whether our simulated

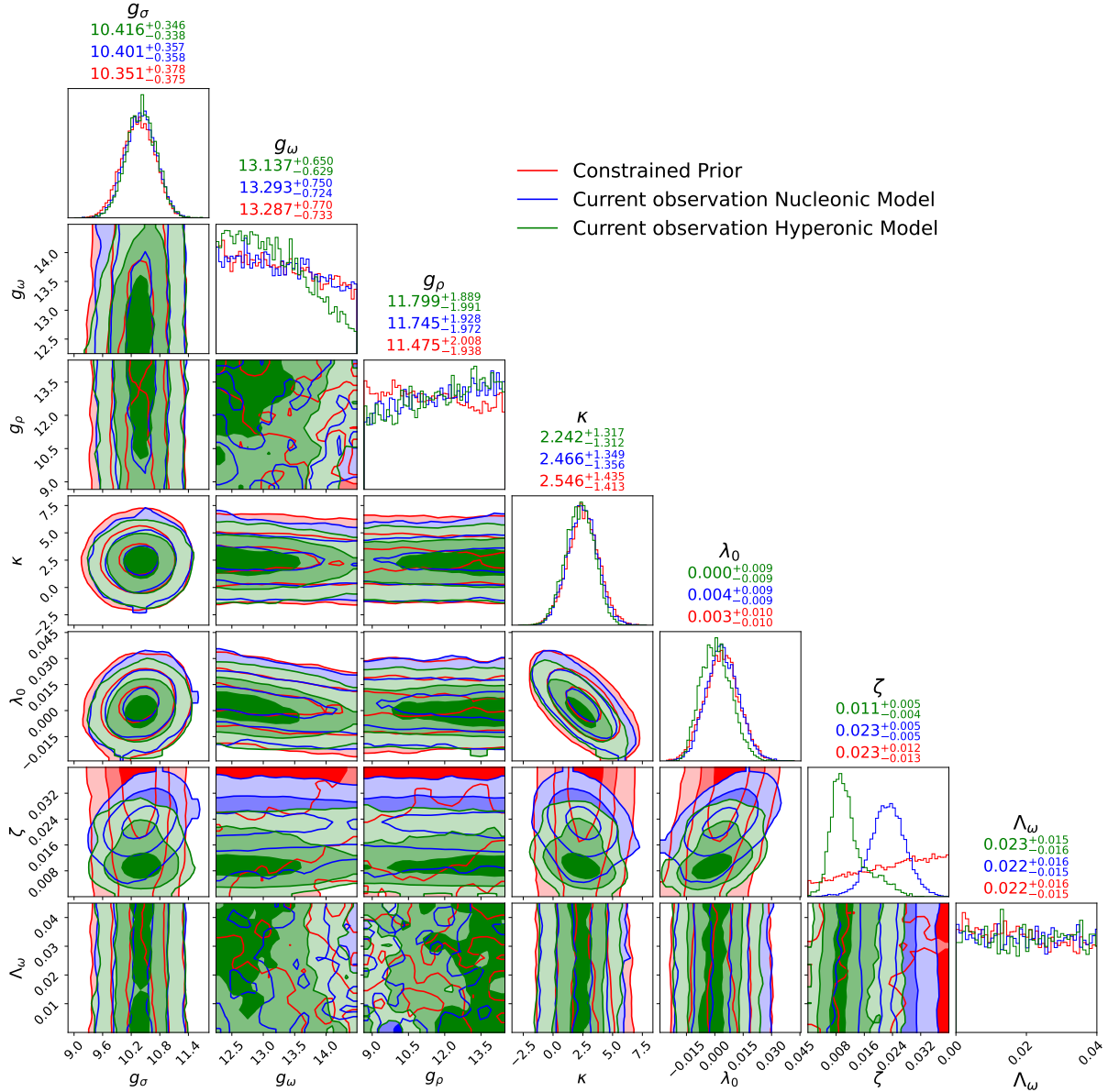


Figure 3. The posterior of the first seven nucleonic EOS model parameters derived from existing observations, for both pure nucleonic and hyperonic models. Blue is the inference result with the current observation but with the nucleonic model, green is the posterior of the same set of observations with the hyperonic model. The red contour is the constrained hyperonic prior space we used in these two analyses. The contour levels in the corner plot, going from deep to light colours, correspond to the 68%, 84% and 98.9% levels. The title of each panel indicates the median of the distribution as well as the range of the 68% credible interval. Here κ is given in MeV.

observational data preferentially support the existence of hyperons in the interior of neutron stars.

The following subsections will be organized according to the different injected data, each of the injected data reflecting the two types of "reality": neutron stars with hyperons (inject-hyp) and neutron stars without hyperons (inject-nucl).

5.1 Nucleonic injected data

In this subsection, we investigate the performance of the models under the nucleonic injected data, inject-nucl.

For the Future-X inject-nucl data, Figure 9 shows the posterior of the nucleonic EOS parameters using the nucleonic model and the hyperonic model. The first general observation is that the same set of EOS parameters is modified with both prior settings, namely g_ω , g_ρ , λ_0 , ζ and Λ_ω . In addition, with the hyperonic model there is a tighter constraint on these nucleonic parameters, since satisfying the observational constraints simultaneously with allowing the existence of hyperons limits the nucleonic EOS parameter space more tightly.

Similar to the analysis performed for the current observations, the Future-X inject-nucl constraints favour smaller ζ in order to reach the largest mass, which now reaches 2.20

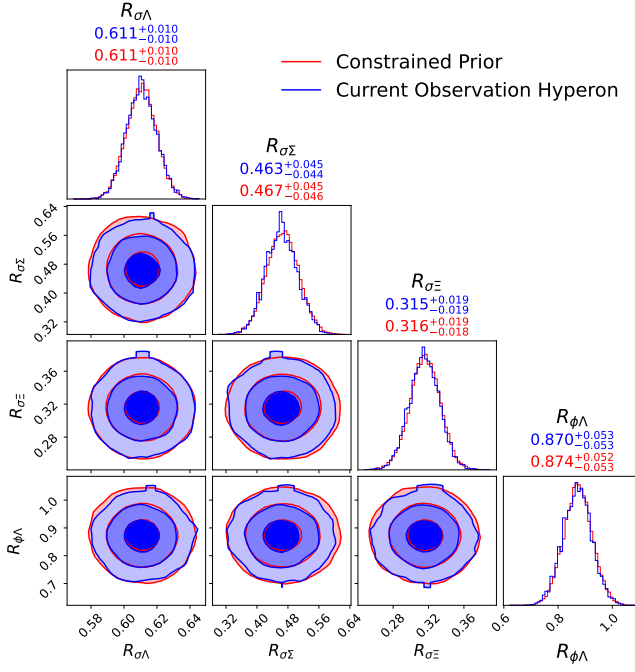


Figure 4. The posterior of the four hyperonic EOS model parameters after applying constraints from existing observations using the hyperonic prior. Red represents the prior of the hyperonic parameters. Blue indicates the inference result with the current observations (assuming the hyperonic model/prior). The contour levels in the corner plot, going from dark to light colours, correspond to the 68%, 84% and 98.9% levels. The title of each panel indicates the median of the distribution as well as the range of the 68% credible interval.

M_\odot , and λ_0 and g_ω reshape accordingly to predict a reasonable radius for $1.4 M_\odot$ star. However, in contrast to the current observation scenario, all EOS parameters shift compared to their priors, indicating the potential for strong EOS constraints from next generation X-ray telescopes. The consistency of the inferred posteriors with the injected parameter values is evident, indicating an effective approach to model recovery. In contrast, the posterior inferred from hyperonic model tend to converge to a distinct region. This discrepancy is due to the inclusion of hyperons, which requires adjustments to the nucleonic model parameters.

In Figure 10 we illustrate the constraints imposed on the hyperonic parameters by the nucleonic injected data. The hyperonic parameters appear to more restricted. However, it is crucial not to interpret this as favoring hyperons in the simulated sources, since the EOS that generated the injected data does not include hyperons. Instead, we should interpret these constraints as indicating a reduction in the hyperonic parameter space due to neutron star measurements, and a shift to a more repulsive interaction. As the measurements continue to improve, it is foreseeable that the hyperonic parameter space will become increasingly constrained, potentially posing challenges in finding suitable parameter values to effectively fit the observations. This underlines the evolving nature of our understanding as observational capabilities improve.

In Figure 11 we illustrate the constraints on the selected nuclear quantities. By comparing the different model con-

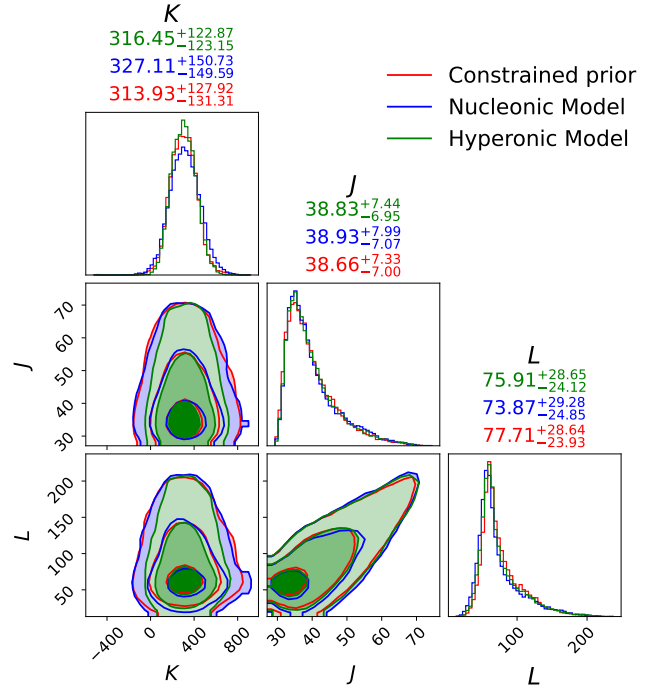


Figure 5. The posterior of all the nuclear quantities after applying constraints from current astrophysical observations using both the nucleonic model (blue contour) and the hyperonic model (green contour). Red shows the constrained hyperonic prior. The contour levels in the corner plot, going from dark to light colours, correspond to the 68%, 84% and 98.9% levels. The title of each panel indicates the median of the distribution as well as the range of the 68% credible interval.

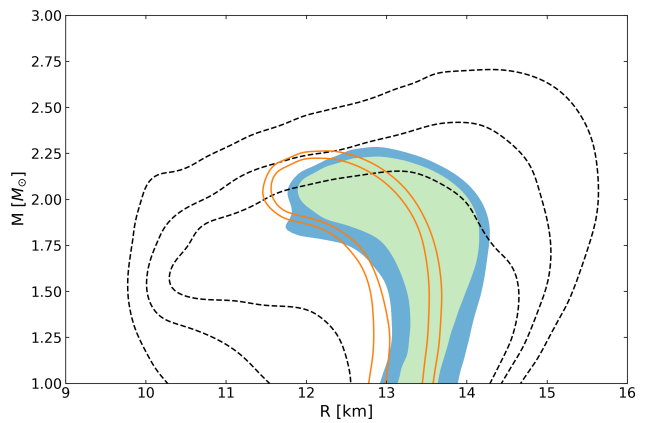


Figure 6. The M-R posterior after applying all current observations (except PSR J0437-4715) using the hyperonic model, showing the 68% (light green) and 84% (blue) credible regions and the nucleonic posterior from (Huang et al. 2024b) (orange line). The black dashed lines show the M-R prior resulting from the initial hyperonic EOS model and priors but after imposing priors on E/A , m^* and n_0 , delineating the 68%, 84% and 100% credible regions (as in Figure 1).

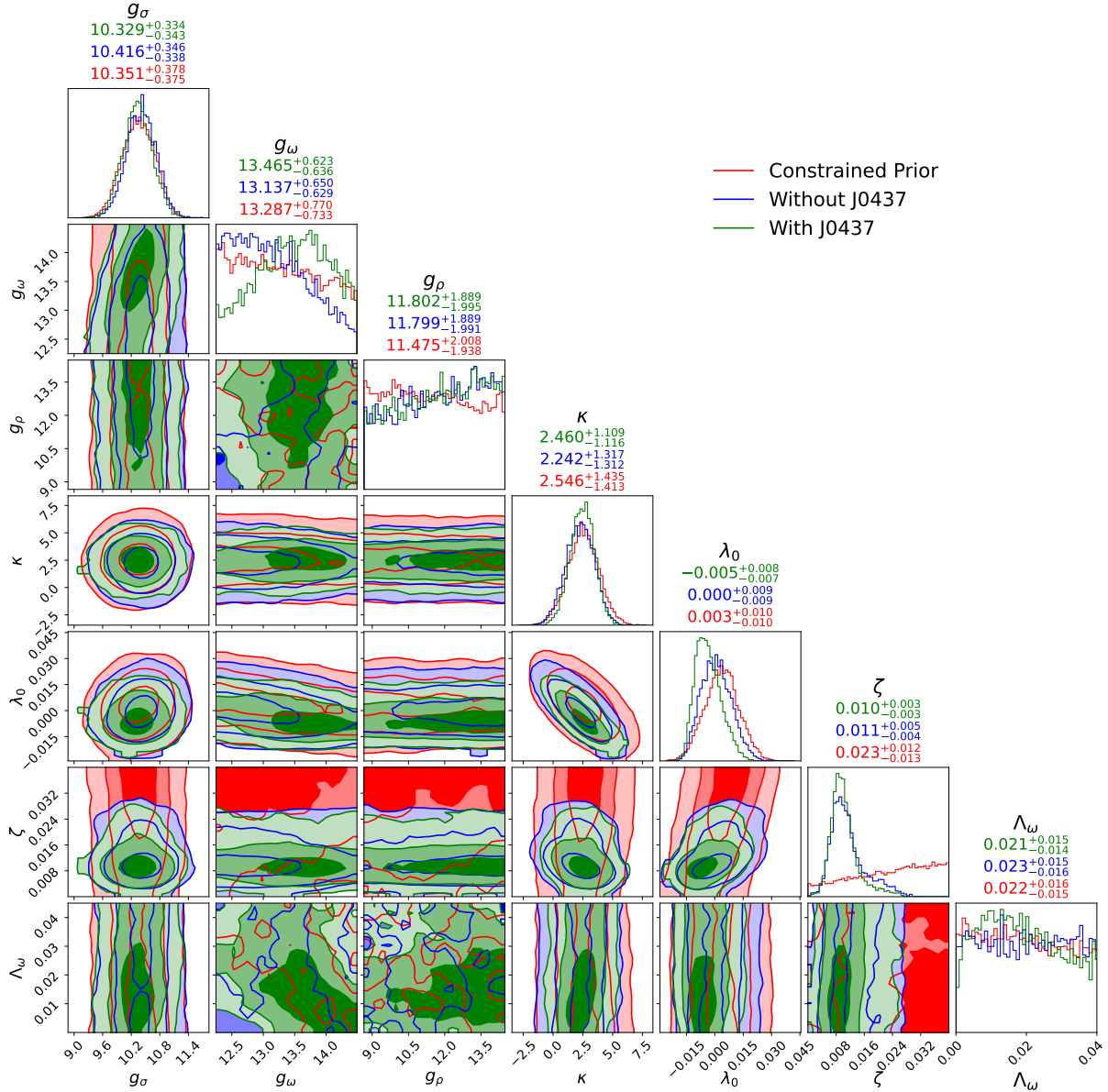


Figure 7. Effect of including the mass-radius measurement of PSR J0437-4715 on the model parameters: a comparison between the constrained hyperonic prior (red contour) and the posteriors obtained without including (blue contour levels) and including (green contour) the constraints from PSR J0437-4715. The contour levels in the corner plot, going from deep to light colors, correspond to the 68%, 84%, and 98.9% levels. The title of each panel indicates the median value of the distribution as well as the range of 68% credible interval. Here κ is given in MeV.

straints, we observe that the hyperonic model imposes tighter constraints on the nuclear properties. This observation is consistent with the constraining power seen in the EOS space shown in Figure 9. It seems that to account for the presence of hyperons, finer adjustments to nuclear quantities are required to mitigate the softening effects on the EOS induced by hyperons.

5.2 Hyperonic injected data

In this subsection, we delve into the constraints introduced by the Future-X hyperon scenario, inject-hyp data.

Figure 12 illustrates the constraints introduced by the inject-hyp data obtained from TM1-2 $\omega\rho nH$. Since the injected EOS predicts a maximum mass neutron star of $1.94 M_\odot$, this places less stringent constraints on hyperons, since hyperons are less likely to exist if large-mass neutron stars are observed. As a result, the posterior shows minimal reshaping, even with a 2% uncertainty in the precision of the mass-radius measurement.

Turning to the nucleonic EOS parameters shown in Figure 13, several notable observations can be made. Firstly, the nucleonic parameters tend to be better constrained when the hyperonic model is used, particularly g_ω and Λ_ω . In the case

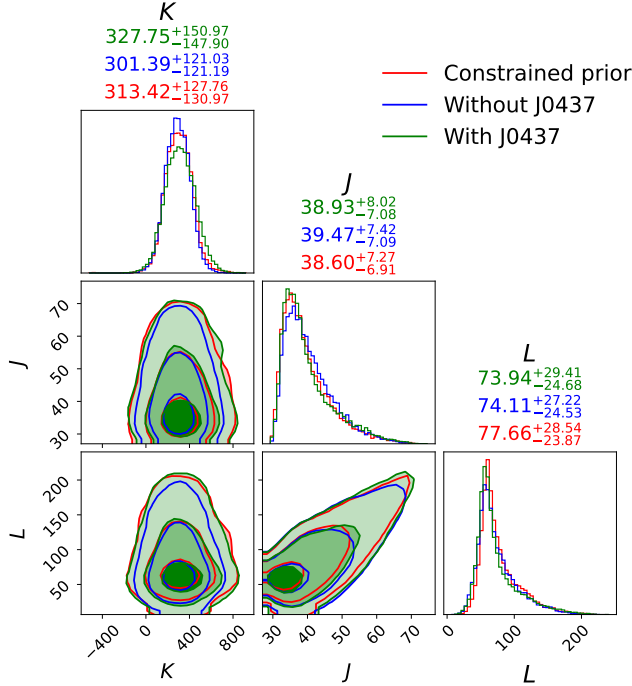


Figure 8. The posterior of all the nuclear quantities after applying constraints from current astrophysical observations with (green) and without (blue) the constraints from PSR J0437-4715. Red shows the constrained hyperonic prior. The contour levels in the corner plot, going from dark to light colours, correspond to the 68%, 84% and 98.9% levels. The title of each panel indicates the median of the distribution as well as the range of the 68% credible interval.

of the nucleonic model, the posteriors on these parameters are not significantly different from the prior distribution.

Another important observation concerns the sensitivity of ζ to the maximum mass of neutron stars. In general, to accommodate neutron stars with a maximum mass of $1.94 M_{\odot}$, a larger ζ value is required to soften the EOS. This explains why both nucleonic and hyperonic model posteriors on ζ tend to cluster at the upper end of prior range. However, as hyperons further soften the EOS, hyperonic models tend to shift towards the lower end compared to the nucleonic models. In fact, a small value of ζ is essential to ensure the description of $\sim 2 M_{\odot}$ stars.

When comparing the recovery of the injected EOS parameters (indicated by the black dashed line), for ζ , the injected value lies outside the 3-sigma range of nucleonic posterior. This observation suggests that the underlying hyperonic EOS is finely-tuned with specific nucleonic and hyperonic parameter choices, making it challenging to recover through inference and necessitating more precise measurements or more measurements.

The resulting distribution of the selected nuclear quantities is shown in Figure 14. Interestingly, this figure shows that the hyperonic posterior is less constrained than the nucleonic posterior. However, it is important to note that these constraints are still not very tight, mainly due to the fact

Injected data + Model	$\ln(Z)$	Bayes' Factor
Nucleonic + Nucleonic	-210.05	...
Nucleonic + Hyperonic	-211.85	$N/H = 6.04$
Hyperonic + Nucleonic	-116.68	...
Hyperonic + Hyperonic	-111.45	$H/N = 186.79$

Table 3. This table gives the global log evidence ($\ln Z$), as returned by Ultranest, for the nucleonic and hyperonic models under two different injected model simulated observations: inject-nucl and inject-hyp. For comparison, we also give the Bayes' factor of these two different groups based on the same injected model, N/H denotes the Bayes' factor of the nucleonic vs. hyperonic model. H/N denotes the hyperonic model compared to the nucleonic one.

that the maximum mass of the neutron star predicted in this injected EOS is not large enough.

5.3 Bayesian Evidence Comparison

In order to compare how well different models can recover the underlying injected EOS, we use Bayes' factors. In [Kass & Raftery \(1995\)](#) a model is deemed ‘substantially preferred’ if the Bayes factor is greater than 3.2 and ‘strongly preferred’ if it is greater than 10, and ‘decisive’ if the Bayes’ factor is greater than 100.

When calculating the Bayes' factor, we extract the logarithm of the Bayesian evidence directly from the inference, denoted as $\ln(Z)$. Here we focus exclusively on the comparison of the Future-X case study. The ultimate goal of the Bayesian inference of the EOS is to use Bayesian techniques to uncover the underlying EOS of neutron star matter or to extract information about neutron star composition.

In this study, the injected EOS act as the “hypothesised” underlying EOS of neutron stars. Our goal is to use different neutron star models (nucleonic or hyperonic) to recover the underlying EOS on which all simulated observations are based. By comparing the Bayesian evidence and then calculating the Bayes factor for each pair of inferences, we can gain unique insights into which model is preferred by the observations. This approach has significant potential for exploring exotic degrees of freedom.

In Table 3, we present the $\ln(Z)$ values along with the Bayes factors based on the performance with the different injected EOS. For the injected EOS that is purely nucleonic, the Bayesian evidence suggests that the nucleonic model performs better in explaining all simulated observations. This result is in line with the expectations, given that the underlying injected EOS is exclusively nucleonic. If we compute the Bayes factor between these two inferences to compare their fitting degree, we obtain a Bayes factor of 6.04. According to the interpretation of the Bayes factor we can confidently say that our simulated observations substantially favour the nucleonic model.

If the underlying injected EOS contains exotic degrees of freedom, such as hyperons, we compute the $\ln(Z)$ values using both nucleonic and hyperonic model frameworks. It is expected that the hyperonic model will exhibit significantly higher $\ln(Z)$ performance in recovering the hyperonic EOS, as the nucleonic model does not account for any exotic degrees of freedom. The resulting Bayes factor between these

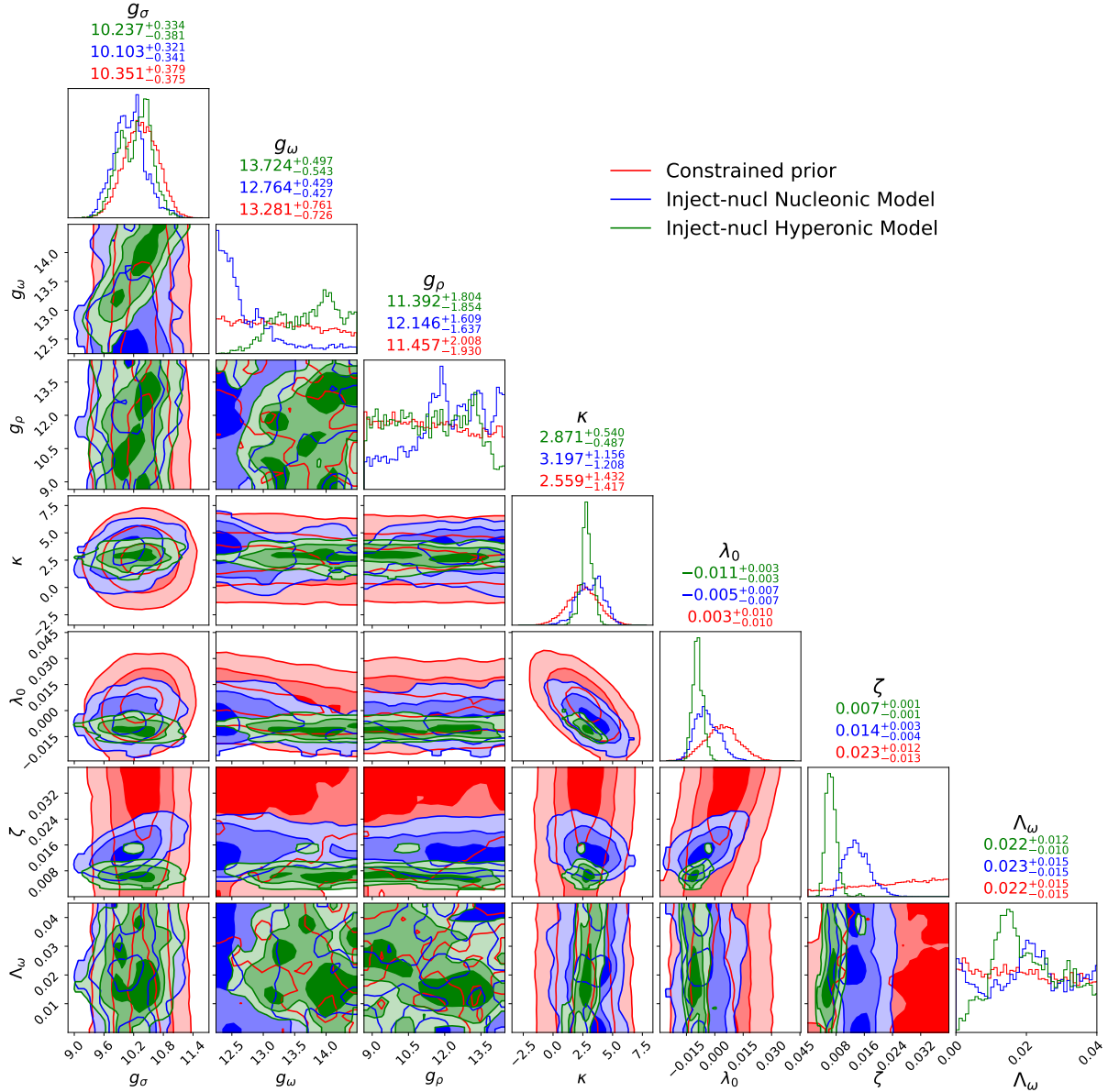


Figure 9. After applying the constraint of simulated Future-X inject-nucl measurements, i.e. six 2% uncertainty M-R measurements along the M-R curve obtained with the TM1- $2\omega\rho n$ EOS (nucleonic EOS), the posterior of all EOS parameters from the nucleonic model (blue contour levels) is compared with the results from the hyperonic model (green contour) and the constrained hyperonic prior (red contour). The contour levels in the corner plot, going from deep to light colours, correspond to the 68%, 84% and 98.9% levels. The title of each panel indicates the median of the distribution as well as the range of the 68% credible interval. Here κ is given in MeV. The black dashed horizontal and vertical lines in the plot and the yellow dots show the values for the injected EOS used to generate the simulated M-R measurements.

two inferences is 186.76. Despite the limitations of our study this is encouraging; even though we cannot fully recover the underlying hyperonic parameters, the presence of hyperons is still (correctly, given our injected data set) supported by the evidence.

6 CONCLUSIONS

We have considered a microscopic phenomenological hadronic model based on a field-theoretical framework, which includes

both nucleonic and hyperonic degrees of freedom to span the neutron star M-R space. Using a Bayesian inference approach, the parameters of the model are constrained using observational data of neutron stars and some minimal information on the saturation properties of nuclear matter at saturation density. Our main objective was to complete the study Huang et al. (2024b) and to understand the capacity of neutron star observations to give information about neutron star interior composition. In Huang et al. (2024b) only nucleonic degrees of freedom were considered. By comparing the hyperonic model inference results calculated in the present

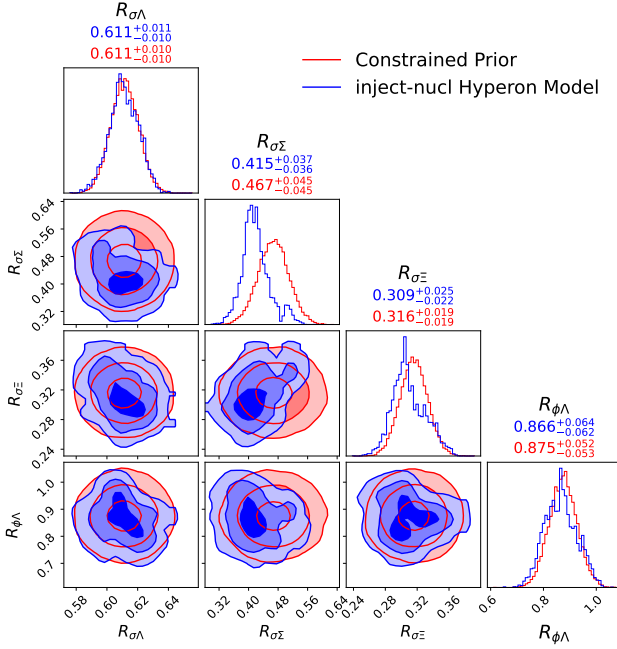


Figure 10. The posterior of the four hyperonic EOS model parameters after applying constraints from the Future-X inject-nucl data using the hyperonic model (blue). Red represents the priors for the hyperonic parameters. The contour levels in the corner plot, going from dark to light colours, correspond to the 68%, 84% and 98.9% levels. The title of each panel indicates the median of the distribution as well as the range of the 68% credible interval.

study with the nucleonic model results built in Huang et al. (2024b), we wanted to understand if it is possible to make a statement about the presence of hyperons in neutron stars.

As constraints, we consider two possibilities: i) the current observational constraints, including electromagnetic radio and X-ray and GWs; ii) simulated observations as expected from future X-ray timing telescopes, i.e. assuming that the neutron star radius and mass are determined with 2% uncertainty. The simulated observations consist of two sets of six mass-radius observations with 2% uncertainty, centered on the M-R predicted by two different EOS, one including only nucleons and leptons as degrees of freedom, and a second including also hyperonic degrees of freedom.

It was shown that current observations do not place a significant constraint on the hyperonic parameters of the model. A similar conclusion was reached in Sun et al. (2023). Regarding other model parameters, it has been shown that the hyperonic inference model favours parameters values that stiffen the EOS to predict stars with larger maximum masses and radii. However, the main conclusion is that the hyperonic inference model constrained by current observations does not lead to significant changes in the nuclear properties.

In a second step we have considered simulated future X-ray data to constrain the hyperonic and the nucleonic inference models. Each one of the models was constrained by simulated observational data generated from an EOS with and without hyperonic degrees of freedom.

The nucleonic injected data placed noticeable constraints on the nucleonic EOS parameters of both inference models, with tighter constraints occurring for the hyperonic inference

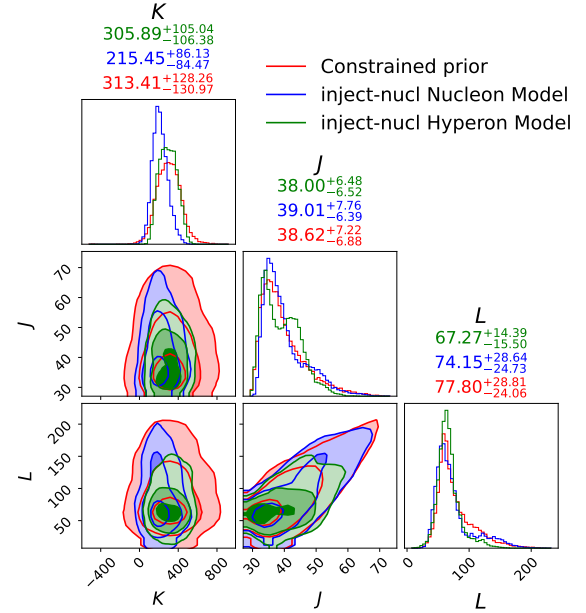


Figure 11. The posterior distributions of the nuclear quantities obtained imposing the Future-X inject-nucl data from TM1-2 $\omega\rho\eta$. Red shows the constrained hyperonic prior, blue and green show, respectively, the posterior resulting from the nucleonic model and the hyperonic model. The contour levels in the corner plots, going from dark to light colours, correspond to the 68%, 84% and 98.9% levels. The title of each panel indicates the median of the distribution as well as the range of the 68% credible interval. The black dashed horizontal and vertical lines in the plot and the yellow dots show the injected values used to generate the simulated M-R measurements.

model due to the difficulty of simultaneously allowing the existence of hyperons and reaching the largest observed mass. The nucleonic injected data also had a non-negligible effect on the hyperonic parameters, showing an effective reduction of the hyperonic parameter space due to neutron star measurements. If no hyperons occur inside neutron stars, we may expect that tighter observational constraints could shift the hyperonic parameter space to make the interaction more repulsive. Finally, it was also shown that the hyperonic model imposes tighter constraints on the nuclear properties.

Imposing as constraints the hyperonic injected data, which includes a maximum mass $1.94M_\odot$ star, the hyperonic parameter space showed only a minimal reshaping. However, the nucleonic EOS parameters of the hyperonic inference model were, in general, better constrained than those of the nucleonic inference model. A parameter that was quite sensitive to the constraints is the parameter ζ that controls the behavior of the EOS at high densities, a larger value corresponding to a softer EOS and a smaller maximum mass, larger values being obtained with the nucleonic inference model. The effect of this parameter on the M-R curve is similar to that due to the presence of hyperons, and the two effects cannot be easily disentangled. For the injected data considered, the ζ parameter of the injected EOS could not be recovered well (lying outside the 3-sigma posterior distribution of nucleonic inference model but still inside the 3-sigma distribution of the

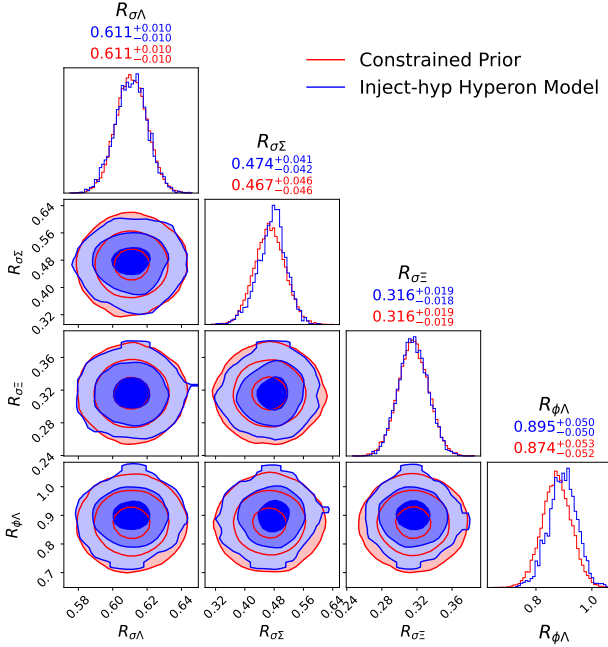


Figure 12. The posterior of the four hyperonic EOS model parameters after applying the constraints from the Future-X hyperon case, inject-hyp data, using the hyperonic model (blue). Red represents the prior of the hyperonic parameters in the hyperonic model. The contour levels in the corner plot, going from deep to light colors, correspond to the 68%, 84%, and 98.9% levels. The title of each panel indicates the median value of the distribution as well as the range of 68% credible interval.

hyperonic parameters posterior), indicating that more precise - and possibly more - data are necessary.

Finally, we also compared the different future X-ray data scenarios by calculating Bayes' factors from the evidence of the two inference models when both sets of injected data (nucleonic and hyperonic) were considered as constraints. Using injected nucleonic data, the nucleonic inference came out as preferred; while when using injected hyperonic data, the Bayes' factor decisively favours the hyperonic inference model. This result allows us to conclude that it is possible to obtain decisive evidence in favour of the hyperonic inference model in this case, even though we are not able to recover the EOS parameters.

ACKNOWLEDGEMENTS

C.H. acknowledges support from an Arts & Sciences Fellowship at Washington University in St. Louis and NASA grant 80NSSC24K1095. L.T. work was supported under contract No. PID2022-139427NB-I00 financed by the Spanish MCIN/AEI/10.13039/501100011033/FEDER,UE and from the project CEX2020-001058-M Unidad de Excelencia ‘María de Maeztu’. Moreover, this project has received funding from the European Union Horizon 2020 research and innovation programme under the program H2020-INFRAIA-2018-1, grant agreement No.824093 of the STRONG-2020 project, from the CRC-TR 211 ‘Strong-interaction matter under extreme conditions’- project Nr.

315477589 - TRR 211, from the Generalitat de Catalunya under contract 2021 SGR 00171 and Generalitat Valenciana under contract CIPROM/2023/59. C.P. received support from Fundação para a Ciéncia e a Tecnologia (FCT), I.P., Portugal, under the projects UIDB/04564/2020 (doi:10.54499/UIDB/04564/2020), UIDP/04564/2020 (doi:10.54499/UIDP/04564/2020), and 2022.06460.PTDC (doi:10.54499/2022.06460.PTDC). A.L.W. acknowledges support from ERC Consolidator Grant No. 865768 AEONS. Computations were carried out on the HELIOS cluster on dedicated nodes funded via this grant.

DATA AVAILABILITY

The posterior samples and scripts to make the plots in this paper are available in a Zenodo repository ([Huang et al. 2024a](#))

REFERENCES

- Abbott B. P., et al., 2017, *Phys. Rev. Lett.*, **119**, 161101
- Abbott B. P., et al., 2018, *Phys. Rev. Lett.*, **121**, 161101
- Abbott B. P., et al., 2020b, *ApJ*, **892**, L3
- Abbott B. P., et al., 2020a, *ApJ*, **892**, L3
- Ahn J. K., et al., 2013, *Phys. Rev. C*, **88**, 014003
- Altiparmak S., Ecker C., Rezzolla L., 2022, *Astrophys. J. Lett.*, **939**, L34
- Ambartsumyan V. A., Saakyan G. S., 1960, Soviet Ast., **4**, 187
- Annala E., Gorda T., Kurkela A., Vuorinen A., 2018, *Phys. Rev. Lett.*, **120**, 172703
- Annala E., Gorda T., Kurkela A., Nättilä J., Vuorinen A., 2020, *Nature Physics*, **16**, 907
- Annala E., Gorda T., Hirvonen J., Komoltsev O., Kurkela A., Nättilä J., Vuorinen A., 2023, *Nature Communications*, **14**, 8451
- Banik S., Hempel M., Bandyopadhyay D., 2014, *ApJS*, **214**, 22
- Barret D., et al., 2013, in Cambresy L., Martins F., Nuss E., Palacios A., eds, SF2A-2013: Proceedings of the Annual meeting of the French Society of Astronomy and Astrophysics. pp 447–453 ([arXiv:1310.3814](#)), doi:10.48550/arXiv.1310.3814
- Baym G., Pethick C., Sutherland P., 1971, *ApJ*, **170**, 299
- Burgio G. F., Schulze H. J., Vidaña I., Wei J. B., 2021, *Progress in Particle and Nuclear Physics*, **120**, 103879
- Chatterjee D., Vidaña I., 2016, *Eur. Phys. J. A*, **52**, 29
- Chen W.-C., Piekarewicz J., 2014, *Phys. Rev. C*, **90**
- Choudhury D., et al., 2024, *ApJ*, **971**, L20
- Cromartie H. T., et al., 2020, *Nature Astronomy*, **4**, 72
- Demorest P. B., Pennucci T., Ransom S. M., Roberts M. S. E., Hessels J. W. T., 2010, *Nature*, **467**, 1081
- Dittmann A. J., et al., 2024, *arXiv e-prints*, p. arXiv:2406.14467
- Dover C. B., Gal A., 1983, *Annals Phys.*, **146**, 309
- Essick R., Tews I., Landry P., Schwenk A., 2021, *Phys. Rev. Lett.*, **127**, 192701
- Fonseca E., et al., 2021, *ApJ*, **915**, L12
- Friedman E., Gal A., 2007, *Phys. Rept.*, **452**, 89
- Friedman E., Gal A., 2021, *Phys. Lett. B*, **820**, 136555
- Friedman E., Gal A., 2023, *Phys. Lett. B*, **837**, 137640
- Fukuda T., et al., 1998, *Phys. Rev. C*, **58**, 1306
- Gendreau K. C., et al., 2016, in den Herder J.-W. A., Takahashi T., Bautz M., eds, Society of Photo-Optical Instrumentation Engineers (SPIE) Conference Series Vol. 9905, Space Telescopes and Instrumentation 2016: Ultraviolet to Gamma Ray. p. 99051H, doi:10.1117/12.2231304
- Gorda T., Komoltsev O., Kurkela A., 2023, *Astrophys. J.*, **950**, 107

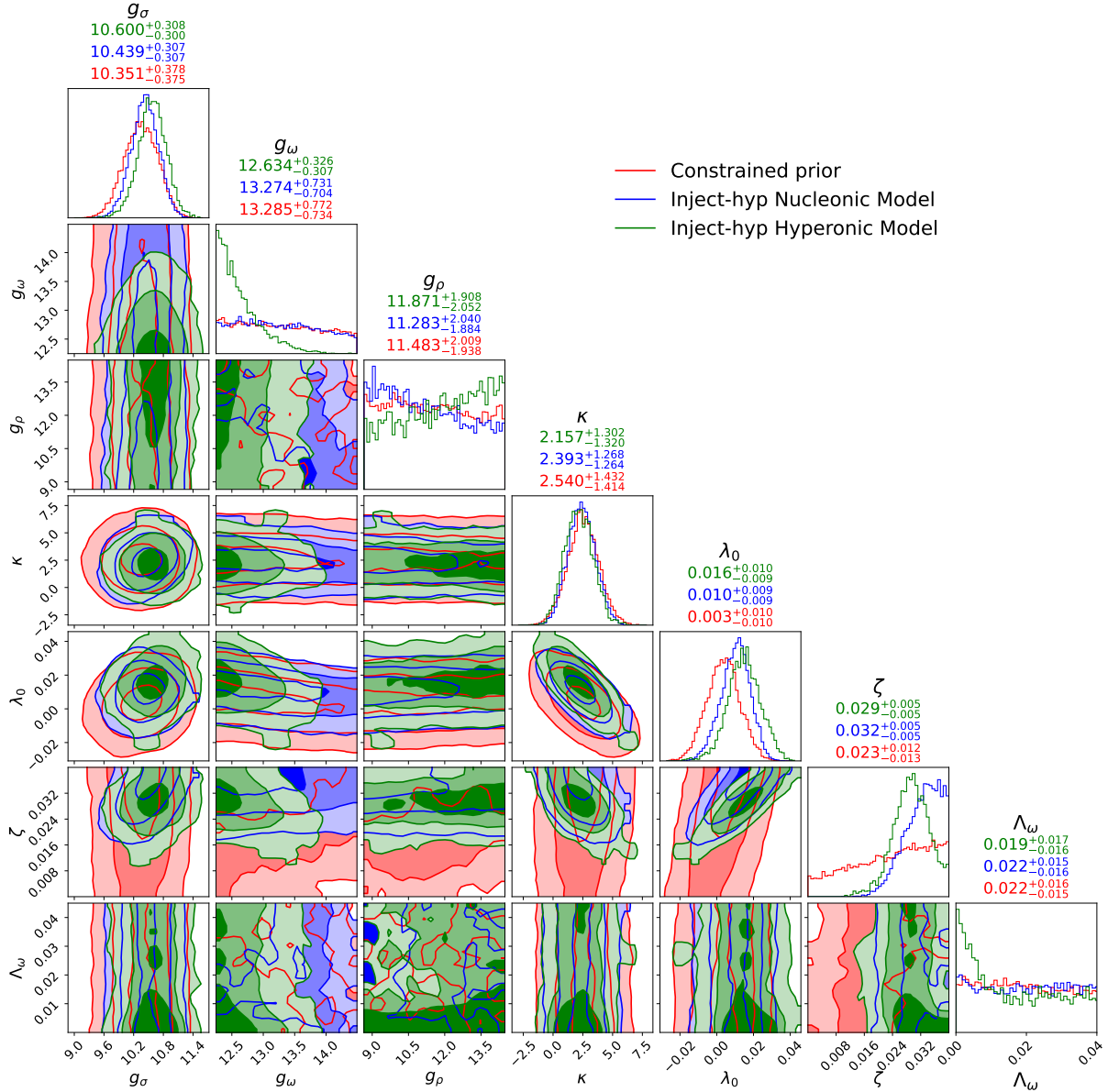


Figure 13. After applying the constraint of simulated Future-X inject-hyp measurements, that is six 2% uncertainty M-R measurements along M-R curve obtained with the TM1- $2\omega\rho nH$ EOS (Hyperonic EOS), the posterior of all the EOS parameters from nucleonic model (blue contour levels) compared to the results from hyperonic model (green contour) and the constrained hyperonic prior (red contour). The contour levels in the corner plot, going from deep to light colors, correspond to the 68%, 84%, and 98.9% levels. The title of each panel indicates the median value of the distribution as well as the range of 68% credible interval. Here κ is given in MeV. The black dashed horizontal and vertical lines in the plot and the yellow dots show the injected values used to generate the simulated M-R measurements.

Greif S. K., Raaijmakers G., Hebeler K., Schwenk A., Watts A. L., 2019, *MNRAS*, 485, 5363
 Harada T., Hirabayashi Y., 2006, *Nucl. Phys. A*, 767, 206
 Huang C., Raaijmakers G., Watts A. L., Tolos L., Providência C., Osborn N., Whitsett N., 2023, CompactObject: An open-source package for neutron star whole workflow Bayesian inference constraining Neutron star EOS package, <https://github.com/ChunHuangPhy/CompactObject>
 Huang C., Watts A. L., Tolos L., Providência C., 2024a, Constraining a relativistic mean field model using neutron star mass-radius measurements II: Hyperonic models, [doi:10.5281/zenodo.13941494](https://doi.org/10.5281/zenodo.13941494)
 Huang C., Raaijmakers G., Watts A. L., Tolos L., Providência C.,

2024b, *MNRAS*, 529, 4650
 Kass R. E., Raftery A. E., 1995, Journal of the American Statistical Association, 90, 773
 Khaustov P., et al., 2000, *Phys. Rev. C*, 61, 054603
 Koehn H., et al., 2024, *arXiv e-prints*, p. arXiv:2402.04172
 Kohno M., Fujiwara Y., Watanabe Y., Ogata K., Kawai M., 2006, *Phys. Rev. C*, 74, 064613
 Kurkela A., Fraga E. S., Schaffner-Bielich J., Vuorinen A., 2014, *Astrophys. J.*, 789, 127
 Landry P., Essick R., Chatzioannou K., 2020, *Phys. Rev. D*, 101, 123007
 Legred I., Chatzioannou K., Essick R., Han S., Landry P., 2021, *Phys. Rev. D*, 104, 063003

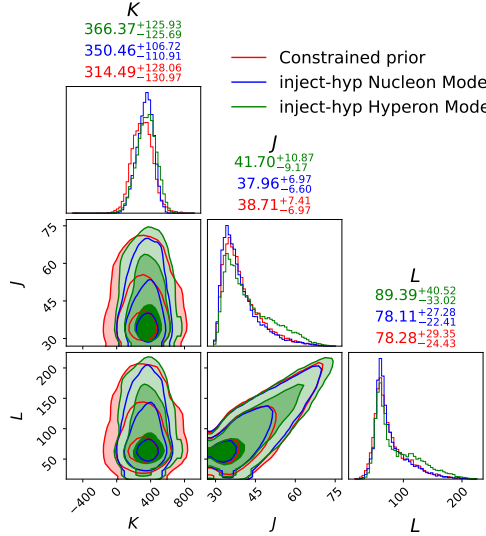


Figure 14. The posterior of all the nuclear quantities after applying constraints of simulated Future-X inject-hyp measurements for both nucleonic model (blue contour) and hyperonic model (green contour). Red shows the constrained hyperonic prior. The contour levels in the corner plot, going from deep to light colors, correspond to the 68%, 84%, and 98.9% levels. The title of each panel indicates the median value of the distribution as well as the range of 68% credible interval.

- Lo K. H., Miller M. C., Bhattacharyya S., Lamb F. K., 2013, *ApJ*, **776**, 19
 Malik T., Providência C., 2022, *Phys. Rev. D*, 106, 063024
 Malik T., Ferreira M., Albino M. B., Providência C., 2023, *Phys. Rev. D*, 107, 103018
 Millener D. J., Dover C. B., Gal A., 1988, *Phys. Rev. C*, 38, 2700
 Miller M. C., et al., 2019, *ApJ*, **887**, L24
 Miller M. C., et al., 2021, *ApJ*, **918**, L28
 Miyatsu T., Yamamoto S., Nakazato K., 2013, *ApJ*, 777, 4
 Noumi H., et al., 2002, *Phys. Rev. Lett.*, 89, 072301
 Oppenheimer J. R., Volkoff G. M., 1939, *Phys. Rev.*, 55, 374
 Pang P. T. H., Sivertsen L., Somasundaram R., Dietrich T., Sen S., Tews I., Coughlin M. W., Van Den Broeck C., 2024, *Phys. Rev. C*, **109**, 025807
 Providência C., Rabhi A., 2013, *Phys. Rev. C*, 87, 055801
 Providência C., Fortin M., Pais H., Rabhi A., 2019, *Frontiers in Astronomy and Space Sciences*, **6**, 13
 Psaltis D., Öznel F., Chakrabarty D., 2014, *ApJ*, **787**, 136
 Raaijmakers G., et al., 2019, *ApJ*, **887**, L22
 Raaijmakers G., et al., 2020, *ApJ*, **893**, L21
 Raaijmakers G., et al., 2021, *ApJ*, **918**, L29
 Ray P. S., et al., 2019, arXiv e-prints, p. arXiv:1903.03035
 Reardon D. J., et al., 2016, *MNRAS*, 455, 1751
 Reardon D. J., et al., 2024, *ApJ*, **971**, L18
 Riley T. E., et al., 2019, *ApJ*, **887**, L21
 Riley T. E., et al., 2021, *ApJ*, **918**, L27
 Rutherford N., et al., 2024, *ApJ*, **971**, L19
 Salmi T., et al., 2022, *ApJ*, **941**, 150
 Salmi T., et al., 2023, *ApJ*, **956**, 138
 Salmi T., et al., 2024a, arXiv e-prints, p. arXiv:2406.14466
 Salmi T., et al., 2024b, arXiv e-prints, p. arXiv:2409.14923
 Schaffner J., Mishustin I. N., 1996, *Phys. Rev. C*, 53, 1416
 Sun X., Miao Z., Sun B., Li A., 2023, *ApJ*, **942**, 55
 Takahashi H., et al., 2001, *Phys. Rev. Lett.*, 87, 212502
 Takátsy J., Kovács P., Wolf G., Schaffner-Bielich J., 2023, *Phys. Rev. D*, **108**, 043002

- Tews I., Carlson J., Gandolfi S., Reddy S., 2018, *ApJ*, **860**, 149
 Tolman R. C., 1939, *Phys. Rev.*, 55, 364
 Tolos L., Fabbietti L., 2020, *Progress in Particle and Nuclear Physics*, **112**, 103770
 Tolos L., Centelles M., Ramos A., 2016, *ApJ*, 834, 3
 Tolos L., Centelles M., Ramos A., 2017, *Publ. Astron. Soc. Australia*, 34
 Vinciguerra S., et al., 2024, *ApJ*, **961**, 62
 Watts A. L., et al., 2016, *Reviews of Modern Physics*, **88**, 021001
 Watts A. L., et al., 2019, *Science China Physics, Mechanics, and Astronomy*, **62**, 29503
 Weissenborn S., Chatterjee D., Schaffner-Bielich J., 2012, *Phys. Rev. C*, 85, 065802
 Yoshimoto M., et al., 2021, *PTEP*, 2021, 073D02

This paper has been typeset from a TeX/LaTeX file prepared by the author.



Relativistic Description of Dense Matter Equation of State and Compatibility with Neutron Star Observables: A Bayesian Approach

Tuhin Malik¹ , Márcio Ferreira¹ , B. K. Agrawal^{2,3} , and Constança Providência¹

¹ CFisUC, Department of Physics, University of Coimbra, 3004-516 Coimbra, Portugal; tuhin.malik@gmail.com, tuhin.malik@uc.pt, marcio.ferreira@uc.pt, cp@uc.pt

² Saha Institute of Nuclear Physics, 1/AF Bidhannagar, Kolkata 700064, India; bijay.agrawal@saha.ac.in

³ Homi Bhabha National Institute, Anushakti Nagar, Mumbai 400094, India

Received 2022 January 21; revised 2022 February 21; accepted 2022 February 28; published 2022 April 28

Abstract

The general behavior of the nuclear equation of state (EOS), relevant for the description of neutron stars (NSs), is studied within a Bayesian approach applied to a set of models based on a density-dependent relativistic mean-field description of nuclear matter. The EOS is subjected to a minimal number of constraints based on nuclear saturation properties and the low-density pure neutron matter EOS obtained from a precise next-to-next-to-next-to-leading order (N^3LO) calculation in chiral effective field theory (χ EFT). The posterior distributions of the model parameters obtained under these minimal constraints are employed to construct the distributions of various nuclear matter properties and NS properties such as radii, tidal deformabilities, central energy densities, speeds of sound, etc. We found that a 90% confidence interval for the allowed NS mass–radius relationship and tidal deformabilities is compatible with GW170817 and recent Neutron star Interior Composition ExploreR observations, without invoking the exotic degrees of freedom. A central speed of sound of the order of $\sqrt{2/3} c$ is obtained. The maximum NS mass allowed by the model is $2.5 M_\odot$.

Unified Astronomy Thesaurus concepts: [Neutron star cores \(1107\)](#); [Neutron stars \(1108\)](#); [Nuclear astrophysics \(1129\)](#); [Nuclear physics \(2077\)](#)

1. Introduction

Neutron stars (NSs), observed as pulsars, are some of the densest and most compact objects in the universe. The core of such compact objects is believed to contain matter at a few times nuclear saturation density ($\rho_0 = 2.7 \times 10^{14} \text{ g cm}^{-3}$; Glendenning 1996; Haensel et al. 2007; Rezzolla et al. 2018). It is the ideal cosmic laboratory to test our present knowledge of the mysterious behavior of matter under extreme densities. The existence of NSs was first hypothesized by Lev Landau (see Yakovlev et al. 2013), and by Walter Baade and Fritz Zwicky in 1933 (Baade & Zwicky 1934a, 1934b). However, Jocelyn Bell and her Ph.D. advisor A. Hewish first observed NSs in 1967 with the discovery of radio pulsars (Hewish et al. 1968). A detailed history of the origin of the NS can be found in Brecher (1999). NS properties—namely the maximum mass, radii, moments of inertia, and tidal Love numbers, all of which are accessible to observation—can be a significant probe to reduce the uncertainty of theoretical models of NS over the decades. High mass pulsars like PSR J1614-2230 ($M = 1.908 \pm 0.016 M_\odot$; Demorest et al. 2010; Fonseca et al. 2016; Arzoumanian et al. 2018), PSR J0348-0432 ($M = 2.01 \pm 0.04 M_\odot$; Antoniadis et al. 2013), PSR J0740+6620 ($M = 2.08 \pm 0.07 M_\odot$; Fonseca et al. 2021), and very recently J1810+1714 with a mass $M = 2.13 \pm 0.04 M_\odot$ (Romani et al. 2021) have drawn attention to the theory of nuclear interactions at high density. The high-precision X-ray space missions, such as the Neutron star Interior Composition ExploreR (NICER) have already shed some light in this direction. Of late, NICER has come up with one measurement

of the radius $12.71_{-1.19}^{+1.14} \text{ km}$ and mass $1.34_{-0.16}^{+0.15} M_\odot$ for the pulsar PSR J0030+0451 (Riley et al. 2019), and other independent analysis shows that the radius is $13.02_{-1.06}^{+1.24} \text{ km}$ and the mass $1.44_{-0.14}^{+0.15} M_\odot$ (Miller et al. 2019). The recent measurement of the equatorial circumferential radius of the pulsar PSR J0740+6620 with mass $M = 2.072_{-0.066}^{+0.067} M_\odot$ and $R = 12.39_{-0.98}^{+1.30} \text{ km}$ (68% confidence interval, CI; Riley et al. 2021) by the NICER group will play an important role in this domain. The empirical estimate of the radius of a canonical NS ($M = 1.4 M_\odot$) is $R_{1.4} = (11.9 \pm 1.22) \text{ km}$ according to Lattimer & Lim (2013). Recently, from the simultaneous analysis of NICER and XMM-Newton X-ray observations, an estimation of $12.45 \pm 0.65 \text{ km}$ at 68% CI was obtained for a $1.4 M_\odot$ star.

The internal structure of an NS depends on the hydrostatic equilibrium between the inward gravitational pull of matter and the outward neutron degeneracy pressure. General relativity allows us to calculate the internal structure of NSs. The first NS model was calculated by Oppenheimer & Volkoff (1939) using the exact form of the equations of hydrostatic equilibrium in general relativity, which they derived simultaneously with Tolman (1939) from the Einstein equations. To solve NS structure equations, i.e., Tolman–Oppenheimer–Volkoff (TOV) equations, one needs the theory of the behavior of matter under extreme conditions, i.e., the theory of the infinite nuclear matter equation of state (EOS). The knowledge of the nuclear many-body theory is necessary for obtaining the nuclear matter EOS. In general, phenomenological models for nuclear EOS can be broadly categorized into two groups: (i) the relativistic and (ii) the nonrelativistic models. Although, nonrelativistic methods have been extremely successful in the description of nucleons inside atomic nuclei (finite nuclei), for infinite dense nuclear matter one needs to consider relativistic effects and assure that the speed of sound is always below the speed of light. A different approach treats the nuclear interaction in a relativistic



Original content from this work may be used under the terms of the [Creative Commons Attribution 4.0 licence](#). Any further distribution of this work must maintain attribution to the author(s) and the title of the work, journal citation and DOI.

framework (Serot & Walecka 1986). Relativistic mean-field (RMF) models are especially adequate to describe high-density matter like that occurring inside NSs, besides also describing finite nuclei. In fact, RMF models successfully deal with the inclusion of many-body effects in the description of finite nuclei and infinite nuclear matter via the exchange of mesons (σ , ω , and ϱ). In order to describe nuclear properties, two different approaches have been developed: nonlinear meson terms are included in the Lagrangian density in order to describe adequately the density dependence of the EOS and symmetry energy (Boguta & Bodmer 1977; Mueller & Serot 1996; Steiner et al. 2005; Todd-Rutel & Piekarewicz 2005); the nonlinearities are described introducing density-dependent coupling parameters and avoiding the introduction of nonlinear mesonic terms (Typel & Wolter 1999; Lalazissis et al. 2005; Typel et al. 2010). These models are phenomenological and need to be constrained by experimental or observational data. However, the presently existing data from the laboratory are obtained from nuclei that have a proton fraction not much smaller than 0.4 and the densities attained are normally of the order of the saturation density or below. This imposes big limitations on these models: their extension to high densities and/or isospin asymmetries has to be taken with care.

Recently, several EOS metamodels constrained by ab initio theoretical calculations for both low and high density have been proposed: nucleon–nucleon chiral potentials for low-density neutron and nuclear matter (Hebeler et al. 2013; Drischler et al. 2016) and perturbative quantum chromodynamics for asymptotically high-density regimes (Kurkela et al. 2010). In order to account for all possible EOSs compatible with these two constraints, the EOS at the two extreme densities is connected using a piecewise polytropic interpolation, a speed of sound interpolation, or a spectral interpolation, and causality is imposed when necessary (Lindblom & Indik 2012; Kurkela et al. 2014; Most et al. 2018; Lope Oter et al. 2019; Annala et al. 2020, 2022). Of late, a nonparametric inference of the NS EOS has also been proposed based on Gaussian processes (Essick et al. 2020) or using machine learning techniques (Han et al. 2021). However, such EOS models have strong limitations because they do not assume any kind of composition of matter in the intermediate density regime. Another approach has been considered that also spans an acceptable NS mass–radius domain such as a Taylor expansion parameterization of the EOS (Margueron et al. 2018a, 2018b; Zhang et al. 2018; Ferreira & Providência 2021b; Ferreira & Providência 2021a). The recovery of the nuclear matter properties from the β -equilibrium EOS has proven to be impossible without the knowledge of the compositions or symmetry energy at high densities (de Tovar et al. 2021; Imam et al. 2022; Mondal & Gulminelli 2021) or the knowledge of the EOS of symmetric nuclear matter along with compositions (Essick et al. 2021b).

The aim of the present study is to generate a set of models using a microscopic approach based on a relativistic description of hadrons through their density-dependent coupling with mesons (DDH), constrained by existing observational, theoretical, and experimental data. This has a basic hypothesis that NS matter is the nucleonic matter with electrons and muons. The approach has the great advantage of being a causal description of matter and it will not be necessary to impose a speed of sound below the speed of light. The framework will, however, be easily extended to allow the inclusion of other

degrees of freedom such as hyperons or a deconfinement transition. Considering only the simplest composition will allow us to evaluate how much the existing constraints require the introduction of exotic degrees of freedom to explain NS. In Thi et al. (2021), the authors have concluded within a meta-model description that the present NS observations are compatible with what they call the “nucleonic hypotheses,” i.e., nucleonic and leptonic degrees of freedom are sufficient to explain the data.

The advantage of a DDH approach with respect to an approach with constant couplings is that it accounts for quantal fluctuations of the baryon fields even in the ground state (Lenske & Fuchs 1995). The rearrangement of self-energies to the baryon field equations is responsible for such effects. Over the decades, several formulations of density-dependent couplings have been studied (Marcos et al. 1989; Haddad & Weigel 1993; Fritz & Muther 1994) employing the usual field equations and definitions of self-energies. However, a closer inspection suggests that not all these models were consistent (Lenske & Fuchs 1995; Fuchs et al. 1995). To obtain Lorentz-invariant Lagrangian and covariant field equations from the Euler–Lagrange equations, the density dependence of the couplings has to be a Lorentz-scalar functional of the baryon fields. The development of a DDH parameterization that simultaneously describes the properties of nuclear matter and finite nuclei has been very successful (Typel & Wolter 1999; Lalazissis et al. 2005; Typel et al. 2010). This model also allows a reasonable extrapolation to extreme conditions of isospin and density.

In the present work, we perform a detailed statistical analysis of the parameters of a DDH description of nuclear matter within a Bayesian approach considering a given set of fit data related to the nuclear saturation properties, the pure neutron matter (PNM) EOS calculated from a precise next-to-next-to-next-to-leading order (N^3LO) calculation in chiral effective field theory (χ EFT), and the lower bound of an observed two-solar-mass NS. We introduce a density dependence of the couplings of isovector and isoscalar fields so that for each field only two parameters are necessary: the dependence of the couplings on the density is compatible with Dirac–Brueckner–Hartree–Fock calculations and similar to the one introduced in Typel & Wolter (1999). One set of models will be inferred with fit data. Once the set is built, a detailed statistical analysis of nuclear matter parameters (NMPs), also some that are not directly accessible in laboratory experiments, and of NS properties will be performed. A comparison of the main results with the ones obtained within other approaches, such as the meta-model description of NS matter, will be discussed. It will be shown that the set of models constrained by χ EFT PNM calculations (Hebeler et al. 2013) and some saturation nuclear matter properties are totally compatible with NICER and GW170817 observations. Besides, it will also be shown that the higher-order NMPs compatible with NS constraints may differ from results determined from the Taylor-expanded EOS.

The paper is organized as follows. In Section 2.1, the field theoretical DDH model for the EOS at zero temperatures is briefly reviewed, followed by a brief description of the Bayesian estimation of model parameters in Section 2.2. The results of our calculation are discussed in Section 3. Section 4 contains the summary and conclusions.

2. Formalism

In this section, the RMF framework used to generate the set of models that will be applied in the present study is introduced. A brief review of the Bayesian approach undertaken to estimate the model parameters will be presented.

2.1. Model

The calculation of the nuclear EOS boils down to a problem of the theoretical modeling of nuclear interactions. In a phenomenological approach, the effective interactions among nucleons can be modeled within a relativistic mean-field framework with an effective Lagrangian involving baryon and meson fields. The force between two nucleons is realized by the exchange of mesons in this framework. The σ meson creates a strong attractive central force and influences the spin-orbit potential; on the other hand, the ω meson is responsible for the repulsive short-range force. The isovector ϱ meson is included to distinguish between neutrons and protons, and introduce the isospin symmetry and independence of the nuclear force. The Lagrangian including the nucleon field, the σ , ω , and ϱ mesons, and their interactions can be written as

$$\begin{aligned} \mathcal{L} = & \bar{\Psi} [\gamma^\mu (i\partial_\mu - \Gamma_\sigma A_\mu^{(\sigma)} - \Gamma_\omega \boldsymbol{\tau} \cdot \mathbf{A}_\mu^{(\omega)}) \\ & - (m - \Gamma_\sigma \phi)] \Psi + \frac{1}{2} \{ \partial_\mu \phi \partial^\mu \phi - m_\sigma^2 \phi^2 \} \\ & - \frac{1}{4} F_{\mu\nu}^{(\omega)} F^{(\omega)\mu\nu} + \frac{1}{2} m_\omega^2 A_\mu^{(\omega)} A^{(\omega)\mu} \\ & - \frac{1}{4} \mathbf{F}_{\mu\nu}^{(\varrho)} \cdot \mathbf{F}^{(\varrho)\mu\nu} + \frac{1}{2} m_\varrho^2 \mathbf{A}_\mu^{(\varrho)} \cdot \mathbf{A}^{(\varrho)\mu}, \end{aligned} \quad (1)$$

where Ψ is the Dirac spinor for spin $\frac{1}{2}$ particles, and, in the present calculation, describes a nucleon doublet (neutron and proton) with bare mass m . γ^μ and $\boldsymbol{\tau}$ are the Dirac matrices and the Pauli matrices, respectively. The vector meson field strength tensors are given by $F^{(\omega, \varrho)\mu\nu} = \partial^\mu A^{(\omega, \varrho)\nu} - \partial^\nu A^{(\omega, \varrho)\mu}$. The Γ_σ , Γ_ω , and Γ_ϱ are the coupling constants of nucleons to the meson fields σ , ω , and ϱ , respectively, and the corresponding meson masses are m_σ , m_ω , and m_ϱ . A DDH model is considered with nucleon-meson density-dependent coupling parameters in the form of

$$\Gamma_M(\rho) = \Gamma_{M,0} h_M(x), \quad x = \rho/\rho_0, \quad (2)$$

where the density ρ is the baryonic density, the $\Gamma_{M,0}$ is the couplings at saturation density ρ_0 , and $M \in \{\sigma, \omega, \varrho\}$. For the isoscalar couplings, in the present study the function h_M is given by

$$h_M(x) = \exp[-(x^{a_M} - 1)], \quad M = \sigma, \omega \quad (3)$$

and the isovector coupling has the form proposed in Typel & Wolter (1999):

$$h_\varrho(x) = \exp[-a_\varrho(x - 1)]. \quad (4)$$

The parameterization defined in Equation (3) introduces only one extra parameter for each coupling, similarly to the ϱ meson coupling, and was chosen so that the σ and ω nucleon couplings may have a dependence on the density as predicted by Dirac–Brückner–Hartree–Fock calculations (Ter Haar & Malfliet 1987; Brockmann & Machleidt 1990; Typel & Wolter 1999), for

$\rho \gtrsim 0.04 \text{ fm}^{-3}$. This range of densities is adequate to describe the NS core EOS.

In the following, we use the mean-field approximation, and we consider that the system is formed of static uniform matter in its ground state. The mesonic fields are replaced by their expectation value $\langle \sigma \rangle$ and $\langle A_\mu^{(\omega, \varrho)} \rangle$, and quantum fluctuations are neglected. In static uniform matter, the source densities and currents $\bar{\psi}(x)\psi(x)$ and $\bar{\psi}(x)\gamma^\mu\psi(x)$ are independent of x . Besides, only the time-like components of vector fields ω_0 and the third isospin component of the ϱ field ϱ_3^0 survive. The Euler–Lagrange equations of all the fields are in the mean-field approximation

$$m_\sigma^2 \sigma = \Gamma_\sigma \bar{\psi} \psi, \quad (5)$$

$$m_\omega^2 \omega_0 = \Gamma_\omega \bar{\psi} \gamma_0 \psi, \quad (6)$$

$$m_\varrho^2 \varrho_3^0 = \frac{1}{2} \Gamma_\varrho \bar{\psi} \gamma_0 \tau_3 \psi. \quad (7)$$

The nucleon number density $\rho = \langle \bar{\psi} \psi \rangle$ and scalar density $\rho_s = \langle \bar{\psi} \psi \rangle$ at zero temperature are defined as

$$\rho = \frac{\gamma}{2\pi^2} \sum_{B=p,n} \int_0^{k_{FB}} k^2 dk, \quad (8)$$

$$\rho_s = \frac{\gamma}{2\pi^2} \sum_{B=p,n} \int_0^{k_{FB}} \frac{m^* k^2}{\sqrt{m^{*2} + k^2}} dk, \quad (9)$$

where k_{FB} is the Fermi momentum of nucleon B and γ is the spin degeneracy factor. The effective nucleon mass is $m^* = m - \Gamma_\sigma \sigma$ and the nucleon B chemical potential is given by $\mu_B = \nu_B + \Gamma_\omega \omega_0 + \Gamma_\varrho \tau_{3B} \varrho_3^0 + \Sigma^r$, where τ_{3B} is the isospin projection and the rearrangement term Σ^r takes care of many-body effects in nuclear interaction (Typel & Wolter 1999) and assures thermodynamic consistency. It arises due to the density dependence of the couplings and is expressed as

$$\Sigma^r = \sum_{B=n,p} \left[-\frac{\partial \Gamma_\sigma}{\partial \rho_B} \sigma \rho_{sB} + \frac{\partial \Gamma_\omega}{\partial \rho_B} \omega_0 \rho_B + \frac{\partial \Gamma_\varrho}{\partial \rho_B} \tau_{3B} \varrho_3^0 \rho_B \right]. \quad (10)$$

The energy density is defined as

$$\begin{aligned} \varepsilon = & \frac{1}{\pi^2} \sum_{B=n,p} \int_0^{k_{FB}} k^2 \sqrt{k^2 + m^{*2}} dk + \frac{1}{2} m_\sigma^2 \sigma^2 \\ & + \frac{1}{2} m_\omega^2 \omega_0^2 + \frac{1}{2} m_\varrho^2 (\varrho_3^0)^2 + \varepsilon_{lep}, \end{aligned} \quad (11)$$

where the last term describes the leptonic (electrons and muons) contribution. The pressure P can be derived from the energy density using the Euler relation,

$$P = \sum_{i=n,p,e,\mu} \mu_i \rho_i - \varepsilon, \quad (12)$$

where μ_i and ρ_i are, respectively, the chemical potential and the number density of particle i .

In the core, the star is mainly composed of neutrons with very high momentum states. β -decay establishes an equilibrium between neutrons, protons, electrons, and muons

$$n \leftrightarrow p + e^- + \bar{\nu}, \quad (13)$$

$$n + \nu \leftrightarrow p + e^-, \quad (14)$$

$$\mu \leftrightarrow e^- + \nu_\mu + \bar{\nu}_e, \quad (15)$$

and muons (μ) will appear when the chemical potential of the electrons reaches the muon rest mass ($m_\mu = 106$ MeV). In a cold catalyzed NS, the wavelength of neutrinos is much larger than the star radius and they escape. Therefore, the β -equilibrium condition is given as

$$\mu_n = \mu_p + \mu_e \quad \text{and} \quad \mu_e = \mu_\mu. \quad (16)$$

For a given baryon density ($\rho = \rho_n + \rho_p$), the charge neutrality imposes

$$\rho_p = \rho_e + \rho_\mu. \quad (17)$$

In order to obtain the NS properties, it is necessary to match the crust EOS to the core EOS. For the outer crust, the Bethe-Pethick-Sutherland (BPS) EOS is chosen. The outer crust and the core are joined using the polytropic form (Carriere et al. 2003) $p(\varepsilon) = a_1 + a_2 \varepsilon^\gamma$, where the parameters a_1 and a_2 are determined in such a way that the EOS for the inner crust matches with the outer crust at one end ($\rho = 10^{-4}$ fm $^{-3}$) and with the core at the other end ($\rho = 0.04$ fm $^{-3}$). The polytropic index γ is taken to be equal to 4/3. This approximation will introduce an uncertainty on the radius of the low-mass NS as shown in Fortin et al. (2016) and Pais & Providência (2016) (see also the recent studies Lopes 2021; Rather et al. 2021). In Fortin et al. (2016) several matching procedures have been tested and it was shown that the uncertainty could be as high as 1 km. One of the methods that introduced a small uncertainty considered a matching to the outer core at a density 0.01 fm $^{-3}$. The justification being the fact that the inner crust EOS does not differ much from the homogeneous EOS for densities close to the transition to the core, as clearly seen in Figure 5 of Avancini et al. (2009) for DDH models. We, therefore, believe that our approximation will introduce an uncertainty in the radius of a $1.4 M_\odot$ star that is at most of the order of 100–200 m for models with a symmetry energy compatible with the χ EFT PNM EOS (see Table 1 of Fortin et al. 2016), and smaller for larger masses. We have estimated for the five models, DDBI, DDBm, DDBu1, DDBu2, and DDBx, the uncertainty on the radius of a $1.4 M_\odot$ star introduced with our approach. For these five models we have calculated the inner crust within an approach that includes the surface energy and Coulomb field after minimization (Avancini et al. 2008) and we have obtained a difference of $\lesssim 10$ m (DDBI and DDBm), $\lesssim 100$ m (DDBu2), ≈ 150 m (DDBu1), and $\lesssim 200$ m for one of the extreme EOSs with $K_0 = 300$ MeV, DDBx.

With a good approximation, the EOS of nuclear matter can be decomposed into two parts: (i) the EOS for symmetric nuclear matter $\epsilon(\rho, 0)$, and (ii) a term involving the symmetry energy coefficient $S(\rho)$ and the asymmetry δ ,

$$\epsilon(\rho, \delta) \simeq \epsilon(\rho, 0) + S(\rho)\delta^2, \quad (18)$$

where ϵ is the energy per nucleon at a given density ρ and isospin asymmetry $\delta = (\rho_n - \rho_p)/\rho$. We can recast the EOS in terms of various bulk nuclear matter properties of order n at saturation density: (i) for the symmetric nuclear matter, the energy per nucleon $\epsilon_0 = \epsilon(\rho_0, 0)$ ($n = 0$), the incompressibility coefficient K_0 ($n = 2$), the skewness Q_0 ($n = 3$), and the

kurtosis Z_0 ($n = 4$), respectively, given by

$$X_0^{(n)} = 3^n \rho_0^n \left(\frac{\partial^n \epsilon(\rho, 0)}{\partial \rho^n} \right)_{\rho_0}, \quad n = 2, 3, 4; \quad (19)$$

(ii) for the symmetry energy, the symmetry energy at saturation $J_{\text{sym},0}$ ($n = 0$),

$$J_{\text{sym},0} = S(\rho_0), \quad S(\rho) = \frac{1}{2} \left(\frac{\partial^2 \epsilon(\rho, \delta)}{\partial \delta^2} \right)_{\delta=0}, \quad (20)$$

the slope $L_{\text{sym},0}$ ($n = 1$), the curvature $K_{\text{sym},0}$ ($n = 2$), the skewness $Q_{\text{sym},0}$ ($n = 3$), and the kurtosis $Z_{\text{sym},0}$ ($n = 4$), respectively, defined as

$$X_{\text{sym},0}^{(n)} = 3^n \rho_0^n \left(\frac{\partial^n S(\rho)}{\partial \rho^n} \right)_{\rho_0}, \quad n = 1, 2, 3, 4. \quad (21)$$

2.2. Bayesian Estimation of Model Parameters

A Bayesian parameter estimation approach enables one to carry out a detailed statistical analysis of the parameters of a model for a given set of fit data (Furnstahl et al. 2015; Wesolowski et al. 2016; Ashton et al. 2019; Landry et al. 2020). In this technique, the basic rules of probabilistic inference are used to update the probability for a hypothesis under the available evidence or information according to Bayes' theorem. The posterior distributions of the model parameters θ in the Bayes' theorem can be written as

$$P(\theta|D) = \frac{\mathcal{L}(D|\theta) P(\theta)}{\mathcal{Z}}, \quad (22)$$

where θ and D denote the set of model parameters and the fit data. $P(\theta)$ in Equation (22) is the prior for the model parameters and \mathcal{Z} is the evidence. The type of prior can be chosen with the preliminary knowledge of the model parameters. One can choose it to be a uniform prior, which has been used as a baseline for many analyses. $P(\theta|D)$ is the joint posterior distribution of the parameters and $\mathcal{L}(D|\theta)$ is the likelihood function. The posterior distribution of a given parameter can be obtained by marginalizing $P(\theta|D)$ over the remaining parameters. The marginalized posterior distribution for a parameter θ_i is obtained as

$$P(\theta_i|D) = \int P(\theta|D) \prod_{k \neq i} d\theta_k. \quad (23)$$

We use a Gaussian likelihood function defined as

$$\mathcal{L}(D|\theta) = \prod_j \frac{1}{\sqrt{2\pi\sigma_j^2}} e^{-\frac{1}{2} \left(\frac{d_j - m_j(\theta)}{\sigma_j} \right)^2}. \quad (24)$$

Here the index j runs over all the data, and d_j and m_j are the data and corresponding model values, respectively. The σ_j are the adopted uncertainties. The Markov Chain Monte Carlo (MCMC) is commonly employed for Bayesian parameter estimation. This algorithm jumps to a new set of parameters from starting parameters with a probability proportional to the ratio of the two points. It is a powerful algorithm for high dimensionality problems. However, the MCMC has its own problems with convergence. To overcome the problem of MCMC, a different Monte Carlo algorithm, nested sampling,

Table 1
Model Parameters that Generate the DDB Set

Constraints			
Quantity	Value/Band	Ref	DDB
NMP (MeV)	ρ_0	0.153 ± 0.005	TypeI & Wolter (1999)
	ϵ_0	-16.1 ± 0.2	Dutra et al. (2014)
	K_0	230 ± 40	Todd-Rutel & Piekarczyc (2005); Shlomo et al. (2006)
PNM (MeV fm ⁻³)	$J_{\text{sym},0}$	32.5 ± 1.8	Essick et al. (2021a)
	$P(\rho)$	$2 \times N^3\text{LO}$	Hebeler et al. (2013)
NS mass (M_\odot)	M_{max}	>2.0	Fonseca et al. (2021)

Note. ϵ_0 is the binding energy per nucleon, K_0 the incompressibility coefficient, and $J_{\text{sym},0}$ the symmetry energy evaluated at the nuclear saturation density ρ_0 . The nuclear saturation properties are listed including a 1σ uncertainty. The PNM indicates the pressure of PNM for the densities 0.08, 0.12, and 0.16 fm⁻³ from $N^3\text{LO}$ calculation in χ EFT (Hebeler et al. 2013). We consider $2 \times N^3\text{LO}$ data in the likelihood of the present calculation.

was first proposed in Skilling (2004). In nested sampling, the posterior is broken into many nested “slices” with starting “*n*-live” points; samples are generated from each of them and then recombined to reconstruct the original distribution. In a dynamic nested sampling, the procedure is similar but the “*n*-live” varies dynamically. We have implemented both the nested sampling and the dynamic nested sampling algorithm in the Bayesian Inference Library (BILBY; Ashton et al. 2019) to populate the posterior distribution of Equation (22) by invoking a PyMultiNest sampler (Buchner et al. 2014; Buchner 2021) and a Dynesty sampler (Speagle 2020), respectively.

We generate samples for starting 3000 “*n*-live” points with both samplers, separately. PyMultiNest selects around 14,000 final models by calling 5.78×10^5 models, and Dynesty selects around 13,000 final models by calling 5×10^7 models. The evidence obtained in both samplers is similar. In Section 3, we will present the resulting sets obtained in PyMultiNest.

3. Results

In this section, we study the dense matter EOS relevant for NSs in the DDH framework as briefly outlined in Section 2.1. A detailed statistical analysis of the DDH model parameters, namely $\Gamma_{\sigma,0}$, $\Gamma_{\omega,0}$, $\Gamma_{\varrho,0}$, a_σ , a_ω , and a_ϱ , is done within a Bayesian parameter estimation approach considering a given set of fit data related to the nuclear saturation properties, the PNM EOS calculated from a precise $N^3\text{LO}$ calculation in χ EFT and the lowest bound of NS observational maximum mass. With the marginalized posterior distributions obtained for the DDH parameters, we perform a statistical analysis of NMPs and NS properties. The marginalized posterior distributions of the DDH parameters, applying a Bayesian estimation of the model parameters, require the definition of the likelihood, the fit data, and the priors for the model parameters. The likelihood has been defined in Section 2.2 (see Equation (24)). We consider a minimal set of fit data, referred to hereafter as the DDB set (see Table 1). The data sets contain four empirical nuclear saturation properties, the low-density pressure for PNM at three different densities, in particular, 0.08, 0.12, and 0.16 fm⁻³, obtained from χ EFT (Hebeler et al. 2013), and the

Table 2
The Considered Uniform Prior Distributions (P) of the DDH Model Parameters

No	Parameters	P	
		Min	Max
1	$\Gamma_{\sigma,0}$	7.5	13.5
2	$\Gamma_{\omega,0}$	8.5	14.5
3	$\Gamma_{\varrho,0}$	2.5	8.0
4	a_σ	0.0	0.30
5	a_ω	0.0	0.30
6	a_ϱ	0.0	1.30

Note. The parameters “min” and “max” denote the minimum and maximum values for the uniform distribution.

lowest bound of the NS maximum mass observational constraint. The four empirical nuclear saturation properties are ρ_0 the nuclear saturation density, ϵ_0 the binding energy per nucleon, K_0 the incompressibility coefficient, and $J_{\text{sym},0}$ the symmetry energy coefficient, all defined at the nuclear saturation density ρ_0 . The range of values considered for $J_{\text{sym},0}$ is the one defined by the χ EFT marginalized values obtained in Essick et al. (2021a) considering four independent calculations (Hebeler & Schwenk 2010; Tews et al. 2013; Lynn et al. 2016; Drischler et al. 2019) with equal weights. The $N^3\text{LO}$ bound for PNM pressure restricts the symmetry energy within a very narrow range and to have a broader range for the symmetry energy, we consider a $2 \times N^3\text{LO}$ uncertainty band for the DDB set. In Table 2, we show the prior set P of the DDH model parameters. The uniform prior has been taken with a reasonable boundary. We initially do a random sampling test with the Latin hypercube sampling (LHS; Loh 1996) to get the overall idea about a reasonable boundary of the parameter space, i.e., the subdomain for which we get a physical EOS. It should be noted that the NMPs that result from the DDH parameters prior also span a reasonable wide range of the domain of acceptable values for these parameters.

In Figure 1, we show the corner plots for the marginalized posterior distributions of the DDH model parameters $\Gamma_{\sigma,0}$, $\Gamma_{\omega,0}$, $\Gamma_{\varrho,0}$, a_σ , a_ω , and a_ϱ , corresponding to the uniform prior set P presented in Table 2 for data set DDB. The number of final sample parameters corresponding to the posterior sets is around 14,000. The plots along the diagonal on the figure compare the 1D marginalized posterior distribution of individual parameters obtained for the DDB set. The vertical lines indicate the 90% min, median, and 90% CI of the distributions, respectively. The CI for the 2D marginalized posterior distributions is plotted with 1σ , 2σ , and 3σ CIs. The elliptical nature of the 2D CI for a few parameters indicates the correlations existing among those parameters, while a circular nature indicates no correlations. For example, as can be seen from the figure, the parameters $\Gamma_{\sigma,0}$ and $\Gamma_{\omega,0}$ as well as the parameters a_σ and a_ω are highly correlated due to the nuclear binding energy at saturation imposed in the DDB set. It should be noted that a_σ and a_ω determine the degree of nonlinearity in the isoscalar part and a_ϱ in the isovector part of the EOS at high density. In Table 3 we list the median value and 68% (90%) CI for all model parameters obtained for the DDB set. The DDB set results in hard enough EOS by having on average a small σ -coupling responsible for the description of the attractive component of the nuclear force, a large ρ meson coupling responsible for the symmetry energy, and small parameters a_i which avoid the

Table 3
The Median Values of DDH Model Parameters

	$\Gamma_{\sigma,0}$	$\Gamma_{\omega,0}$	$\Gamma_{\varrho,0}$	a_{σ}	a_{ω}	a_{ϱ}
DDB	$8.983^{+0.547(0.855)}_{-0.541(0.802)}$	$10.699^{+0.833(1.299)}_{-0.851(1.273)}$	$3.974^{+0.218(0.361)}_{-0.229(0.393)}$	$0.079^{+0.019(0.030)}_{-0.016(0.025)}$	$0.038^{+0.038(0.059)}_{-0.027(0.034)}$	$0.544^{+0.116(0.185)}_{-0.142(0.255)}$

Note. Namely $\Gamma_{\sigma,0}$, $\Gamma_{\omega,0}$, $\Gamma_{\varrho,0}$, a_{σ} , a_{ω} , and a_{ϱ} along with 68% (90%) CI obtained for the DDB set using prior sets P defined in Table 2. The nucleon, ω meson, σ meson, and ϱ meson masses are 939, 783, 550, and 763 MeV, respectively.

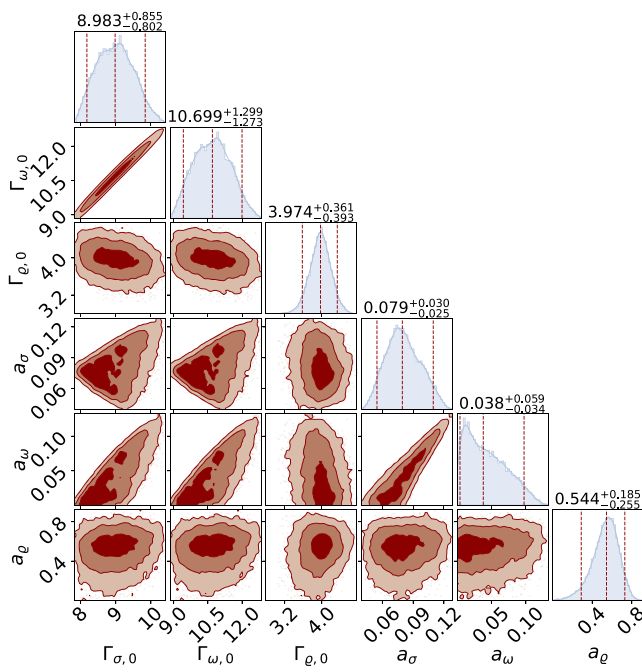


Figure 1. Corner plots for the marginalized posterior distributions of our DDH model parameters. The results are obtained for the DDB set with the prior set P of Table 2. 1D posterior distributions are given along the diagonal plots. The vertical lines indicate the 90% min, median, and 90% max confidence interval of the model parameters, respectively. The confidence ellipses for 2D posterior distributions are plotted with 1 σ , 2 σ , and 3 σ confidence intervals.

couplings of the vector mesons that predominate at high densities and reduce too fast with density.

In Figure 2 we plot the low-density EOS for PNMs with 90% CI for DDB. The results are obtained from the posterior distributions of the DDH parameters corresponding to DDB as listed in Table 3. For comparison, we also show the low-density pressure band for PNM from χ EFT. The 90% CI of low-density PNM pressure obtained for the constrained DDB model is in good agreement with these results: it overlaps mostly with the two times χ EFT band. The low-density pressure constraints for PNM play a key role to constrain the density dependence of the symmetry energy and, thus, NS properties at low mass.

Figure 3 shows the 90% CIs for the pressure of β -equilibrium NS matter obtained from the posterior distributions of the DDH parameters of the DDB (dark-red band) set. For comparison we also plot the constraints for β -equilibrium NS matter EOS obtained from the GW170817 analysis (Abbott et al. 2018). The 90% CI of β -equilibrium pressure as a function of baryon density obtained for DDB is fully compatible with the GW170817 constraints. The analysis performed for GW170817 did not impose the $2 M_{\odot}$ constraint.

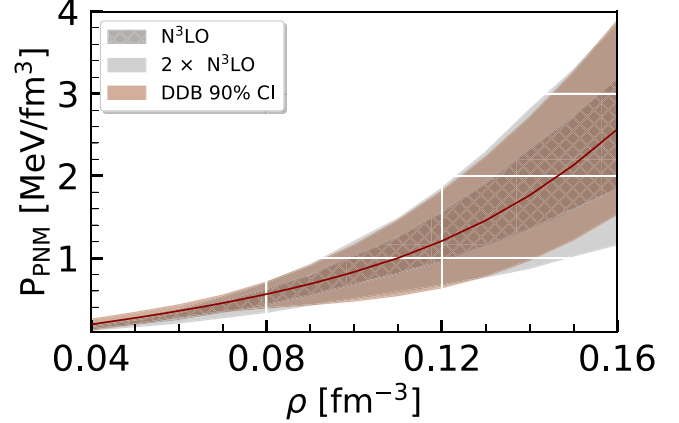


Figure 2. The pressure of low-density neutron matter from an N³LO calculation in χ EFT (Hebeler et al. 2013). The 90% CIs of the pressure of the low-density neutron matter for DDB is also compared. It should be noted that we consider 2 \times N³LO uncertainty and three intermediate points in the likelihoods of the present calculation.

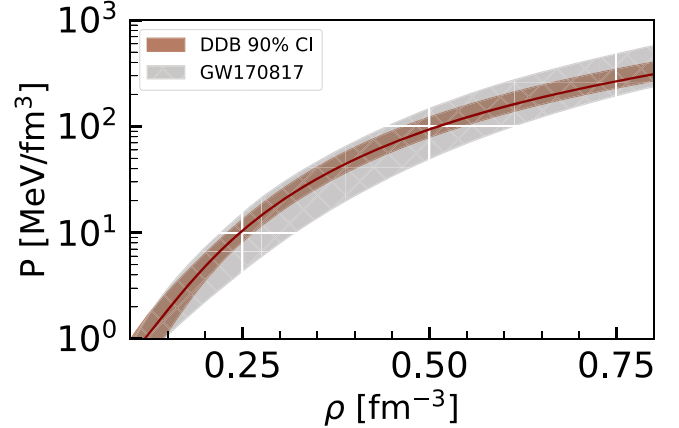


Figure 3. The 90% CIs for the pressure of NS matter as a function of the baryon density ρ for DDB (dark red). For comparison we also plot the constraints for pressure obtained in GW170817 (gray band).

With the calculated posterior sets of DDH parameters, we perform a statistical analysis of the NMPs and NS properties, namely, mass, radius, central speed of sound and energy density, and dimensionless tidal deformability. In Table 4, we present the median values and the associated 50%, 68%, 90%, and 95% uncertainties of the NMPs and of some NS properties —namely, the following properties of the maximum mass star: the gravitational mass M_{\max} , the baryonic mass $M_{B,\max}$, the square of the central speed of sound c_s^2 , the central energy density ε_c , and the radius R_{\max} , as well as the radius and the dimensionless tidal deformability for 1.4, 1.6, 1.8, and $2.08 M_{\odot}$ NS obtained for the marginalized posterior distributions of the DDH parameters. The NS masses and radii were calculated

Table 4
Median Values and Uncertainties of NMPs Introduced in Section 2.1 and a few selected NS Properties for DDB

Quantity	Units	Median	Confidence Interval (CI)					
			50%		68%		90%	
			Min	Max	Min	Max	Min	Max
NMP	ρ_0	fm^{-3}	0.153	0.150	0.155	0.149	0.156	0.147
	ε_0	MeV	-16.10	-16.23	-15.98	-16.29	-15.93	-16.41
	K_0		231	216	250	210	259	201
	Q_0		-109	-182	-16	-211	33	-256
	Z_0		1621	1340	1826	1159	1902	735
	$J_{\text{sym},0}$		32.19	31.11	33.22	30.56	33.73	29.38
	$L_{\text{sym},0}$		41.26	33.50	50.26	29.82	54.90	22.79
NS	$K_{\text{sym},0}$		-116	-130	-100	-137	-92	-150
	$Q_{\text{sym},0}$		966	710	1186	583	1277	317
	$Z_{\text{sym},0}$		-6014	-8156	-4043	-9234	-3232	-11564
	M_{max}	M_\odot	2.144	2.076	2.234	2.052	2.277	2.021
	$M_{\text{B,max}}$	M_\odot	2.552	2.461	2.672	2.428	2.731	2.386
	c_s^2	c^2	0.65	0.60	0.69	0.58	0.70	0.53
	ρ_c	fm^{-3}	0.946	0.929	0.959	0.919	0.963	0.879
NS	ε_c	MeV fm^{-3}	1282	1211	1348	1180	1375	1122
	R_{max}	km	11.09	10.84	11.37	10.74	11.49	10.56
	$R_{1.4}$		12.62	12.37	12.87	12.27	12.98	12.07
	$R_{1.6}$		12.53	12.27	12.81	12.15	12.93	11.95
	$R_{1.8}$		12.36	12.06	12.69	11.94	12.83	11.72
	$R_{2.08}$		12.01	11.59	12.43	11.41	12.60	11.10
	$\Lambda_{1.4}$...	454	398	523	375	555	339
NS	$\Lambda_{1.6}$		185	158	218	148	234	132
	$\Lambda_{1.8}$		79	65	97	60	106	52
	$\Lambda_{2.08}$		22	16	31	14	34	11
	$\tilde{\Lambda}_{q=1.0}$		529	465	608	439	645	398

Note. The “min” and “max” are the minimum and maximum values of uncertainties for 50%, 68%, 90%, and 95% CI. The NS properties are the gravitational mass M_{max} , baryonic mass $M_{\text{B,max}}$, radius R_{max} , central energy density ε_c , central number density for baryon ρ_c , and square of central speed of sound c_s^2 of the maximum mass NS, as well as the radius and the dimensionless tidal deformability for 1.4, 1.6, 1.8, and 2.08 M_\odot NS, and also the combined tidal deformability $\tilde{\Lambda}$ for the GW merger with $q = 1$.

from the TOV equations (Tolman 1939; Oppenheimer & Volkoff 1939), and the tidal deformability Λ from the equations obtained by Hinderer (2008). Figures 4 and 5 show the corner plots for the same quantities, respectively, NMPs, and NS properties.

In Figure 6 we plot (left) the pressure for symmetric nuclear matter P_{SNM} and (right) symmetry energy ($S(\rho)$) as a function of number density together with 90% CI for the DDB set. In the left panel we also include for reference the constraint obtained from heavy ion collision flow data on the pressure of symmetry nuclear matter (Danielewicz et al. 2002), which, however, is not totally model independent. Let us recall that the nuclear model used to analyze the experimental data in Danielewicz et al. (2002) does not predict two-solar masses (Constantinou et al. 2015) and, therefore, it is not surprising that the set DDB contains a large set of stiffer EOSs. The median value of set DDB essentially coincides with the upper limit of the HIC constraint in the intermediate density region, and, therefore, more than 50% of the EOSs are out of the HIC predicted region. For comparison, in the right panel we also plot the constraints on symmetry energy obtained in nuclear structure studies involving excitation energies to isobaric analog states (IAS; Danielewicz & Lee 2014) and our result is in good agreement with them. The χ EFT PNM EOS constraints affect quite strongly the density dependence of symmetry energy: for instance, the slope of the symmetry energy, $L_{\text{sym},0}$ is

concentrated between ≈ 30 and 55 MeV, (68% CI) although we may have values as high as ≈ 70 MeV.

In Vidana et al. (2009), a linear correlation was found between $L_{\text{sym},0}$ and $K_{\text{sym},0}$ from a set of nuclear matter models based on Skyrme forces, an RMF approach, or a microscopic approach. A similar correlation was determined in Tews et al. (2017) just from Skyrme forces (see the review Li et al. 2019) also discussing the role of $K_{\text{sym},0}$ on the determination of the core–curst transition density. Our predictions for $K_{\text{sym},0}$ are compatible with the values expected from that correlation and the predicted $L_{\text{sym},0}$. Based on a Taylor-expanded EOS, in Zhang & Li (2019) NS mass constraints have been imposed to define the valid domain for the NMPs $Q_0 - K_{\text{sym},0} - Q_{\text{sym},0}$. While our median value for $Q_{\text{sym},0}$ is within the range obtained in this study, it lies 20% above the Zhang & Li (2019) upper limit, 800 MeV. Our 90% CI value indicates that $Q_{\text{sym},0}$ can be as large as ≈ 1500 MeV. Recently, a Bayesian analysis was done in the framework of a Taylor-expanded EOS with the prior informed through LIGO-Virgo as well as NICER measurements to constrain the NMPs (see Thi et al. 2021). Our NMPs associated with the symmetry energy are somewhat more constrained. However, the choice of the likelihood for χ EFT is very different in both approaches and this may justify the differences.

Concerning the isoscalar skewness, in Zhang & Li (2019) it is shown that Q_0 is strongly constrained by the NS maximum

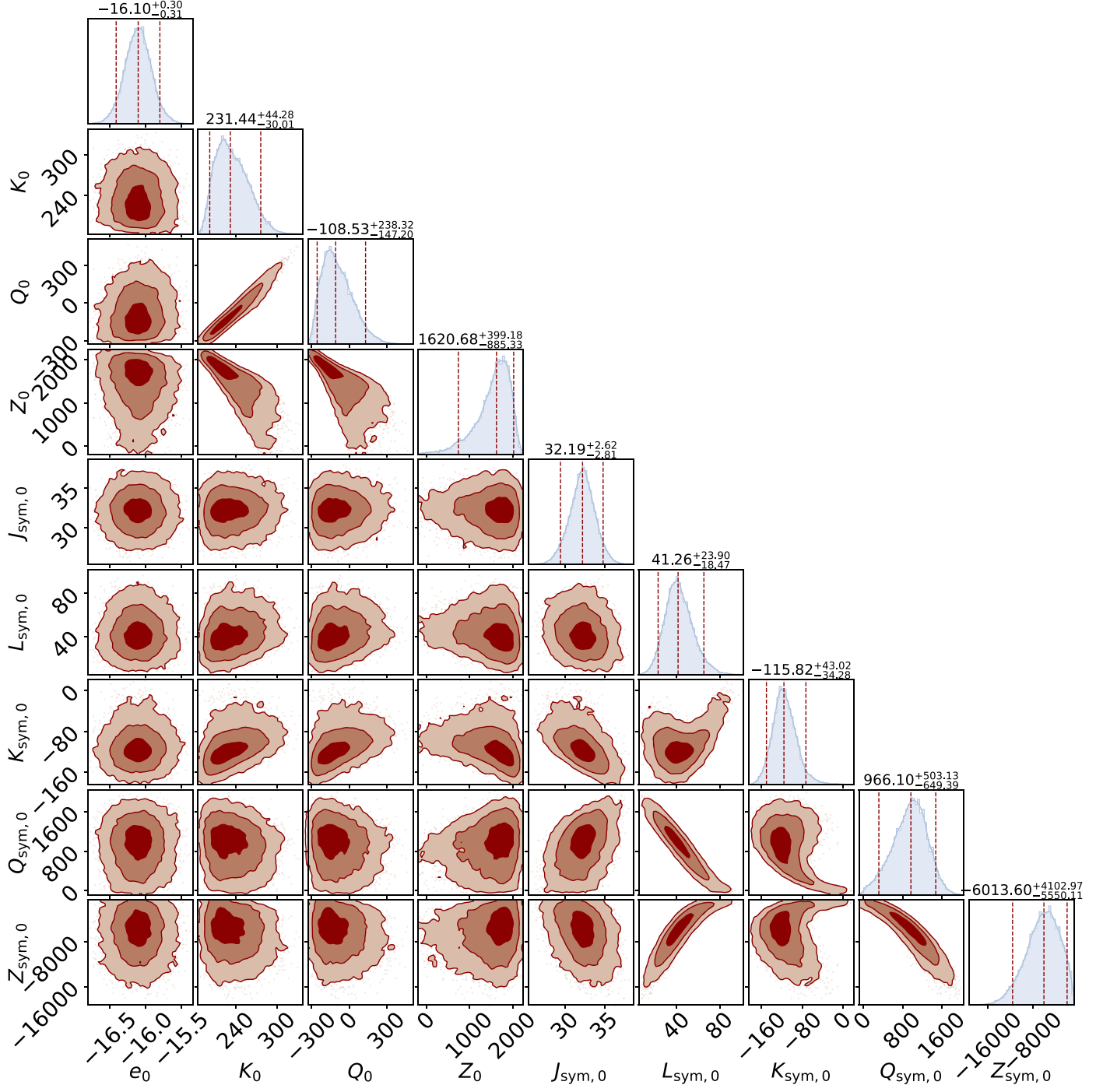


Figure 4. Corner plots for the marginalized posterior distributions of the NMPs (MeV) obtained from the DDB set of EOSs for the NS matter (Equations (19) and (21)). The vertical lines indicate 90% min, median, and 90% max CI, respectively, and the different tonalities from dark to light indicate, respectively, the 1σ , 2σ , and 3σ CI.

mass and causality, and the range $-200 \text{ MeV} < Q_0 < 200 \text{ MeV}$ has been identified as compatible with observations. In our study at 90% (95%) CI, we have determined $-256 \text{ MeV} < Q_0 < 130 \text{ MeV}$ ($-271 \text{ MeV} < Q_0 < 183 \text{ MeV}$) with similar observational constraints, quite compatible with the range calculated in Zhang & Li (2019), although with a smaller lower limit.

Two aspects may explain the different parameters determined in both studies: on one side our approach is causal from the beginning, and a second reason is the fact that in

Zhang & Li (2019) the higher-order parameters should be interpreted as an effective one since the Taylor-expanded EOS does not contain terms beyond the third order, as discussed in de Tovar et al. (2021).

Concerning the NS properties, we conclude that: (i) the NS maximum mass is predicted in the range from 2.052 – 2.277 (2.021 – 2.355) M_\odot for DDB in 68% (90%) CI, with the 95% CI extreme $2.383 M_\odot$ for the DDB set. Note that this value is just slightly smaller than the DD2 and DDME2 maximum mass, respectively, $2.42 M_\odot$ (Typel et al. 2010) and $2.48 M_\odot$

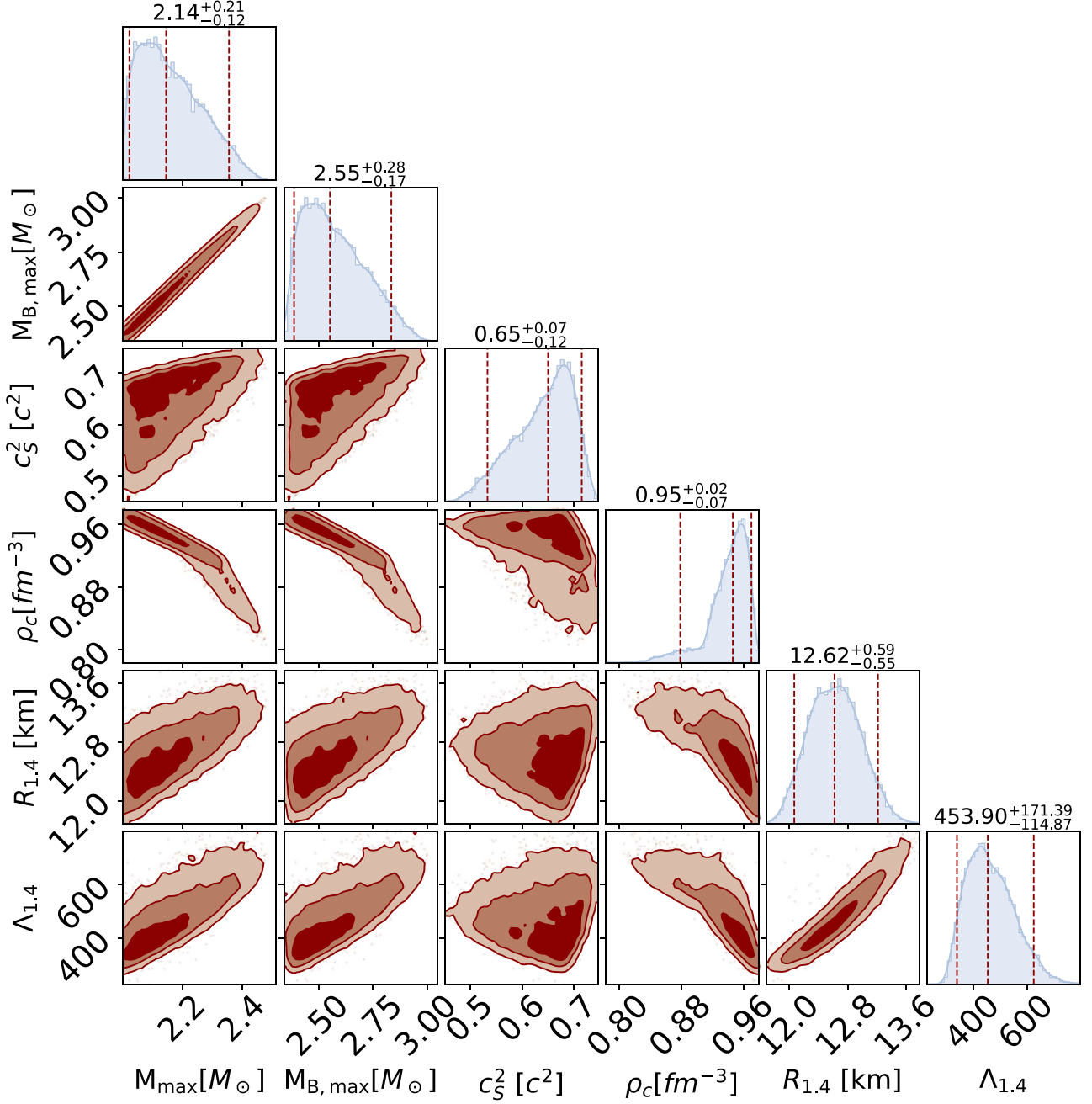


Figure 5. Corner plots for the marginalized posterior distributions of NS properties, namely gravitational mass M_{max} , baryonic mass $M_{B,\text{max}}$, the square of the central speed of sound c_s^2 , the central baryonic density ρ_c , the radius $R_{1.4}$, and the dimensionless tidal deformability $\Lambda_{1.4}$ for $1.4 M_{\odot}$ NS for the model DDB with prior set P defined in Table 2. The vertical lines indicate 90% min, median, and 90% max CI, respectively, and the different tonalities from dark to light indicate, respectively, the 1 σ , 2 σ , and 3 σ CI.

(Fortin et al. 2016). Outside the 95% CI, we find the DDB EOS that also describes stars with $M \sim 2.5 M_{\odot}$ but these will be discussed later; (ii) the square of the speed of sound at the center of the maximum star is strongly constrained and the value is in the range $0.58\text{--}0.70 c^2$ ($0.53\text{--}0.72 c^2$) at 68% (90%) CI. Having undertaken a causal approach it is interesting to notice that the speed of sound in maximum mass stars is still far from c ; (iii) the central energy density of the maximum mass star for the DDB set is about 10% smaller than the value obtained not imposing the two-solar-mass constraint, signaling a stiffer EOS, e.g., less compressible; (iv) the radius and tidal deformability are quantities that are also strongly affected by the two-solar-mass constraint (for the DDB set, the minimum

radius is $\approx 0.5\text{--}1$ km larger and the minimum tidal deformability $\approx 150\text{--}230$ larger). For a $1.4 M_{\odot}$ star we get at 90% CI $R_{1.4} \in [12.07, 13.21]$ and $\Lambda_{1.4} \in [339, 625]$. At 95% CI, we do not get radii below ~ 12 km. The radius and dimensionless tidal deformability are in good agreement with NICER and GW170817, respectively, as seen in Figure 7 and discussed below. Let us point out that the prediction for the tidal deformability $\Lambda_{1.4}$ is coincident with the range of values predicted in Abbott et al. (2018) imposing no mass constraint as shown in Figure 9.

We next discuss the lower bounds of the tidal deformability of a $1.36 M_{\odot}$ star, which would be the NS mass of each NS in the binary associated with the GW170817 if it would have been

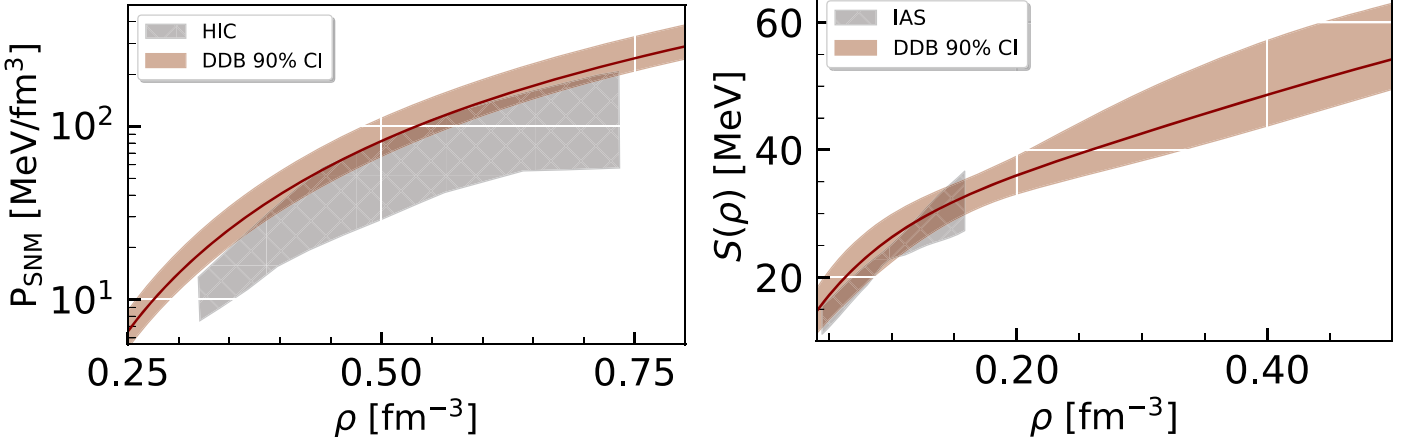


Figure 6. Left: the 90% credible interval of the pressure for symmetric nuclear matter P_{SNM} . Right: the symmetry energy $S(\rho)$ as a function of number density, together with the median (full lines) for DDB (dark red) sets. In the left panel, heavy ion collision flow data for symmetry nuclear matter (gray band) have also been included (Danielewicz et al. 2002). The constraints on the symmetry energy from IAS (Danielewicz & Lee 2014) are also displayed in the right panel.

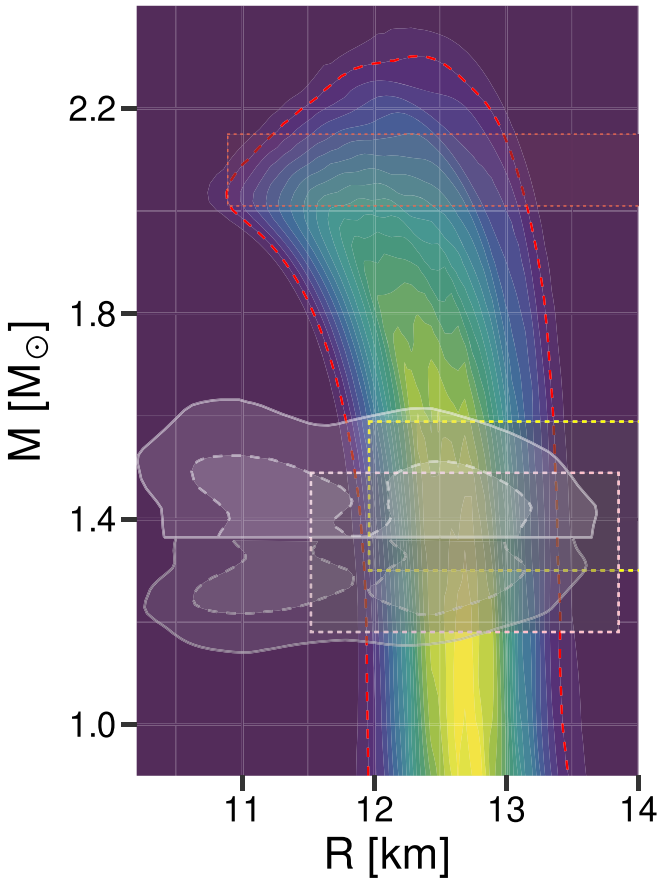


Figure 7. Plot of the joint probability distribution $P(M, R)$ for model DDB. The color levels are $\blacksquare(0\text{--}0.05)$, $\blacksquare(0.05\text{--}0.10)$, $\blacksquare(0.10\text{--}0.15)$, ..., $\blacksquare(0.85\text{--}0.90)$, $\blacksquare(0.90\text{--}0.95)$, $\blacksquare(0.95\text{--}1.00)$. The red dashed line represents the 90% CI. The top and bottom gray regions indicate, respectively, the 90% (solid) and 50% (dashed) CI of the LIGO/Virgo analysis for each binary component from the GW170817 event (Abbott et al. 2019). The rectangular regions enclosed by dotted lines indicate the constraints from the analysis of the millisecond pulsar PSR J0030+0451 NICER X-ray data (Miller et al. 2019; Riley et al. 2019), and PSR J0740+6620 (Miller et al. 2021).

symmetric, i.e., $m_1 = m_2$. In this case the effective $\tilde{\Lambda} = \Lambda(M = 1.36 M_\odot)$. It was shown by several authors that the follow up electromagnetic counterparts, the gamma-ray burst GRB170817A (Abbott et al. 2017a), and the

electromagnetic transient AT2017gfo (Abbott et al. 2017a), set constraints on the lower limit of the effective tidal deformability $\tilde{\Lambda}$, in particular, in Radice et al. (2018) the lower limit $\tilde{\Lambda} \gtrsim 300$ was obtained and in Kiuchi et al. (2019) $\tilde{\Lambda} \gtrsim 242$. From our set DDB, satisfying the two-solar-mass constraint, we get $\Lambda_{1.36} > 382$ at 95% CI for the DDB set, slightly larger than the proposed limits.

In Figure 7, we plot the joint probability distributions (PDs) $P(M, R)$ of the mass and the radius for DDB. The red dashed line represents the 90% CI. The color gradient from yellow to blue represents the highest to lowest probability. It can be seen that the probability $P(M, R)$ is highest for a radius ≈ 12.7 km and a mass from $1\text{--}1.75 M_\odot$. The lower bound of NS maximum mass with 68% CI from marginalized PDs is $2.05 M_\odot$ (see Table 4). So, below this lower bound all masses have a similar number of points and as we go to higher masses the number of points reduces as all the EOSs correspond to PDs that have a different maximum mass. We also compare the 90% CI of the $P(M, R)$ for the DDB set with those results obtained in GW170817 and NICER analysis (right). The upper gray region limited by a solid (dashed) line is the 90% (50%) CI of marginalized posterior for the mass M and radius R obtained in the GW170817 analysis of the heaviest NS in the binary component using a parametrized EOS, where a lower limit on the maximum mass of $1.97 M_\odot$ was imposed. On the other hand, the similar lower shaded region represents the same but for the lighter mass in the binary of the GW170817 event. The rectangular regions enclosed by dotted lines indicate the constraints from the analysis of the millisecond pulsar PSR J0030+0451 NICER X-ray data (Miller et al. 2019; Riley et al. 2019). It should be noted that the 90% CI in the NS mass and radius space for DDB, as represented by the red dashed line, is in very good agreement with both the GW170817 and NICER overlap region. The highest probability for the mass and radius calculated with the DDB model lies precisely in the middle of the GW170817 and NICER overlap region. Considering a $1.4 M_\odot$ star, the dimensionless tidal deformability Λ is $375\text{--}555$ ($326\text{--}655$), and the radius is $12.27\text{--}12.98$ ($11.99\text{--}13.30$) km at 68% (95%) CI. The dimensionless tidal deformability for $1.4 M_\odot$ NS predicted in the GW170817 event with 90% CI is below 780: this constraint is satisfied by DDB. It should be pointed out, however, that the predicted value for

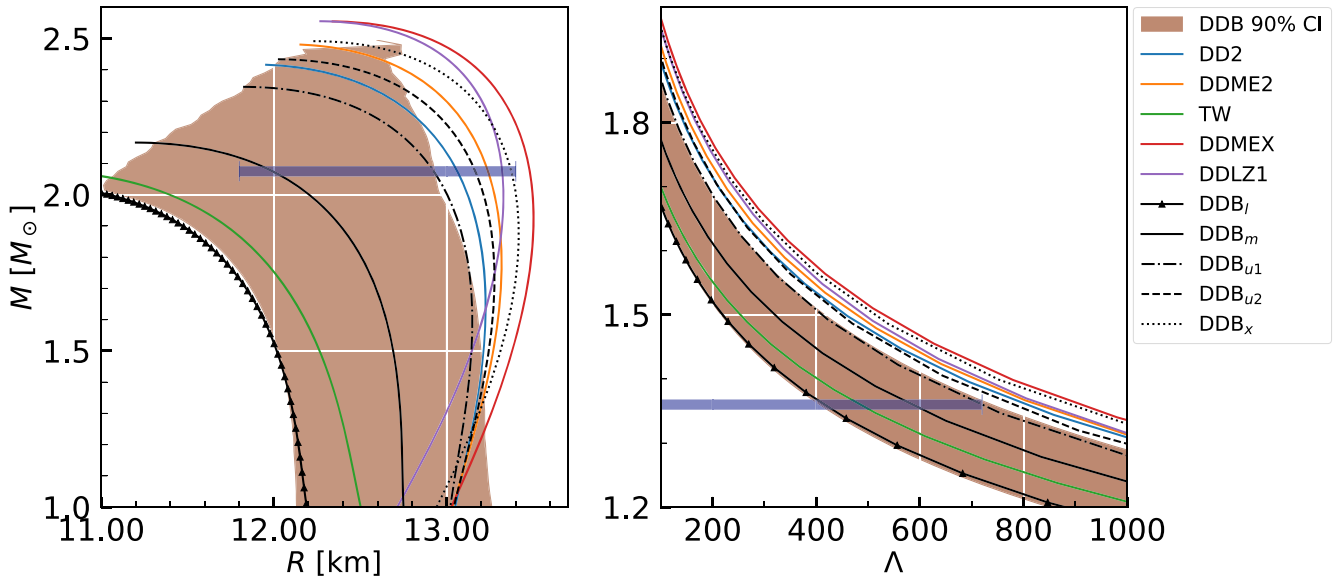


Figure 8. The 90% CI for the conditional probabilities $P(R|M)$ (left) and $P(\Lambda|M)$ (right) for DDB (dark red). For reference on the left panel, results for models TW (Typel & Wolter 1999), DD2 (Typel et al. 2010), DDME2 (Lalazissis et al. 2005), DD-MEX (Taninah et al. 2020; Huang et al. 2020), DD-LZ1 (Wei et al. 2020), and DDBI, DDBm, DDBu1, DDBu2, and DDBx are also shown. The blue horizontal bars indicate, on the left panel, the 90% CI radius for a $2.08 M_{\odot}$ star determined in Miller et al. (2021) combining observational data from GW170817 and NICER as well as nuclear data, and on the right panel, the 90% CI obtained for the tidal deformability of a $1.36 M_{\odot}$ star in Abbott et al. (2018).

the dimensionless tidal deformability in GW170817 requires the specification of an EOS, and, therefore, is model dependent. We conclude that the present NICER and GW170817 data cannot constrain further the uncertainties present in the DDB model for the EOS, NMPs, and the mass–radius region. We expect that in the future, further strict constraints on joint PDs of mass and radius from either NICER or GW will reduce these uncertainties.

The above results have been obtained within two different methods, corresponding to around the final selected 14,000 EOSs in PyMultiNest and 13,000 EOSs in Dynesty which give very similar results. In order to understand which is the maximum mass described by our DDH model, we have looked for EOSs that predict maximum masses above $2.48 M_{\odot}$. From the 225 EOSs obtained, most of them have a mass $\lesssim 2.5 M_{\odot}$ and an incompressibility of the order of 300 MeV. Parameterization DDBx plotted in Figure 8 is one of these EOSs; it predicts a maximum mass of $2.5 M_{\odot}$ and has the following nuclear matter properties: $K_0 = 300$ MeV, $J_{\text{sym},0} = 30$ MeV, and $L_{\text{sym},0} = 39$ MeV. As discussed below, part of the mass–radius curve lies outside the 90% CI for the conditional probabilities $P(R|M)$.

In Figure 8, we plot the 90% CI for the conditional probabilities $P(R|M)$ (left) and $P(\Lambda|M)$ (right) from the posterior distributions of the DDH parameters in the DDB set (dark-red shaded region). This means that from all the radii and tidal deformabilities obtained for a given mass, 90% lie inside the interval represented. In this case the maximum mass corresponds precisely to the maximum mass inside the set DDB.

For reference, we have also included in both panels of Figure 8 several other DDH EOSs known from the literature, in particular, TW (Typel & Wolter 1999), DD2 (Typel et al. 2010), DDME2 (Lalazissis et al. 2005), DD-MEX (Taninah et al. 2020; Huang et al. 2020), DD-LZ1 (Wei et al. 2020), and five DDB models (DDBI, DDBm, DDBu1, DDBu2, and DDBx). The first five EOSs are determined from models with

density-dependent couplings fitted to nuclear properties, and the last five have been chosen from the set DDB and are provided on GitHub and Zenodo. DDBI, DDBm, and DDBu2 were chosen so that the radius of the $1.4 M_{\odot}$ star has the lower limit, a medium value, and the upper limit of the 90% CI for the conditional probabilities $P(R|M)$. We have also included DDBu1, which has a slightly lower $R_{1.4}$ than the upper limit but lies completely inside the 90% CI for the conditional probabilities $P(R|M)$. In the left panel we have also included a horizontal bar indicating the predicted radius of a $2.08 M_{\odot}$ star to 90% credibility (11.8–13.4 km) as calculated in Miller et al. (2021) combining nuclear data and observational data from GW170817 and NICER (from PSR J0030+0451 and PSR J0740+6620). This interval shrinks to 12.2–13.1 km at 68% credibility. The present PSR J0704+6620 radius determination by NICER ignoring other information undertaken in Miller et al. (2021); Riley et al. (2021) predicts a quite large interval and does not allow any conclusions to be drawn.

It is seen that several mass–radius curves lie partially outside the 90% CI: DD2, DDME2, DD-MEX, DD-LZ1, DDBx, and DDBu2. On the right panel, it is clear that these same models lie outside the 90% CI obtained for the tidal deformability, even for low masses. None of these models satisfy the constraint that GW170817 sets on the tidal deformability, $70 < \tilde{\Lambda} = \Lambda(1.36 M_{\odot}) < 720$, as indicated by the blue horizontal bar on the right panel.

What distinguishes the set of models plotted in Figure 8 is the high-density behavior of the EOSs and a more precise determination of the radius of a two-solar-mass star will allow distinguishing between them. In fact, the density dependence of the couplings allows for quite different behaviors in the high-density range. The harder EOSs are the ones that predict the larger masses. In common, we see that many of these mass–radius curves present a back-bending behavior. If the radius of the canonical star with $1.4 M_{\odot}$ and a two-solar-mass NS are determined with a small enough uncertainty the different models may be filtered. The 90% credibility radius of a

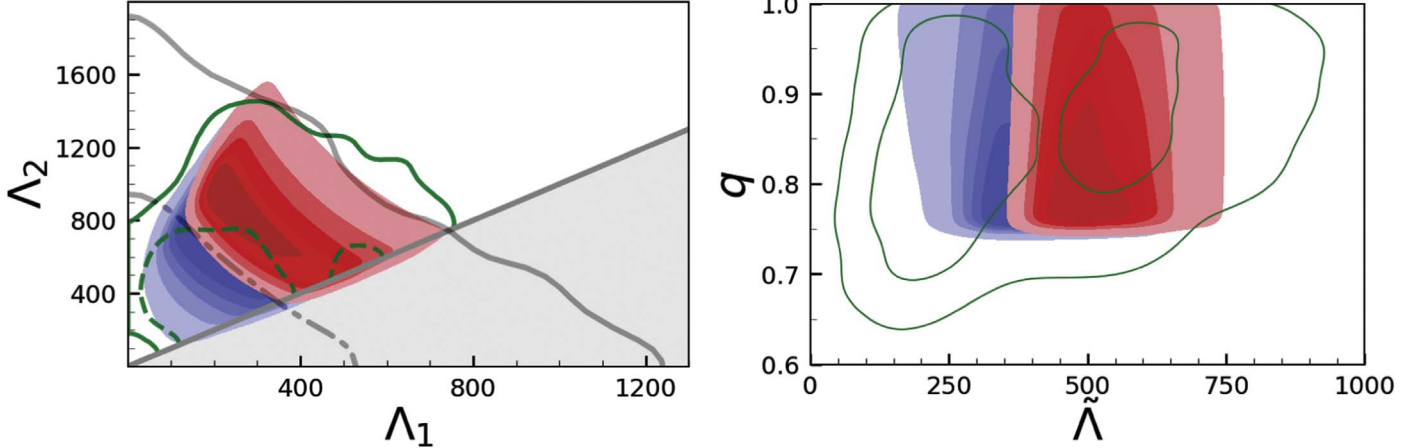


Figure 9. Left: the probability distribution $P(\Lambda_1, \Lambda_2)$, where Λ_1 and Λ_2 are the dimensionless tidal deformability parameters of the binary NS merger from the GW170817 event, using the observed chirp mass of $M_{\text{chirp}} = 1.188 M_\odot$ and mass ratio $q = m_2/m_1$ ($0.7 < q < 1$), for the marginalized posterior distribution of DDH model parameters with the prior set P , allowing, however, that the two-solar-mass constraint is not imposed (blue region). The gray solid (dashed) line represents the 90% (50%) CI from the marginalized posterior for the tidal deformabilities of the two binary components of GW170817. The green solid (dashed) lines represent the 90% (50%) CI of the marginalized posterior for the tidal deformabilities of the two binary components of GW170817 using a parametrized EOS with a maximum mass requirement. Right: the PD $P(q, \tilde{\Lambda})$, the $\tilde{\Lambda}$ is the effective tidal deformability in the binary with mass ratio q . The LIGO/Virgo Collaboration results from Abbott et al. (2019) for the probability distribution function of the joint posterior are shown by the green color for 90% CI and 50% CI, respectively. The blue and red regions in both the panels represent samples not imposing and imposing the two-solar-mass constraint, respectively. The last case corresponds to the DDB set.

$2.08 M_\odot$ star indicated by the horizontal bar does not exclude a region of the mass–radius diagram that within our model lies outside the 90% CI.

In Wei et al. (2020), Taninah et al. (2020) the models DD-MEX and DD-LZ1 predicting a $2.55 M_\odot$ maximum mass and having, simultaneously, reasonable saturation nuclear matter properties have been proposed (see the discussion in Huang et al. 2020). These models are based on the same framework as DD2 and DDME2. This parameterization seems to offer more freedom than the one proposed in the present work, allowing for a harder EOS at high densities and predicting larger radii. Our parameterization does not allow for masses above $\approx 2.5 M_\odot$. In the future a more careful investigation of the possible density behavior of the couplings and consequences will be carried out.

Other models have predicted masses above $2.44 M_\odot$: (i) NL3 $\omega\rho$ with $L_{\text{sym},0} = 55$ MeV predicts a maximum mass of $2.75 M_\odot$, but this EOS has a very hard isoscalar EOS, in particular, $K_0 = 271$ MeV (Fortin et al. 2016) and $\Lambda_{1,4} = 1040$; (ii) BigApple (Fattoyev et al. 2020) describes a $2.6 M_\odot$ NS but does not satisfy PNM χ EFT constraints; (iii) using a Taylor-expanded EOS to describe nuclear matter, maximum masses as high as $2.66 M_\odot$ were obtained. However, this is a nonrelativistic approach and it is necessary to filter the models that do not satisfy $c_s < 1$, precisely the condition that defines the maximum mass upper limits.

In Figure 9 (left), we show the probability distribution of the dimensionless tidal deformability parameters Λ_1 and Λ_2 as $P(\Lambda_1, \Lambda_2)$ for the two objects involved in the BNS event from GW170817, with masses m_1 and m_2 , using the observed chirp mass of $M_{\text{chirp}} = 1.188 M_\odot$ and mass ratio $q = m_2/m_1$ ($0.7 < q < 1$), for the marginalized posterior distribution of DDH model parameters of two cases: (i) a set similar to DDB but without having NS maximum mass constraints (blue), and (ii) for the DDB set (red). For each EOS, we obtain a curve in the Λ_1 and Λ_2 plane by varying m_1 in the range $1.36 < m_1 < 1.6 M_\odot$, and calculating m_2 by keeping the chirp mass fixed at $M_{\text{chirp}} = 1.188 M_\odot$, as observed in the GW170817

event. We also show the constraints from GW170817 for comparison. The black solid (dashed) line represents the 90% (50%) CI from the marginalized posterior for the tidal deformabilities of the two binary components of GW170817. The green solid (dashed) lines represent the 90% (50%) CI of the marginalized posterior for the tidal deformabilities of the two binary components of GW170817 using a parametrized EOS with a maximum mass requirement of at least $1.97 M_\odot$. In the right panel, we present the PDs for $P(q, \tilde{\Lambda})$ in the mass ratio q and combined tidal deformability $\tilde{\Lambda}$ for the GW merger. The green lines are the 50% (90%) CI given by the LIGO analysis (Abbott et al. 2019). We see that both the $P(\Lambda_1, \Lambda_2)$ and $P(q, \tilde{\Lambda})$ obtained with DDH parameters are in very good agreement with the GW170817 LIGO results.

NICER has measured the equatorial circumferential radius of one of the highest mass ($2.072^{+0.067}_{-0.066} M_\odot$) pulsar PSR J0740 +6620. This measurement of the radius with 68% CI is $12.39^{+1.30}_{-0.98}$ (Riley et al. 2021). We also investigate the prediction for the radius of a $2.08 M_\odot$ NS within the DDB set: we have determined the radius median value ≈ 12.01 km, and the 90% CI ≈ 11.1 – 12.9 km.

The composition of NS may be constrained by cooling information: as soon as the nucleonic direct Urca process sets in the NS undergoes a superfast cooling (Lattimer et al. 1991; Yakovlev et al. 2001). This is possible if the proton fraction attains the minimum threshold that, if muons are excluded, corresponds to 1/9 (Lattimer et al. 1991). Including muons increases this fraction to above 0.14 after muon onset, in Thi et al. (2021) a threshold of 0.135 and 0.138 was obtained, respectively for 1.4 and $2.0 M_\odot$ stars. In Figure 10, the proton, electron, and muon fractions are plotted as a function of density. NS central densities in our sets lie below 1.1 fm^{-3} . We have verified that the present set of models does not predict nucleonic direct Urca inside NS. A more careful analysis, also considering the opening of hyperonic Urca processes will be studied in the future. This agrees with conclusions drawn by Fortin et al. (2016, 2020, 2021) for DDH models such as DD2 and DDME2.

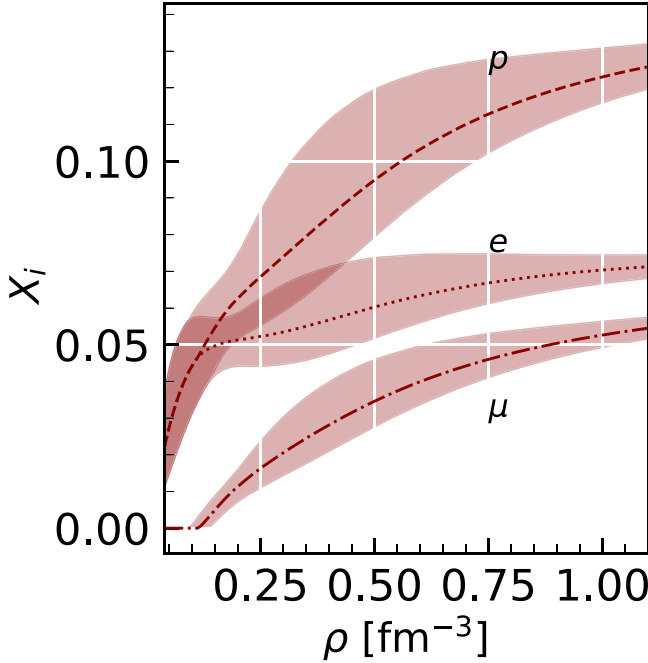


Figure 10. The plot for the particle fraction X_i , for protons (p), electrons (e), and muons (μ), along with 90% CI as a function of baryon density ρ for DDB.

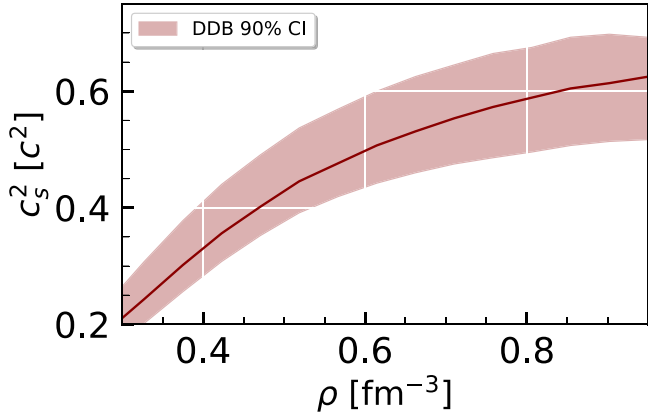


Figure 11. The square of sound velocity c_s^2 with 90% CI as a function of baryon density for the DDB set.

Finally, let us also refer to the behavior of the sound velocity of the models within our DDB set (see Figure 11). As discussed in other works by Bedaque & Steiner (2015), Alford et al. (2013), Moustakidis et al. (2017), Tews et al. (2018), Reed & Horowitz (2020), $2 M_\odot$ NSs require a speed of sound well above the conformal limit $1/\sqrt{3}$, implying that NS matter is a strongly interacting system. This indicates that in order for NS matter to be able to counterbalance the gravitational attraction, the energy density should increase slowly enough compared with the pressure increase, resulting in a large speed of sound. In the center of the NS, the square of the speed of sound squared is, on average, 0.65, but taking the 95% CI $0.51 < c_s^2 < 0.73$. As referred before, the present description of hadronic matter automatically limits the speed of sound to values below 1. In Ferreira et al. (2021), a larger central speed of sound was necessary to attain $2 M_\odot$ hybrid stars, always above $\sqrt{0.7}$. As explained in Alford et al. (2013), this is

necessary so that the quark core is able to support the nuclear mantle.

4. Conclusions

Within a Bayesian approach, we have generated a set of models based on the RMF framework with density-dependent coupling parameters and no nonlinear mesonic terms. This set was constrained by the neutron matter χ EFT EOS and four saturation properties of nuclear matter: the saturation density, binding energy per particle and incompressibility, and the symmetry energy. For the last property, an interval compatible with χ EFT calculations was considered. Besides, the set was also constrained by imposing that the maximum star mass should be at least $2 M_\odot$. It was verified that the 90% CI for the low-density PNM calculated within the DDB set is compatible with the one obtained from a precise N³LO calculation in χ EFT (Hebeler et al. 2013).

The main objective of the study is the determination of the domain of nucleonic NS EOS based on a relativistic approach with minimal constraints. In particular, we have analyzed the behavior of the density dependence of the symmetry energy, the high-density behavior of the EOS, and the upper and lower limits for several NS properties. We have verified that the posterior distribution of NS maximum mass, radii, and tidal deformabilities are compatible with recent NS observables.

The recent determination of the neutron skin thickness of ²⁰⁸Pb through PREX-II measurements from Reed et al. (2021), $\Delta R_{\text{skin}} = 0.283 \pm 0.071$ fm, seems to indicate that the slope of the symmetry energy could be rather high, $L_{\text{sym},0} = (106 \pm 37)$ MeV according to Reed et al. (2021), showing some tension with the results we have obtained. Other studies, however, have obtained smaller values for the slope. In Essick et al. (2021b), undertaking an analysis that combines the astrophysical data with constraints from PREX-II and χ EFT calculations, the authors have determined a ²⁰⁸Pb neutron skin thickness equal to 0.17 ± 0.04 fm and a symmetry energy slope $L_{\text{sym},0} = 53^{+14}_{-15}$ MeV. This last prediction for the slope is compatible with the range of values determined with the DDB set.

The present study has enabled us to understand which are the limitations of the Taylor-expanded EOS approach to determine the acceptable range of values for higher-order NMPs as the skewness Q_0 for the symmetric nuclear matter and the incompressibility $K_{\text{sym},0}$ and skewness $Q_{\text{sym},0}$ for symmetry energy. Within a 90% CI these last three quantities take the values $-256 < Q_0 < 130$ MeV, $-150 < K_{\text{sym},0} < -73$ MeV, and $317 < Q_{\text{sym},0} < 1469$ MeV. In the Taylor expansion approach, the isoscalar NMPs are constrained by causality conditions not intrinsic to the model. Besides, they should be interpreted as effective parameters since they have to describe the effects of the missing higher terms (de Tovar et al. 2021).

NS properties have been studied and compared with recent observations, the masses of pulsars PSR J1614-2230 (Demorest et al. 2010; Fonseca et al. 2016; Arzoumanian et al. 2018), PSR J0348-0432 (Antoniadis et al. 2013), PSR J0740+6620 (Fonseca et al. 2021), and very recently J1810+1714 (Romani et al. 2021), the gravitational waves detected from the NS binary merger GW170817 (Abbott et al. 2017c, 2019), the NICER determination of the mass and radius of the PSR J0030+0451 (Miller et al. 2019; Riley et al. 2019), together with the determination of the radius of the PSR J0740+6620 from the joint analysis of data obtained by NICER and XMM-Newton

(Riley et al. 2021). The total compatibility of the DDB set predictions with the observations of NICER and of the LIGO-Virgo Collaboration indicates that more constraints are required to get more precise information on the high-density EOS. The presently existing constraints on the mass and radius are totally compatible with a composition restricted to nucleons and leptons. The lowest limit obtained for effective tidal deformability, $\tilde{\Lambda}_{q=1} \approx 382$ at 95% CI, is above but compatible with the values $\tilde{\Lambda} \gtrsim 300$ and 242 determined in Radice et al. (2018) and Kiuchi et al. (2019), respectively, from the electromagnetic counterparts that followed up the GW170817 emission, i.e., the gamma-ray burst GRB170817A (Abbott et al. 2017a) and the electromagnetic transient AT2017gfo (Abbott et al. 2017a).

It has been shown that the generated set of models contains models with properties similar to TW (Typel & Wolter 1999), DD2 (Typel et al. 2010), and DDME2 (Lalazissis et al. 2005), and three DDH models frequently used in the literature, in particular DD2 and DDME2. A common property of the DDB set of EOS with these DDH models is the prediction that no nucleonic direct Urca occurs inside nucleonic NS (see Fortin et al. 2016, 2021). This behavior requires the onset of hyperons inside the star to explain presently known cooling curves of the thermal evolution of nonmagnetized and nonrotating spherically symmetric isolated NS and accreting NS (Providência et al. 2019; Fortin et al. 2021), which, however, may raise the problem of making the EOS too soft, not allowing for the existence of $2 M_{\odot}$ NSs. The effect of the onset of hyperons in models of the set DDB will be investigated in the future.

It was verified that within the parameterization proposed for the couplings of the DDB set, the maximum NS masses obtained are $\leq 2.51 M_{\odot}$, which is just above the DD2 and DDME2 maximum mass and could still be compatible with the low-mass object of the binary merger that originated GW190814 (Abbott et al. 2020). All models with a mass above $2.48 M_{\odot}$ have an incompressibility $300 \geq K_0 \geq 315$, inside the range of values proposed in Stone et al. (2014) where the incompressibility for the infinite matter was determined from finite nuclei properties.

This work was partially supported by national funds from FCT (Fundação para a Ciência e a Tecnologia, IP, Portugal) under the Projects No. UID/FIS/04564/2019, No. UIDP/04564/2020, No. UIDB/04564/2020, and No. POCI-01-0145-FEDER-029912 with financial support from Science, Technology and Innovation, in its FEDER component, and by the FCT/MCTES budget through national funds (OE). BKA acknowledges partial support from the Department of Science and Technology, Government of India with grant No. CRG/2021/000101. The authors acknowledge the Laboratory for Advanced Computing at the University of Coimbra for providing HPC resources that have contributed to the research results reported in this paper, URL: <https://www.uc.pt/lca>.

Data: We are publicly releasing five tabulated EOSs, namely DDB1, DDBm, DDBu1, DDBu2, and DDBx (see Section 3 for details). We also release our entire sets of 14K NS matter EOS. All the EOSs are for the NS core and starting baryon density is 0.04 fm^{-3} . One has to add their own choice of crust EOS to it for the calculation of star properties. The uncertainty in star properties for the choice of the different crusts has been discussed in Section 2.1 of this manuscript. All of these data files are available on GitHub (https://github.com/tuhinuct/DDH_EOS)

and a copy of these files has been deposited in Zenodo: [10.5281/zenodo.6342100](https://zenodo.org/record/6342100).

ORCID iDs

- Tuhin Malik <https://orcid.org/0000-0003-2633-5821>
Márcio Ferreira <https://orcid.org/0000-0002-5879-6262>
B. K. Agrawal <https://orcid.org/0000-0001-5032-9435>
Constança Providência <https://orcid.org/0000-0001-6464-8023>

References

- Abbott, B. P., Abbott, R., Abbott, T. D., et al. 2017a, *ApJL*, 848, L13
Abbott, B. P., Abbott, R., Abbott, T. D., et al. 2017b, *ApJL*, 848, L12
Abbott, B. P., Abbott, R., Abbott, T. D., et al. 2017c, *PhRvL*, 119, 161101
Abbott, B. P., Abbott, R., Abbott, T. D., et al. 2018, *PhRvL*, 121, 161101
Abbott, B. P., Abbott, R., Abbott, T. D., et al. 2019, *PhRvX*, 9, 011001
Abbott, R., Abbott, T., Abraham, S., et al. 2020, *ApJL*, 896, L44
Alford, M. G., Han, S., & Prakash, M. 2013, *PhRvD*, 88, 083013
Annala, E., Gorda, T., Katerini, E., et al. 2022, *PhRvX*, 12, 011058
Annala, E., Gorda, T., Kurkela, A., Nättilä, J., & Vuorinen, A. 2020, *NatPh*, 16, 907
Antoniadis, J., Freire, P. C. C., Wex, N., et al. 2013, *Sci*, 340, 448
Arzoumanian, Z., Brazier, A., Burke-Spolaor, S., et al. 2018, *ApJS*, 235, 37
Ashton, G., Hübner, M., Lasky, P. D., et al. 2019, *ApJS*, 241, 27
Avancini, S. S., Brito, L., Marinelli, J. R., et al. 2009, *PhRvC*, 79, 035804
Avancini, S. S., Menezes, D. P., Alloy, M. D., et al. 2008, *PhRvC*, 78, 015802
Baade, W., & Zwicky, F. 1934a, *PNAS*, 20, 259
Baade, W., & Zwicky, F. 1934b, *PhRv*, 46, 76
Bedaque, P., & Steiner, A. W. 2015, *PhRvL*, 114, 031103
Boguta, J., & Bodmer, A. R. 1977, *NuPhA*, 292, 413
Brecher, K. 1999, AAS Meeting Abstracts, 195, 130.05
Brockmann, R., & Machleidt, R. 1990, *PhRvC*, 42, 1965
Buchner, J. 2021, Nested Sampling Methods, arXiv:2101.09675
Buchner, J., Georgakakis, A., Nandra, K., et al. 2014, *A&A*, 564, A125
Carriere, J., Horowitz, C. J., & Piekarewicz, J. 2003, *ApJ*, 593, 463
Constantinou, C., Mucciali, B., Prakash, M., & Lattimer, J. M. 2015, *PhRvC*, 92, 025801
Danielewicz, P., Lacey, R., & Lynch, W. G. 2002, *Sci*, 298, 1592
Danielewicz, P., & Lee, J. 2014, *NuPhA*, 922, 1
de Tovar, P. B., Ferreira, M., & Providência, C. 2021, *PhRvD*, 104, 123036
Demorest, P., Pennucci, T., Ransom, S., Roberts, M., & Hessels, J. 2010, *Natur*, 467, 1081
Drischler, C., Hebeler, K., & Schwenk, A. 2016, *PhRvC*, 93, 054314
Drischler, C., Hebeler, K., & Schwenk, A. 2019, *PhRvL*, 122, 042501
Dutra, M., Lourenço, O., Avancini, S. S., et al. 2014, *PhRvC*, 90, 055203
Essick, R., Landry, P., & Holz, D. E. 2020, *PhRvD*, 101, 063007
Essick, R., Landry, P., Schwenk, A., & Tews, I. 2021a, *PhRvC*, 104, 065804
Essick, R., Tews, I., Landry, P., & Schwenk, A. 2021b, *PhRvL*, 127, 192701
Fattoyev, F. J., Horowitz, C. J., Piekarewicz, J., & Reed, B. 2020, *PhRvC*, 102, 065805
Ferreira, M., Câmara Pereira, R., & Providência, C. 2021, *PhRvD*, 103, 123020
Ferreira, M., & Providência, C. 2021a, *PhRvD*, 104, 063006
Ferreira, M., & Providência, C. 2021b, *JCAP*, 2021, 011
Fonseca, E., Cromartie, H. T., Pennucci, T. T., et al. 2021, *ApJL*, 915, L12
Fonseca, E., Pennucci, T. T., Ellis, J. A., et al. 2016, *ApJ*, 832, 167
Fortin, M., Providencia, C., Raduta, A. R., et al. 2016, *PhRvC*, 94, 035804
Fortin, M., Raduta, A. R., Avancini, S., & Providência, C. 2020, *PhRvD*, 101, 034017
Fortin, M., Raduta, A. R., Avancini, S., & Providência, C. 2021, *PhRvD*, 103, 083004
Fritz, R., & Muther, H. 1994, *PhRvC*, 49, 633
Fuchs, C., Lenske, H., & Wolter, H. H. 1995, *PhRvC*, 52, 3043
Furnstahl, R. J., Klco, N., Phillips, D. R., & Wesolowski, S. 2015, *PhRvC*, 92, 024005
Glendenning, N. K. 1996, Compact Stars (New York: Springer)
Haddad, S., & Weigel, M. K. 1993, *PhRvC*, 48, 2740
Haensel, P., Potekhin, A. Y., & Yakovlev, D. G. 2007, Neutron Stars 1: Equation of State and Structure (New York: Springer), 326
Han, M.-Z., Jiang, J.-L., Tang, S.-P., & Fan, Y.-Z. 2021, *ApJ*, 919, 11
Hebeler, K., Lattimer, J. M., Pethick, C. J., & Schwenk, A. 2013, *ApJ*, 773, 11
Hebeler, K., & Schwenk, A. 2010, *PhRvC*, 82, 014314

- Hewish, A., Bell, S. J., Pilkington, J. D. H., Scott, P. F., & Collins, R. A. 1968, *Natur*, **217**, 709
- Hinderer, T. 2008, *ApJ*, **677**, 1216
- Huang, K., Hu, J., Zhang, Y., & Shen, H. 2020, *ApJ*, **904**, 39
- Imam, S. M. A., Patra, N. K., Mondal, C., Malik, T., & Agrawal, B. K. 2022, *PhRvC*, **105**, 015806
- Kiuchi, K., Kyutoku, K., Shibata, M., & Taniguchi, K. 2019, *ApJL*, **876**, L31
- Kurkela, A., Fraga, E. S., Schaffner-Bielich, J., & Vuorinen, A. 2014, *ApJ*, **789**, 127
- Kurkela, A., Romatschke, P., & Vuorinen, A. 2010, *PhRvD*, **81**, 105021
- Lalazissis, G. A., Niksic, T., Vretenar, D., & Ring, P. 2005, *PhRvC*, **71**, 024312
- Landry, P., Essick, R., & Chatzioannou, K. 2020, *PhRvD*, **101**, 123007
- Lattimer, J. M., & Lim, Y. 2013, *ApJ*, **771**, 51
- Lattimer, J. M., Prakash, M., Pethick, C. J., & Haensel, P. 1991, *PhRvL*, **66**, 2701
- Lenske, H., & Fuchs, C. 1995, *PhRvB*, **345**, 355
- Li, B.-A., Krastev, P. G., Wen, D.-H., & Zhang, N.-B. 2019, *EPJA*, **55**, 117
- Lindblom, L., & Indik, N. M. 2012, *PhRvD*, **86**, 084003
- Loh, W.-L. 1996, *AnSta*, **24**, 2058
- Lope Oter, E., Windisch, A., Llanes-Estrada, F. J., & Alford, M. 2019, *JPhG*, **46**, 084001
- Lopes, L. L. 2021, *EPL*, **134**, 52001
- Lynn, J. E., Tews, I., Carlson, J., et al. 2016, *PhRvL*, **116**, 062501
- Marcos, S., Niembro, R., Lopez-Quelle, M., Van Giai, N., & Malfliet, R. 1989, *PhRvC*, **39**, 1134
- Margueron, J., Hoffmann Casali, R., & Gulminelli, F. 2018a, *PhRvC*, **97**, 025805
- Margueron, J., Hoffmann Casali, R., & Gulminelli, F. 2018b, *PhRvC*, **97**, 025806
- Miller, M. C., Lamb, F. K., Dittmann, A. J., et al. 2019, *ApJL*, **887**, L24
- Miller, M. C., Lamb, F. K., Dittmann, A. J., et al. 2021, *ApJL*, **918**, L28
- Mondal, C., & Gulminelli, F. 2021, arXiv:2111.04520
- Most, E. R., Weih, L. R., Rezzolla, L., & Schaffner-Bielich, J. 2018, *PhRvL*, **120**, 261103
- Moustakidis, C. C., Gaitanos, T., Margaritis, C., & Lalazissis, G. A. 2017, *PhRvC*, **95**, 045801
- Mueller, H., & Serot, B. D. 1996, *NuPhA*, **606**, 508
- Oppenheimer, J. R., & Volkoff, G. M. 1939, *PhRv*, **55**, 374
- Pais, H., & Providência, C. 2016, *PhRvC*, **94**, 015808
- Providência, C., Fortin, M., Pais, H., & Rabhi, A. 2019, *FrASS*, **6**, 13
- Radice, D., Perego, A., Zappa, F., & Bernuzzi, S. 2018, *ApJL*, **852**, L29
- Rather, I. A., Usmani, A. A., & Patra, S. K. 2021, *NuPhA*, **1010**, 122189
- Reed, B., & Horowitz, C. J. 2020, *PhRvC*, **101**, 045803
- Reed, B. T., Fattoyev, F. J., Horowitz, C. J., & Piekarewicz, J. 2021, *PhRvL*, **126**, 172503
- Rezzolla, L., Pizzochero, P., Jones, D. I., Rea, N., & Vidaña, I. (ed.) 2018, *The Physics and Astrophysics of Neutron Stars*, Vol. 457 (Berlin: Springer)
- Riley, T. E., Watts, A. L., Bogdanov, S., et al. 2019, *ApJL*, **887**, L21
- Riley, T. E., Watts, A. L., Ray, P. S., et al. 2021, *ApJL*, **918**, L27
- Romaní, R. W., Kandel, D., Filippenko, A. V., Brink, T. G., & Zheng, W. 2021, *ApJL*, **908**, L46
- Serot, B. D., & Walecka, J. D. 1986, *AdNuP*, **16**, 1
- Shlomo, S., Kolomeit, V. M., & Colò, G. 2006, *EPJA*, **30**, 23
- Skilling, J. 2004, in *AIP Conf. Ser.* 735, *Bayesian Inference and Maximum Entropy Methods in Science and Engineering*, ed. R. Fischer, R. Preuss, & U. V. Toussaint (Melville, NY: AIP), 395
- Speagle, J. S. 2020, *MNRAS*, **493**, 3132
- Steiner, A. W., Prakash, M., Lattimer, J. M., & Ellis, P. J. 2005, *PhR*, **411**, 325
- Stone, J. R., Stone, N. J., & Moszkowski, S. A. 2014, *PhRvC*, **89**, 044316
- Taninah, A., Agbemava, S. E., Afanasjev, A. V., & Ring, P. 2020, *PhRvB*, **800**, 135065
- Ter Haar, B., & Malfliet, R. 1987, *PhR*, **149**, 207
- Tews, I., Carlson, J., Gandolfi, S., & Reddy, S. 2018, *ApJ*, **860**, 149
- Tews, I., Krüger, T., Hebeler, K., & Schwenk, A. 2013, *PhRvL*, **110**, 032504
- Tews, I., Lattimer, J. M., Ohnishi, A., & Kolomeitsev, E. E. 2017, *ApJ*, **848**, 105
- Thi, H. D., Mondal, C., & Gulminelli, F. 2021, *Univ*, **7**, 373
- Todd-Rutel, B. G., & Piekarewicz, J. 2005, *PhRvL*, **95**, 122501
- Tolman, R. C. 1939, *PhRv*, **55**, 364
- Typel, S., Ropke, G., Klahn, T., Blaschke, D., & Wolter, H. H. 2010, *PhRvC*, **81**, 015803
- Typel, S., & Wolter, H. H. 1999, *NuPhA*, **656**, 331
- Vidana, I., Providencia, C., Polls, A., & Rios, A. 2009, *PhRv*, **C80**, 045806
- Wei, B., Zhao, Q., Wang, Z.-H., et al. 2020, *ChPhC*, **44**, 074107
- Wesolowski, S., Klco, N., Furnstahl, R. J., Phillips, D. R., & Thapaliya, A. 2016, *JPhG*, **43**, 074001
- Yakovlev, D. G., Haensel, P., Baym, G., & Pethick, C. J. 2013, *Phys. Usp.*, **56**, 289
- Yakovlev, D. G., Kaminker, A. D., Gnedin, O. Y., & Haensel, P. 2001, *PhR*, **354**, 1
- Zhang, N.-B., & Li, B.-A. 2019, *ApJ*, **879**, 99
- Zhang, N.-B., Li, B.-A., & Xu, J. 2018, *ApJ*, **859**, 90

Neutron star equation of state: identifying hadronic matter characteristics

Constança Providência,^{1,*} Tuhin Malik,^{1,†} Milena Bastos Albino,^{1,‡} and Márcio Ferreira^{1,§}

¹*CFisUC, Department of Physics, University of Coimbra, 3004-516 Coimbra, Portugal.*

(Dated: July 12, 2023)

The general behavior of the nuclear equation of state (EOS), relevant for the description of neutron stars (NS), is studied within a relativistic mean field description of nuclear matter. Different formulations, both with density dependent couplings and with non-linear mesonic terms, are considered and their predictions compared and discussed. A special attention is drawn to the effect on the neutron star properties of the inclusion of exotic degrees of freedom as hyperons. Properties such as the speed of sound, the trace anomaly, the proton fraction and the onset of direct Urca processes inside neutron stars are discussed. The knowledge of the general behavior of the hadronic equation of state and the implication it has on the neutron star properties will allow to identify signatures of a deconfinement phase transition discussed in other studies.

I. INTRODUCTION

Neutron stars (NS) are objects with several extreme properties which make them a true laboratory for dense baryonic matter. Under the extreme conditions existing in their interior it is expected, for instance, that quark deconfinement may occur in the center of NS. These are also the ideal objects to study very asymmetric nuclear matter which cannot be tested in the laboratory. In the present multi-messenger era, astrophysical observations are starting to impose some stringent constraints on the equation of state (EOS) of the high density baryonic matter. These constraints come from the gravitational wave detection by the LIGO Virgo collaboration as the detection of the binary neutron star merger GW170817 [1] or the GW190425 [2], from radio data [3–7] or the recent x-ray observations of NICER allowing a prediction of both the NS mass and radius [8–12].

The nuclear matter EOS at low densities is constrained not only by well known nuclear matter properties as the binding energy, saturation density and incompressibility [13], but also from *ab-initio* calculations of pure neutron matter based on a chiral effective field theoretical description [14–16]. At very high densities, $\sim 40\rho_0$ where ρ_0 is the nuclear saturation density, perturbative QCD calculations have been performed and they also impose strong constraints [17, 18]. Although the pQCD EOS is determined at densities that are not attained inside neutron stars, it was shown recently that these constraints may affect in a non-trivial way the EOS inside neutron stars [19].

From the measurement of mass and radius of several NS, one expects to be able to recover the EOS. The integration of the Tolman-Oppenheimer-Volkoff (TOV) equations establishes a one-to-one relation between the mass-radius curve and the pressures-energy density function [20]. Several methods have been used to obtain the EoS from the known mass-radius curve such as Bayesian inference [21–24] or neural network techniques [25–30], see [31] for a recent review on

the application of machine learning techniques to learn about QCD matter under extreme conditions. Another problem is the determination of the NS composition from the knowledge of the EOS. Several studies have been carried out with the objective of extracting the proton fraction. Starting from a Taylor expansion representation of the EOS in the parabolic approximation for the asymmetry, it was shown that the proton fraction could not be recovered from the β -equilibrium EOS [32–34]. In [32], the authors attribute the failure to the existence of multiple solutions. In [33], the reason was assigned to the occurrence of correlations between the nuclear matter parameters.

Many studies have been performed with the objective of determining the EOS of strongly interacting matter constrained by observations and well accepted *ab-initio* calculations as the ones reported above. In order to span the whole phase space that joins the low density to the high density constraints different interpolation schemes have been undertaken based in agnostic descriptions of the EOS. Among these we can point out the use of a piecewise polytropic interpolation [18, 35], a spectral interpolation [36], a speed-of-sound interpolation [37–39], meta-models based on Taylor expansions [40–46] or a nonparametric inference of the EOS [19, 47–49]. These studies have been used to infer signatures of the presence of deconfined matter inside neutron stars, for instance, by analyzing the behavior of the speed of sound with density [38, 39] or the trace anomaly which may signal the restoration of conformal symmetry [50, 51]. However, the above approaches are not able to determine the composition of neutron stars.

The present chapter reviews recent work developed within the framework of a relativistic mean-field (RMF) description of hadronic matter at zero temperature having as main objective the determination of the region in the neutron star mass-radius diagram, and corresponding EOS, in conformity with present observations and *ab-initio* constraints. A Bayesian inference will be applied in the search for the parameters of the models. In comparison with the agnostic approaches described above, our perspective has an underlying microscopic model, which allows us to discuss composition, including proton fraction or hyperon content. We consider this information completes the one obtained from the agnostic descriptions of the EOS, and may bring extra clues into the interpretation of the results obtained. In the following chapters we will review

* cp@uc.pt

† tm@uc.pt

‡ milena.albino@usp.br

§ marcio.ferreira@uc.pt

the methodology and results obtained in the works [52–55]. In particular, we will compare outputs obtained considering the different microscopic models in order to assess the generality and the specificity of the conclusions. The microscopic models based in a Lagrangian formulation used in these works may be divided in two classes: i) the Lagrangian density is formulated in terms of constant parameters and include non-linear mesonic terms as proposed in [56, 57]. These models are designated by NL; ii) the Lagrangian density contains only quadratic mesonic terms and is expressed in terms of couplings that have an explicit density dependence as explored in [58, 59]. In this class, we consider two different parametrizations of the couplings, the one proposed in [58] which we designate by DDH and the one used in [52] designated as DDB. We will also discuss the limitations of this second class of models concerning the high density behavior of the coupling to the ϱ -meson, which defines the density dependence of the symmetry energy, and we will propose a generalization that overcomes the limitation [54]. Lastly, and considering recent interest in identifying signatures of deconfinement and of imposing high density pQCD constraints, we will discuss some of the physical quantities examined, including the speed of sound, polytropic index and trace anomaly and discuss the limitations enforced by pQCD.

Some other works have been developed in the last years using a Bayesian inference approach to constraint the parameters of RMF models including, [60] where a simpler version of the NL description was considered, [61] which has restricted the $\Lambda - \omega$ couplings in hyperonic stellar matter imposing as constraints the GW and NICER observations, [62] where the authors have studied how the pure neutron matter pressure and energy per particle constrains the isovector behavior of nuclear matter, and studied several correlations between nuclear matter properties (NMP) and NS properties, [63] where the authors have constrained the NL model from the present available NS observations and tested how constraining might be the future observations programmed for eXTP [64] and STROBE-X [65].

In the present chapter, we will first present the microscopic models used to perform the study, the Bayesian inference methodology, together with the priors, the data chosen to fit the models. We next compare the behavior of the different data sets generated, including the nuclear matter properties (NMP) and the neutron star properties, including the speed of sound and the proton fraction. The inclusion of hyperons will be discussed as well as the onset of the nucleon direct Urca processes. We will also refer to some properties that are directly connected to QCD, in particular the trace anomaly and the constraints imposed by pQCD on the generated data sets of EOS.

II. FORMALISM

In this section, we briefly summarize the frameworks that will be applied to describe the nuclear or hadronic matter EOS. We will start by introducing the models through the definition of the Lagrangian density. As referred in the In-

roduction, two different classes are considered. They define the density dependence of the EOS through completely different approaches: i) density dependent couplings are introduced (DDH and DDB models); ii) non-linear mesonic terms are included (NL).

A. The model

The equation of state of nuclear matter is determined from the Lagrangian density that describes the nuclear system. The degrees of freedom include the nucleons of mass m described by Dirac spinors Ψ , and the meson fields, the scalar isoscalar σ field, the vector isoscalar ω field, and the vector isovector ϱ field, with masses m_i , $i = \sigma, \omega, \varrho$, which describe the nuclear interaction. The parameters Γ_i or g_i , $i = \sigma, \omega, \varrho$ designate the couplings of the mesons to the nucleons. The Lagrangian density is given by

$$\begin{aligned} \mathcal{L} = & \bar{\Psi} \left[\gamma^\mu \left(i\partial_\mu - \Gamma_\omega A_\mu^{(\omega)} - \Gamma_\varrho \mathbf{t} \cdot \mathbf{A}_\mu^{(\varrho)} \right) - (m - \Gamma_\sigma \phi) \right] \Psi \\ & + \frac{1}{2} (\partial_\mu \phi \partial^\mu \phi - m_\sigma^2 \phi^2) \\ & - \frac{1}{4} F_{\mu\nu}^{(\omega)} F^{(\omega)\mu\nu} + \frac{1}{2} m_\omega^2 A_\mu^{(\omega)} A^{(\omega)\mu} \\ & - \frac{1}{4} \mathbf{F}_{\mu\nu}^{(\varrho)} \cdot \mathbf{F}^{(\varrho)\mu\nu} + \frac{1}{2} m_\varrho^2 \mathbf{A}_\mu^{(\varrho)} \cdot \mathbf{A}^{(\varrho)\mu} + \mathcal{L}_{NL}, \end{aligned} \quad (1)$$

where the last term \mathcal{L}_{NL} is null if density dependent couplings Γ_i are chosen, or includes self-interacting and mixed meson terms if the meson-nucleon couplings are taken as constant parameters. In order to distinguish, we will designate the constant couplings by the lower case letter g_i in the NL formulation. In the above expression γ^μ and \mathbf{t} designate, respectively, the Dirac matrices and the isospin operator. The vector meson field strength tensors are defined as $F^{(\omega,\varrho)\mu\nu} = \partial^\mu A^{(\omega,\varrho)\nu} - \partial^\nu A^{(\omega,\varrho)\mu}$.

1. Density dependent description

The density dependent models include meson-nucleon couplings Γ_i , that depend on the total nucleonic density ρ , and is defined as

$$\Gamma_i(\rho) = \Gamma_{i,0} h_i(x), \quad x = \rho/\rho_0, \quad i = \sigma, \omega, \varrho, \quad (2)$$

with $\Gamma_{i,0}$ the couplings at saturation density ρ_0 . For the isoscalar mesons, σ and ω , two parametrizations h_i are considered:

$$h_i(x) = \exp[-(x^{a_i} - 1)] \quad (3)$$

as in [54], giving origin to the DDB sets, and

$$h_i(x) = a_M \frac{1 + b_i(x + d_i)^2}{1 + c_i(x + d_i)^2}, \quad (4)$$

as in [58, 59], and originating the DDH data sets. The ϱ -meson nucleon coupling is defined as in [58]

$$h_\varrho(x) = \exp[-a_\varrho(x - 1)]. \quad (5)$$

2. Non-linear meson terms

The model introduced in [66] is defined with constant couplings, which we designate by g_i , $i = \sigma, \omega, \varrho$, and, instead, includes non-linear meson terms in the Lagrangian density, which are defined by

$$\mathcal{L}_{NL} = -\frac{1}{3}bg_\sigma^3(\sigma)^3 - \frac{1}{4}cg_\sigma^4(\sigma)^4 + \frac{\xi}{4!}(g_\omega^2\omega_\mu\omega^\mu)^2 + \Lambda_\omega g_\varrho^2\varrho_\mu \cdot \varrho^\mu g_\omega^2\omega_\mu\omega^\mu. \quad (6)$$

The parameters multiplying each one of these terms $b, c, \xi, \Lambda_\omega$ will be fixed together with the meson-nucleon couplings g_i by imposing nuclear matter and NS observational constraints.

The parameters b, c , in front of the σ self interacting terms control the nuclear matter incompressibility at saturation [56]. The ξ term was introduced in [67] to modulate the high density dependence of the EoS, the larger ξ the softer the EOS. The non-linear $\omega - \varrho$ term influences the density dependence of the symmetry energy [68].

The equations of motion for the meson fields are given by

$$\sigma = \frac{g_\sigma}{m_{\sigma,\text{eff}}^2} \sum_i \rho_i^s \quad (7)$$

$$\omega = \frac{g_\omega}{m_{\omega,\text{eff}}^2} \sum_i \rho_i \quad (8)$$

$$\varrho = \frac{g_\varrho}{m_{\varrho,\text{eff}}^2} \sum_i t_{3i}\rho_i, \quad (9)$$

where ρ_i^s and ρ_i are, respectively, the scalar density and the number density of nucleon i , and the effective meson masses are defined as

$$m_{\sigma,\text{eff}}^2 = m_\sigma^2 + bg_\sigma^3\sigma + cg_\sigma^4\sigma^2 \quad (10)$$

$$m_{\omega,\text{eff}}^2 = m_\omega^2 + \frac{\xi}{3!}g_\omega^4\omega^2 + 2\Lambda_\omega g_\varrho^2 g_\omega^2 \varrho^2 \quad (11)$$

$$m_{\varrho,\text{eff}}^2 = m_\varrho^2 + 2\Lambda_\omega g_\omega^2 g_\varrho^2 \omega^2. \quad (12)$$

The non-linear meson terms define effective meson masses that depend on the density: i) $m_{\omega,\text{eff}}$ increases with the ω -field and, as a consequence, the ω field is not proportional to the density for a non zero ξ , but increases with a power of ρ smaller than one; ii) $m_{\varrho,\text{eff}}$ increases with the density ρ , and, therefore, as the density increases the ϱ field becomes weaker, resulting in a softer symmetry energy. The magnitude of the softening depends on ξ : the larger ξ the smaller the softening.

Notice that the meson equations, i.e. Eqs. (7), (8) and (9), are also valid for the DDB and DDH models with the replacement $m_{i,\text{eff}} \rightarrow m_i$, since in the last two descriptions non-linear terms are not present.

B. Bayesian inference procedure

The model parameters are determined within a Bayesian inference procedure, i.e. applying Bayes' theorem [69], based on observed or experimental data, designated by fit data. The Bayesian parameter optimization system is determined from

four different inputs that must be given: the prior, the likelihood function, the fit data, and the sampler.

The Prior:- The prior domain in our Bayesian setup is determined from a Latin hypercube sampling, allowing the parameters of the underlying RMF model to vary so that a broad range of nuclear matter saturation properties is spanned. For each of the different RMP models considered a uniform prior is defined.

The Fit Data:- As fit data we have considered for the three RMF models (see Table I): the nuclear saturation density ρ_0 , the binding energy per nucleon ϵ_0 , the incompressibility coefficient K_0 , and the symmetry energy $J_{\text{sym},0}$, all evaluated at ρ_0 . We also include the pressure of pure neutron matter (PNM) at densities of 0.08, 0.12, and 0.16 fm⁻³ from N³LO calculations in chiral effective field theory (chEFT) [14], considering 2×N³LO data uncertainty. Finally, it is also required that the maximum NS mass is at least $2M_\odot$. This requirement is introduced in the likelihood with uniform probability.

The Log-Likelihood:- A log-likelihood function is optimized as a cost function for the fit data defined in Table I. It is defined by the equation below, Eq. 13, taking into account the uncertainties σ_j associated with each data point j ,

$$\text{Log}(\mathcal{L}) = -0.5 \times \sum_j \left\{ \left(\frac{d_j - m_j(\boldsymbol{\theta})}{\sigma_j} \right)^2 + \text{Log}(2\pi\sigma_j^2) \right\}. \quad (13)$$

The maximum NS mass is treated differently, using a step function probability.

To populate the multi-dimensional posterior, we employ the nested sampling algorithm [70], specifically the PyMultinest sampler [71, 72], which is well-suited for low-dimensional problems. The EoS data set for subsequent analyses will be generated using the full posterior, which contains 25287 EoS. The posterior obtained for the three data sets is given in Table VI, in Appendix A.

TABLE I. The constraints used as fit data in the Bayesian inference are: binding energy per nucleon ϵ_0 , incompressibility K_0 , symmetry energy $J_{\text{sym},0}$ at the nuclear saturation density ρ_0 , each with a 1σ uncertainty, the pressure of pure neutron matter (PNM) at densities of 0.08, 0.12, and 0.16 fm⁻³, obtained from a chEFT calculation [14], considering a 2×N³LO uncertainty for the PNM pressure and the maximum mass of neutron stars must exceed $2M_\odot$.

Quantity	Constraints		
		Value/Band	Ref
NMP [MeV]	ρ_0	0.153 ± 0.005	[58]
	ϵ_0	-16.1 ± 0.2	[73]
	K_0	230 ± 40	[74, 75]
	$J_{\text{sym},0}$	32.5 ± 1.8	[76]
PNM [MeV fm ⁻³]	$P(\rho)$	2×N ³ LO	[14]
	$dP/d\rho$	> 0	
NS mass [M_\odot]	M_{max}	> 2.0	[6]

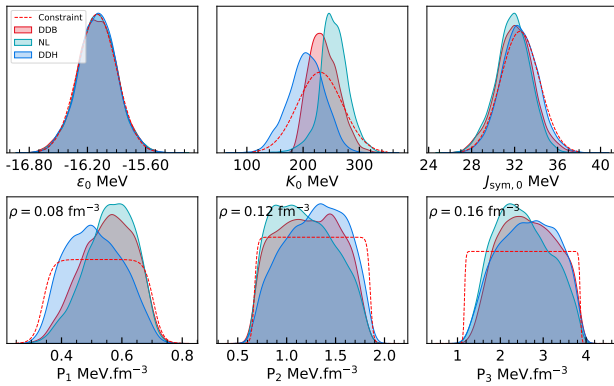


FIG. 1. Fit data considered to constrain all EOS data set built for the present study, both for nucleonic and for hyperonic matter.

III. RESULTS

In the following subsections, we compare the performance of the three different microscopic models used to generate the data sets within Bayesian inference calculations that consider as fit data the ones presented in Table I. Both NS and NMP will be compared. We will also discuss the effect of including hyperons, as well as the proton fraction and the onset of the nucleonic direct Urca processes. Finally, the behavior of the speed of sound and trace anomaly with the baryonic density will be discussed and the compatibility with pQCD constraints will be commented.

A. NL, DDB and DDH: a comparison

A comparison of the performance of the three frameworks concerning the reproduction of the fit data is summarized in Fig. 1. The chosen fit data were the same for the three frameworks and are given in Table I. All models reproduce the binding energy ϵ_0 and symmetry energy $J_{sym,0}$ at saturation in a similar way. The largest differences concern the incompressibility with DDH preferring smaller values and NL preferring larger ones. DDB peaks at the maximum of the fit data but with a much smaller width. Concerning the pure neutron matter (PNM) constraints the three frameworks satisfy the constraint imposed at the larger density in a similar way, but there are differences at the lowest and intermediate densities with DDH concentrating at lower pressure values for the lowest density. These behaviors will be reflected in the NMP and NS properties.

Having verified that the three frameworks reproduce the fit data, we analyze next the NMP at saturation. This is summarized in the corner plot shown in Fig. 2 and in Table II, where, considering the parabolic approximation for the energy of nuclear matter per particle with the isospin asymmetry $\delta = (\rho_p - \rho_n)/\rho$ at nuclear density ρ ,

$$\epsilon(\rho, \delta) \simeq \epsilon(\rho, 0) + S(\rho)\delta^2, \quad (14)$$

the parameters corresponding to the symmetric nuclear matter

energy per particle $\epsilon(\rho, 0)$ and the symmetry energy $S(\rho)$ expansion around saturation density till fourth order n are given by: (i) for the symmetric nuclear matter, the energy per nucleon $\epsilon_0 = \epsilon(\rho_0, 0)$ ($n = 0$), the incompressibility coefficient K_0 ($n = 2$), the skewness Q_0 ($n = 3$), and the kurtosis Z_0 ($n = 4$), respectively, defined by

$$X_0^{(n)} = 3^n \rho_0^n \left(\frac{\partial^n \epsilon(\rho, 0)}{\partial \rho^n} \right)_{\rho_0}, \quad n = 2, 3, 4; \quad (15)$$

(ii) for the symmetry energy, the symmetry energy at saturation $J_{sym,0}$ ($n = 0$),

$$J_{sym,0} = S(\rho_0) = \frac{1}{2} \left(\frac{\partial^2 \epsilon(\rho, \delta)}{\partial \delta^2} \right)_{\delta=0}, \quad (16)$$

the slope $L_{sym,0}$ ($n = 1$), the curvature $K_{sym,0}$ ($n = 2$), the skewness $Q_{sym,0}$ ($n = 3$), and the kurtosis $Z_{sym,0}$ ($n = 4$), respectively, defined as

$$X_{sym,0}^{(n)} = 3^n \rho_0^n \left(\frac{\partial^n S(\rho)}{\partial \rho^n} \right)_{\rho_0}, \quad n = 1, 2, 3, 4. \quad (17)$$

Some comments are in order: i) as discussed before the incompressibility of DDH models peaks at a lower values than the other two, which present a similar behavior, and spreads over a larger range of values; ii) concerning the skewness and kurtosis, which define the high density behavior of the EOS, DDH presents a very wide spread for the skewness from low negative to high positive values, and the kurtosis takes the largest values, to compensate the low incompressibility values it may take. This is necessary for the model to satisfy the $2M_\odot$ constraint imposed. Concerning the other two models, DDB presents the most restricted distribution which we can identify as a subset of the one NL defines, that is disjoint from the set defined by DDH for the kurtosis; it is interesting to verify that NL may take small and even negative values of the kurtosis; iv) concerning the symmetry energy the distribution presented by the three models for the symmetry energy and slope at saturation is similar. However, there are differences in the higher order parameters, in particular, $K_{sym,0}$ and $Z_{sym,0}$: the two models with density dependent coupling, DDH and DDB, behave in a similar way but NL spreads along a wider range of values and $K_{sym,0}$ may take positive values and $Z_{sym,0}$ takes very large negative values. The differences encountered are in part due to the fact that for DDH and DDB models the coupling of the ϱ -meson to the nucleons tends to zero at sufficiently large densities. Generalizing the parametrization of the ϱ -meson coupling will allow to go beyond this limitation. We will come back to this problem in one of the following sections.

NS properties, as the mass and radius, are determined from the integration of the Tolmann-Oppenheimer-Volkoff equations for spherical stars in statiscal equilibrium [78, 79], see [80] for a review. The tidal deformabilities Λ , quantities that are obtained from the detection of gravitational waves [81], are obtained integrating the equations obtained in [82].

The radius and tidal deformability for NS with a given mass have been calculated within the three frameworks and the results are plotted in Fig. 3, on the left side the radius-mass

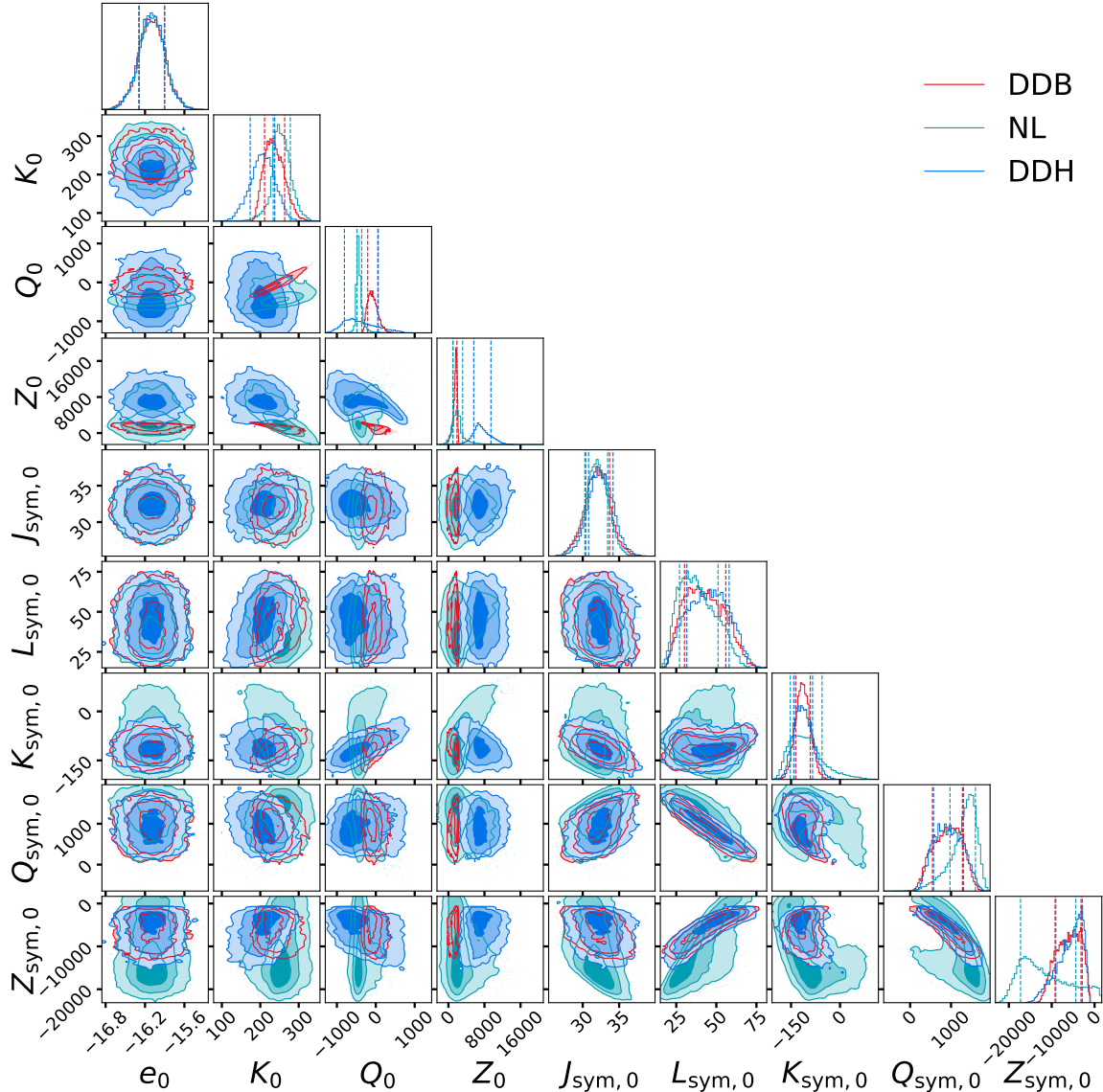


FIG. 2. Corner plot comparing the nuclear matter properties of the three nucleonic data sets DDB, NL and DDH, in particular, the symmetric nuclear matter properties at saturation density ρ_0 defined by Eq. (15): binding energy ϵ_0 , incompressibility K_0 , skewness Q_0 and kurtosis Z_0 ; the symmetry energy properties at saturation defined by Eq. (17): symmetry energy $J_{\text{sym},0}$, slope $L_{\text{sym},0}$, incompressibility $K_{\text{sym},0}$, skewness $Q_{\text{sym},0}$ and kurtosis $Z_{\text{sym},0}$.

and on the right side the tidal deformability-mass. Results of several observations, in particular, from the LIGO Virgo Collaboration for the GW170817 [83] and from NICER [8–11] for the pulsars PSR J0030+0451 and PSR J0740 + 6620, have been included. The three data sets show different properties which reflect the different NMP the different sets have as discussed before. The main conclusions that can be drawn are: i) NL data set is the most restricted for low mass stars presenting intermediate radii mostly between 12 and 13 km. DDH, the data set with smallest K_0 values, presents the smallest radii for low mass stars, $\sim 11.5 - 12.5$ km, while the DDB set predicts the largest radii, $\sim 12 - 13.5$ km. The density dependence of the EOS at high densities is strongly influenced by the non-linear terms in the NL data set and the function

that defines the density dependence of the meson couplings in the other two sets, DDB and DDH. DDH data set is soft at low densities so that low mass stars have a quite small radius, but at large densities becomes stiff to allow maximum mass stars with almost $2.5M_\odot$. The DDB data set allows for larger maximum masses than DDH, however, NL data set attains the largest masses, close to $2.75M_\odot$. All data sets agree with the presently available NS observations. In the right panel, the tidal deformabilities are plotted as a function of the mass for the three data sets. Their behavior follows the one obtained for the radii, with DDH having the smallest values and DDB the highest. Only some models of DDB are outside the 90% CI obtained from GW170817 value for a $1.36M_\odot$ star (see the blue horizontal bar).

TABLE II. Nuclear matter properties at saturation density, median values and 90% CI, of the three data sets, DDB, NL and DDH. Symmetric nuclear matter properties at saturation density ρ_0 defined by Eq. (15): binding energy ϵ_0 , incompressibility K_0 , skewness Q_0 and kurtosis Z_0 . Symmetry energy properties at saturation defined by Eq. (17): symmetry energy $J_{\text{sym},0}$, slope $L_{\text{sym},0}$, incompressibility $K_{\text{sym},0}$, skewness $Q_{\text{sym},0}$ and kurtosis $Z_{\text{sym},0}$.

Model		ρ_0	ϵ_0	K_0	Q_0	Z_0	$J_{\text{sym},0}$	$L_{\text{sym},0}$	$K_{\text{sym},0}$	$Q_{\text{sym},0}$	$Z_{\text{sym},0}$	
		fm^{-3}					MeV					
DDB	median	0.152	-16.10	235	-90	1585	32.05	42	-114	935	-5941	
	90 % CI	min	0.142	-16.43	199	-262	486	29.15	25	-149	364	-10751
		max	0.164	-15.76	282	162	2043	34.81	63	-76	1434	-2128
NL	median	0.152	-16.10	254	-440	1952	31.89	37	-109	1367	-12613	
	90 % CI	min	0.145	-16.43	213	-516	243	29.08	23	-171	629	-19118
		max	0.160	-15.77	297	-247	5295	34.41	58	-3	1710	-394
DDH	median	0.156	-16.10	206	-460	7189	32.44	45	-114	930	-5215	
	90 % CI	min	0.144	-16.43	150	-978	4459	29.68	25	-157	412	-11529
		max	0.167	-15.78	257	395	10908	35.24	65	-64	1491	-2078

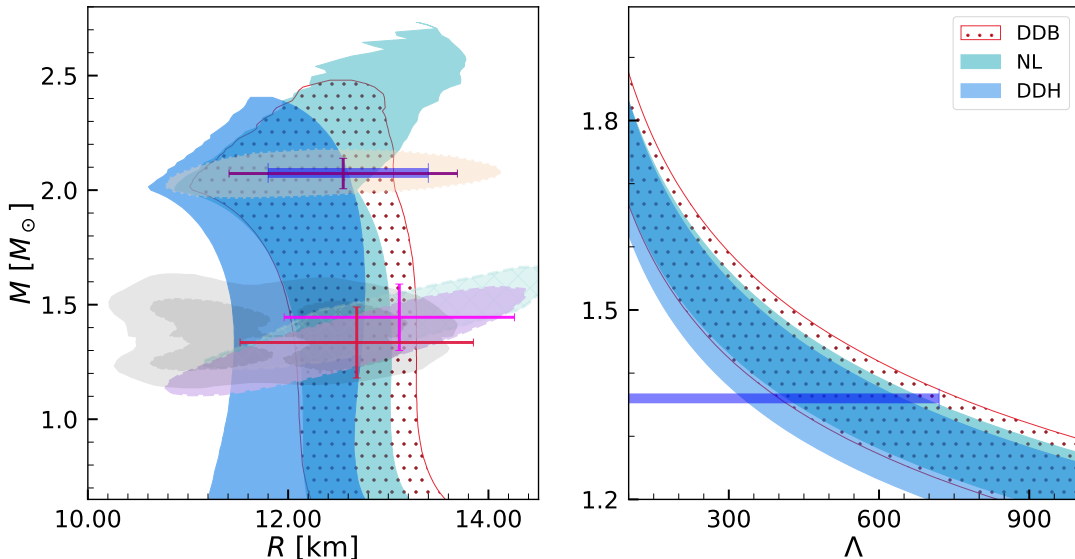


FIG. 3. NS mass-radius (left) and tidal deformability-mass regions obtained from the 90% CI for the conditional probabilities $P(R|M)$ and $P(\Lambda|M)$ for DDB (dotted red), DDH (blue) and NL (green) frameworks. The blue horizontal bar on the left panel indicates the 90% CI radius for the pulsar PSR J0740+6620 with $M = 2.08M_\odot$ obtained combining observational data from GW170817 and NICER as well as nuclear saturation properties [11]. The gray shaded regions indicate the 90% (solid) and 50% (dashed) CI of the LIGO/Virgo analysis for high mass (top) and low mass (bottom) components of the NS binary that originated the GW170817 event [77]. The NICER 1 σ (68%) credible zone of the 2-D mass-radii posterior distribution for the PSR J0030+0451 (lilac and light green) [8, 9], and the PSR J0740 + 6620 (light orange) [10, 11] are also included. The horizontal (radius) and vertical (mass) error bars reflect the 1 σ credible interval derived for NICER data's 1-D marginalized posterior distribution.

The corner plot shown in Fig. 4 involving some NS properties allows some interesting conclusions: i) there is some correlation between the radius and the star maximum mass; ii) the central speed of sound squared of the maximum mass star is clearly model dependent: for DDH model, $c_s^2 \sim 0.7 - 0.8$ is practically constant and quite high, while for the other two models c_s^2 can be as low as 0.45 or even lower and as high as 0.75; iii) it is precisely DDH with the largest speed of sound that predicts

the smallest radii for $1.4M_\odot$ stars.

B. Including hyperons

In the inner core of a NS, non-nucleonic degrees of freedom may set in. In the present section we will discuss the onset of hyperons. As in [54], we will introduce only two hyperons, the neutral Λ -hyperon and the negatively charged

TABLE III. The Neutron star properties, median values and 90% CI, of the three nucleon data sets, DDB, NL and DDH. The following properties are given: the maximum mass M_{\max} and respective baryon mass $M_{B,\max}$, radius R_{\max} , speed of the sound squared at the center c_s^2 and central baryonic density ρ_c , and the radius and tidal deformability of the $1.4M_\odot$ star, $R_{1.4}$ and $\Lambda_{1.4}$.

Model	M_{\max}	$M_{B,\max}$	R_{\max}	$R_{1.4}$	$\Lambda_{1.4}$	C_s^2	ρ_c
	M_\odot		km	...	c^2	fm^{-3}	
median	2.148	2.567	11.13	12.66	466	0.649	1.002
DDB	min	2.022	2.396	10.54	12.04	334	0.520 0.865
	max	2.366	2.857	11.85	13.28	648	0.718 1.121
median	2.062	2.446	10.92	12.44	423	0.576	1.051
NL	min	2.006	2.370	10.52	12.08	347	0.446 0.904
	max	2.260	2.715	11.70	13.03	582	0.685 1.127
median	2.242	2.712	10.97	12.21	423	0.750	0.986
DDH	min	2.037	2.439	10.15	11.46	273	0.727 0.887
	max	2.380	2.898	11.52	12.75	546	0.763 1.170

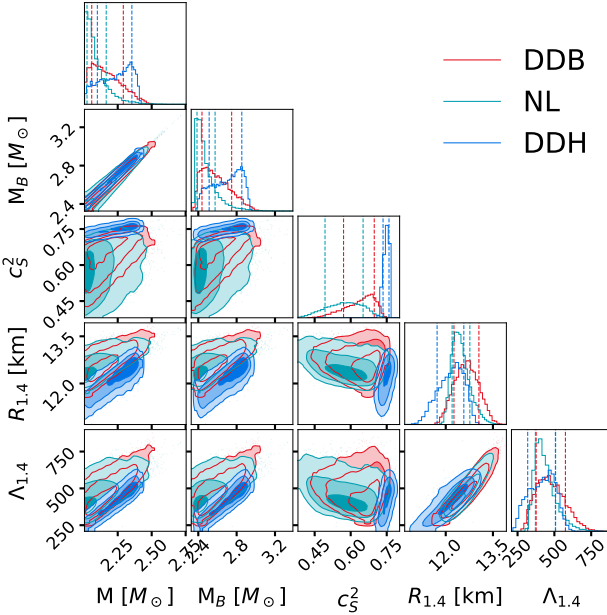


FIG. 4. Corner plot comparing the following NS properties obtained with the three data sets, DDB, NL and DDH: maximum gravitational mass M , maximum baryonic mass M_B and respective central speed of sound squared c_s^2 , radius R and tidal deformability Λ of a $1.4M_\odot$ star.

Ξ^- -hyperon. These two hyperons are the ones that appear in the largest fractions, either because of having the smallest hyperon mass as the Λ , or because of being negatively charged (the Ξ^-), and, therefore, favorably replace the electrons and reduce the total pressure of the system. Both hyperons have an attractive potential in symmetric nuclear matter, and form hypernuclei. The binding energy of hyperons in hypernuclei has been used to fit the couplings of the hyperons to mesons

in the RMF description of hadronic matter [84, 85]. Although the mass of the Σ^- -hyperon is smaller than the one of Ξ^- , it interacts repulsively with nuclear matter, as the non-existence of Σ -hypernuclei seems to show [86]. As a consequence, in NS matter its onset occurs at larger densities than the Ξ^- onset [87–90].

The introduction of hyperons requires a generalization of the Dirac term of Eq. (6) to include Λ and Ξ^- besides protons and neutrons,

$$\mathcal{L}_D = \sum_{j=p,n,\Lambda,\Xi^-} \bar{\Psi}_j \left[\gamma^\mu \left(i\partial_\mu - \Gamma_{\omega,j} A_\mu^{(\omega)} - \Gamma_{\varrho,j} \mathbf{t}_j \cdot \mathbf{A}_\mu^{(\varrho)} \right) - (m - \Gamma_{\sigma,j} \phi) \right] \Psi \quad (18)$$

For the couplings of the hyperons to the vector-mesons we consider the SU(6) values for the vector isoscalar mesons, $g_{\omega\Xi} = \frac{1}{3}g_{\omega N} = \frac{1}{2}g_{\omega\Lambda}$ and $g_{\phi\Xi} = 2g_{\phi\Lambda} = -\frac{2\sqrt{2}}{3}g_{\omega N}$ and for the isovector ϱ -meson, $g_{\varrho\Xi} = g_{\varrho N}$. In this last case the hyperon isospin also defines the strength of the coupling. Having assumed these values for the couplings of the hyperons to the vector mesons, the coupling to the σ -meson is fitted to hypernuclei properties [84, 85, 91]. In general, we express the couplings to the mesons as a fraction of the nucleon couplings, $g_{m,i} = x_{m,i} g_\sigma$ with $m = \sigma, \omega, \varrho$ and $i = \Lambda$ and Ξ^- . Considering the results of the fits done in [84, 85, 91], values between 0.609 and 0.622 were determined for the fraction $x_{\sigma\Lambda}$, and will be adopted in the present study. For the fraction $x_{\sigma\Xi^-}$, the range 0.309 to 0.321 will be used, as determined from fits to the binding energy of Ξ^- in the hypernuclei $^{15}_{\Xi^-}\text{C}$ and $^{12}_{\Xi^-}\text{Be}$ [89].

We have performed calculations for hyperonic stars within two models, DDB and NL, imposing the same fit data that was considered to constrain the EOS data sets of nucleon matter, and which is summarized in Table 1. Chemical equilibrium dictates that:

$$\mu_\Lambda = \sqrt{(m_\Lambda^*)^2 + k_{F\Lambda}^2} + x_{\omega\Lambda} g_\omega \omega = \mu_n \quad (19)$$

$$\mu_{\Xi^-} = \sqrt{(m_{\Xi^-}^*)^2 + k_{F\Xi^-}^2} + x_{\omega\Xi^-} g_\omega \omega - \frac{1}{2}g_\varrho \varrho = \mu_n + \mu_e, \quad (20)$$

where m_i^* is the effective mass of hyperon i and k_{Fi} its Fermi momentum. Charge neutrality imposes that $\rho_p = \rho_{\Xi^-} + \rho_e + \rho_\mu$.

In Fig. 5, predictions obtained for the NS radius (left) and tidal deformability (right) for different NS masses are plotted. In Table IV, the median and the 90% CI nuclear matter properties of both data sets are summarized and in Table III B some NS properties are given, in particular, the median and the 90%CI of the maximum mass, respective, baryonic mass, radius, central speed of sound squared and central baryonic density, together with the radius and tidal deformability of a $1.4M_\odot$ star.

We first discuss the effect on the nuclear matter properties of including hyperons, comparing results of Tables II and IV. Isovector properties are essentially not affected for the DDB data set, and only slightly for the NL data set reflected in a small increase of the different properties. Isoscalar properties

TABLE IV. Nuclear matter properties at saturation density, median values and 90% CI, of the two data sets including hyperons, DDB-hyp and NL-hyp. Symmetric nuclear matter properties at saturation density ρ_0 defined by Eq. (15): binding energy ϵ_0 , incompressibility K_0 , skewness Q_0 and kurtosis Z_0 . Symmetry energy properties at saturation defined by Eq. (17): symmetry energy $J_{\text{sym},0}$, slope $L_{\text{sym},0}$, incompressibility $K_{\text{sym},0}$, skewness $Q_{\text{sym},0}$ and kurtosis $Z_{\text{sym},0}$.

Model		ρ_0	ϵ_0	K_0	Q_0	Z_0	$J_{\text{sym},0}$	$L_{\text{sym},0}$	$K_{\text{sym},0}$	$Q_{\text{sym},0}$	$Z_{\text{sym},0}$	
		fm^{-3}					MeV					
DDB-hyp	median	0.152	-16.09	272	130	1425	32.15	43	-98	966	-6713	
	90% CI	min	0.147	-16.39	247	-16	803	29.48	26	-127	354	-12178
		max	0.157	-15.79	309	349	1680	34.83	65	-59	1453	-2723
NL-hyp	median	0.150	-16.09	296	-117	2105	31.85	42	-70	1312	-13592	
	90% CI	min	0.144	-16.41	270	-246	-405	29.16	31	-127	895	-18989
		max	0.157	-15.76	341	104	3078	34.44	57	-12	1607	-3893

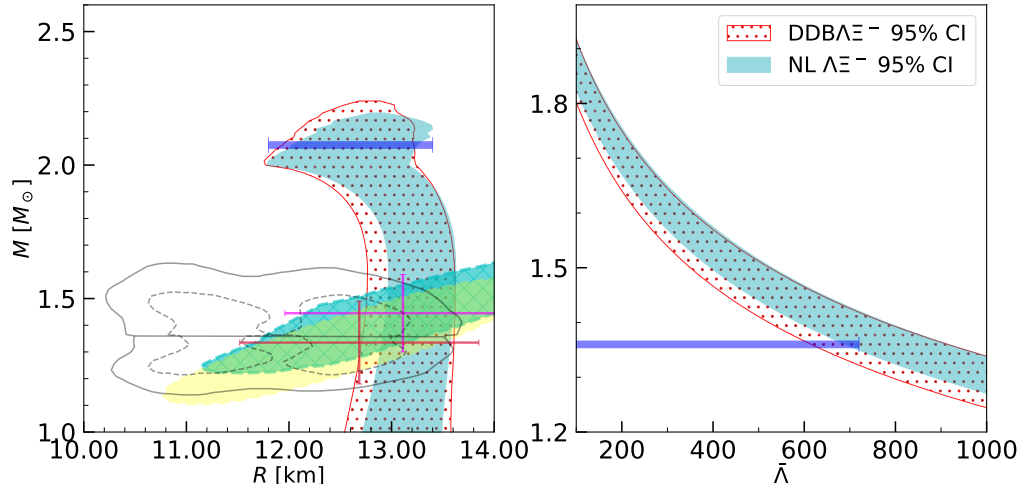


FIG. 5. The 90% CI region for the hyperon data sets DDB-hyp (dotted red) and NL-hyp (green) derived using the conditional probabilities $P(R|M)$ (left) and $P(\Lambda|M)$ (right). The lines in the left panel indicate the 90% (solid) and 50% (dashed) CI for the binary components of the GW170817 event [77]. Also shown is the 1σ (68%) credible 2-D posterior distribution in the mass-radius domain from the millisecond pulsar PSR J0030+0451 (cyan and yellow) [8, 9] obtained from the NICER x-ray data. The horizontal (radius) and vertical (mass) error red bars reflect the 1σ credible interval derived for the same NICER data's 1-D marginalized posterior distribution. The blue bars represent the radius of the PSR J0740+6620 at $2.08 M_\odot$ (left panel) and the tidal deformability at $1.36 M_\odot$ (right panel) [83].

are the mostly affected: the incompressibility K_0 suffers an increase of 15%-20%, and the median skewness becomes positive. The reason for this change is the fact that the presence of the onset of hyperons relieves the pressure inside the NS and the condition that $2M_\odot$ stars must be described obliges the EOS to be harder, mainly affecting the isoscalar channel of the EOS.

The implication of the hardening of the EOS is that larger NS radii are predicted (compare Fig. 5 left with 3 left). The median values of the radius of $1.4 M_\odot$ stars reflect clearly this effect: they increase from 12.66 (12.44) km for DDB (NL) to 14.22 (13.11) km, i.e. more than ~ 0.5 km or $\sim 5\%$. Measurements of the NS radius with an uncertainty smaller than 5%, such as the ones programmed with eXTP [64] and STROBE-X [65], could distinguish between these two scenarios. Also the tidal deformability is strongly affected increasing its median value from 466 (423) to 650 (610), respectively,

for DDB (NL), and the constraint imposed by GW170817 is essentially not satisfied (see Fig. 5 middle panel). Another important property that distinguishes both scenarios is the NS maximum mass that decreases from a maximum value at 90% CI of 2.37 (2.26) M_\odot for DDB (NL) to 2.08 (2.13) M_\odot . Concerning the NS properties in the center of the star it is pointed out the decrease of the speed of sound, its square decreasing essentially to values of the order of 0.5 or below in the presence of hyperons, when it takes values of the order of 0.6 going up to ~ 0.7 if only nucleon matter is considered. In Sec. III D the speed of sound in matter with hyperons will be compared with the one obtained with nucleonic models.

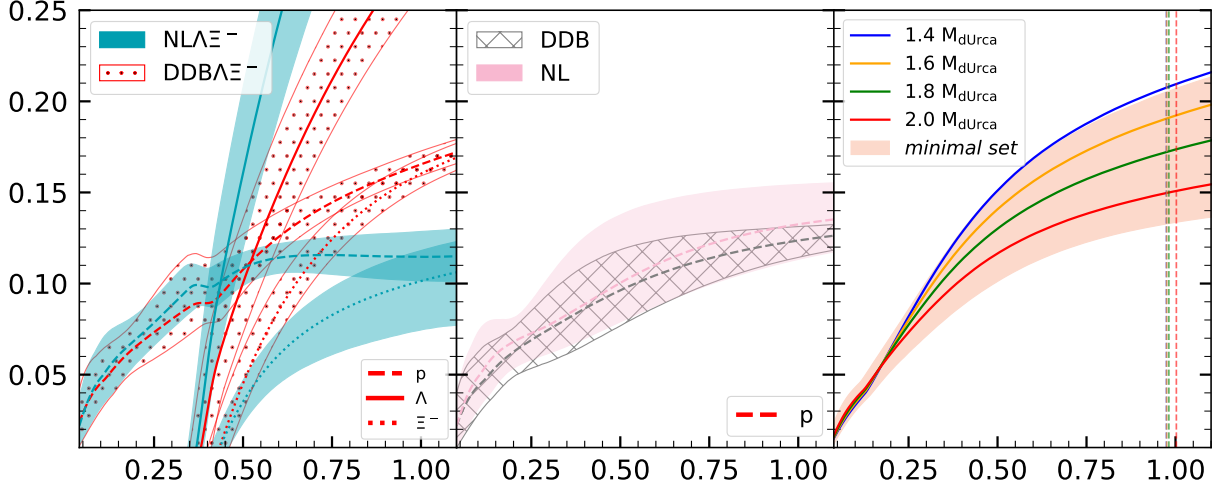


FIG. 6. Proton and hyperons fractions for data sets DDB-hyp (red dotted) and NL-hyp (blue) (left panel), proton fractions for the data sets DDB (slashed region) and NL (pink region) (middle panel), proton fraction defining the minimal set compatible with chEFT PNM calculations at 2σ obtained varying the parameter y introduced in Eq. (21) (pink region), or fixing y to a given M_{dUrca} , i.e. 1.4, 1.6, 1.8, 2.0 M_\odot (full lines).

TABLE V. NS properties, the median and the 90% CI, of the data sets with hyperons, DDB-hyp and NL-hyp. The following properties are given: the maximum mass M_{\max} and respective baryonic mass $M_{B,\max}$, radius R_{\max} , speed of the sound squared at the center c_s^2 and central baryonic density ρ_c , and the radius and tidal deformability of the $1.4M_\odot$ star, $R_{1.4}$ and $\Lambda_{1.4}$.

Model	M_{\max}	$M_{B,\max}$	R_{\max}	$R_{1.4}$	$\Lambda_{1.4}$	C_s^2	ρ_c		
	M_\odot		km	...	c^2	fm^{-3}			
median	2.024	2.357	11.82	13.22	659	0.47	0.920		
NL-hyp	90 % CI	min	2.003	2.329	11.55	12.97	595		
		max	2.083	2.433	12.20	13.52	758		
					0.41	0.860	0.968		
NL-hyp	median	2.040	2.385	11.73	13.11	610	0.48	0.932	
	90 % CI	min	1.992	2.322	11.48	12.76	526	0.44	0.871
		max	2.130	2.501	12.08	13.51	743	0.50	0.964

C. Onset of direct Urca

In this subsection the dependence on the baryon density of the proton fraction of β -equilibrium matter will be discussed. We consider two of the microscopic models discussed in Sec. III A, DDB and NL. Within the same models, the onset of hyperons and its influence on the proton fraction will also be commented using the data sets described in the previous section, Sec. III B.

The ϱ -meson coupling to the nucleon in DDB and DDH data sets decreases exponentially with the density. At high densities it approaches zero, and, as a consequence, these models allow for very asymmetric matter at high densities since the symmetry energy is low. Therefore, the opening of nucleon direct Urca processes [92, 93] does not occur inside NS [89, 94, 95]. This is clearly seen from the middle panel in Fig. 6, where the median and 90% CI bands of the pro-

ton fraction are plotted as a function of the baryonic density for the data sets DDB (slashed band) and for NL (pink band): at large densities the proton fraction for DDB is smaller and narrower than the NL proton fraction. The smaller width is also an indication that the g_ϱ coupling of all models tends to the same value, zero, at high densities. NL models, however, span a wider range of proton fractions, and in particular, the opening of direct Urca processes may occur in some models.

In the left panel of the same figure the fraction of protons is plotted together with the Λ and Ξ^- hyperon fractions for matter including hyperons. The Λ -hyperon is the first hyperon to set in just above twice saturation density, while the Ξ^- sets in just below $3 \rho_0$. The onset of the Λ -hyperon implies a decrease of the neutron fraction, decreasing the pressure caused by this species and, therefore, the system energy. As a consequence the proton fraction also decreases (see discussion in [53]). As soon as the Ξ^- -hyperon sets in the proton fraction suffers an increase to compensate for the negatively charged hyperon. This behavior is well illustrated in the left panel of 6. The effect is much stronger for the DDB-hyp data set because the ϱ -meson coupling is weaker and, therefore, the repulsive term that enters the Ξ chemical potential is weaker, see Eq. (20). The coupling g_ϱ (Γ_ϱ) varies at 90% CI within the range [9.55, 14.60] ([6.97, 8.78]) for NL (DDB) at saturation density. Including hyperons in the model these values change only slightly to [9.79, 14.31] for NL-hyp and [7.13, 8.58] for DDB-hyp at saturation density.

It was shown in Sec. III A, in particular, with the corner plot 2, that while DDB and DDH data sets differ a lot when comparing the symmetric nuclear matter properties, the symmetry energy properties are very similar considering all orders of the Taylor expansion studied. In order to overcome the special feature of these models of not allowing for nucleon direct Urca processes, in [52] a generalization of the ϱ -meson coupling was proposed including a new parameter y . For the

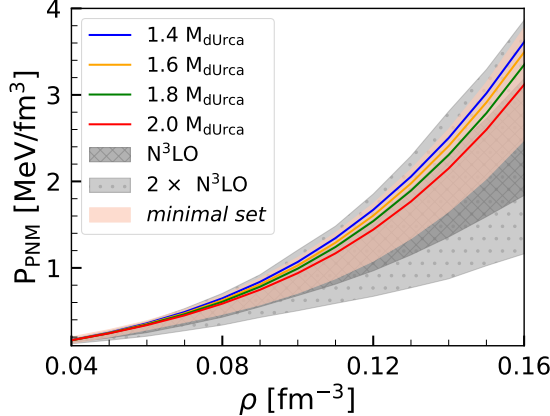


FIG. 7. Pure neutron matter pressure as a function of the baryon density for the DDB model using Eq. (21) to define the ϱ -meson coupling: the minimal set compatible with chEFT PNM calculations at 2σ obtained varying the parameter y (pink region), or fixing y to a given $M_{d\text{Urca}}$, i.e. $1.4, 1.6, 1.8, 2.0 M_{\odot}$ (full lines). The dark (light) gray bands define the chEFT pressure at $1\sigma(2\sigma)$ from [14].

function $h_{\varrho}(x)$ that defines the density dependence of the coupling Γ_{ϱ} , see Eq. (21), we consider

$$h_{\varrho}(x) = y \exp[-a_{\varrho}(x-1)] + (y-1), \quad 0 < y \leq 1. \quad (21)$$

Allowing y , imposing the constraints defined in Table I, we have generated the PNM pink band in Fig. 7. In the same figure, the chEFT PNM EOS from [14] is also included considering 1σ (dark gray) and 2σ (light gray), as well as the PNM EOS imposing that $M_{d\text{Urca}}$ is $1.4, 1.6, 1.8$ and $2.0 M_{\odot}$, where we designate by $M_{d\text{Urca}}$, the mass of the star where nucleon direct Urca processes set in its center. In fact, the new parameter y must be determined from NS properties that are sensitive to the high density behavior of the symmetry energy, such as the proton fraction. In particular, the onset of nucleon direct Urca (dUrca) processes are an appropriate observation and were used in [52] to constraint y . In Fig. 6 right panel, we show the proton fraction (full lines) corresponding to different $M_{d\text{Urca}}$. This was possible by choosing the adequate y . The pink region spans the proton fraction compatible with PNM chEFT calculation at 2σ , already defined in Fig. 7.

These constraints derived from pure neutron matter exclude dUrca processes from stars with a mass $\lesssim 1.4 M_{\odot}$ at 2σ . If we restrict ourselves to 1σ , $M_{d\text{Urca}}$ rises to a value above $1.6 M_{\odot}$. These results are in agreement with the analysis performed in [96], where it is concluded that NS cooling curves seem to indicate that $M_{d\text{Urca}} \sim 1.6 - 1.8 M_{\odot}$.

D. Speed of sound, trace anomaly, and pQCD constraints

Lately, some discussion has been concentrated on the behavior of the speed of sound with density. This quantity, which is directly related to the dependence of the pressure on the energy density, is sensitive to the onset of new degrees of freedom and first-order phase transitions. In particular, at

high densities, it is expected that matter is deconfined and exhibits conformal symmetry with the square of the speed of sound being equal to $1/3$. One of the present great interests is to identify possible signatures of the presence of deconfined quark matter inside NS.

The general behavior of the speed of sound squared obtained from agnostic descriptions of the EOS of baryonic matter, that has been constrained by low-density pure neutron matter *ab-initio* calculations [14–16] and the pQCD EOS at densities of the order $\gtrsim 40\rho_0$, and by NS observations, includes a steep increase until an energy density of the order of ~ 500 MeV/fm is attained, followed by a decrease or flattening, approaching $1/3$ at high densities [19, 37–39, 51, 97], see also the discussion in [98].

In Fig. 8, the top panels of the three columns show the behavior of the speed of sound squared for the three data sets DDB, NL and DDH, in particular, the 68% and 95% CI are shown. The different sets present a different behavior: for set DDH c_s^2 increases monotonically with a small dispersion, and attains values close to 0.8 for densities of the order of 1 fm^{-3} ; set NL is on the other extreme, and above $\rho \sim 0.3 \text{ fm}^{-3}$ shows a quite large dispersion including a flattening or slight decrease, never attaining values above 0.7 and presenting values that can go below 0.4 ; DDB shows an intermediate behavior, not so extreme as DDH, but also showing a monotonic increase.

The NL data set contains EOS with quite different behaviors at high densities, controlled by the ω^4 term. In the left panel of Fig. 9, the speed of sound squared is plotted for different ranges of the parameter ξ , for set 1 $\xi \in [0.0, 0.004]$, for set 2 $\xi \in [0.004, 0.015]$ and for set 3 $\xi \in [0.014, 0.04]$. This parameter controls the contribution of the ω^4 term in the Lagrangian density, and as discussed in [55, 66], in the high density limit it makes the speed of sound squared go to $1/3$. This indicates that a quite large range of values of the speed of sound squared are possible considering just nuclear degrees of freedom. In the middle panel, c_s^2 for the NL-hyp set has also been included. This set presents a peak above $2\rho_0$, when the hyperons set in, followed by a monotonous increase of the speed of sound, attaining values $c_s^2 \lesssim 0.6$ at 1 fm^{-3} .

Several quantities have been proposed as indicators of the presence of deconfined matter, including the polytropic index $\gamma = d\ln P/d\ln e$ [37], which takes the value 1 in conformal matter, the trace anomaly scaled by the energy density introduced in [50] $\Delta = 1/3 - P/\epsilon$ which should approach zero in the conformal limit, and the derived quantity proposed in [51] $d_c = \sqrt{\Delta^2 + \Delta'^2}$, where $\Delta' = c_s^2 (1/\gamma - 1)$ is the logarithmic derivative of Δ with respect to the energy density, which approaches zero in the conformal limit. In the following, we will discuss how these quantities behave when we consider the different EOS data sets introduced in the present study. This will allow to identify properties that are still present in hadronic matter from properties that totally characterize deconfined matter.

In middle and bottom lines of Fig. 8, the polytropic index γ and the trace anomaly Δ are plotted as a function of the baryonic density in units of the saturation density. The horizontal line in the γ panels identifies the value 1.75 that has

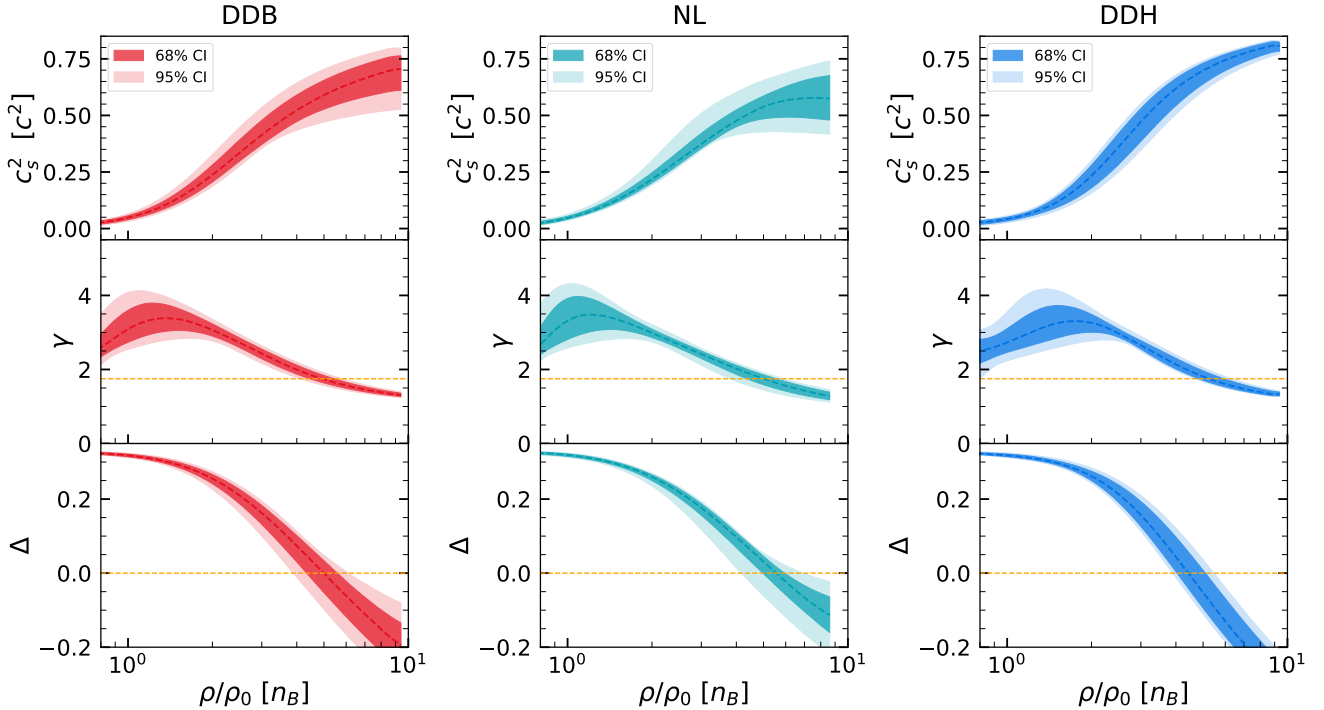


FIG. 8. The speed of sound squared c_s^2 , the polytropic index $\gamma = d\ln P/d\ln e$ and the trace anomaly $\Delta = 1/3 - P/\epsilon$ for the three data sets, DDB, NL and DDH. The horizontal lines in the γ plots identifies the value 1.75.

been proposed as indicating the transition to deconfined quark matter [37]. For all models the polytropic index γ increases until $\sim \rho_0$, followed by a monotonous decrease that goes below 1.75 at a density above $\sim 0.4 \text{ fm}^{-3}$. The behavior of the three sets is quite consistent and it seems to indicate that a value of $\gamma < 1.75$ is not enough to identify a phase transition to deconfined matter. The normalized trace anomaly shows a behavior similar to the one discussed in [50], where results from several studies [12, 19, 99, 100] have been compared, and it crosses the zero axis at densities of the order of $0.4\text{--}0.8 \text{ fm}^{-3}$, becoming afterwards negative. At sufficiently high densities this quantity should tend to the pQCD values that are slightly positive. Considering the models studied, for the NL data set (and even DDB) Δ shows a change of slope around 1 fm^{-3} , which could match a positive trace anomaly in finite density QCD.

We have added to Fig. 9 the right panel where the effective nucleon mass is plotted as a function of the baryon density. It is seen that the mass decreases quite fast with density and at $\sim 1 \text{ fm}^{-3}$ the effective masses are below 300 MeV, and may even reach $\sim 100 \text{ MeV}$ for some NL samples. This corresponds to an approximate chiral symmetry restoration and could be the explanation for a behavior similar to the one expected for deconfined matter.

We complete this discussion with Fig. 10, where the ratio of the pressure to the free particle pressure p/p_{free} is plotted as a function of the baryon chemical potential and the quantity d_c defined in [51] as a function of the baryon density. For all sets the ratio p/p_{free} saturates and even decreases for chemical potentials greater than 1300 MeV, after attaining a value

of the order of 0.3. Although the dispersion is quite large, this ratio takes values approximately 0.1 smaller than the ones obtained in [51]. In [51], it is proposed that $d_c < 0.2$ could identify the presence of deconfined matter. In fact, d_c never goes below 0.2 for DDH, and for DDB the median stays above 0.2 although values below 0.2 are compatible with the 95% CI. For the NL data set, the median of d_c may take values below 0.2 for densities above 1 fm^{-3} , and it will be interesting to understand the reason of this behavior.

As already referred before, several studies based in an agnostic description of the EOS constrain the generated EOS imposing at high densities the pQCD EOS. The baryon density for which pQCD EOS is defined, $\gtrsim 40\rho_0$, is outside the range of densities where the RMF models defined in Sec. II A are valid. Using thermodynamic relations and causality [101] showed that pQCD EOS impose constraints at densities existing in the interior of NS, in particular, for densities $\gtrsim 2.2\rho_0$. In the following, we study how these constraints affect our different data sets. In order to build the geometric construction proposed in [101], we consider the same constraints these authors chose although other choice could have been done, in particular, at low densities, since our EOS may be considered well constrained until $2\rho_0$, the density above which non-nucleon degrees of freedom may set in. Note also that the pQCD constraints depend on the renormalization scale [18]: we show results in Fig. 11 for the scale imposing the strongest constraints, $X = 4$, [55]. The analysis was performed for sets NL, NL-hyp, NL restricted to $\xi \in [0.015 : 0.04]$ (labelled as set 3) and DDB and the following conclusions may be drawn: a) the constraints are satisfied for $\xi > 0.015$, i.e.

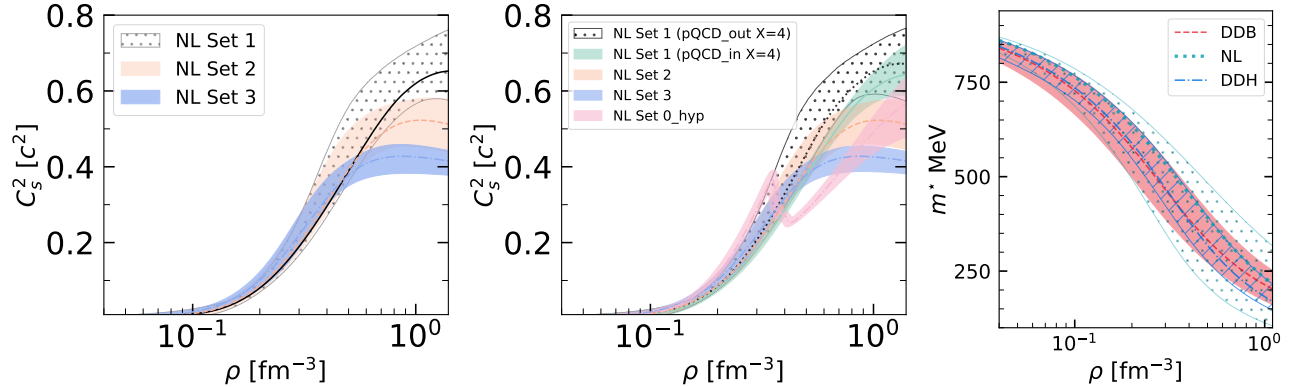


FIG. 9. The figure displays the median and 95% credible interval of the square of sound velocity (c_s^2) for the NL model (left and middle panels) and the effective mass (right) for DDB, NL, and DDH models as a function of baryon density. The left panel highlights three distinct intervals of the parameter ξ : NL Set 1, NL Set 2, and NL Set 3. In the plot, NL Set 1 is represented by a black dotted region and corresponds to ξ values within the interval $[0, 0.004]$. NL Set 2 is represented by an orange region and encompasses ξ values within the range $[0.004, 0.015]$. NL Set 3 is depicted in blue and represents ξ values within the interval $[0.015, 0.04]$. Each set of EOS contains a comparable number of samples, approximately 18,000 samples, providing a robust statistical basis for the displayed results. In the middle panel, Set 1 was divided into two parts: green (black dotted) EoS that satisfy (do not satisfy) pQCD constraints with $X=4$. In this panel the c_s^2 for the NL-hyp set is also shown (pink band). The right panel was obtained with the data sets presented in Sec. III A, which contain $\sim 15,000$ to $17,000$ samples.

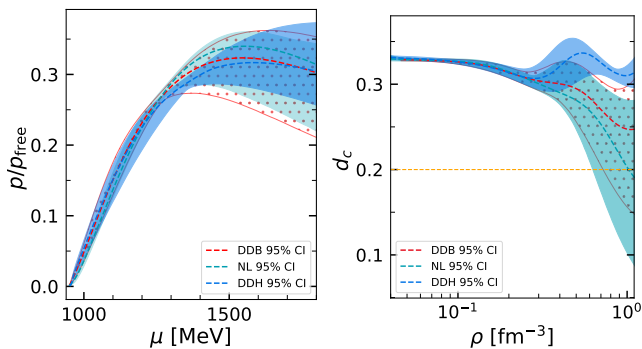


FIG. 10. The figure illustrates the pressure normalized by the free pressure with respect to the baryon chemical potential μ , and the relationship between d_c and ρ for three data sets: DDB, NL, and DDH, arranged from left to right. The median values are represented by lines, while the 95% confidence interval regions are depicted as shaded bands.

set 3; b) only a few EOS from the set NL-hyp do not satisfy the constraints at $8n_s$. Notice, however, that at 90% CI the largest density in the center of NS within this set is $\sim 6n_s$, and, therefore all hyperonic stars are compatible with pQCD. In [55], it was shown that for smaller QCD renormalization scales the total set satisfies the pQCD constraints up to $8n_s$; c) several EOS from the set NL do not satisfy the pQCD constraints at densities $\sim 8n_s$ or even $\sim 5n_s$. These models have $\xi < 0.004$, and the highest maximum masses. If these EOS are removed from the NL set, the absolute maximum mass drops from $\sim 2.75M_\odot$ to $\sim 2.5M_\odot$ for models that satisfy pQCD with $X = 1$, and to $\sim 2.15M_\odot$ if $X = 4$. In the middle panel of Fig. 9, the speed of sound squared for the NL EOS with $\xi < 0.004$, has been divided in two subsets, according to their capacity to satisfying (green band) or

not (black dotted band) the pQCD constraints. The EOS that satisfy these constraints present smaller values of c_s^2 at high densities. The bottom line of Fig. 11, we also show results for the DDB set, again taking the most constraining QCD scale: some EOS do not satisfy the $8n_s$ constraints, but at 90% CI no star with a central density above $7n_s$ was obtained.

IV. CONCLUSIONS

It was an objective of the present work to analyze in a critical way the capacity that RMF models have to describe hadronic matter, and the overall implications when they are used to extract nuclear matter properties from NS observations. As RMF models, we have considered two of the main frameworks frequently used, RMF models including non-linear mesonic terms with constant coupling parameters, designated as NL [55, 56, 66, 67, 102], and models with coupling parameters with an explicit dependence on the density, which do not include mesonic terms beyond quadratic terms [54, 58, 59, 103]. Other relativistic mean-field approaches have been left out, such as the chiral invariant nuclear model discussed in [104] and developed later in [105–108], or the inclusion of the isovector scalar meson as studied in [109]. They will be considered in a future work.

A set of fit-data has been imposed, constituted by some nuclear matter properties, the pure neutron matter pressure obtained within a chEFT, and a maximum star mass above $2M_\odot$. A Bayesian inference formalism was applied to determine the coupling parameters probability distribution, and from these the NMP and NS properties were calculated. We have shown the the mass-radius domain spanned by the posterior of the three data sets are not totally coincident, with the DDH framework predicting smaller radii, DDB larger radii and the NL larger maximum masses, all at 90% confidence intervals.

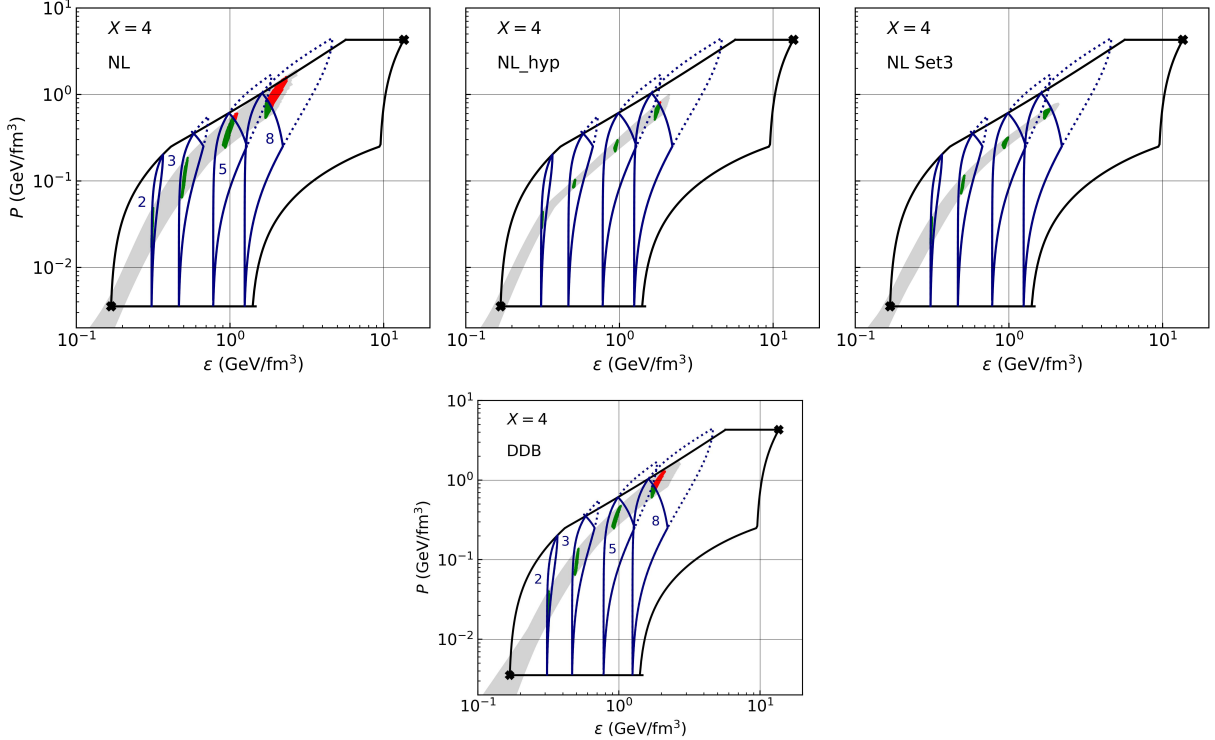


FIG. 11. The pressure versus the energy density is shown for NL, NL-hyp and NL restricted to $\xi \in [0.015 : 0.04]$ (set 3) (top line, from left to right) and DDB (bottom line). The constraints from Ref. [101] that ensure stability, causality, and thermodynamic consistency delimit the region inside the black solid line. The application of the constraints specifically to some baryon number densities, $n = 2, 3, 5$, and $8 n_s$, defines the regions enclosed by the solid (dotted) blue lines that satisfy (do not satisfy) the pQCD constraints, respectively, from left to right (where $n_s = 0.16 \text{ fm}^{-3}$). Results for the most constraining renormalization scale parameter, $X = 4$, [17] are given. The green and red dots represent, respectively, the models in our sets that satisfy and do not satisfy pQCD constraints. Notice that the central density of the maximum mass stars is $\rho_c \lesssim 7 n_s$.

The inclusion of hyperons in these models was also discussed. It was shown that hyperons do not exclude $2M_\odot$ stars, although maximum masses are much smaller than the ones attained with nucleonic models. However, the radius of canonical stars are larger if hyperonic degrees of freedom are introduced. This is due to the fact that in order to attain a $2M_\odot$ mass, and since the onset of hyperons softens de EOS, the nuclear matter parameters describing the symmetric nuclear matter EOS have to be larger. This confirms similar conclusions drawn in [53, 110].

The behavior of the proton fraction with density inside NS was also discussed. It was shown that the frameworks DDH and DDB have too small high density couplings to the ϱ -meson and as a consequence no nucleonic direct Urca processes are predicted inside NS, as already discussed in [52, 89, 94]. This limitation of the models with density dependent couplings was overcome with a generalization of the ϱ -meson coupling. The new parameter introduced may be constrained by observations on the cooling of NS. In fact, in [52] it was shown that above three times saturation density the symmetry energy is strongly correlated with the mass of NS characterized by the onset of nucleonic direct Urca processes at their center. Constraints from chEFT seem to rule out the direct Urca onset inside NS with a mass below $1.4 M_\odot$.

We have analysed several EOS properties as the speed of sound, the trace anomaly, and the consistence of the RMF EOS with the predictions of pQCD. It was shown that within DDH and DDB models the speed of sound are monotonically increasing functions of the density, while within the NL model, the speed of sound behavior is sensitive to the coupling of ω^4 term, and may present a maximum followed by a decreasing tendency with density. Its behavior may be confused with the onset of a non-nucleonic degree of freedom, as discussed in [35, 37, 39]. The different behaviors of the three frameworks reflect the different functionals that define the EOS of each one and the lack of constraining high density observations or experimental data. It was shown that the three models predict values of the polytropic index below 1.75 for densities above 0.4 to 0.7 fm^{-3} and that the trace anomaly becomes negative for these densities. It was also discussed that the quantity related to the trace anomaly and its derivative introduced in [51], d_c , takes values generally above 0.2, a limit proposed in [51] as defining a transition to deconfined quark matter, although within the models NL and DDB values below 0.2 are not excluded at densities above $\gtrsim 0.6 \text{ fm}^{-3}$. Notice, however, while in [51] this quantity may take values above 0.5, for the present three models it never takes values above 0.35.

Using thermodynamic and causality arguments together with low density nuclear matter and high density pQCD constraints, a discussion similar to the one proposed in [101] was developed, and some of the models within RMF that do not satisfy the high density constraints have been identified. These are models with a very stiff high density EOS, although still causal.

ACKNOWLEDGMENTS

This work was partially supported by national funds from FCT (Fundação para a Ciência e a Tecnologia, I.P., Portu-

gal) under Projects No. UIDP/04564/2020, No. UIDB/04564/2020 and 2022.06460.PTDC and No. POCI-01-0145-FEDER-029912. The authors acknowledge the Laboratory for Advanced Computing at the University of Coimbra for providing HPC resources that have contributed to the research results reported within this paper, URL: <https://www.uc.pt/lca>.

Appendix A

The posterior parameters for the three models DDB, NL and DDH, obtained in Sec. II B are given in Table VI.

-
- [1] B. P. Abbott *et al.* (LIGO Scientific, Virgo), *Phys. Rev. Lett.* **119**, 161101 (2017), arXiv:1710.05832 [gr-qc].
 - [2] B. P. Abbott *et al.* (LIGO Scientific, Virgo), *Astrophys. J. Lett.* **892**, L3 (2020), arXiv:2001.01761 [astro-ph.HE].
 - [3] P. Demorest, T. Pennucci, S. Ransom, M. Roberts, and J. Hessels, *Nature* **467**, 1081 (2010).
 - [4] J. Antoniadis, P. C. C. Freire, N. Wex, T. M. Tauris, R. S. Lynch, M. H. van Kerkwijk, M. Kramer, C. Bassa, V. S. Dhillon, T. Driebe, J. W. T. Hessels, V. M. Kaspi, V. I. Kondratiev, N. Langer, T. R. Marsh, M. A. McLaughlin, T. T. Pennucci, S. M. Ransom, I. H. Stairs, J. van Leeuwen, J. P. W. Verbiest, and D. G. Whelan, *Science* **340**, 448 (2013).
 - [5] H. T. Cromartie *et al.* (NANOGrav), *Nature Astron.* **4**, 72 (2019), arXiv:1904.06759 [astro-ph.HE].
 - [6] E. Fonseca *et al.*, *Astrophys. J. Lett.* **915**, L12 (2021), arXiv:2104.00880 [astro-ph.HE].
 - [7] R. W. Roman, D. Kandel, A. V. Filippenko, T. G. Brink, and W. Zheng, *Astrophys. J. Lett.* **908**, L46 (2021), arXiv:2101.09822 [astro-ph.HE].
 - [8] T. E. Riley *et al.*, *Astrophys. J. Lett.* **887**, L21 (2019), arXiv:1912.05702 [astro-ph.HE].
 - [9] M. C. Miller *et al.*, *Astrophys. J. Lett.* **887**, L24 (2019), arXiv:1912.05705 [astro-ph.HE].
 - [10] T. E. Riley *et al.*, *Astrophys. J. Lett.* **918**, L27 (2021), arXiv:2105.06980 [astro-ph.HE].
 - [11] M. C. Miller *et al.*, *Astrophys. J. Lett.* **918**, L28 (2021), arXiv:2105.06979 [astro-ph.HE].
 - [12] G. Raaijmakers, S. K. Greif, K. Hebeler, T. Hinderer, S. Nissande, A. Schwenk, T. E. Riley, A. L. Watts, J. M. Lattimer, and W. C. G. Ho, *Astrophys. J. Lett.* **918**, L29 (2021), arXiv:2105.06981 [astro-ph.HE].
 - [13] J. Margueron, R. Hoffmann Casali, and F. Gulminelli, *Phys. Rev.* **C97**, 025805 (2018), arXiv:1708.06894 [nucl-th].
 - [14] K. Hebeler, J. M. Lattimer, C. J. Pethick, and A. Schwenk, *Astrophys. J.* **773**, 11 (2013), arXiv:1303.4662 [astro-ph.SR].
 - [15] C. Drischler, K. Hebeler, and A. Schwenk, *Phys. Rev. Lett.* **122**, 042501 (2019), arXiv:1710.08220 [nucl-th].
 - [16] C. Drischler, J. A. Melendez, R. J. Furnstahl, and D. R. Phillips, *Phys. Rev. C* **102**, 054315 (2020), arXiv:2004.07805 [nucl-th].
 - [17] A. Kurkela, P. Romatschke, and A. Vuorinen, *Phys. Rev. D* **81**, 105021 (2010), arXiv:0912.1856 [hep-ph].
 - [18] A. Kurkela, E. S. Fraga, J. Schaffner-Bielich, and A. Vuorinen, *Astrophys. J.* **789**, 127 (2014), arXiv:1402.6618 [astro-ph.HE].
 - [19] T. Gorda, O. Komoltsev, and A. Kurkela, (2022), arXiv:2204.11877 [nucl-th].
 - [20] L. Lindblom, *Astrophys. J.* **398**, 569 (1992).
 - [21] A. W. Steiner, J. M. Lattimer, and E. F. Brown, *Astrophys. J.* **722**, 33 (2010), arXiv:1005.0811 [astro-ph.HE].
 - [22] F. Ozel, G. Baym, and T. Guver, *Phys. Rev. D* **82**, 101301 (2010), arXiv:1002.3153 [astro-ph.HE].
 - [23] A. W. Steiner, J. M. Lattimer, and E. F. Brown, *Astrophys. J. Lett.* **765**, L5 (2013), arXiv:1205.6871 [nucl-th].
 - [24] C. A. Raithel, F. Ozel, and D. Psaltis, *Astrophys. J.* **831**, 44 (2016), arXiv:1605.03591 [astro-ph.HE].
 - [25] Y. Fujimoto, K. Fukushima, and K. Murase, *Physical Review D* **98**, 10.1103/physrevd.98.023019 (2018).
 - [26] Y. Fujimoto, K. Fukushima, and K. Murase, *Physical Review D* **101**, 10.1103/physrevd.101.054016 (2020).
 - [27] Y. Fujimoto, K. Fukushima, and K. Murase, *Journal of High Energy Physics* **2021**, 1 (2021).
 - [28] M. a. Ferreira and C. Providênci, *JCAP* **07**, 011, arXiv:1910.05554 [nucl-th].
 - [29] F. Morawski and M. Bejger, *Astronomy & Astrophysics* **642**, A78 (2020).
 - [30] V. Carvalho, M. Ferreira, T. Malik, and C. Providênci, (2023), arXiv:2306.06929 [nucl-th].
 - [31] K. Zhou, L. Wang, L.-G. Pang, and S. Shi, (2023), arXiv:2303.15136 [hep-ph].
 - [32] C. Mondal and F. Gulminelli, (2021), arXiv:2111.04520 [nucl-th].
 - [33] S. M. A. Imam, N. K. Patra, C. Mondal, T. Malik, and B. K. Agrawal, *Phys. Rev. C* **105**, 015806 (2022), arXiv:2110.15776 [nucl-th].
 - [34] P. B. de Tovar, M. Ferreira, and C. Providênci, *Phys. Rev. D* **104**, 123036 (2021), arXiv:2112.05551 [nucl-th].
 - [35] E. Annala, T. Gorda, E. Katerini, A. Kurkela, J. Näättilä, V. Paschalidis, and A. Vuorinen, (2021), arXiv:2105.05132 [astro-ph.HE].
 - [36] L. Lindblom, *Phys. Rev. D* **82**, 103011 (2010), arXiv:1009.0738 [astro-ph.HE].
 - [37] E. Annala, T. Gorda, A. Kurkela, J. Näättilä, and A. Vuorinen, *Nature Phys.* **16**, 907 (2020), arXiv:1903.09121 [astro-ph.HE].
 - [38] S. Altiparmak, C. Ecker, and L. Rezzolla, *Astrophys. J. Lett.* **939**, L34 (2022), arXiv:2203.14974 [astro-ph.HE].
 - [39] R. Somasundaram, I. Tews, and J. Margueron, *Phys. Rev. C* **107**, L052801 (2023), arXiv:2204.14039 [nucl-th].

TABLE VI. Based on the posterior distribution for DDB, NL, and DDH restricted to nucleonic degrees of freedom, the median values and the 90% confidence intervals (CI) for the parameters were calculated. Please refer to Section II B for the specific terminology used for parameter names. The masses of the nucleon, ω meson, and ρ meson in all models are 939 MeV, 783 MeV, and 763 MeV, respectively. However, the σ meson mass is fixed to 500 MeV for NL and 550 MeV for DDB and DDH.

DDB				NL				DDH			
Parameters	median	90% CI		Parameters	median	90% CI		Parameters	median	90% CI	
		min	max			min	max			min	max
g_σ	9.024	8.170	10.059	g_σ	8.454	8.010	9.691	g_σ	8.827	8.146	9.322
g_ω	10.761	9.413	12.313	g_ω	9.915	9.084	12.167	g_ω	10.475	9.378	11.224
g_ρ	3.954	3.485	4.389	g_ρ	12.193	9.546	14.599	g_ρ	3.976	3.475	4.434
a_σ	0.080	0.054	0.113	B	4.586	2.205	6.903	a_σ	1.247	1.158	1.499
a_ω	0.039	0.004	0.105	C	-1.985	-4.627	3.530	b_σ	1.392	0.585	4.082
a_ρ	0.542	0.318	0.703	ξ	0.004	0.000	0.016	c_σ	1.867	0.775	6.011
				Λ	0.064	0.036	0.103	d_σ	0.423	0.235	0.656
								a_ω	1.215	1.022	1.663
								b_ω	7.544	1.876	14.074
								c_ω	9.546	2.307	19.140
								d_ω	0.187	0.132	0.380
								a_ρ	0.500	0.304	0.720

- [40] J. Margueron, R. Hoffmann Casali, and F. Gulminelli, *Phys. Rev. C* **97**, 025805 (2018), arXiv:1708.06894 [nucl-th].
- [41] J. Margueron, R. Hoffmann Casali, and F. Gulminelli, *Phys. Rev. C* **97**, 025806 (2018), arXiv:1708.06895 [nucl-th].
- [42] M. Ferreira, M. Fortin, T. Malik, B. K. Agrawal, and C. Providência, *Phys. Rev. D* **101**, 043021 (2020), arXiv:1912.11131 [nucl-th].
- [43] W.-J. Xie and B.-A. Li, *Astrophys. J.* **883**, 174 (2019), arXiv:1907.10741 [astro-ph.HE].
- [44] W.-J. Xie and B.-A. Li, *Astrophys. J.* **899**, 4 (2020), arXiv:2005.07216 [astro-ph.HE].
- [45] M. Ferreira and C. Providência, *Phys. Rev. D* **104**, 063006 (2021), arXiv:2110.00305 [nucl-th].
- [46] H. D. Thi, C. Mondal, and F. Gulminelli, *Universe* **7**, 373 (2021), arXiv:2109.09675 [astro-ph.HE].
- [47] P. Landry and R. Essick, *Phys. Rev. D* **99**, 084049 (2019), arXiv:1811.12529 [gr-qc].
- [48] R. Essick, P. Landry, and D. E. Holz, *Phys. Rev. D* **101**, 063007 (2020), arXiv:1910.09740 [astro-ph.HE].
- [49] W. Zhou, J. Hu, Y. Zhang, and H. Shen, *Astrophys. J.* **950**, 186 (2023), arXiv:2305.03323 [nucl-th].
- [50] Y. Fujimoto, K. Fukushima, L. D. McLerran, and M. Praszalowicz, *Phys. Rev. Lett.* **129**, 252702 (2022), arXiv:2207.06753 [nucl-th].
- [51] E. Annala, T. Gorda, J. Hirvonen, O. Komoltsev, A. Kurkela, J. Nättilä, and A. Vuorinen, (2023), arXiv:2303.11356 [astro-ph.HE].
- [52] T. Malik, B. K. Agrawal, and C. Providência, *Phys. Rev. C* **106**, L042801 (2022), arXiv:2206.15404 [nucl-th].
- [53] T. Malik and C. Providência, (2022), arXiv:2205.15843 [nucl-th].
- [54] T. Malik, M. Ferreira, B. K. Agrawal, and C. Providência, *Astrophys. J.* **930**, 17 (2022), arXiv:2201.12552 [nucl-th].
- [55] T. Malik, M. Ferreira, M. B. Albino, and C. Providência, (2023), arXiv:2301.08169 [nucl-th].
- [56] J. Boguta and A. R. Bodmer, *Nucl. Phys. A* **292**, 413 (1977).
- [57] H. Mueller and B. D. Serot, *Nucl. Phys. A* **606**, 508 (1996), arXiv:nucl-th/9603037.
- [58] S. Typel and H. H. Wolter, *Nucl. Phys. A* **656**, 331 (1999).
- [59] S. Typel, G. Ropke, T. Klähn, D. Blaschke, and H. H. Wolter, *Phys. Rev. C* **81**, 015803 (2010), arXiv:0908.2344 [nucl-th].
- [60] S. Traversi, P. Char, and G. Pagliara, *Astrophys. J.* **897**, 165 (2020), arXiv:2002.08951 [astro-ph.HE].
- [61] X. Sun, Z. Miao, B. Sun, and A. Li, *Astrophys. J.* **942**, 55 (2023), arXiv:2205.10631 [astro-ph.HE].
- [62] M. V. Beznogov and A. R. Raduta, *Phys. Rev. C* **107**, 045803 (2023), arXiv:2212.07168 [nucl-th].
- [63] C. Huang, G. Raaijmakers, A. L. Watts, L. Tolos, and C. Providência, (2023), arXiv:2303.17518 [astro-ph.HE].
- [64] A. L. et al., Watts, *Science China Physics, Mechanics, and Astronomy* **62**, 29503 (2019), arXiv:1812.04021 [astro-ph.HE].
- [65] P. S. et al., Ray, arXiv e-prints , arXiv:1903.03035 (2019), arXiv:1903.03035 [astro-ph.IM].
- [66] H. Mueller and B. D. Serot, *Nucl. Phys. A* **606**, 508 (1996), arXiv:nucl-th/9603037.
- [67] Y. Sugahara and H. Toki, *Nucl. Phys. A* **579**, 557 (1994).
- [68] R. Cavagnoli, D. P. Menezes, and C. Providencia, *Phys. Rev. C* **84**, 065810 (2011), arXiv:1108.1733 [hep-ph].
- [69] A. Gelman, J. B. Carlin, H. S. Stern, D. B. Dunson, A. Vehtari, D. B. Rubin, J. Carlin, H. Stern, D. Rubin, and D. Dunson, *Bayesian Data Analysis Third edition* (CRC Press, Boca Raton, Florida, 2013).
- [70] J. Skilling, in *Bayesian Inference and Maximum Entropy Methods in Science and Engineering: 24th International Workshop on Bayesian Inference and Maximum Entropy Methods in Science and Engineering*, American Institute of Physics Conference Series, Vol. 735, edited by R. Fischer, R. Preuss, and U. V. Toussaint (2004) pp. 395–405.
- [71] J. Buchner, A. Georgakakis, K. Nandra, L. Hsu, C. Rangel, M. Brightman, A. Merloni, M. Salvato, J. Donley,

- and D. Kocevski, *Astron. Astrophys.* **564**, A125 (2014), arXiv:1402.0004 [astro-ph.HE].
- [72] J. Buchner, Nested sampling methods (2021), arXiv:2101.09675 [stat.CO].
- [73] M. Dutra, O. Lourenço, S. S. Avancini, B. V. Carlson, A. Delfino, D. P. Menezes, C. Providência, S. Typel, and J. R. Stone, *Phys. Rev. C* **90**, 055203 (2014), arXiv:1405.3633 [nucl-th].
- [74] Shlomo, S., Kolomietz, V. M., and Colò, G., *Eur. Phys. J. A* **30**, 23 (2006).
- [75] e. a. Todd-Rutel, *Phys. Rev. Lett.* **95**, 122501 (2005), arXiv:nucl-th/0504034.
- [76] R. Essick, P. Landry, A. Schwenk, and I. Tews, *Phys. Rev. C* **104**, 065804 (2021), arXiv:2107.05528 [nucl-th].
- [77] B. P. Abbott *et al.* (LIGO Scientific, Virgo), *Phys. Rev. X* **9**, 011001 (2019), arXiv:1805.11579 [gr-qc].
- [78] R. C. Tolman, *Phys. Rev.* **55**, 364 (1939).
- [79] J. R. Oppenheimer and G. M. Volkoff, *Phys. Rev.* **55**, 374 (1939).
- [80] N. K. Glendenning, *Compact Stars* (1996).
- [81] B. P. Abbott *et al.*, *848*, L12, arXiv:1710.05833.
- [82] T. Hinderer, *Astrophys. J.* **677**, 1216 (2008), arXiv:0711.2420 [astro-ph].
- [83] B. P. Abbott *et al.* (LIGO Scientific, Virgo), *Phys. Rev. Lett.* **121**, 161101 (2018), arXiv:1805.11581 [gr-qc].
- [84] M. Fortin, S. S. Avancini, C. Providência, and I. Vidaña, *Phys. Rev. C* **95**, 065803 (2017), arXiv:1701.06373 [nucl-th].
- [85] C. Providência, M. Fortin, H. Pais, and A. Rabhi 10.3389/fspas.2019.00013 (2018), arXiv:1811.00786 [astro-ph.HE].
- [86] A. Gal, E. V. Hungerford, and D. J. Millener, *Rev. Mod. Phys.* **88**, 035004 (2016), arXiv:1605.00557 [nucl-th].
- [87] S. Weissenborn, D. Chatterjee, and J. Schaffner-Bielich, *Nucl. Phys. A* **881**, 62 (2012), arXiv:1111.6049 [astro-ph.HE].
- [88] M. Fortin, C. Providência, A. R. Raduta, F. Gulminelli, J. L. Zdunik, P. Haensel, and M. Bejger, *Phys. Rev. C* **94**, 035804 (2016), arXiv:1604.01944 [astro-ph.SR].
- [89] M. Fortin, A. R. Raduta, S. Avancini, and C. Providência, *Phys. Rev. D* **101**, 034017 (2020), arXiv:2001.08036 [hep-ph].
- [90] J. R. Stone, V. Dexheimer, P. A. M. Guichon, A. W. Thomas, and S. Typel, *Mon. Not. Roy. Astron. Soc.* **502**, 3476 (2021), arXiv:1906.11100 [nucl-th].
- [91] M. Fortin, M. Oertel, and C. Providência, *Publ. Astron. Soc. Austral.* **35**, 44 (2018), arXiv:1711.09427 [astro-ph.HE].
- [92] D. G. Yakovlev, A. D. Kaminker, O. Y. Gnedin, and P. Haensel, *Phys. Rept.* **354**, 1 (2001), arXiv:astro-ph/0012122.
- [93] D. G. Yakovlev and C. J. Pethick, *Ann. Rev. Astron. Astrophys.* **42**, 169 (2004), arXiv:astro-ph/0402143.
- [94] M. Fortin, C. Providência, A. R. Raduta, F. Gulminelli, J. L. Zdunik, P. Haensel, and M. Bejger, *Phys. Rev. C* **94**, 035804 (2016), arXiv:1604.01944 [astro-ph.SR].
- [95] M. Fortin, A. R. Raduta, S. Avancini, and C. Providência, *Phys. Rev. D* **103**, 083004 (2021), arXiv:2102.07565 [nucl-th].
- [96] M. V. Beznogov and D. G. Yakovlev, *Mon. Not. Roy. Astron. Soc.* **452**, 540 (2015), arXiv:1507.04206 [astro-ph.SR].
- [97] A. Kurkela, in *15th Conference on Quark Confinement and the Hadron Spectrum* (2022) arXiv:2211.11414 [hep-ph].
- [98] T. Kojo, *AAPPs Bull.* **31**, 11 (2021), arXiv:2011.10940 [nucl-th].
- [99] M. Al-Mamun, A. W. Steiner, J. Nätilä, J. Lange, R. O’Shaughnessy, I. Tews, S. Gandolfi, C. Heinke, and S. Han, *Phys. Rev. Lett.* **126**, 061101 (2021), arXiv:2008.12817 [astro-ph.HE].
- [100] C. Drischler, S. Han, and S. Reddy, *Phys. Rev. C* **105**, 035808 (2022), arXiv:2110.14896 [nucl-th].
- [101] O. Komoltsev and A. Kurkela, *Phys. Rev. Lett.* **128**, 202701 (2022), arXiv:2111.05350 [nucl-th].
- [102] C. J. Horowitz and J. Piekarewicz, *Phys. Rev. Lett.* **86**, 5647 (2001), arXiv:astro-ph/0010227.
- [103] G. A. Lalazissis, T. Niksic, D. Vretenar, and P. Ring, *Phys. Rev. C* **71**, 024312 (2005).
- [104] V. Koch, T. S. Biro, J. Kunz, and U. Mosel, *Phys. Lett. B* **185**, 1 (1987).
- [105] C. da Providencia, J. da Providencia, and S. A. Moszkowski, *Ser. Adv. Quant. Many Body Theor.* **6**, 242 (2002).
- [106] I. N. Mishustin, L. M. Satarov, and W. Greiner, *Phys. Rept.* **391**, 363 (2004), arXiv:hep-ph/0304296.
- [107] H. Pais, D. P. Menezes, and C. Providência, *Phys. Rev. C* **93**, 065805 (2016), arXiv:1603.01239 [nucl-th].
- [108] S.-N. Wei, W.-Z. Jiang, R.-Y. Yang, and D.-R. Zhang, *Phys. Lett. B* **763**, 145 (2016), arXiv:1511.07144 [nucl-th].
- [109] B. Liu, V. Greco, V. Baran, M. Colonna, and M. Di Toro, *Phys. Rev. C* **65**, 045201 (2002), arXiv:nucl-th/0112034.
- [110] M. Fortin, J. L. Zdunik, P. Haensel, and M. Bejger, *Astron. Astrophys.* **576**, A68 (2015), arXiv:1408.3052 [astro-ph.SR].

RELATIVISTIC MEAN FIELD THEORY OF NUCLEI WITH A VECTOR MESON SELF-INTERACTION*

A.R. BODMER

Department of Physics, University of Illinois at Chicago, IL 60680, USA
and
Physics Division, Argonne National Laboratory, Argonne, IL 60439-4843, USA

Received 3 July 1990
(Revised 24 September 1990)

Abstract: The inclusion of an isoscalar vector-meson quartic self-interaction (VSI) in the relativistic mean field theory of nuclei is discussed. We consider mostly nuclear matter, and in particular the equation of state (EOS) at $T=0$. A VSI softens the EOS; in particular a moderately strong VSI gives an EOS similar to those obtained from nonrelativistic many-body calculations. Estimates of the spin-orbit splitting in light nuclei indicate that this splitting is not sensitive to the strength of the VSI and will depend mostly on the effective mass M^* . The energy dependence of the optical potential gives $M^*/M \approx 0.6$ independent of the VSI, and consistent with that obtained from the spin-orbit splitting.

1. Introduction

In ref.¹⁾ (hereafter denoted by (I)) we explored the consequences of the standard lagrangian of nuclear relativistic mean field theory [see refs.^{2,3)} for reviews] but with a rather general class of scalar potential functions $U(\phi)$ of the scalar field ϕ , with a minimum $U(0)=0$ at $\phi=0$. Specifically, we considered a U_{34} potential function which has cubic and quartic self-interactions and which is specified by three parameters. The vector lagrangian was the usual quadratic one involving the vector coupling constant c_V^2 which is uniquely related to the effective mass M^* at saturation. These four parameters are the only ones for symmetric nuclear matter and can be adjusted to reproduce the saturation density ρ_0 , saturation energy per particle e_0 as well as any reasonable value of the incompressibility constant K , say between 100 and 300 MeV. Since ρ_0 and e_0 are well determined, in contrast to K , only K and M^* remain as free parameters. We also showed (see also sect. 4) that any U with at least three parameters is effectively equivalent to a U_{34} function if the parameters can be adjusted to give the same M^* , e_0 , ρ_0 , K . Furthermore, as shown in (I), one can choose “healthy” functional forms for such an equivalent U which do not have a maximum and which are always positive for large $|\phi| \rightarrow \infty$.

* This work has been supported in part by the U.S. Department of Energy, Nuclear Physics Division, under contract W-31-109-ENG-38.

We argued in (I) that M^* is determined within rather narrow limits to be $M^*/M \approx 0.6$ by the spin-orbit splitting in light nuclei, in particular by the splitting $\delta\epsilon$ in ^{16}O . As shown in particular by Rufa *et al.*⁴⁾ this seems equivalent to requiring an adequate fit to the sizes and energies of spherical nuclei for the whole range of A -values. Furthermore, this is found to be consistent with the empirical deformations of both light and heavy nuclei⁵⁾. Very recently, ref.⁶⁾ has also argued strongly in favor of $M^*/M \approx 0.6$ from deformation properties. The equation of state at $T=0$ (EOS) is then effectively determined by the incompressibility constant K and by $\delta\epsilon$, and is very stiff. There is then very little freedom left to vary the EOS, in particular to obtain a significantly softer EOS.

In this paper we explore a minimal one-parameter extension of the standard lagrangian which involves the introduction of a quartic self-interaction of the isoscalar vector meson field, denoted by VSI, which is always positive or zero and whose strength is determined by a parameter z . The free parameters are now K , M^* and z . We discuss the implications of the spin-orbit splitting and of the optical potential and make plausible that independently of z one has $M^*/M \approx 0.6$. The effect of a VSI on the EOS shows that this is softened by an extent depending on the strength of the VSI. Our viewpoint is primarily phenomenological: The VSI should be considered in the context of relativistic mean field theory where its effect in softening the EOS is similar to that of short-range two-body correlations treated explicitly in the Brueckner-Dirac approach. Also in the context of effective interactions, aside from questions of renormalizability, a VSI has equal justification to that of scalar-meson self-interactions. We also use this paper to make quite explicit the determination of the parameters of the scalar and vector potential functions from the saturation properties of nuclear matter.

2. Relativistic mean field theory for nuclear matter with a vector self-interaction

The lagrangian we consider is

$$\mathcal{L} = \bar{\psi}(i\gamma_\mu\gamma^\mu - m^*)\psi + \frac{1}{2}\partial_\mu\phi\partial^\mu\phi - U(\phi) + \mathcal{L}_v + \mathcal{L}_\rho, \quad (1)$$

with

$$\mathcal{L}_v = \frac{1}{2}m_v^2 V_\mu V^\mu \left(1 + \frac{g_v^2}{2} \frac{V_\mu V^\mu}{Z^2} \right) - g_v \rho_\mu V^\mu - \frac{1}{2}V_{\mu,\nu} V^{\mu,\nu}. \quad (2)$$

\mathcal{L}_ρ is the standard quadratic lagrangian for the isovector “ ρ ” field and enters only for asymmetric nuclear matter, i.e. $N \neq Z$. This has been extensively discussed [see (I) and ref.²⁾ and references quoted therein] and will not be further considered here, where we consider only symmetric nuclear matter. The field ψ is the nucleon field and M the nucleon mass. The meson fields, associated masses and Yukawa couplings are: scalar (“ σ ”) field ϕ , m_s , g_s , and isoscalar vector (“ ω ”) field: V_μ , m_v , g_v . \mathcal{L}_v is the (isoscalar) vector part of \mathcal{L} and has a quartic VSI determined

by the parameter Z . In the limit $Z = \infty$ the standard quadratic lagrangian $\mathcal{L}_v^{(0)}$ is recovered. The effective mass m^* is defined by

$$m^* = M - \Phi \quad \text{with} \quad \Phi = g_s \phi. \quad (3)$$

The effective mass at saturation is denoted by M^* . We specifically consider a U_{34} potential function:

$$U_{34} = \frac{1}{2} m_s^2 \phi^2 + \frac{1}{3} a \phi^3 + \frac{1}{4} b \phi^4. \quad (4)$$

In terms of Φ :

$$U_{34} = \frac{1}{2} \frac{\Phi^2}{c_s^2} + \frac{1}{3} A \Phi^3 + \frac{1}{4} B \Phi^4, \quad (5)$$

with

$$c_s = \frac{g_s}{m_s}, \quad A = \frac{a}{g_s^3}, \quad B = \frac{b}{g_s^4}. \quad (6)$$

Thus $U_{34}(\Phi)$ is specified by the three parameters c_s^2, A, B . For uniform static symmetric nuclear matter in the mean field approximation the fields are replaced by their expectation values and the derivative terms can be ignored. The Fermi momentum k_F and baryon density ρ are related by

$$\rho = 2k_F^3/3\pi^2. \quad (7)$$

ρ_0 denotes the saturation density. For the vector field only the expectation value of the time component $V \equiv V_0$ enters for nuclear matter. It is convenient to use

$$W = g_v V, \quad c_v = g_v/m_v, \quad (8)$$

and also the nondimensional variables:

$$w = W/Z \quad (9)$$

$$z = \frac{Z}{c_v^2 \rho_0}, \quad z' = \frac{Z}{c_v^2 \rho} = z \frac{\rho_0}{\rho}. \quad (10)$$

Thus

$$W = c_v^2 \rho_0 z w. \quad (11)$$

$c_v^2 \rho_0$ is the value of $W(\rho_0)$ for $\mathcal{L}_v^{(0)}$. The parameter z is a nondimensional measure of the strength of the quartic VSI. The vector part of the energy density for nuclear matter is then

$$\epsilon_v = -\mathcal{L}_v = W\rho - \frac{1}{2} \frac{W^2}{c_v^2} \left(1 + \frac{W^2}{2Z^2} \right). \quad (12)$$

The equation of motion for V is

$$\frac{\partial \epsilon_v}{\partial V} = 0, \quad (13)$$

which gives

$$W\left(1 + \frac{W^2}{Z^2}\right) = c_v^2 \rho \quad \text{or} \quad w(1 + w^2) = \frac{1}{z'}. \quad (14)$$

For the quadratic $\mathcal{L}_v^{(0)}$, eq. (14) gives $W = c_v^2 \rho$. For $\rho = \rho_0$ one has $z' = z$ and

$$w_0(1 + w_0^2) = z^{-1}, \quad (15)$$

where w_0 is the value of w for ρ_0 and is shown in fig. 1. If eq. (14) is used to replace ρ in terms of W in eq. (12) one obtains

$$\epsilon_v = \frac{1}{2} c_v^2 \rho_0^2 z^2 w^2 (1 + \frac{3}{2} w^2), \quad (16)$$

where $\frac{1}{2} c_v^2 \rho_0^2$ is the energy density at ρ_0 for $\mathcal{L}_v^{(0)}$. Thus for a given z and ρ the equation of motion eq. (14) determines $w(z\rho_0/\rho)$ which in turn determines ϵ_v for a given c_v^2 . Also the equation of motion (13) together with eq. (12) gives

$$\frac{d\epsilon_v}{d\rho} = W. \quad (17)$$

For $z \gg 1$ ($Z \gg c_v^2 \rho_0$), which corresponds to the low-density limit, one obtains with $w'_0 = z'^{-1}$:

$$w = w'_0(1 - w_0'^2 + 3w_0'^4 - 12w_0'^6 + \dots), \quad (18)$$

$$\epsilon_v \sim \frac{1}{2} c_v^2 \rho^2 (1 + O(w_0'^2)). \quad (19)$$

For $z \ll 1$, which corresponds to the high-density limit, one obtains

$$W \sim (c_v^2 \rho Z^2)^{1/3}, \quad \epsilon_v \sim \frac{1}{2} c_v^2 (\rho^{4/3} \rho_0^{2/3})^3 z^{2/3}. \quad (20)$$

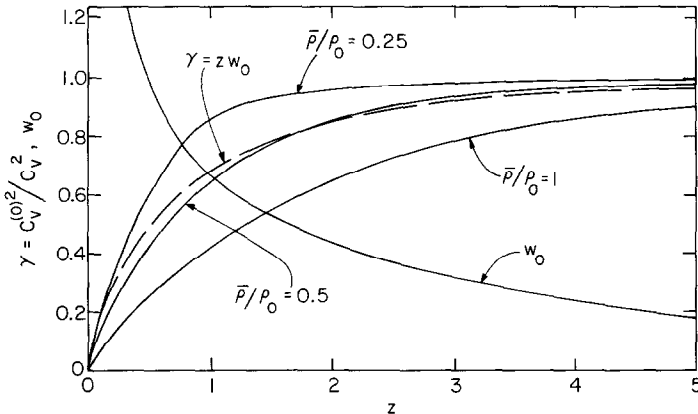


Fig. 1. The nondimensional vector field w_0 and $\gamma = zw_0$ versus the nondimensional strength z of the VSI. The full curves are the values of γ obtained from eq. (57) for the indicated average densities $\bar{\rho}$ in the nuclear surface.

Thus at (extremely) high ρ one has $\varepsilon_v \sim \rho^{4/3}$, i.e. ε_v behaves like an (extreme relativistic) Fermi gas and is no longer proportional to ρ^2 as for $\mathcal{L}_v^{(0)}$. In practice the ρ dependence of ε_v is close to ρ^2 for the densities we considered ($\rho \leq 10\rho_0$).

The equation of motion for the scalar field gives

$$U'(\Phi) = \frac{dU}{d\Phi} = \rho_s, \quad (21)$$

where the scalar density is given by

$$\rho_s = \rho_s(\rho, m^*) = \frac{4}{(2\pi)^3} \int_0^{k_F} d^3k \frac{m^*}{\sqrt{k^2 + m^{*2}}}, \quad (22)$$

or

$$\rho_s = \frac{m^*}{\pi^2} \left[k_F T_F^* - m^{*2} \ln \left(\frac{k_F + E_F^*}{m^*} \right) \right]. \quad (23)$$

ρ_s is an increasing function of m^* and of the baryon density ρ with $\rho_s < \rho$. For small $\rho \leq \rho_0$ one has $\rho_s \approx \rho$. The total energy density ε is

$$\varepsilon = \varepsilon_v + U(\Phi) + \varepsilon_K - M\rho. \quad (24)$$

Here $\varepsilon_K - M\rho$ is the effective kinetic energy density for the effective mass m^* with:

$$\varepsilon_K = \frac{4}{(2\pi)^3} \int_0^{k_F} d^3k \sqrt{k^2 + m^{*2}} = \frac{1}{2\pi^2} \left[k_F T_F^{*3} - \frac{1}{2} m^{*2} k_F T_F^* - \frac{1}{2} m^{*4} \ln \left(\frac{k_F + E_F^*}{m^*} \right) \right], \quad (25)$$

where

$$T_F^* = \sqrt{k_F^2 + m^{*2}}. \quad (26)$$

Solution of eq. (21), with $\Phi = M - m^*$ and with ρ_s given by eq. (23), then determines Φ , or equivalently m^* , in terms of ρ and of the parameters of U . This in turn determines ε_K and U as a function of ρ . The vector density $\varepsilon_v(\rho)$ is determined from eq. (16) in terms of c_v^2 and z using the solution of eq. (14). The equation of state, i.e. the energy per particle ε/ρ and the pressure p (eq. (28)), is then determined in terms of the parameters of the model which with U_{34} are the 5 parameters: c_v^2 , z for ε_v and c_s^2 , A , B for U_{34} .

For later use we give the expressions for p , $d\varepsilon/d\rho$ and $d^2\varepsilon/d\rho^2$ (see the appendix for derivations):

$$\rho \frac{d(\varepsilon/\rho)}{d\rho} = \frac{d\varepsilon}{d\rho} - \frac{\varepsilon}{\rho} = W + T_F^* - M - \frac{\varepsilon}{\rho}, \quad (27)$$

where ε/ρ is the energy per particle obtained from eq. (24); w is the solution of eq. (14) ($W = Zw$); T_F^* is obtained from eq. (26). The pressure is given by

$$p = \rho^2 \frac{d(\varepsilon/\rho)}{d\rho} = -\varepsilon + \rho W + \rho T_F^* - \rho M. \quad (28)$$

Eqs. (14) and (17) give

$$\frac{d^2\epsilon_v}{d\rho^2} = \frac{dW}{d\rho} = \frac{c_v^2}{1+3w^2}. \quad (29)$$

With

$$U'' \equiv \frac{d^2U}{d\Phi^2}, \quad (30)$$

one then obtains:

$$\frac{d^2\epsilon}{d\rho^2} = \frac{c_v^2}{1+3w^2} + \frac{1}{T_F^{*2}} \left[\frac{T_F^* k_F^2}{3\rho} - \frac{m^{*2}}{U'' + d\rho_s/dm^*} \right], \quad (31)$$

where w is the solution of eq. (14) and $d\rho_s/dm^*$ is obtained from eq. (23) and is given by

$$\frac{d\rho_s}{dm^*} = \frac{\rho_s}{m^*} + \frac{m^{*2}}{\pi^2} \left[1 + \frac{k_F}{T_F^*} - 2 \ln \left(\frac{k_F + T_F^*}{m^*} \right) - \frac{m^{*2}}{T_F^*(k_F + T_F^*)} \right]. \quad (32)$$

The incompressibility coefficient $K(\rho)$ at ρ is then obtained from

$$\frac{1}{9}K(\rho) \equiv \frac{\rho^2 d(\epsilon/\rho)}{d\rho^2} = \rho \frac{d^2\epsilon}{d\rho^2} - 2\rho \frac{d(\epsilon/\rho)}{d\rho}. \quad (33)$$

3. Saturation properties and determination of parameters

The parameters of the model are constrained by the conditions at the saturation density ρ_0 . Our strategy is to leave the parameters of ϵ_v as free and then determine the parameters of U in terms of the saturation data and the parameters of ϵ_v . The saturation data, given below, are ρ_0 , the energy/particle e_0 , and the incompressibility constant K . Since e_0, ρ_0 are well determined, only K is considered as variable input. Our specific model has 5 parameters: c_v^2, z for ϵ_v and A, B, c_s^2 for U_{34} . Instead of c_v^2, z we may use M^*, z (see eq. (37) and discussion). The 3 parameters of U_{34} are then determined in terms of M^*, z, ρ_0, e_0, K . Thus with ρ_0, e_0 fixed (at the values of eq. (35)), the model is determined by M^*, z, K . The situation is essentially the same for any 3-parameter U . For $z = \infty$ (no VSI) the model is completely determined by just M^*, K as fully discussed in (I). The suffix zero is used for quantities at ρ_0 except that we use the notation

$$M^* = m^*(\rho_0) \quad \text{with} \quad \Phi_0 = M - M^*. \quad (34)$$

At saturation, the density and energy/nucleon are

$$\rho_0 = 0.1484 \text{ fm}^{-3}, \quad (k_F = 1.30 \text{ fm}^{-1}),$$

$$e_0 = \frac{\epsilon_0}{\rho_0} = -a_v, \quad a_v = 15.75 \text{ MeV}. \quad (35)$$

The numerical values are those used in (I). For the incompressibility coefficient K the empirical values 100–300 MeV encompass all values suggested so far [ref.⁷] for a review], with K close to 300 MeV most favored by recent evidence⁸).

The condition for saturation is $d(\epsilon/\rho)/d\rho = 0$ at ρ_0 . From eqs. (17) and (27) this gives the “saturation condition”

$$W_0 = \left. \frac{d\epsilon_v}{d\rho} \right|_{\rho_0} = e_0 + M - \sqrt{k_F^2 + M^{*2}}, \quad (36)$$

and with eq. (11)

$$c_v^2 \rho_0 = (e_0 + M - \sqrt{k_F^2 + M^{*2}})/zw_0, \quad (37)$$

where $w_0(z)$ is the solution of eq. (15) and is shown in fig. 1. For $z \rightarrow \infty$ we obtain $W_0 = c_v^2 \rho_0$ and the saturation condition reduces to that for no VSI:

$$c_v^{(0)2} \rho_0 = e_0 - (\sqrt{k_F^2 + M^{*2}} - M). \quad (38)$$

This gives the relation between $c_v^{(0)2}$ and M^* first given in ref.⁹). For finite z the generalization of this relation is obtained from eq. (37) with $w_0(z)$ obtained from eq. (15). This gives c_v^2 as a function now of both M^* and z , shown in table 1 and fig. 2. Instead of c_v^2 and z it is more convenient to use M^* and z as the parameters specifying ϵ_v . Then M^* determines Φ_0 from eq. (34).

From eq. (37) the value of M^* at which $c_v^2 = 0$ is given by

$$e_0 = \sqrt{k_F^2 + M^{*2}} - M,$$

giving $M^*/M = 0.95$ independent of z .

From eqs. (37) and (38),

$$\gamma \equiv c_v^{(0)2}/c_v^2 = zw_0(z). \quad (39)$$

This depends only on z and is shown in fig. 1. For $z \rightarrow \infty$: $zw_0 \rightarrow 1$ and $c_v^2 \rightarrow c_v^{(0)2}$. It is to be noted that eqs. (34) and (36) relate Φ_0 and W_0 , giving

$$\Phi_0 \approx 0.91 W_0 + 100 \text{ MeV}. \quad (40)$$

For a given M^* (or Φ_0) and z the parameters of any 3-parameter U , in particular of U_{34} , are then obtained from the values of U , U' , U'' at ρ_0 , denoted by U_0 , U'_0 , U''_0 . These in turn are obtained in terms of ρ_0 , e_0 , K , M^* , z as follows:

(i) U_0 is obtained from eq. (24):

$$U_0 = e_0 \rho_0 - \epsilon_v(\rho_0) - \epsilon_k(\rho_0) + M \rho_0, \quad (41)$$

where e_0 , ρ_0 are given by eq. (35); $\epsilon_v(\rho_0)$ is given by eq. (16) with $w_0(z)$. $\epsilon_k(\rho_0)$ is given by eq. (25) for $m^* = M^*$.

(ii) U'_0 is obtained from eq. (21) for $\Phi = \Phi_0$:

$$U'_0 = \rho_s(\rho_0, M^*), \quad (42)$$

where ρ_s is given by eq. (23).

TABLE I

Scalar and vector coupling constants and scalar nonlinear parameters as a function of M^*/M , K and the VSI strength z

z	M^*/M	K (MeV)	c_v^2 (MeV · fm ⁻³)	s (MeV · fm ⁻³)	χ (MeV · fm ⁻³)	$c_s^{-2}\Phi_0^2$ (MeV · fm ⁻³)	$A\Phi_0^3$ (MeV · fm ⁻³)	$B\Phi_0^4$ (MeV · fm ⁻³)
∞	0.4	200	3156	-26.2	36.2	68.1	44.3	-38.3
∞	0.5	200	2615.9	-5.4	38.1	57.9	24.5	-18.1
∞	0.54	550	2391.9	-0.07	-0.44	59.8	-0.15	0.07
∞	0.6	100	2049.6	6.0	57.4	43.0	22.7	-13.2
∞	0.6	200	2049.6	6.0	46.3	44.9	17.2	-9.5
∞	0.6	300	2049.6	6.0	34.4	46.9	11.2	-5.5
∞	0.6	500	2049.6	6.0	7.8	51.3	-2.0	3.4
∞	0.7	200	1466.6	12.5	53.2	31.2	14.0	-5.2
∞	0.7	300	1466.6	12.5	39.2	33.5	7.1	-0.5
∞	0.7	500	1466.6	12.5	6.6	39.0	-9.3	10.4
∞	0.8	200	872.2	16.5	54.5	17.9	10.8	-1.7
∞	0.8	300	872.2	16.5	35.8	21.0	1.4	4.5
∞	0.8	500	872.2	16.5	-14.0	29.3	-23.4	21.1
5	0.4	200	3273.4	-18.8	54.6	65.1	46.1	-37.0
5	0.5	200	2713.1	0.8	49.9	55.9	24.2	-15.9
5	0.6	100	2125.8	10.8	65.6	41.7	22.0	-11.0
5	0.6	200	2125.8	10.8	53.0	43.8	15.7	-6.8
5	0.6	300	2125.8	10.8	39.4	46.0	8.9	-2.3
5	0.6	500	2125.8	10.8	8.7	51.2	-6.5	7.9
5	0.7	200	1521.1	16.0	55.4	30.8	11.7	-2.5
5	0.8	200	904.7	18.5	52.6	18.2	7.8	1.0
2	0.4	100	3723	5.5	130.0	52.5	59.5	-37.8
2	0.4	200	3723	5.5	116.0	54.8	52.5	-33.1
2	0.4	300	3723	5.5	101.1	57.3	45.0	-28.2
2	0.5	100	3085.8	20.9	105.8	46.6	32.0	-14.4
2	0.5	200	3085.8	20.9	89.6	49.3	23.9	-9.0
2	0.5	300	3085.8	20.9	72.2	52.2	15.2	-3.2
2	0.6	100	2417.8	26.6	93.8	37.0	20.3	-4.7
2	0.6	200	2417.8	26.6	75.6	40.0	11.2	1.4
2	0.6	300	2417.8	26.6	55.6	43.3	1.2	8.0
2	0.7	100	1730	27.3	84.2	26.0	14.8	-0.77
2	0.7	200	1730	27.3	63.4	29.5	4.4	6.1
2	0.7	300	1730	27.3	39.9	33.4	-7.4	14.0
2	0.8	100	1028.9	25.2	72.7	14.8	11.1	0.98
2	0.8	200	1028.9	25.2	46.9	19.1	-1.8	9.6
2	0.8	300	1028.9	25.2	15.0	24.4	-17.7	20.2
2	0.85	100	674.68	23.6	64.5	9.5	8.7	2.1
2	0.85	200	674.68	23.6	32.3	14.9	-7.4	12.8
2	0.85	300	674.68	23.6	-12.2	22.3	-29.7	27.6
1	0.4	200	4625.4	40.0	206.6	39.7	63.3	-28.8
1	0.5	200	3833.8	49.5	148.9	39.5	25.0	-0.14
1	0.6	100	3003.9	49.0	137.6	29.7	19.8	3.1
1	0.6	200	3003.9	49.0	110.0	34.3	6.0	12.3
1	0.6	300	3003.9	49.0	79.1	39.4	-9.4	22.6
1	0.6	500	3003.9	49.0	5.0	51.8	-46.5	47.3
1	0.7	100	2149.4	43.3	108.0	22.0	10.7	7.3
1	0.7	200	2149.4	43.3	76.6	27.3	-5.0	17.8
1	0.7	300	2149.4	43.3	39.9	33.8	-23.3	30.0
1	0.7	500	2149.4	43.3	-55.9	49.4	-71.3	62.0
1	0.8	100	1278.3	34.8	79.0	13.8	4.7	8.4
1	0.8	200	1278.3	34.8	40.4	20.2	-14.6	21.3
1	0.8	300	1278.3	34.8	-9.9	28.6	-39.7	38.1
1	0.8	500	1278.3	34.8	-176	56.3	-122.8	93.4
0.5	0.4	200	6312.1	78.0	310.9	22.3	77.4	-25.6
0.5	0.5	200	5231.8	81.0	218.0	27.9	28.0	8.3
0.5	0.6	100	4099.2	73.7	190.6	20.8	21.6	10.1
0.5	0.6	200	4099.2	73.7	151.0	27.4	1.8	23.3
0.5	0.6	300	4099.2	73.7	105.6	35.0	-20.9	38.5
0.5	0.6	500	4099.2	73.7	-8.0	53.9	-77.7	76.3
0.5	0.7	200	2933.1	61.0	93.6	24.4	-14.2	29.8
0.5	0.8	200	1744.5	45.3	35.0	21.1	-27.8	33.6

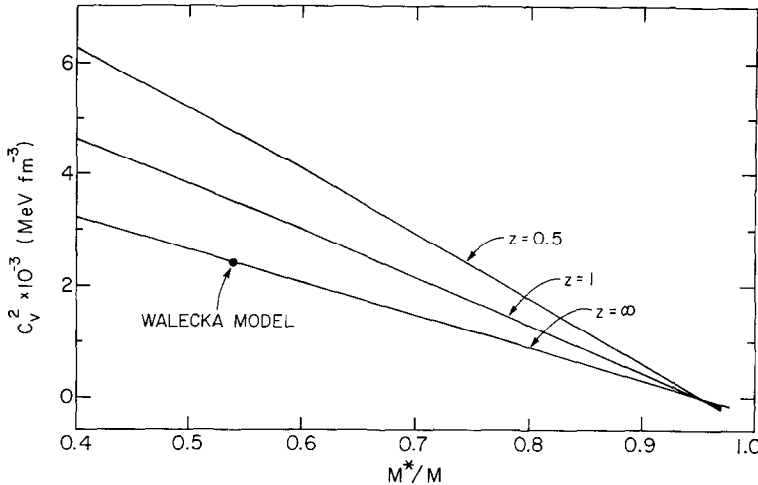


Fig. 2. The vector coupling c_v^2 versus M^*/M for the indicated values of z .

(iii) U_0'' is obtained in terms of the incompressibility coefficient K at ρ_0 , which from eq. (33) is

$$K = 9\rho_0 \frac{d\varepsilon^2}{d\rho^2} \Big|_{\rho=\rho_0}. \quad (43)$$

This relation together with eq. (31) solved for U'' then gives:

$$U_0'' = \frac{M^{*2}}{k_F^2 + M^{*2}} \left(\tilde{c}_v^2 + \frac{k_F^2}{3\rho_0 \sqrt{k_F^2 + M^{*2}}} - \frac{K}{9\rho_0} \right)^{-1} - \frac{d\rho_s}{dm^*} \Big|_{\rho=\rho_0}, \quad (44)$$

where $d\rho_s/dm^*$ is given by eq. (32), and where

$$\tilde{c}_v^2 = c_v^2 (1 + 3w_0^2)^{-1}. \quad (45)$$

For $z \rightarrow \infty$: $\tilde{c}_v^2 = c_v^2$ and eq. (44) reduces to that for no VSI.

The above expressions are independent of the functional form of $U(\Phi)$. Then for some assumed form of $U(\Phi)$ one has

$$U(\Phi_0) = U_0, \quad U'(\Phi_0) = U'_0, \quad U''(\Phi_0) = U''_0. \quad (46)$$

If $U(\Phi)$ has 3 parameters, as does U_{34} , then these parameters are determined by these 3 equations in terms of ρ_0 , e_0 , K , M^* , z .

It is useful to introduce the following two quantities defined at ρ_0 in terms of U_0 , U'_0 , U''_0 :

$$s = 12(\frac{1}{2}U'_0\Phi_0 - U_0), \quad \chi = 6(s - U'_0\Phi_0^2 + U''_0\Phi_0). \quad (47)$$

Apart from the dependence on e_0 , ρ_0 , one has: $s = s(M^*)$, $\chi = \chi(M^*, K)$, only χ depending on K . For U_{34} one obtains

$$s = 2A\Phi_0^3 + 3B\Phi_0^4, \quad \chi = 6(A\Phi_0^3 + B\Phi_0^4). \quad (48)$$

The solution of eqs. (5) and (48) for c_s^2, A, B is

$$A\Phi_0^3 = \frac{1}{2}\chi - s, \quad B\Phi_0^4 = \frac{1}{3}\chi + s, \quad \frac{\Phi_0^2}{c_s^2} = U'_0\Phi_0 - \frac{1}{6}\chi. \quad (49)$$

Since $\Phi_0 = M - M^*$ there is a rapid increase especially in A and B as $M^* \rightarrow M$. However, the more relevant combinations for $U(\Phi)$ are in fact those given in eq. (49). The quantities $\frac{1}{12}s$ and $\frac{1}{6}\chi$ are measures of the nonlinearity of $U(\Phi_0)$ and of $U'(\Phi_0)$, respectively. Thus for $U \sim \Phi^2$ one has $s = \chi = 0$. Results for the coefficients and coupling constants are shown in table 1. We note from eq. (47) that

$$U_0 = \frac{1}{2}U'_0\Phi_0 - \frac{1}{12}s. \quad (50)$$

$U'_0\Phi_0$ depends only on M^* (for fixed ρ_0) and is shown in fig. 3. However, U_0 depends on both M^* and z . Fig. 3 shows s versus M^*/M for various z , and χ is shown in fig. 4. For fixed M^* and K , both s and χ increase as z decreases, i.e. as the strength of the VSI increases, and are smallest for $z = \infty$. This is illustrated in fig. 5 for the phenomenological favored value $M^*/M = 0.6$. Thus not surprisingly, a larger VSI gives larger nonlinear effects in nuclear matter.

For $z \leq 5$, s is quite small for $0.4 \leq M^*/M \leq 0.9$, as already pointed out in (I) for $z = \infty$. For $z = \infty$ one obtains $s = 0$ for $M^*/M = 0.54$. For decreasing z , $M^*(s=0)/M$

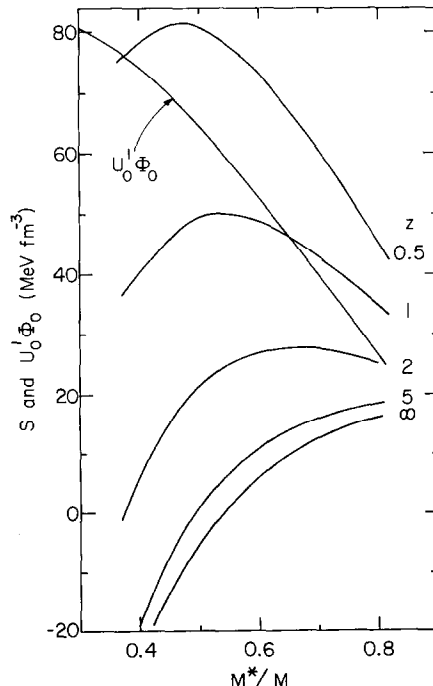


Fig. 3. $U'_0\Phi_0$ and the nonlinearity s versus M^*/M . $U'_0\Phi_0$ depends only on M^*/M , s also on z . There is no dependence on K .

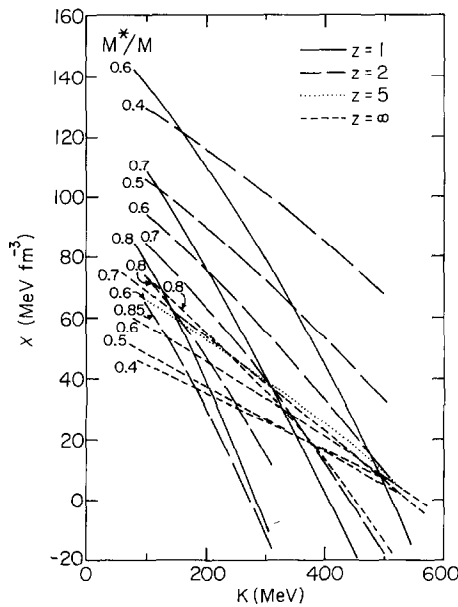


Fig. 4. The nonlinearity χ versus K for the indicated values of M^*/M and z .

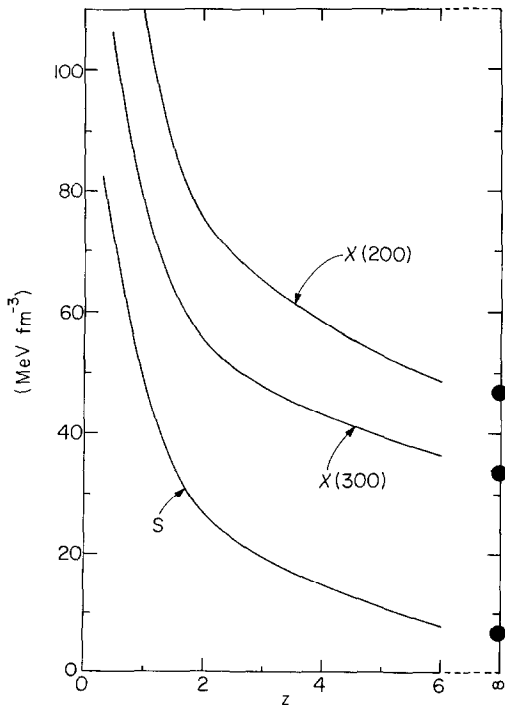


Fig. 5. The nonlinearities s and χ versus z for $M^*/M = 0.6$. The values of χ are for $K = 200, 300$ MeV.

decreases to quite small values (0.495 for $z = 5$, and 0.375 for $z = 2$). For $z \geq 3$, s has a maximum which moves toward smaller M^* for smaller z .

For all z , χ decreases as M^* and K increase. For $z = \infty$ the dependence of χ on M^* is fairly small for $K \geq 200$ MeV as discussed in (I). For smaller z the dependence on both M^* and K increases. Thus for $z = 1$, χ becomes quite large for $K \leq 200$ MeV and $M^*/M \leq 0.7$. A quadratic scalar potential function corresponds to $s = \chi = 0$. For $z = \infty$ this is obtained for $M^*/M = 0.54$, $K = 550$ MeV (linear Walecka model). For $z = 2$ one has $s = \chi = 0$ for $M^*/M = 0.375$, $K = 935$ MeV. A quadratic scalar potential function can thus be obtained only for values of M^* and K , which become empirically less and less acceptable for increasing VSI.

The cubic and quartic terms $A\Phi_0^3$, $B\Phi_0^4$ of U are determined by s , and χ through eq. (49). For all z , $A\Phi_0^3$ decreases with both M^* and K , whereas $B\Phi_0^4$ increases with M^* and K (table 1). In particular B becomes negative for sufficiently small M^* and K . For negative B the quartic term in U_{34} is negative and for sufficiently large Φ the potential function U then becomes negative and physically unacceptable. If the associated (positive) maximum Φ_m of U occurs for $\Phi_m > M$ then there is no bifurcation of solutions (see (I)), whereas for $\Phi_m < M$ such a bifurcation will occur. For $z = \infty$ one has both $B < 0$ and $\Phi_m > M$ for acceptable values of M^* and K (see I). As z decreases, $B\Phi_0^4$ increases (for given M^* and K) and for a sufficiently strong VSI, i.e. for sufficiently small z , the coefficient B becomes positive for phenomenologically acceptable values of M^* and K , and hence the problems associated with a negative U for large Φ disappear. Thus for $z = 2$ one has $B > 0$ for $M^*/M \geq 0.6$, $K \geq 200$ MeV.

4. Equation of state, effective mass and scalar density

The dependences of m^* on ρ and of ρ_s on ρ are shown in figs. 6 and 7. They are related through eq. (23). This relation implies that larger m^*/M^* gives larger ρ_s/ρ (for $\rho > \rho_0$), i.e. less suppression of ρ_s relative to ρ (and thus a more nearly linear dependence of ρ_s on ρ). Smaller z is seen to give larger m^*/M^* for $\rho > \rho_0$ (fig. 6) and hence larger values of ρ_s for large ρ than are obtained with $z = \infty$ for the same M^* . For $z \leq 3$ the ratio m^*/M^* does not depend much on M^* (for a given ρ) and decreases as K increases. For larger z (including $z = \infty$), ρ_s versus ρ has a maximum which is associated with $B < 0$ and with the associated maximum in U at $\Phi_m > M$ (see (I)).

Thus a VSI gives a larger m^*/M^* (for $\rho > \rho_0$) than is obtained for $z = \infty$. Such larger m^*/M^* are closer to the results of nonrelativistic many-body calculations¹⁰⁾. Thus for $M^*/M \approx 0.6$ and for $\rho/\rho_0 \geq 2$ one obtains quite small $m^*/M \leq 0.25$ for $z = \infty$, whereas for $z = 2$ one has $m^*/M \leq 0.4$.

Some results for the energy per particle (ε/ρ) - M versus ρ/ρ_0 are shown in fig. 8 where ε is given by eq. (24). The "kinetic energy" contribution $\varepsilon_K - Mp$ (eq. (25)) is negative, with $\varepsilon_K \sim \rho^{4/3}$ for extremely large ρ . The scalar potential contribution

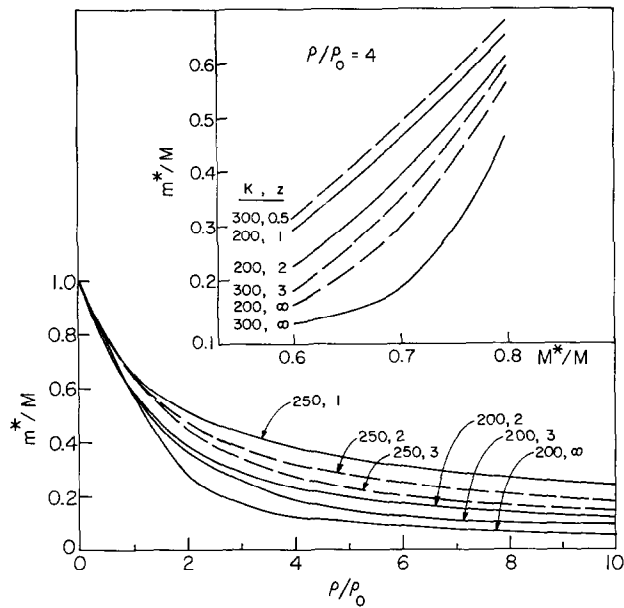


Fig. 6. The effective mass m^*/M versus ρ/ρ_0 for the indicated parameters. The inset shows m^*/M versus M^*/M for $\rho/\rho_0 = 4$ and for the indicated values of K, z .

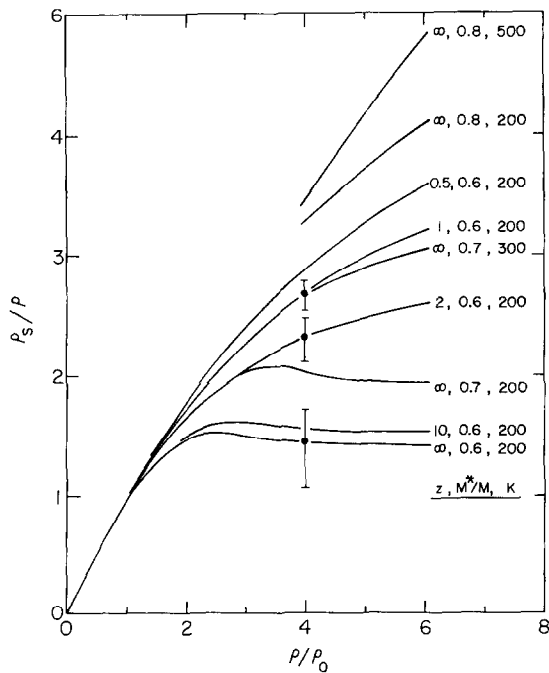


Fig. 7. The ratio ρ_s/ρ of the scalar and baryon densities versus ρ/ρ_0 for the indicated parameters.

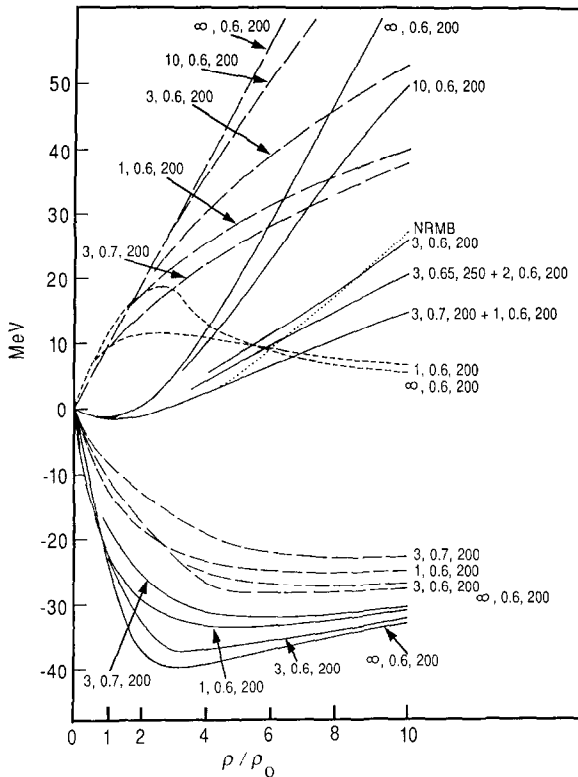


Fig. 8. Energy per particle and related quantities versus ρ / ρ_0 . For the upper part of the figure the full lines are for $\epsilon / \rho a_v$, and the dotted line is for the corresponding results of nonrelativistic many-body calculations including 3-body forces (UV14+TNI, ref. ¹⁰)), the short dashed lines are for $U / \rho a_v$, the long dashed lines are for $\epsilon_v / \rho a_v$. For the lower part, the full lines are for $(\epsilon_K / \rho - M) / a_v$ and the dashed lines for $((\epsilon_K + U) / \rho - M) / a_v$. $a_v = 15.75$ MeV is the saturation binding energy. The labels are the values of z , M^*/M , K .

U approaches the constant value $U(\Phi = M)$ at large ρ (see (I)), and the vector contribution ϵ_v varies between $\rho^{4/3}$ and ρ^2 , depending on z ; for larger $z \geq 1$ the dependence is close to ρ^2 unless ρ is extremely large. Fig. 8 shows that for $\rho \geq 4\rho_0$ both $|(\epsilon_K / \rho) - M|$ and U / ρ decrease slowly with ρ and at about the same rate, and that $(U + \epsilon_K) / \rho - M$ is then negative and almost constant. Thus for $\rho \geq 4\rho_0$ nearly all the ρ -dependence of ϵ / ρ effectively arises from ϵ_v / ρ which then has an approximate linear dependence on ρ ; and thus $d(\epsilon / \rho) / d\rho \approx \text{constant}$. Then from eq. (28): $p \approx \rho^2 d(\epsilon_v / \rho) / d\rho$, and thus $p \sim \rho^2$ for $\rho \geq 4\rho_0$. Since ϵ_v depends only on M^* and z the EOS is effectively independent of K at large ρ : thus $\epsilon / \rho - M$ depends only slightly on K , and p is effectively independent of K . Fig. 8 shows that for large ρ / ρ_0 , ϵ_v / ρ and hence ϵ / ρ and p increase with z for a given M^* and are largest for $z = \infty$, but decrease with increasing M^* for given z . Thus for a fixed M^* the EOS is stiffest for $z = \infty$ (no VSI). One can thus obtain a softer EOS at large ρ either

through smaller z or larger M^* ; thus $M^*/M = 0.7$, $z = 1$ and $M^*/M = 0.6$, $z = 2$ give very similar EOS (fig. 8). For fixed M^* , the EOS can thus be softened by turning on the VSI, i.e. by reducing z from ∞ . Thus for $M^*/M \approx 0.6$ reducing z from ∞ (appropriate to a very stiff EOS) to $z = 3$ gives a much softer EOS not too different from that obtained from nonrelativistic many-body calculations which include three-body forces¹⁰⁾.

The discussion of the following section indicates that the spin-orbit splitting in light nuclei probably does not depend sensitively on z , and thus depends mostly on M^* . Thus the introduction of a VSI allows one to obtain a whole family of EOS depending on z which are all softer at large ρ than the EOS for $z = \infty$, and for which an adequate description of finite nuclei for $M^*/M \approx 0.6$ can be obtained. Of course this conjecture must be confirmed by detailed calculations for finite nuclei.

For smaller $\rho/\rho_0 \leq 4$ the incompressibility coefficient K becomes increasingly important. The absolute variation with K does not depend too much on z , M^* and thus the relative dependence becomes more important for smaller z and larger M^* , i.e. for EOS which are softer at large ρ .

In (I) we showed that for $z = \infty$ the EOS is expected to be independent of the specific form of U for a given K and M^* and (e_0, ρ_0) , since K fixes the low- ρ behavior and M^* the high- ρ behavior (M^* determines $c_v^{(0)2}$ and hence ε_v). For $z < \infty$ the low- ρ behavior will again be determined by K whereas the high- ρ behavior is now fixed by both M^* and z since these determine ε_v . Thus the EOS is expected to be effectively independent of the precise form of U so long as the parameters of U are adjusted to a given M^* , z and K (and e_0, ρ_0). This requires that U has at least three parameters, as U_{34} has. Functionally different U which are chosen in this way are then expected to give effectively the same EOS. In particular for larger z for which $B < 0$ one could choose a $U \geq 0$ which has no maxima but which remains positive for $\Phi \rightarrow \infty$ and is equivalent to U_{34} (see (I)).

5. Vector coupling and spin-orbit potential

With no VSI, the coupling $c_v^{(0)2}$ is determined within fairly narrow limits by the spin-orbit splitting $\delta\varepsilon$ in ^{16}O , as discussed in (I) (see also refs. ^{4,5})). Here we make an approximate estimate of the constraint imposed on c_v^2 by $\delta\varepsilon$ when a VSI is present by estimating the ratio $\gamma = c_v^{(0)2}/c_v^2$ (considered in eq. (39)) as a function of z . The spin-orbit potential is approximately given by

$$V_{LS} = \alpha(r) \mathbf{L} \cdot \mathbf{S}, \quad (51)$$

$$\alpha(r) = \frac{1}{2Mr^2} \frac{d}{dr} (W + \Phi). \quad (52)$$

Thus $\delta\varepsilon$ will be approximately proportional to $d(W + \Phi)/dr$ at some representative density $\bar{\rho}$ (and corresponding \bar{r}) in the nuclear surface. For a first estimate we use

$\bar{\rho} = 0.5\rho_0$. Equation (29) gives

$$\frac{dW}{dr} = \frac{c_v^2}{1+3w^2} \frac{d\rho}{dr}. \quad (53)$$

For $\mathcal{L}_v^{(0)}$ one has

$$\frac{dW^{(0)}}{dr} = c_v^{(0)2} \frac{d\rho}{dr}. \quad (54)$$

Approximately, for the range of densities in the surface: $\Phi^{(0)} \propto W^{(0)}$ (note eq. (40)); thus $\Phi^{(0)} \approx \beta W^{(0)}$ with $\beta \approx 1-1.3$). We expect that $\Phi \approx \Phi^{(0)}$ if $U(\Phi)$ does not change too much with a VSI present.

For a given $\delta\varepsilon$ the ratio γ is then approximately given by the condition

$$\frac{d}{dr}(W + \Phi) = \frac{d}{dr}(W^{(0)} + \Phi^{(0)}) \quad (55)$$

i.e.

$$\frac{dW}{dr} = \frac{dW^{(0)}}{dr} \quad \text{for } \bar{\rho}. \quad (56)$$

Then for a fixed $\delta\varepsilon$ with use of eqs. (53) and (54),

$$\gamma \approx (1+3\bar{w}^2)^{-1}, \quad (57)$$

where

$$\bar{w} = w(\bar{z}), \quad \bar{z} = \rho_0 z / \bar{\rho}, \quad (58)$$

and \bar{w} is obtained from eq. (14) for $z' = \bar{z}$. (A fair approximation for $z \geq 1$ is $\gamma \approx (1+0.62 z^{-2})^{-1}$).

Fig. 1 shows γ versus z obtained in this way for $\bar{\rho} = 0.25\rho_0, 0.5\rho_0, \rho_0$. These values of γ are to be compared with $\gamma = zw_0$ (eq. (39)) as determined quite independently by the saturation condition with $w_0 = w(z)$. The close agreement between γ obtained from eq. (39) and from eq. (57) for $\bar{\rho} = 0.5\rho_0$ is quite striking, in view of the entirely different considerations involved. For $\bar{\rho} = 0.25\rho_0, \rho_0$ there is no such agreement. Of course our crude estimates are subject to confirmation by more definitive calculations for finite nuclei.

Accepting our estimate of γ for $\bar{\rho} = 0.5\rho_0$ as reasonably reliable, the agreement of this estimate with $\gamma = zw_0$ then implies that for a given M^* the calculated value of $\delta\varepsilon$ will effectively be independent of z , and thus conversely that the results obtained for M^* from the experimental $\delta\varepsilon$ using $\mathcal{L}_v^{(0)}$ will not be appreciably changed by the introduction of a VSI of any strength z . If this is confirmed by finite nucleus calculations, then for any z agreement with the empirical $\delta\varepsilon$ would be obtained for $M^*/M \approx 0.6$ as obtained for $\mathcal{L}_v^{(0)}$. Hence a whole family of EOS parameterized by z and with $M^*/M \approx 0.6$ (and illustrated in fig. 8) should be consistent with the empirical value of $\delta\varepsilon$.

6. Optical potential

We discuss possible constraints imposed by the empirical energy dependence of the optical potential.

The Dirac equation for a nucleon of energy E and momentum k propagating through nuclear matter gives the dispersion relation

$$E = W + \sqrt{k^2 + m^{*2}}. \quad (59)$$

At saturation where $k = k_F$, $E = e_0 + M$ and $m^* = M^*$, eq. (59) then just gives the saturation condition eq. (36). We define the optical potential following ref.²⁾ (see also refs.¹¹⁻¹⁶⁾) by

$$(\nabla^2 + (E^2 - M^2))\psi = V_{\text{opt}}\psi. \quad (60)$$

For uniform nuclear matter this gives

$$V_{\text{opt}} = E^2 - (k^2 + M^2). \quad (61)$$

Substituting for k from eq. (59) gives

$$V_{\text{opt}} = M^{*2} - M^2 - W^2 + c_E E, \quad (62)$$

where the energy dependence c_E is given by

$$c_E = 2W. \quad (63)$$

[Eqs. (62) and (63) are a generalization, when a VSI is included, of eq. 3.168 of ref.²⁾.] The data gives $c_E \approx 0.6M$ [see ref.²⁾] and hence (for $\rho_0 = 0.15 \text{ fm}^{-3}$)

$$W_0 \approx 280 \text{ MeV}, \quad M^*/M \approx 0.62 \quad (\Phi \approx 356 \text{ MeV}) \quad (64)$$

with considerable errors, where M^* has been obtained from W_0 using eq. (36). The considerations leading to the values of eq. (64) are quite independent of z !

For $\mathcal{L}_v^{(0)}$, the dependence of $\delta\varepsilon$ on M^*/M together with the empirical value $\delta\varepsilon = 6 \text{ MeV}$ gives

$$M^*/M \approx 0.6 \pm 0.03, \quad W_0 \approx 300 \pm 20 \text{ MeV}, \quad (65)$$

where eq. (36) has now been used to obtain W_0 from M^* . These values are completely consistent with the optical potential values of eq. (64). The considerations of the previous section suggest that the estimates of eq. (65) obtained from the spin-orbit splitting should be insensitive to the strength z of the VSI. The agreement between eqs. (64) and (65) is certainly consistent with this.

7. Summary and remarks

We have shown that a VSI can give a large softening of the EOS at large ρ . In particular for the favored phenomenological values of $M^*/M \approx 0.6$, $K \approx 200-300 \text{ MeV}$, a VSI with $z = 3$ gives an EOS which is much closer to that obtained

from nonrelativistic many-body calculations than the EOS for $z = \infty$ (no VSI). Also m^*/M^* is then considerably larger at large ρ than for $z = \infty$, and is again closer to the values obtained from many-body calculations. Our analysis, admittedly very approximate, of the spin-orbit splitting $\delta\varepsilon$ in light nuclei indicates that $\delta\varepsilon$ should be approximately independent of z , and in particular about equal to the value for $z = \infty$. Analysis of ^{16}O for $z = \infty$ [refs. ^{1,4-6}] then gives $M^*/M \approx 0.6$, and this value should then be the appropriate one also for other z . Of course this conclusion needs confirmation by finite nucleus calculations.

Independence of $\delta\varepsilon$ on z has the important consequence that the whole family of EOS for $M^*/M \approx 0.6$, $K \approx 200\text{--}300$ MeV, with z as parameter, should then be consistent with the phenomenology of finite nuclei (binding energies, sizes, spin-orbit splitting in light nuclei, nuclear deformations in both light and heavy nuclei). This family of EOS may then be used to (hydrodynamically) model relativistic heavy-ion collisions with z as parameter. Without a VSI there would be very little freedom to vary the EOS from the very stiff one required by nuclear phenomenology for $z = \infty$. For neutron stars, one will have a corresponding family of EOS, depending on z , when the isovector lagrangian is included. For consistency this should also include an isovector VSI.

It is possible that for some range of values of z there are density oscillations in nuclear matter and/or unacceptable solutions for finite nuclei just as with the scalar field for which large values of m_s give density oscillations and unacceptable finite nuclei ¹⁵).

We again emphasize that the EOS is expected to be independent of the detailed form of U so long as its parameters can be adjusted to a given M^* , z and K . This implies that U in general has at least 3 parameters and furthermore has sufficient functional flexibility to permit such an adjustment. Also, rather than a U_{34} function one could choose an equivalent but healthy U which is always positive and has no maxima at $\Phi < M$.

The author would like to thank C.E. Price and S. Moszkowski for their crucial comments on an earlier version of this work.

Appendix

We derive eqs. (27)–(31). From eqs. (24) and (25):

$$\frac{d\varepsilon}{d\rho} = \frac{d\varepsilon_v}{d\rho} + T_F^* - \rho_s \frac{d\Phi}{d\rho} + U' \frac{d\Phi}{d\rho} - M. \quad (\text{A.1})$$

With eqs. (17) and (21):

$$\frac{d\varepsilon}{d\rho} = W + T_F^* - M \equiv Zw + T_F^* - M, \quad (\text{A.2})$$

which is equivalent to eq. (27).

From eq. (A.2)

$$\frac{d^2\epsilon}{d\rho^2} = \frac{dW}{d\rho} + \frac{dT_F^*}{d\rho}, \quad (\text{A.3})$$

where from eqs. (7) and (26)

$$\frac{dT_F^*}{d\rho} = \frac{1}{T_F^*} \left[\frac{1}{3} \frac{k_F^2}{\rho} + m^* \frac{dm^*}{d\rho} \right]. \quad (\text{A.4})$$

To obtain $dm^*/d\rho$ we differentiate eq. (22),

$$\frac{d\rho_s}{d\rho} = \frac{m^*}{T_F^*} + \frac{d\rho_s}{dm^*} \frac{dm^*}{d\rho}. \quad (\text{A.5})$$

From eqs. (3) and (21)

$$\frac{dm^*}{d\rho} = -\frac{d\Phi}{d\rho} = -\frac{1}{U''} \frac{d\rho_s}{d\rho}, \quad (\text{A.6})$$

where U'' is defined by eq. (30). Eqs. (A.5) and (A.6) then give

$$\frac{dm^*}{d\rho} = -\frac{m^*}{T_F^*} \left(U'' + \frac{d\rho_s}{dm^*} \right)^{-1}, \quad (\text{A.7})$$

where $d\rho_s/dm^*$ is given by eq. (32). Combining the above results and also using eq. (29) then gives eq. (31).

References

- 1) A.R. Bodmer and C.E. Price, Nucl. Phys. **A505** (1989) 123 as I
- 2) B.D. Serot and J.D. Walecka, Adv. Nucl. Phys. **16** (1986) 1
- 3) P.-G. Reinhard, Rep. Prog. Phys. **52** (1989) 439
- 4) M. Rufa, P.-G. Reinhard, J.A. Maruhn, W. Greiner and M.R. Strayer, Phys. Rev. **C38** (1988) 390
- 5) R.J. Furnstahl, C.E. Price and G.E. Walker, Phys. Rev. **C36** (1987) 2590;
W. Pannert, P. Ring and J. Boguta, Phys. Rev. Lett. **59** (1987) 2420;
Y.K. Gambhir and P. Ring, Phys. Lett. **B202** (1988) 5
- 6) V. Blum *et al.*, Phys. Lett. **A223** (1989) 123
- 7) N.K. Glendenning, Phys. Rev. **C37** (1988) 2733
- 8) M.M. Sharma, W.T.A. Borghols, S. Brandenburg, S. Crona, A. van der Woude and M.N. Harakeh, Phys. Rev. **C38** (1988) 2562
- 9) J. Boguta and A.R. Bodmer, Nucl. Phys. **A292** (1977) 413
- 10) R.B. Wiringa, V. Fiks, and A. Fabrocini, Phys. Rev. **C38** (1988) 1010
- 11) J. Boguta and S. Moszkowski, Nucl. Phys. **A403** (1983) 445
- 12) J. Boguta and H. Stöcker, Phys. Lett. **B120** (1983) 289
- 13) A. Bouyssy, S. Marcos and Pham van Thieu, Nucl. Phys. **A422** (1984) 541
- 14) B.M. Waldhauser, J.A. Maruhn, H. Stöcker, and W. Greiner, Z. Phys. **A328** (1987) 19
- 15) C.E. Price, J.R. Shepard and J.A. McNeil, Phys. Rev. **C41** (1990) 1234; **C42** (1990) 247

Relativistic Mean-Field Theory and the High-Density Nuclear Equation of State

Horst Müller and Brian D. Serot

*Physics Department and Nuclear Theory Center
Indiana University, Bloomington, Indiana 47405*

(November 26, 2024)

Abstract

The properties of high-density nuclear and neutron matter are studied using a relativistic mean-field approximation to the nuclear matter energy functional. Based on ideas of effective field theory, nonlinear interactions between the fields are introduced to parametrize the density dependence of the energy functional. Various types of nonlinearities involving scalar-isoscalar (σ), vector-isoscalar (ω), and vector-isovector (ρ) fields are studied. After calibrating the model parameters at equilibrium nuclear matter density, the model and parameter dependence of the resulting equation of state is examined in the neutron-rich and high-density regime. It is possible to build different models that reproduce the same observed properties at normal nuclear densities, but which yield maximum neutron star masses that differ by more than one solar mass. Implications for the existence of kaon condensates or quark cores in neutron stars are discussed.

I. INTRODUCTION

Numerous calculations have established that relativistic mean-field models provide a realistic description of the bulk properties of finite nuclei and nuclear matter [1,2]. In addition to this successful low-energy phenomenology, these models are often extrapolated into regimes of high density and temperature to extract the nuclear equation of state (EOS), which is the basic ingredient in many astrophysical applications and in microscopic models of energetic nucleus–nucleus collisions.

Based on the original version of Walecka [3] and its extensions [4,5], relativistic mean-field models generally involve the interaction of Dirac nucleons with neutral scalar and vector mesons and with isovector ρ mesons. One of the key observations in their success is that to provide sufficient flexibility, nonlinear self-interactions for the scalar meson must be included [2,4,6–11]. Since these models were proposed to be renormalizable, the scalar self-interactions are limited to a quartic polynomial, and scalar–vector and vector–vector interactions are not allowed [12]. One of the motivations for renormalizability, as discussed in Walecka’s seminal paper, is that once the model parameters are calibrated to observed nuclear properties, one can extrapolate into regimes of high density or temperature without the appearance of new, unknown parameters.

An alternative approach is inspired by *effective* field theories, such as chiral perturbation theory [13,14], which successfully describes the low-energy phenomenology of hadronic Goldstone bosons [15,16]. Although a lagrangian usually serves as the starting point, the meson and baryon fields are no longer considered elementary, and the constraint of renormalizability is dropped. This has several important consequences. First, there is no reason to restrict meson self-interactions to a simple quartic polynomial in the scalar field; on the contrary, one should include all interaction terms that are consistent with the underlying symmetries of QCD. Second, since there are an infinite number of coupling constants, one must find suitable expansion parameters for the systems under consideration, and one must develop a systematic truncation scheme for the effective theory to have any predictive power. Third, extrapolation of calculated results into new regimes of the physical parameters becomes problematic, because the truncation scheme may break down, and predictions can become sensitive to unknown parameters.

Within the framework of effective field theory, mean-field models of nuclear structure and the EOS must be interpreted in a new context. One important observation is that near normal nuclear density, the mean scalar and vector fields (or nucleon self-energies), which we denote as Φ and W , are large on nuclear energy scales but are small compared to the nucleon mass M and vary slowly in finite nuclei. This implies that the ratios Φ/M and W/M and the gradients $|\nabla\Phi|/M^2$ and $|\nabla W|/M^2$ are useful expansion parameters. The assumption of “naturalness” in effective field theory is also important. Naturalness implies that the coefficients of the various terms in the lagrangian, when expressed in appropriate dimensionless form, should all be of order unity. When combined with meaningful expansion parameters, this means that one can anticipate the approximate magnitude of mean-field contributions to the energy (at least up to moderate nuclear densities) and thereby motivate a suitable truncation scheme; if the coefficients are natural, the omitted terms will be numerically

unimportant.¹ Naturalness also implies that one should include *all* possible terms (that is, those allowed by the symmetries) through a given order of truncation; it is *unnatural* for some coefficients to vanish without a relevant symmetry argument.

From this point of view, it is difficult to justify nuclear mean-field models that include only scalar self-interactions [4,6,7,10], and recently, generalizations that also include quartic self-interactions for the neutral vector meson have been discussed [9,19,20]. Moreover, a new analysis involving all meson self-interactions through fourth order in the isoscalar scalar and vector fields has been performed [21]. These extensions give rise to additional model parameters (coupling constants) that must be constrained by calibrating to observed nuclear properties. For the truncation at fourth order to be sensible, the parameters so obtained should exhibit naturalness.

Although it is possible to discuss effective hadronic field theory from the point of view of a lagrangian, as above, the expansion in powers of the mean fields is a low-density expansion, and it is hard to justify the neglect of many-body corrections, which are known to be relevant in nuclear structure and in the EOS. Alternatively, one can consider this expansion at the level of an energy functional or effective action [21]. In such a formulation of the relativistic nuclear many-body problem, the central object is an energy functional of scalar and vector densities (or more generally, vector four-currents) [22–24]. Extremization of the functional gives rise to Dirac equations for occupied orbitals with *local* scalar and vector potentials, not only in the Hartree approximation, but in the general case as well. Rather than work solely with the densities, one can introduce auxiliary variables corresponding to the local potentials, so that the functional depends also on mean meson fields. The resulting field equations have the same form as in a Dirac–Hartree calculation [21], but correlation effects can be included, if the proper energy functional can be found. This procedure is analogous to the well-known Kohn–Sham [25] approach in density-functional theory, with the local meson fields playing the role of (relativistic) Kohn–Sham potentials; by introducing nonlinear couplings between these fields, one can implicitly include additional density dependence in the potentials. Thus the nonlinear meson interaction terms simulate more complicated physics, such as one- and two-pion exchange, or vacuum-loop corrections, which might be calculated directly in a more microscopic many-body approach [20,24]. The fields (and their gradients) again serve as useful expansion parameters at moderate density, so the nonlinear interaction terms can be truncated, leaving a finite number of unknown couplings.

Rather than focus on the calculation of the nonlinear couplings from an underlying effective lagrangian, we wish to concentrate instead on how well the energy functional can be calibrated by fitting the couplings to observed nuclear properties, and on the limitations on the extrapolation of the resulting EOS into the high-density regime. In general, even with a significant truncation, the number of unknown couplings exceeds the number of normalization conditions, which we take to be five properties of infinite nuclear matter: the equilibrium density and binding energy (ρ_0 , $-e_0$), the nucleon effective (or Dirac) mass at equilibrium (M_0^*), the compression modulus (K_0), and the bulk symmetry energy (a_4). (Experience has shown that an accurate reproduction of these five properties leads to realistic

¹It has also been shown recently that the naturalness assumption is consistent with dimensional counting in chiral perturbation theory [17,18].

results when the calculations are extended to finite nuclei [6,7,10,11,21].) Thus families of models can be generated which describe exactly the same nuclear matter properties at equilibrium [19]. We then investigate the differences in the high-density EOS predicted by models within a given family. This question is important for astrophysical applications, particularly in the study of neutron stars; it will be difficult to deduce the existence of “exotic” neutron-star structure (for example, hyperonic matter, kaon condensates, or quark cores) unless the EOS of the more mundane components (neutrons, protons, and electrons) is well constrained.

If our truncation of the energy functional is motivated by low-density behavior, why should we have any confidence at all in a high-density extrapolation? This is indeed the crucial question, and we are not attempting here to justify such an extrapolation; we are merely recognizing that this procedure is often used in neutron-star calculations, even recent ones, without any mention of the implicit assumptions about the absence of additional contributions at high density [26–32]. We therefore feel it is timely to investigate quantitatively the uncertainties in the extrapolated equation of state.

We begin the theoretical analysis with a model that contains meson-meson and meson self-interactions described by an *arbitrary* finite polynomial in the fields. We find that both the asymptotic (high-density) limit of the EOS and the approach to this limit (*i.e.*, the “stiffness”) are model dependent. In particular, one can construct models with the *same* equilibrium nuclear matter properties that yield high-density equations of state ranging all the way from the causal limit ($p = \mathcal{E}$) to one that resembles a free relativistic gas ($p = \mathcal{E}/3$) [9,19]. (Here p is the pressure and \mathcal{E} is the energy density.)

As an explicit example, we consider a model that includes self-interactions for the isoscalar scalar and vector mesons and for the ρ meson up to fourth order in the fields. To our knowledge, this is the first time nonlinear terms in the ρ meson mean field have been included. (Note that the ρ field enters here as an *effective* field whose purpose is to parametrize the isospin dependence; thus, fundamental questions about causal propagation [33,34] and spin mixing [35] are not relevant.) To provide a quantitative measure of the variations in the EOS, we compute neutron star masses, which turn out to be sensitive to the model types and to changes in the parametrizations, *even for models that reproduce the same equilibrium nuclear matter properties*. In some cases, variations in the calculated maximum mass are more than one solar mass.

These results lead us to two basic conclusions. First, existing methods for calibration of the EOS at normal density are *not* sufficient to provide a satisfactory extrapolation into the density regime relevant for neutron stars. The basic problem rests with the quartic neutral vector meson (ω) interaction, which produces major modifications in the high-density behavior. We discuss the existing situation regarding the specification of this term and prospects for improved calibration. Second, we find that if the quartic ω term can be accurately determined, additional higher-order terms (and the quartic ρ term) produce relatively minor changes in the neutron star mass. This occurs because the W^4 term softens the high-density EOS so completely that additional interactions have little effect, at least in the density regime relevant for neutron stars.

These conclusions have important implications, because the contributions to the EOS from the neutrons and protons are commonly believed to be the best understood part of the physical input necessary to describe a dense stellar object. Without well-constrained results

from this part of the EOS, it will be impossible to determine the importance of additional dynamics, for example, the transition from nuclear matter to quark matter in the interiors of neutron stars [36,37,27], or the role of strangeness in the form of hyperons [38,39] or a kaon condensate [40]. As an example of how uncertainties in the basic nuclear EOS can influence these interesting effects, we study the transition from hadronic matter to quark matter using a simple model [37,41] and show the possible variations in the results.

The outline of this paper is as follows: In Sec. II, we present the general model, which involves an arbitrary number of nonlinear meson interactions, and derive the EOS. Based on this general model, Section III is devoted to the high-density limit of the EOS. In Sec. IV, we apply our model to neutron stars. For the quantitative analysis, we initially include self-interactions up to fourth order in the ρ and ω fields and then investigate the consequences of sixth-order and eighth-order ω self-interactions. We also briefly discuss the parameter and model dependence of the transition to quark matter in the central region of the star. Section V contains a short summary and our conclusions.

II. THE NUCLEAR EQUATION OF STATE

We describe the nuclear equation of state using a relativistic approach involving valence Dirac nucleons and effective mesonic degrees of freedom, which are taken to be neutral scalar and vector fields, plus the isovector ρ meson field. Rather than focus directly on a lagrangian, we consider instead as a starting point an *effective action*

$$\Gamma = \Gamma[\phi, V_\mu, \mathbf{b}_\mu] , \quad (1)$$

which is a functional of the meson fields denoted by ϕ , V_μ , and \mathbf{b}_μ for the scalar, vector-isoscalar, and vector-iso-vector field, respectively. In principle, this functional can be calculated in a many-body approach based on a Lagrangian for the nucleon–nucleon interaction, or its general form might be obtained from an underlying theory. Here we will be satisfied to parametrize the effective action, calibrate it as accurately as we can to observed nuclear properties, and then examine the predicted high-density equation of state.

The effective action is related to the thermodynamic potential Ω [41] by

$$i\beta\Omega = \Gamma[\phi, V_\mu, \mathbf{b}_\mu] , \quad (2)$$

where the fields are determined by the general thermodynamic principle that they should make Ω stationary:

$$\frac{\partial\Gamma}{\partial\phi} = \frac{\partial\Gamma}{\partial V_\mu} = \frac{\partial\Gamma}{\partial\mathbf{b}_\mu} = 0 . \quad (3)$$

A basic property of the functional is that it reflects the underlying symmetries [42]. Thus, if we assume that the system possesses two conserved charges, namely, baryon number B and the third component of total isospin I_3 , this gives rise to two chemical potentials μ and ν :

$$\Omega \equiv \Omega(\beta, \mu, \nu) , \quad (4)$$

with

$$B = \int d^3x \rho = -\frac{\partial \Omega}{\partial \mu} , \quad (5)$$

$$I_3 = \frac{1}{2} \int d^3x \rho_3 = -\frac{\partial \Omega}{\partial \nu} , \quad (6)$$

β the inverse temperature, and $\rho_3 \equiv \rho_p - \rho_n$. Note that the fields can be held fixed in evaluating the partial derivatives in Eqs. (5) and (6) by virtue of the extremization conditions (3).

In the field theoretical context [43], one can show that the effective action can be expanded as a power series in gradients of the fields. Thus, after taking the zero-temperature limit, one usually writes

$$\Gamma[\phi, V_\mu, \mathbf{b}_\mu] = \int d^4x \left[-\mathcal{V}_{\text{eff}}(\phi, V_\mu, \mathbf{b}_\mu) + \mathcal{Z}(\phi, V_\mu, \mathbf{b}_\mu, \partial_\nu \phi, \partial_\nu V_\mu, \partial_\nu \mathbf{b}_\mu) \right] , \quad (7)$$

where the second term vanishes in a uniform system, and the dependence on the chemical potentials has been suppressed. For the effective potential, we make the following *Ansatz*:

$$\begin{aligned} \mathcal{V}_{\text{eff}}(\phi, V_\mu, \mathbf{b}_\mu; \mu, \nu) &= \frac{1}{2} m_s^2 \phi^2 - \frac{1}{2} m_v^2 V_\mu V^\mu - \frac{1}{2} m_\rho^2 \mathbf{b}_\mu \cdot \mathbf{b}^\mu \\ &\quad + i \text{tr} \ln Z_\psi(\mu, \nu) - i \text{tr} \ln Z_\psi(0, 0) \\ &\quad + \Delta \mathcal{V}(\phi, V_\mu V^\mu, \mathbf{b}_\nu \cdot \mathbf{b}^\nu; \mu, \nu) , \end{aligned} \quad (8)$$

with a nonlinear potential

$$\Delta \mathcal{V}(\phi, V_\mu V^\mu, \mathbf{b}_\nu \cdot \mathbf{b}^\nu; \mu, \nu) \equiv - \sum_{i,j,k} a_{ijk}(\mu, \nu) \phi^i (V_\mu V^\mu)^j (\mathbf{b}_\nu \cdot \mathbf{b}^\nu)^k \quad (9)$$

that contains at least three powers of the fields: $i + 2j + 2k \geq 3$. The fermionic contributions are represented by a one-body term $\text{tr} \ln Z_\psi$ (with the appropriate zero-density subtraction [44]) and by terms where the fermions have been “integrated out”, which results in a (generally nonanalytic) dependence of the mesonic coefficients a_{ijk} on the chemical potentials μ and ν . There will also be contributions to the a_{ijk} that are independent of the chemical potentials; these arise from integrating out heavy degrees of freedom and vacuum loops. Thus \mathcal{V}_{eff} contains explicit contributions only from valence nucleons and classical meson fields.

The fermionic part $\text{tr} \ln Z_\psi$ is obtained by evaluating the trace of the kernel

$$K(\mu, \nu) = (i\partial^\mu - g_v V^\mu - \frac{1}{2} g_\rho \boldsymbol{\tau} \cdot \mathbf{b}^\mu) \gamma_\mu + \mu \gamma^0 + \frac{1}{2} \nu \tau_3 \gamma^0 - (M - g_s \phi) \quad (10)$$

using Dirac wave functions calculated in the presence of static background fields. The subtraction removes contributions from negative-energy states, which are already included implicitly in the nonlinear parameters a_{ijk} . (See Ref. [44] for an analogous calculation.) The values of the fields are determined by extremization at the given values of μ and ν .

The potential of Eq. (8) represents an effective field theory for the interacting nucleons. Although the exact form of the effective potential is not known, we introduce the meson mean fields as relativistic Kohn–Sham potentials [25] and consider the valence nucleons moving in the resulting local fields. The nonlinear interactions of the fields generate implicit density dependence above and beyond that arising from the couplings in Eq. (10). Thus the

series in Eq. (9) can be interpreted as a Taylor series parametrization of the unknown part of the effective potential, which includes the effects of nucleon exchange and correlations, as well as contributions from other mesons and the quantum vacuum. (See the discussion in Refs. [21,44].)

Although the couplings a_{ijk} generally depend on the chemical potentials, experience with calculations for finite nuclei and nuclear matter, together with explicit computations of exchange and correlation corrections [45], implies that mean fields and *constant* couplings a_{ijk} provide an adequate (albeit approximate) parametrization of these many-body effects. Thus we consider the a_{ijk} as constants in the sequel and leave the study of their dependence on μ and ν as a topic for future investigation. Moreover, at low densities and temperatures, the mean meson fields are small compared to the nucleon mass, and so provide useful expansion parameters [21]. Thus, in practice, the series in Eq. (9) can be truncated at some reasonable order, and the relevant question in this paper is how far one can extrapolate the truncated potential into the high-density regime.

In principle, the unknown coefficients (coupling constants) can be constrained by imposing chiral symmetry and other symmetries of the underlying QCD, such as broken scale invariance. (Lorentz covariance and isospin symmetry are already incorporated explicitly.²⁾ As has been discussed recently, however [11,21], if one assumes a *nonlinear* realization of the chiral symmetry for the pions and nucleons [46], the meson interaction terms are essentially unconstrained.³⁾ We therefore take the couplings as free model parameters in our approach. Obviously, an infinite number of normalization conditions is generally needed to fix their values. Since this is not feasible in practice, we terminate the summation at the finite values i_{\max} , j_{\max} , and k_{\max} .

According to Eq. (3), the thermodynamic potential Ω must be stationary with respect to changes in the fields for fixed values of the proton and neutron chemical potentials

$$\mu_p \equiv \mu + \frac{\nu}{2} = (k_{Fp}^2 + M^{*2})^{1/2} + W + \frac{1}{2}R , \quad (11)$$

$$\mu_n \equiv \mu - \frac{\nu}{2} = (k_{Fn}^2 + M^{*2})^{1/2} + W - \frac{1}{2}R . \quad (12)$$

Here, following Bodmer [19], we define the scaled meson fields $\Phi \equiv g_s \phi$, $W \equiv g_v V_0$, and $R \equiv g_\rho b_0$, with b_0 the timelike, neutral part of the ρ meson field; the effective nucleon mass is $M^* \equiv M - \Phi$. (We work in the rest frame of the infinite matter, where the spatial parts of the vector fields vanish.) The Fermi momenta for protons (k_{Fp}) and neutrons (k_{Fn}) are related to the conserved baryon density

$$\rho = \frac{1}{3\pi^2} (k_{Fp}^3 + k_{Fn}^3) \quad (13)$$

²⁾Note that since the energy functional is an effective functional, we presently know of no reason to exclude terms that explicitly contain the medium four-velocity u^μ , such as $u^\mu V_\mu V^\nu V_\nu$. This issue will be considered in a later publication.

³⁾Broken scale invariance leads to restrictions on the purely scalar interactions, as shown in Refs. [47] and [44], but we will not consider these limitations here. As discussed in the next section, the details of the scalar dynamics do not play a major role in our analysis.

and isovector density

$$\rho_3 = \frac{1}{3\pi^2} (k_{\text{FP}}^3 - k_{\text{Fn}}^3). \quad (14)$$

Using Eqs. (2), (5), and (6), together with relations (11) and (12) for the chemical potentials, it is straightforward to eliminate the chemical potentials in favor of the densities and to compute the pressure p and the energy density $\mathcal{E} = -p + \mu\rho + \frac{1}{2}\nu\rho_3$:

$$p = \frac{1}{3\pi^2} \int_0^{k_{\text{FP}}} dk \frac{k^4}{(k^2 + M^{*2})^{1/2}} + \frac{1}{3\pi^2} \int_0^{k_{\text{Fn}}} dk \frac{k^4}{(k^2 + M^{*2})^{1/2}} \\ + \frac{1}{2c_v^2} W^2 + \frac{1}{2c_\rho^2} R^2 - \frac{1}{2c_s^2} \Phi^2 + \sum_{i,j,k} \bar{a}_{ijk} \Phi^i W^{2j} R^{2k}, \quad (15)$$

$$\mathcal{E} = \frac{1}{\pi^2} \int_0^{k_{\text{FP}}} dk k^2 (k^2 + M^{*2})^{1/2} + \frac{1}{\pi^2} \int_0^{k_{\text{Fn}}} dk k^2 (k^2 + M^{*2})^{1/2} \\ + W\rho + \frac{1}{2} R\rho_3 - \frac{1}{2c_v^2} W^2 - \frac{1}{2c_\rho^2} R^2 + \frac{1}{2c_s^2} \Phi^2 - \sum_{i,j,k} \bar{a}_{ijk} \Phi^i W^{2j} R^{2k}. \quad (16)$$

Here the ratios $c_i^2 = g_i^2/m_i^2$ and $\bar{a}_{ijk} \equiv a_{ijk}/(g_s^i g_v^{2j} g_\rho^{2k})$ have been introduced for convenience.

As noted earlier, the pressure in Eq. (15) and the energy density in Eq. (16) also contain vacuum contributions arising from the partition function of the nucleons. However, at least at the one-baryon-loop level, these vacuum terms can be absorbed in the definition of the nonlinear couplings in Eq. (9) [44], and thus we include explicitly only the contributions from valence nucleons.

At zero temperature, the stationarity conditions of Eq. (3) with fixed chemical potentials are equivalent to an extremization of the energy at fixed baryon and isovector density. This leads to the self-consistency equations

$$\frac{1}{c_s^2} \Phi - \sum_{i,j,k} i \bar{a}_{ijk} \Phi^{i-1} W^{2j} R^{2k} = \rho_s, \quad (17)$$

$$\frac{1}{c_v^2} W + \sum_{i,j,k} 2j \bar{a}_{ijk} \Phi^i W^{2j-1} R^{2k} = \rho, \quad (18)$$

$$\frac{1}{c_\rho^2} R + \sum_{i,j,k} 2k \bar{a}_{ijk} \Phi^i W^{2j} R^{2k-1} = \frac{1}{2} \rho_3, \quad (19)$$

where the scalar density is given by

$$\rho_s = \frac{M^*}{\pi^2} \int_0^{k_{\text{FP}}} dk \frac{k^2}{(k^2 + M^{*2})^{1/2}} + \frac{M^*}{\pi^2} \int_0^{k_{\text{Fn}}} dk \frac{k^2}{(k^2 + M^{*2})^{1/2}}. \quad (20)$$

Because of the factor of 1/2 on the right-hand side of Eq. (19), it follows that the relevant expansion parameters for the energy density are Φ/M , W/M , and $2R/M$. Moreover, by dividing \mathcal{E} by M^4 and expressing the result in terms of these expansion parameters, one can identify the scaled couplings that should all be of roughly the same size if they are “natural”, namely,

$$\frac{1}{2c_s^2 M^2}, \quad \frac{1}{2c_v^2 M^2}, \quad \frac{1}{8c_\rho^2 M^2}, \quad \text{and} \quad \frac{\bar{a}_{ijk} M^{i+2j+2k-4}}{2^{2k}}.$$

III. THE HIGH-DENSITY LIMIT

The coupling constants c_v^2 , c_s^2 , c_ρ^2 , and \bar{a}_{ijk} in Eqs. (15) and (16) enter as unknown model parameters. According to the generally accepted procedure, these parameters will be chosen to reproduce the properties of nuclear matter near equilibrium. The basic ingredient in many astrophysical problems, *e.g.*, neutron-star calculations, is the EOS

$$p = p(\mathcal{E}) , \quad (21)$$

which is then extrapolated into the neutron-rich and high-density regime. Anticipating the results of the next section, one can expect that different parameter sets that lead to identical equilibrium properties produce qualitatively similar equations of state at low densities. The relevant question is whether this qualitatively similar behavior persists at high densities, particularly in the regime important for neutron stars. As a first step in this direction, we investigate the high-density limit of the EOS generated by the model introduced in the previous section.

To make the discussion more transparent, we focus here on pure neutron matter ($k_{Fp} = 0$, $k_{Fn} \equiv k_F$), although nuclear matter in β -decay equilibrium with a finite proton to neutron ratio is necessary to achieve accurate results for maximum neutron star masses. We will return to this issue in the next section.

It is clear that a sufficiently large number of couplings introduces a high degree of flexibility. Due to the nonlinearity of the problem, not all families of parameter sets lead to physically acceptable results, which provides one way to restrict the parameter space. Classes of models can be ruled out if basic physical requirements are violated. For example, one certainly requires that the pressure p be a smooth function of the energy density \mathcal{E} . Moreover, it is necessary that the speed of (first) sound c_1 respect causality and also be real, to ensure stability. That is,

$$0 \leq c_1^2 = \frac{\partial p}{\partial \mathcal{E}} \leq 1 .$$

In addition to these general principles, we require a positive and bounded value of the nucleon effective mass, *i.e.*,

$$0 \leq M^* \leq M . \quad (22)$$

This is motivated by the expectation that physically reasonable models will demonstrate some degree of chiral-symmetry restoration at finite density, leading to a reduction in the nucleon mass, with the most extreme situation corresponding to total restoration of the symmetry. The consequences of Eq. (22) will become more transparent in the following.

By specializing the formalism of the preceding section to pure neutron matter and by using the self-consistency equations (17)–(19), the pressure and energy density can be expressed as

$$\begin{aligned} p &\equiv p_0(k_F, M^*) + \Delta p(\Phi, W, R) \\ &= \frac{1}{3\pi^2} \int_0^{k_F} dk \frac{k^4}{(k^2 + M^{*2})^{1/2}} \\ &\quad + \frac{1}{2c_v^2} W^2 + \frac{1}{2c_\rho^2} R^2 - \frac{1}{2c_s^2} \Phi^2 + \sum_{i,j,k} \bar{a}_{ijk} \Phi^i W^{2j} R^{2k} , \end{aligned} \quad (23)$$

$$\begin{aligned}
\mathcal{E} &\equiv \mathcal{E}_0(k_F, M^*) + \Delta\mathcal{E}(\Phi, W, R) \\
&= \frac{1}{\pi^2} \int_0^{k_F} dk k^2 (k^2 + M^{*2})^{1/2} \\
&\quad + \frac{1}{2c_v^2} W^2 + \frac{1}{2c_\rho^2} R^2 + \frac{1}{2c_s^2} \Phi^2 + \sum_{i,j,k} (2j+2k-1) \bar{a}_{ijk} \Phi^i W^{2j} R^{2k} ,
\end{aligned} \tag{24}$$

where p_0 and \mathcal{E}_0 denote the results for a relativistic, noninteracting gas of spin-1/2 baryons with mass M^* . Note that these expressions include, as a special case, models where only the \bar{a}_{0jk} are nonzero, so that there are no scalar–vector couplings. Moreover, the isovector density in Eq. (19) is replaced by

$$\rho_3 = -\rho = -\frac{1}{3\pi^2} k_F^3 . \tag{25}$$

At high densities, the left-hand sides of the self-consistency equations (18) and (19) must grow linearly in ρ , and thus we start with the *Ansatz*

$$\lim_{\rho \rightarrow \infty} W = w_0 \rho^\alpha , \quad \lim_{\rho \rightarrow \infty} R = r_0 \rho^\beta , \tag{26}$$

where $0 < \alpha, \beta \leq 1$, $w_0 > 0$, and $r_0 < 0$. Since we assume that the effective mass is bounded, we can replace the scalar field by the limit

$$\Phi_\infty \equiv \lim_{\rho \rightarrow \infty} (M - M^*) \leq M . \tag{27}$$

To fulfill the resulting self-consistency equations:

$$\frac{1}{c_v^2} W + \sum_{i,j,k} 2j \bar{a}_{ijk} \Phi_\infty^i W^{2j-1} R^{2k} = \rho , \tag{28}$$

$$\frac{1}{c_\rho^2} R + \sum_{i,j,k} 2k \bar{a}_{ijk} \Phi_\infty^i W^{2j} R^{2k-1} = \frac{1}{2} \rho_3 = -\frac{1}{2} \rho , \tag{29}$$

there must be integers (j_m, k_m) and (j'_m, k'_m) with

$$(2j_m - 1)\alpha + 2k_m\beta = 1 > (2j - 1)\alpha + 2k\beta \quad \text{for all } j \neq j_m, k \neq k_m , \tag{30}$$

$$2j'_m\alpha + (2k'_m - 1)\beta = 1 > 2j\alpha + (2k - 1)\beta \quad \text{for all } j \neq j'_m, k \neq k'_m . \tag{31}$$

(This assumes that only one term in each sum produces the leading asymptotic behavior; if this actually happens for more than one term in a sum, the conclusions below are unchanged.) Using

$$\lim_{\rho \rightarrow \infty} p_0 = \frac{(3\pi^2)^{1/3}}{4} \rho^{4/3} + O(\rho^{2/3}) , \quad \lim_{\rho \rightarrow \infty} \mathcal{E}_0 = \frac{3(3\pi^2)^{1/3}}{4} \rho^{4/3} + O(\rho^{2/3}) , \tag{32}$$

the leading contributions to the pressure and the energy density are found to be

$$\begin{aligned} \lim_{\rho \rightarrow \infty} p &= \frac{(3\pi^2)^{1/3}}{4} \rho^{4/3} + \frac{1}{2c_v^2} w_0^2 \rho^{2\alpha} + \frac{1}{2c_\rho^2} r_0^2 \rho^{2\beta} \\ &\quad + w_0^{2j_m} r_0^{2k_m} \rho^{1+\alpha} \sum_i \bar{a}_{ij_m k_m} \Phi_\infty^i + w_0^{2j'_m} r_0^{2k'_m} \rho^{1+\beta} \sum_i \bar{a}_{ij'_m k'_m} \Phi_\infty^i , \end{aligned} \quad (33)$$

$$\begin{aligned} \lim_{\rho \rightarrow \infty} \mathcal{E} &= \frac{3(3\pi^2)^{1/3}}{4} \rho^{4/3} + \frac{1}{2c_v^2} w_0^2 \rho^{2\alpha} + \frac{1}{2c_\rho^2} r_0^2 \rho^{2\beta} \\ &\quad + w_0^{2j_m} r_0^{2k_m} \rho^{1+\alpha} (2j_m + 2k_m - 1) \sum_i \bar{a}_{ij_m k_m} \Phi_\infty^i \\ &\quad + w_0^{2j'_m} r_0^{2k'_m} \rho^{1+\beta} (2j'_m + 2k'_m - 1) \sum_i \bar{a}_{ij'_m k'_m} \Phi_\infty^i . \end{aligned} \quad (34)$$

To this point, the discussion is rather general. To make the conclusions more concrete, we discuss two distinct situations separately:

1. No coupling between W and R .

In this special case, the asymptotic behavior of the fields is governed by their highest powers in the potential (9). From Eqs. (30) and (31), we obtain

$$\alpha = \frac{1}{2j_{\max} - 1} \quad , \quad \beta = \frac{1}{2k_{\max} - 1} .$$

For $j_{\max} = 1, k_{\max} \geq 1$ or $j_{\max} \geq 1, k_{\max} = 1$, the quadratic terms dominate the right-hand sides of Eqs. (33) and (34), so that

$$\lim_{\rho \rightarrow \infty} \frac{1}{c_v^2} W^2 \propto \rho^2 \quad \text{or} \quad \lim_{\rho \rightarrow \infty} \frac{1}{c_\rho^2} R^2 \propto \rho^2 .$$

This case includes the original version of the Walecka model [3] and generates the limiting behavior

$$\lim_{\rho \rightarrow \infty} p = \mathcal{E} . \quad (35)$$

The sums in Δp and $\Delta \mathcal{E}$ contribute to the leading order only if $j_{\max} = 2, k_{\max} \geq 2$ or $j_{\max} \geq 2, k_{\max} = 2$. In this case, the quadratic terms can be neglected, and Δp and $\Delta \mathcal{E}$ are of the same order as the contributions from the ideal-Fermi-gas terms. However, the factors in Eq. (34) conspire such that

$$\lim_{\rho \rightarrow \infty} \Delta p = \frac{1}{3} \Delta \mathcal{E} , \quad (36)$$

and the functional form of the limiting EOS resembles that of an ideal Fermi gas:

$$\lim_{\rho \rightarrow \infty} p = \frac{1}{3} \mathcal{E} . \quad (37)$$

In the remaining cases ($j_{\max} > 2, k_{\max} > 2$), the dominant contributions arise solely from p_0 and \mathcal{E}_0 , which also leads to Eq. (37). Note here the importance of Eq. (22), which implies that in the high-density limit, M^* becomes negligible, at least to leading order.

2. At least one coupling between W and R .

From Eqs (30) and (31), it follows directly that

$$\alpha \leq \frac{1}{3} \quad \text{and} \quad \beta \leq \frac{1}{3}.$$

The quadratic contributions in the fields are negligible, and Δp and $\Delta\mathcal{E}$ contribute to the leading term only if $\alpha = \beta = 1/3$, where again Eq. (36) holds. In any event, this leads to the limit of Eq. (37).

To summarize, we conclude that the high-density limit of the EOS is strongly influenced by nonlinear meson–meson interactions, which agrees with the conclusion of Bodmer and Price [9,19]. The limit in Eq. (35) obtained in the original version of the Walecka model [3] is a special case; in the more general situation, the nuclear matter EOS approaches that of an ideal Fermi gas, given by Eq. (37). We will show in the next section that these two limits can be achieved using different models with parameter sets that reproduce the same equilibrium properties of nuclear matter.

IV. CONSEQUENCES FOR NEUTRON STARS

The high-density limit of the EOS and the way in which the matter approaches the asymptotic regime have important consequences in neutron star calculations. The masses and radii of stars are sensitive to the stiffness of the EOS, thus providing a quantitative measure for studying the impact of the nonlinear interaction terms in Eq. (9).

To be specific, it is necessary to choose an explicit potential, and we begin with the form

$$\sum_{i,j,k} a_{ijk} \phi^i (V_\mu V^\mu)^j (\mathbf{b}_\mu \cdot \mathbf{b}^\mu)^k = -\frac{\kappa}{3!} \phi^3 - \frac{\lambda}{4!} \phi^4 + \frac{\zeta}{4!} g_v^4 (V_\mu V^\mu)^2 + \frac{\xi}{4!} g_\rho^4 (\mathbf{b}_\mu \cdot \mathbf{b}^\mu)^2, \quad (38)$$

which includes a subset of the meson self-interactions up to fourth order in the fields. As discussed in the Introduction, setting some of the allowed cubic and quartic couplings to zero is “unnatural”, but as we will discover, the model defined by Eq. (38) is already general enough to produce significant differences in predicted neutron star masses, and restoring the omitted couplings will lead to even more variation in the results. Moreover, the present model can be related to the most common models discussed in the literature, and it generalizes them to include a nonlinear isovector interaction. The motivation for adding the quartic rho-meson term is that one expects this coupling to be essentially unconstrained by normal nuclear observables, where the neutron–proton asymmetry is low, but it may have significant impact on the neutron-rich matter in neutron stars. As noted earlier, since the meson fields are effective (Kohn–Sham) potentials, we are not concerned here with their elementary excitations, and considerations of causality [33,34] are unimportant.

In nuclear matter calculations, this model contains seven free parameters. The polynomial in Eq. (38) contains four couplings that we may write as $\bar{\kappa} \equiv \kappa/g_s^3$, $\bar{\lambda} \equiv \lambda/g_s^4$, ζ , and ξ ; in addition, values for the three ratios $c_i^2 = g_i^2/m_i^2$ ($i = s, v, \rho$) are needed. Five of the seven parameters can be chosen to reproduce the equilibrium properties of symmetric nuclear matter, which we take as the equilibrium density and binding energy $(\rho_0, -e_0)$, the

nucleon effective (or Dirac) mass at equilibrium (M_0^*), the compression modulus (K_0), and the bulk symmetry energy (a_4). The first three of these are tightly constrained [11], whereas the latter two are not. In principle, the sensitivity of the high-density EOS to reasonable variations in K_0 and a_4 could be examined, but for simplicity, we keep their values fixed in most of our calculations. The “standard” set of equilibrium properties used here are listed in Table I; these are motivated by successful descriptions of bulk and single-particle nuclear properties [11, 44, 21]. The nucleon mass is fixed at its empirical value ($M = 939$ MeV).

Our primary goal is to study the influence of the nonlinear vector-meson interactions on neutron star masses. Since there are more free couplings than normalization conditions, we proceed as follows: We choose values for the couplings ζ and ξ and determine the remaining couplings by requiring that they reproduce the desired equilibrium properties. This is achieved by solving a set of transcendental equations that relate the parameters directly to the nuclear matter properties [19, 21]. Although we have no specific guidance on the allowed values of ζ and ξ , we rely on the assumption of naturalness, and based on the discussion at the end of Sec. II, we observe that the following parameter combinations should all be of roughly equal size:

$$\frac{1}{2c_s^2 M^2}, \quad \frac{1}{2c_v^2 M^2}, \quad \frac{1}{8c_\rho^2 M^2}, \quad \frac{\bar{\kappa}}{6M}, \quad \frac{\bar{\lambda}}{24}, \quad \frac{\zeta}{24}, \quad \text{and} \quad \frac{\xi}{384}.$$

Typical values for the first three parameters are between 0.001 and 0.002, so that the natural values of ζ and ξ are roughly limited to $0 \leq \zeta \lesssim 0.06$ and $0 \leq \xi \lesssim 1.0$. (To avoid abnormal solutions of the vector field equations, *i.e.*, those with finite mean fields at zero density, ζ and ξ must be positive.⁴⁾ We will include results for vanishing ζ and ξ , which are in a strict sense unnatural, in order to make contact with earlier calculations. For a more thorough discussion of naturalness and its implications, see Ref. [21].

Using the notation of Sec. II, the self-consistency equations (17)–(19) can be written as

$$\frac{1}{c_s^2} \Phi + \frac{\bar{\kappa}}{2} \Phi^2 + \frac{\bar{\lambda}}{6} \Phi^3 = \rho_s, \tag{39}$$

$$W \left(\frac{1}{c_v^2} + \frac{\zeta}{6} W^2 \right) = \rho, \tag{40}$$

$$R \left(\frac{1}{c_\rho^2} + \frac{\xi}{6} R^2 \right) = \frac{1}{2} \rho_3 = -\frac{1}{2} \rho. \tag{41}$$

The expressions for the pressure and the energy density follow as

$$\begin{aligned} p &= \frac{1}{3\pi^2} \int_0^{k_F} dk \frac{k^4}{(k^2 + M^{*2})^{1/2}} \\ &\quad + \frac{1}{2c_v^2} W^2 + \frac{\zeta}{24} W^4 + \frac{1}{2c_\rho^2} R^2 + \frac{\xi}{24} R^4 - \frac{1}{2c_s^2} \Phi^2 - \frac{\bar{\kappa}}{6} \Phi^3 - \frac{\bar{\lambda}}{24} \Phi^4, \end{aligned} \tag{42}$$

⁴⁾Note that positive ζ and ξ imply that the resulting nonlinear interactions are *attractive*. This constraint on the highest-order vector interactions appears to be general and explains why our earlier analysis finds that nonlinear interactions soften the equation of state.

$$\begin{aligned}\mathcal{E} = & \frac{1}{\pi^2} \int_0^{k_F} dk k^2 (k^2 + M^{*2})^{1/2} \\ & + \frac{1}{2c_v^2} W^2 + \frac{\zeta}{8} W^4 + \frac{1}{2c_\rho^2} R^2 + \frac{\xi}{8} R^4 + \frac{1}{2c_s^2} \Phi^2 + \frac{\bar{\kappa}}{6} \Phi^3 + \frac{\bar{\lambda}}{24} \Phi^4.\end{aligned}\quad (43)$$

We begin our discussion with the model introduced by Bodmer and Price [9], which corresponds to $\zeta = 0$. According to the discussion in the preceding section, this model has the interesting feature that the high-density EOS of pure neutron matter approaches $p = \mathcal{E}$, while in symmetric matter, where the mean-field of the ρ meson vanishes, the EOS approaches the massless Fermi gas limit, given by Eq. (37). In Fig. 1, we show the binding energy curves for symmetric and pure neutron matter for different values of the nonlinear coupling ζ . We emphasize that all parametrizations reproduce the same equilibrium properties listed in Table 1.

At low densities, all the curves approach a common limit, because the nonlinear terms do not contribute at leading order in a low-density expansion. At higher densities, the softening of the EOS as ζ increases is clearly visible, at least for symmetric matter. The softening in neutron matter is more apparent in Fig. 2. In the regime of intermediate density, $200 \lesssim \mathcal{E} \lesssim 1000$ MeV/fm³, the EOS becomes softer with increasing values of ζ [19]. To study the approach to the asymptotic limit, we examine the nonleading terms in the high-density expansion:

$$\lim_{\mathcal{E} \rightarrow \infty} p = \mathcal{E} - \frac{1}{6\pi^2} \left(\frac{72\pi^4}{4c_v^2 + c_\rho^2} \right)^{2/3} \mathcal{E}^{2/3} + O(\mathcal{E}^{1/3}) \quad \text{for } \zeta = 0, \quad (44)$$

$$\lim_{\mathcal{E} \rightarrow \infty} p = \mathcal{E} - \frac{1}{6\pi^2} \left(\frac{72\pi^4}{c_\rho^2} \right)^{2/3} \left[1 + \left(\frac{2}{\pi^2 \zeta} \right)^{1/3} \right] \mathcal{E}^{2/3} + O(\mathcal{E}^{1/3}) \quad \text{for } \zeta \neq 0, \quad (45)$$

which reveals two important features. First, the $\zeta \neq 0$ results are *nonanalytic* in ζ . Thus one cannot reproduce Eq. (44) by taking the $\zeta \rightarrow 0$ limit of Eq. (45); at least as far as ζ is concerned, the high-density expansion is essentially a strong coupling expansion. Second, we observe that the coefficient of the nonleading term is smaller for $\zeta = 0$ for two reasons: the appearance of the isoscalar coupling c_v^2 in the denominator and the absence of the multiplicative factor containing ζ . (Note that c_ρ^2 is independent of ζ .) These two features produce a coefficient that is roughly an order of magnitude smaller for $\zeta = 0$ than for $\zeta \neq 0$, which explains the relatively slow approach to the asymptotic limit in the latter case, as is evident from Fig. 2.

The consequences for neutron stars can be studied in Fig. 3, where the star masses are shown as a function of the central mass density ρ_c . As expected from Fig. 2, the maximum mass decreases with increasing ζ . This decrease is substantial: from $M_{\max} = 2.9 M_\odot$ for $\zeta = 0$ to $M_{\max} = 2.1 M_\odot$ for $\zeta = 0.06$, which is roughly 30%. The shifts in the maximum mass are most dramatic for small couplings; for larger couplings, the softening effects begin to saturate.

To understand this result, it is useful to identify the regime of energy density that is most important in determining the mass of the star. This regime can be deduced from Fig. 4, where we show the radial mass density distributions for several neutron stars, as well as the corresponding energy densities. Observe that most of the mass is generated at radii between

6 and 12 km, which corresponds to energy densities of several hundred MeV/fm³. As can be seen from Fig. 2, this includes the regime where the EOS is sensitive to ζ , because this is where the W^4 contribution to the EOS begins to become important. Note, however, that the contribution of the W^4 term in this regime is still smaller than that of the W^2 term; the quartic term does not begin to dominate until the energy density reaches several thousand MeV/fm³, as indicated by the coalescence of the dashed and dotted curves in Fig. 2.

We now return to the general form in Eq. (38) and allow nonlinear self-interactions of the ρ mesons. In contrast to the isoscalar coupling ζ , the new quantity ξ does not enter in the calculation of our five “standard” equilibrium properties of nuclear matter, and the other parameters are determined independently. This is true even for the symmetry energy, because the new coupling ξ first appears at order $(N-Z)^4$ in an expansion around symmetric nuclear matter. In principle, ξ could be constrained by fits to liquid-drop expansions of the energy, but in most such fits this parameter is set to zero. (We found only one nonzero value in the literature [48].) Thus, at present, contributions to the symmetry energy beyond terms of order $(N-Z)^2$ are practically unconstrained.

Fig. 3 shows the binding energy of nuclear matter as a function of the proton fraction y for two different densities. The curves are calculated for various values of ξ with ζ held fixed. For clarity, we plot the fractional shift in \mathcal{E} relative to its value with $\xi = 0$. At normal nuclear density, results for different ξ are virtually indistinguishable, but at high density, the curves differ by a few percent when the proton fraction becomes very small. This demonstrates that it is possible to generate families of models that reproduce identical properties of nuclear matter at low and normal densities, but which generate different predictions at high densities.

According to the analysis in the preceding section, the EOS asymptotically approaches the massless Fermi gas limit for both symmetric and neutron matter. The high-density expansion for neutron matter corresponding to Eq. (45) is

$$\lim_{\mathcal{E} \rightarrow \infty} p = \frac{1}{3}\mathcal{E} + \frac{2\pi}{3} \frac{\left[\frac{1}{c_v^2} \left(\frac{2}{\pi^2 \zeta} \right)^{2/3} + \frac{1}{c_\rho^2} \left(\frac{1}{\pi^2 \xi} \right)^{2/3} \right]}{\left[1 + \left(\frac{2}{\pi^2 \zeta} \right)^{1/3} + \left(\frac{1}{\pi^2 \xi} \right)^{1/3} \right]^{1/2}} \mathcal{E}^{1/2} + O(\mathcal{E}^0). \quad (46)$$

In contrast to the previous case, the asymptotic limit is now approached from above. Moreover, the analytical form has changed, since Eq. (46) indicates a series in powers of $\mathcal{E}^{1/2}$.

The dependence of the neutron star masses on ξ follows the same trend as found for ζ . This can be gleaned from Fig. 3, which shows results for pure neutron matter. For fixed ζ , the maximum mass decreases with increasing ξ , although the effect of this new parameter is smaller (less than a 10% change in the maximum mass), given the limitation on parameter values imposed by naturalness.

A more complete picture of M_{\max} is given in Fig. 7, where the variations with both ζ and ξ are shown. It is apparent that parameter sets that yield identical properties near nuclear equilibrium can still generate values of the maximum mass that differ by as much as one solar mass. We find variations between $M_{\max} = 2.9 M_\odot$ and $M_{\max} = 1.9 M_\odot$ for stars composed of pure neutron matter. The masses are most sensitive to changes at small values of the couplings, particularly for $\zeta \approx 0$, which can be related to the nonanalytic form of the EOS in terms of ζ and ξ . [See Eqs. (44)–(46).] As seen earlier, the effect of ξ is smaller than that of ζ .

So far, we have considered pure neutron matter, which gives only a qualitative picture of neutron star properties. For a more realistic description, it is necessary to consider beta-stable matter, as this includes the protons, which softens the EOS. Maximum neutron star masses for beta-stable matter are also shown in Fig. 7. The dependence on the isoscalar coupling ζ is similar to that obtained earlier (the maximum mass varies between $M_{\max} = 2.8 M_{\odot}$ and $M_{\max} = 1.8 M_{\odot}$), but the influence of the isovector coupling ξ is less drastic, since the matter becomes significantly more symmetric in the region that gives the largest contribution to the mass.

In Fig. 8, we examine the dependence of the maximum mass on the compression modulus at equilibrium, which is not particularly well known. (Relativistic mean-field models with $200 \lesssim K_0 \lesssim 350$ MeV can produce accurate nuclear binding-energy systematics and surface energetics [21].) The shaded band shows the total predicted variation in maximum mass when both ζ and ξ are varied within the bounds imposed by naturalness. The dashed curve shows the predicted variation when K_0 is varied at fixed ζ and ξ . Evidently, the variations in the maximum mass arising from the possibility of nonlinear vector meson interactions is much greater than that arising from the uncertainty in the compressibility.

These results raise the interesting question of whether the only significant nonlinearity is the quartic, isoscalar vector interaction. In other words, once one takes $\zeta \neq 0$ to soften the EOS at high densities, does the addition of further nonlinearities produce only small effects? To examine this question, we extend the model of Eq. (38) to include sixth-order and eighth-order terms involving the vector-isoscalar meson:

$$\Delta\mathcal{V}' = -\frac{\zeta'}{6!}g_v^6(V_\mu V^\mu)^3 - \frac{\zeta''}{8!}g_v^8(V_\mu V^\mu)^4. \quad (47)$$

Thus $\zeta'/6!$ and $\zeta''/8!$ are the relevant ratios to be included in the parameter list given earlier, and we will initially set ξ to zero and examine the consequences of varying ζ , ζ' , and ζ'' within the bounds imposed by naturalness.

Figure 9 shows neutron star masses as higher-order vector nonlinearities are included sequentially. Evidently, the quartic interactions are the most important, producing a roughly 30% variation in the maximum. The effects of the sixth-order term are quite modest (roughly 10%), while the eighth-order contributions are essentially negligible (roughly 2%). Here the parameters are varied within the natural ranges $0 \leq \zeta \leq 0.06$, $0 \leq \zeta' \leq 1.2$, and $0 \leq \zeta'' \leq 60$. Thus we have the encouraging result that once the W^4 interaction has been accurately calibrated, contributions from higher-order nonlinearities are relatively unimportant. To indicate the most extreme reduction in maximum mass possible in the present model, the cross in Fig. 9 shows $M_{\max} = 1.58 M_{\odot}$, which is obtained for *beta-stable matter* when the couplings $\zeta = 0.06$, $\zeta' = 1.2$, $\zeta'' = 60$, and $\xi = 1.5$ are included. Note that this value of M_{\max} is only slightly ($\approx 10\%$) larger than that of the most massive observed neutron stars.

Our analysis to this point has revealed significant model and parameter dependence in the high-density EOS. It is therefore of interest to see if these variations influence predictions arising from other relevant dynamics in systems with high densities. As an example, we study the effect of the high-density hadronic EOS on the existence of quark-matter cores in neutron stars. We adopt a simple two-phase model [37,4] based on a first-order (van der Waals) phase transition between the hadronic and quark phase. Although there are indications from QCD lattice calculations that the hadron/quark phase transition is second-order at vanishing chemical potential [50,51] (for massless quarks), the true behavior of the

transition at finite density (and indeed, whether one actually exists) is unknown at present. Until more reliable information is available, one must resort to a separate description of the quark phase and the hadronic phase. Moreover, whereas a detailed description involving beta-stable matter requires a careful treatment of the phase transition in systems with two conserved charges (baryon number and isospin) [27,49], here we will be satisfied with a qualitative discussion based on pure neutron matter. This is certainly reasonable, given the large uncertainties we have already found in the hadronic EOS at high density.

We adopt the simple EOS involving massless u and d quarks given by

$$p = \frac{1}{3}\mathcal{E} - \frac{4}{3}b, \quad (48)$$

where the confinement property of QCD (or alternatively, the anomaly in the trace of the energy-momentum tensor) is modeled by a positive constant b , which represents the energy per unit volume in the vacuum.

We return to the hadronic model of Eq. (38), which leads to the high-density expansion in Eq. (46). Our discussion is based on the simple observation that independent of the actual nature of the transition, it is driven purely by the energetics in the two phases.

By comparing Eq. (48) with the expansion in Eq. (46), one observes that in the quark phase, the limit $p = \mathcal{E}/3$ is approached from below, whereas in neutron matter, for the general case $\zeta > 0$ and $\xi > 0$, the limit is approached from above. To decide whether a transition takes place, it is necessary to compare the energy/baryon in both phases. For the quark phase it is expressed as [37]

$$\mathcal{E}/\rho = \frac{3}{4}\pi^{2/3}f(\alpha_s)\rho^{1/3} + b/\rho, \quad (49)$$

with

$$f(\alpha_s) = (1 + 2^{4/3})(1 + \frac{2\alpha_s}{3\pi}),$$

which includes the lowest-order contribution in α_s (the exchange energy). As discussed in the preceding section, in hadronic models that are characterized by Eqs. (44) and (45), the quadratic terms dominate at high densities, so that

$$\lim_{\mathcal{E} \rightarrow \infty} \mathcal{E}/\rho \propto \rho, \quad (50)$$

for $\zeta \geq 0$ and $\xi = 0$. This is also true if $\zeta = 0$ and $\xi \geq 0$. Thus, at sufficiently high densities, neutron matter always has higher energy compared to the quark phase [37], and the two phases can be connected by a Maxwell construction, which signals the transition from hadron to quark matter.

The situation is different in the general case $\zeta > 0$, $\xi > 0$. For the asymptotic form of the energy corresponding to Eq. (46), one obtains

$$\lim_{\mathcal{E} \rightarrow \infty} \mathcal{E}/\rho = \frac{3}{4}(3\pi^2)^{1/3} \left[1 + \left(\frac{2}{\pi^2 \zeta} \right)^{1/3} + \frac{1}{2} \left(\frac{1}{\pi^2 \xi} \right)^{1/3} \right] \rho^{1/3} + O(\rho^{-1/3}), \quad (51)$$

which is, up to the prefactor, the same leading behavior as in Eq. (49) for the quark phase. Therefore a phase transition is possible, *i.e.*, neutron matter has higher energy, only if

$$3^{1/3} \left[1 + \left(\frac{2}{\pi^2 \zeta} \right)^{1/3} + \frac{1}{2} \left(\frac{1}{\pi^2 \xi} \right)^{1/3} \right] > f(\alpha_s) . \quad (52)$$

This remarkable observation implies that for sufficiently large values of the nonlinear couplings, the matter remains in the hadron (neutron) phase, at least in the simple model discussed here. More generally, one observes that independent of the asymptotic form, increasing the couplings ζ and ξ increases the density at which the phase transition occurs (if it does), since the hadronic EOS becomes softer as the nonlinear couplings increase.

The different possibilities are illustrated in Fig. 10. The curve labeled *a* corresponds to Eq. (50); the asymptotic behavior is clearly different from the quark EOS. The phase transition occurs at roughly $3\rho_0$, and the Maxwell construction is indicated by the dotted line. In the situation described by curve *b*, neutron matter and quark matter have a similar asymptotic behavior, but the condition (52) remains true, and the two curves cross, leading to a phase transition at roughly $6\rho_0$. Finally, curve *c* lies completely below the quark EOS and a transition is not possible; neutron matter is stable at all densities.

If one introduces interaction terms of higher than fourth order in the fields, for example, $(V_\mu V^\mu)^3$, the hadronic energy is dominated by the Fermi gas contribution, and Eq. (51) must be replaced by

$$\lim_{\mathcal{E} \rightarrow \infty} \mathcal{E}/\rho = \frac{3}{4} (3\pi^2)^{1/3} \rho^{1/3} + O(\rho^{-1/3}) . \quad (53)$$

Since $3^{1/3} < f(\alpha_s)$, no transition is possible in the asymptotic regime for any choice of hadronic parameters in this case. On the other hand, the transition regime also depends on the model and parameters used for the description of the quark phase. In our model, the vacuum constant b and strong coupling α_s can be used to shift the transition point substantially [52,53], so that a transition may occur outside the asymptotic regime. It is clear, however, that the strong model dependence in the hadronic EOS introduces large uncertainties in any attempted prediction of these values.

The consequences for neutron stars in this model follow straightforwardly. Nonlinear vector meson interactions soften the hadronic EOS, which lowers the maximum neutron star mass and increases the density of the transition to quark matter. In contrast, a stiff hadronic EOS lowers the density of the phase transition, and since the quark matter EOS is soft, also tends to decrease the maximum star mass. Thus it may be impossible to decide, from neutron star masses alone, whether quark matter cores exist in neutron stars, and similar conclusions may be drawn about other exotic phenomena that soften the EOS. (The situation is complicated further by the continuous nature of the transition when two conserved charges are involved, which is the more physical case [27].) Whereas it might be possible, using the results of more advanced calculations of the finite-density hadron/quark phase transition, to rule out certain parametrizations of the hadronic EOS, existing uncertainties in both the nature of the phase transition and in the high-density hadronic EOS preclude any definite conclusions at this time.

V. SUMMARY

In this paper we study the equation of state of nuclear and neutron-star matter based on relativistic mean-field theory. Our starting point is an effective action (or energy functional)

containing Dirac nucleons and local scalar and vector fields. These fields are interpreted as relativistic Kohn–Sham potentials, and nonlinear interactions between the fields are introduced to parametrize the density dependence of the energy functional. We calibrate the energy functional by observing that at normal nuclear densities, the ratios of the mean fields to the nucleon mass are small, and thus the nonlinear interactions can be truncated at some low order in the fields. The unknown parameters can then be fit to properties of nuclear matter near equilibrium that are known to be characteristic of the observed bulk and single-particle properties of nuclei.

We then extrapolate the resulting equation of state into the neutron-rich, high-density regime to calculate the properties of neutron stars. Two problems arise in the extrapolation: First, even with a significant truncation of the energy functional, the unknown parameters are underdetermined. Thus there exist families of parameters that reproduce exactly the same nuclear matter properties near equilibrium, but which produce potentially different high-density equations of state. Second, terms omitted from the functional because they are negligible at normal density may become important at densities relevant for neutron stars. This is true even if we assume that the coupling parameters are “natural”, which means that they are all of roughly the same size when expressed in appropriate dimensionless ratios.

Our basic goal is to determine, in light of these two problems, whether the calibration at equilibrium nuclear matter density is sufficient to predict a maximum neutron star mass within a reasonably small range. This is relevant in view of recent calculations that hope to see evidence for “new” physics in neutron stars (such as quark cores, strange matter, or kaon condensates) based on the need for a softer high-density equation of state than that provided by neutrons, protons, and electrons alone. These calculations assume that the high-density behavior of these more mundane components is well known, and in particular, that the contributions of many-nucleon forces are negligible [27–32]. These many-body, density-dependent forces are precisely the ones that are difficult to calibrate using observed nuclear properties; the question is whether one can build nuclear equations of state with different types of many-body forces that all reproduce the observed properties near equilibrium, but which yield significantly different results at high density.

By beginning with a meson self-interaction potential containing arbitrary powers of scalar-isoscalar (σ), vector-isoscalar (ω), and vector-isovector (ρ) fields, we show that the meson nonlinearities can have a profound effect on the high-density equation of state. In models where the vector mesons enter the potential at most quadratically, the equation of state is stiff and asymptotically approaches $p = \mathcal{E}$. (The Walecka model is a special case.) In models where the vector fields enter with high powers, these fields become negligible at high density, and the asymptotic equation of state resembles that of a free, relativistic gas: $p = \mathcal{E}/3$. The intermediate case occurs when the vector fields enter quartically; the asymptotic equation of state is still soft ($p = \mathcal{E}/3$), but the approach to the asymptotic limit is determined by the coupling parameters.

We illustrate these results using specific models containing quartic ω and ρ meson couplings and also sixth- and eighth-order ω couplings. All models are calibrated to exactly the same nuclear properties at equilibrium, for all choices of parameters. We find that by far the most important coupling constant is that of the quartic ω term; even when restricted by the requirements of naturalness, variations in this parameter can produce variations of nearly one solar mass in the predicted maximum neutron star mass. (This is true for both

pure neutron matter and for beta-stable matter.) This uncertainty is clearly relevant on the scale on which one hopes to identify new, exotic effects. Moreover, increasing the strength of the quartic coupling softens the equation of state, which is precisely the effect sought from the exotica. The impact of a quartic ρ meson coupling is smaller, and its effects are only appreciable in stars made of pure neutron matter; the maximum masses of stars computed with beta-stable matter show little change when this parameter is varied within the bounds imposed by naturalness. Similarly, sixth-order ω interactions have only a modest effect on the predicted maximum mass, and by the time the eighth-order terms are included, the high-density equation of state is already so soft that these terms are negligible.

We emphasize that the importance of these many-body effects is not limited to the domain of relativistic mean-field theories; equations of state based on nonrelativistic potentials [26] use interactions that are calibrated to few-body systems and that are insensitive to possible six- or eight-body forces that may be relevant at high density. This is especially important because a mean-field calculation with four-component spinors and just *two-body* Lorentz scalar forces already implicitly contains an infinite string of many-body forces if it is recast in terms of two-component spinors.

To illustrate these difficulties more concretely, we also study the role of the hadron/quark phase transition in a simple two-phase model with a first-order transition. We find that with couplings well within the bounds of naturalness, it is possible to push the phase transition to arbitrarily high density, and even to make it disappear altogether. Although the absence of a phase transition is probably unrealistic and could serve to exclude some values of the hadronic parameters, there are still too many uncertainties on both sides of the transition (as well as in the nature of the transition itself!) to make any definitive statements.

We therefore conclude that existing methods for calibrating the nuclear equation of state for extrapolation into the neutron-rich, high-density regime appropriate for neutron stars cannot constrain the predicted maximum star mass well enough to make reliable statements about the existence of “new” physics beyond the dynamics of neutrons, protons, and electrons. We show that the uncertainties arising from an incomplete knowledge of the hadronic many-body forces are much larger than those arising from an imperfect knowledge of the properties of nuclear matter near equilibrium, such as the nuclear matter compression modulus. Even the old question of the role of the hadron/quark phase transition is problematic, since the high-density hadronic equation of state can be made essentially as soft as desired by the addition of nonlinear interactions that are still consistent with equilibrium nuclear matter properties.

One positive conclusion is that the most important nonlinear parameter is that of the quartic ω interaction. If this term could be accurately calibrated, the uncertainties introduced by other nonlinear interactions are likely to be tolerable. (One caveat: we do not study carefully the sensitivity to variations in mixed scalar–vector interactions because of the overwhelming sensitivity to the quartic ω term; if the latter were well constrained, the role of scalar–vector interactions should be examined in more detail.) Although this coupling has not been extensively studied in mean-field calculations, there are several possibilities for determining it reasonably well. First, since a quartic ω interaction leads to a nonlinear density dependence in the vector part of the baryon self-energy, one could calibrate this interaction by fitting to the self-energy obtained in a Dirac–Brueckner–Hartree–Fock calculation, for example. Although some initial attempts at this procedure have been made [20],

the resulting parameters are not always natural; it is probably necessary to repeat the procedure using all possible scalar and vector self-interactions through fourth order and to fit both the scalar and vector part of the self-energy simultaneously. Second, the nonlinearities in the energy functional can be interpreted in terms of effective masses for the vector and scalar mesons (defined by diagonalizing the matrix of appropriate second derivatives of the energy functional). This may provide useful constraints in the future, if concrete empirical information on these effective masses becomes available. Third, it is possible that additional observables in finite nuclei could constrain the nonlinear interactions. For example, some recent work suggests that the ratio of the nuclear matter “skewness” (which is related to the third derivative of the energy with respect to density at equilibrium) to the compression modulus K is constrained by monopole vibrations. Although a recent calculation of nuclear ground-state properties shows little correlation with this ratio [21], a more detailed examination of dynamical effects could provide meaningful constraints.

To summarize, precise predictions of the properties of neutron stars apparently require more accurate calibrations of the nuclear equation of state than are currently available. It is especially important to have the high-density behavior of the “standard” components (neutrons, protons, and electrons) under control before one can make reliable statements about the existence of “new” physics. Since the window on experimentally observable nuclear properties is a narrow one, producing an equation of state that can be extrapolated with confidence remains a major challenge.

ACKNOWLEDGMENTS

We thank R. J. Furnstahl and H.-B. Tang for useful comments. This work was supported in part by the Department of Energy under Contract No. DE-FG02-87ER40365.

REFERENCES

- [1] B. D. Serot and J. D. Walecka, *Adv. Nucl. Phys.* 16 (1986) 1.
- [2] B. D. Serot, *Rep. Prog. Phys.* 55 (1992) 1855.
- [3] J. D. Walecka, *Ann. Phys. (N.Y.)* 83 (1974) 491.
- [4] J. Boguta and A. R. Bodmer, *Nucl. Phys. A* 292 (1977) 413.
- [5] B. D. Serot, *Phys. Lett.* 86 B (1979) 146; 87 B (1979) 403 (E).
- [6] P. G. Reinhard, M. Rufa, J. Maruhn, W. Greiner, and J. Friedrich, *Z. Phys. A* 323 (1986) 13.
- [7] R. J. Furnstahl, C. E. Price, and G. E. Walker, *Phys. Rev. C* 36 (1987) 2590.
- [8] R. J. Furnstahl and C. E. Price, *Phys. Rev. C* 40 (1989) 1398.
- [9] A. R. Bodmer and C. E. Price, *Nucl. Phys. A* 505 (1989) 123.
- [10] Y. K. Gambhir, P. Ring, and A. Thimet, *Ann. Phys. (N.Y.)* 198 (1990) 132.
- [11] R. J. Furnstahl and B. D. Serot, *Phys. Rev. C* 47 (1993) 2338.
- [12] D. G. Boulware, *Ann. Phys. (N.Y.)* 56 (1970) 140.
- [13] S. Weinberg, *Phys. Rev.* 166 (1968) 1568; *Physica A* 96 (1979) 327.
- [14] R. Dashen and M. Weinstein, *Phys. Rev.* 183 (1969) 1261.
- [15] J. Gasser and H. Leutwyler, *Ann. Phys. (N.Y.)* 158 (1984) 142; *Nucl. Phys. B* 250 (1985) 465, 517, 539.
- [16] H. Leutwyler, *Ann. Phys. (N.Y.)* 235 (1994) 165.
- [17] J. L. Friar, D. G. Madland, and B. W. Lynn, “QCD Scales in Finite Nuclei,” preprint [nucl-th/9512011](#) (December, 1995).
- [18] R. J. Furnstahl, B. D. Serot, and H.-B. Tang, in preparation.
- [19] A. R. Bodmer, *Nucl. Phys. A* 526 (1991) 703.
- [20] S. Gmuca, *Z. Phys. A* 342 (1992) 387; *Nucl. Phys. A* 547 (1992) 447.
- [21] R. J. Furnstahl, B. D. Serot, and H.-B. Tang, *Nucl. Phys. A* 598 (1996) 539.
- [22] R. M. Dreizler and E. K. U. Gross, *Density functional theory* (Springer, Berlin, 1990).
- [23] C. Speicher, R. M. Dreizler, and E. Engel, *Ann. Phys. (N.Y.)* 213 (1992) 312.
- [24] R. N. Schmid, E. Engel, and R. M. Dreizler, *Phys. Rev. C* 52 (1995) 164.
- [25] W. Kohn and L. J. Sham, *Phys. Rev. A* 140 (1965) 1133.
- [26] B. Friedman and V. R. Pandharipande, *Nucl. Phys. A* 361 (1981) 502.
- [27] N. K. Glendenning, *Phys. Rev. D* 46 (1992) 1274.
- [28] T. Maruyama, H. Fujii, T. Moto, T. Tatsumi, *Phys. Lett. B* 337 (1994) 19.
- [29] R. Knorren, M. Prakash, and P. J. Ellis, *Phys. Rev. C* 52 (1995) 3470.
- [30] M. Prakash, J. Cooke, and J. M. Lattimer, *Phys. Rev. D* 52 (1995) 661.
- [31] M. Prakash, I. Bombaci, M. Prakash, P. J. Ellis, J. M. Lattimer, and R. Knorren, *Phys. Reports* (in press).
- [32] H. Fujii, T. Maruyama, T. Moto, and T. Tatsumi, Kyoto University preprint KUNS–1348 (1995).
- [33] G. Velo and D. Zwanzinger, *Phys. Rev.* 188 (1969) 2218.
- [34] G. Velo, *Nucl. Phys. B* 65 (1973) 427.
- [35] V. I. Ogievetskij and I. V. Polubarinov, *Ann. Phys. (N.Y.)* 25 (1963) 358.
- [36] J. C. Collins and M. J. Perry, *Phys. Rev. Lett.* 34 (1975) 1353.
- [37] G. Baym and S. A. Chin, *Phys. Lett.* 62 B (1976) 241.
- [38] N. K. Glendenning, *Ap. J.* 293 (1985) 470; *Nucl. Phys. A* 493 (1989) 521.
- [39] J. Ellis, J. I. Kapusta, and K. A. Olive, *Nucl. Phys. B* 348 (1991) 345.

- [40] H. D. Politzer and M. B. Wise, Phys. Lett. B 273 (1991) 156.
- [41] A. L. Fetter and J. D. Walecka, Quantum theory of many-particle systems (McGraw–Hill, New York, 1971).
- [42] C. Itzykson and J. B. Zuber, Quantum field theory (McGraw–Hill, New York, 1980) sec. 11–4–2.
- [43] J. Iliopoulos, C. Itzykson, and A. Martin, Rev. Mod. Phys. 47 (1975) 165.
- [44] R. J. Furnstahl, H.-B. Tang, and B. D. Serot, Phys. Rev. C 52 (1995) 1368.
- [45] C. J. Horowitz and B. D. Serot, Nucl. Phys. A 399 (1983) 529; A 464 (1987) 613; A 473 (1987) 760 (E).
- [46] H. Georgi, Weak interactions and modern particle theory (Benjamin/Cummings, Menlo Park, CA, 1984).
- [47] E. K. Heide, S. Rudaz, and P. J. Ellis, Nucl. Phys. A 571 (1994) 713.
- [48] W. D. Myers and W. J. Swiatecki, preprint LBL–36557 (1995).
- [49] H. Müller and B. D. Serot, Phys. Rev. C 52 (1995) 2072.
- [50] F. R. Brown, F. P. Butler, H. Chen, N. H. Christ, Z. Dong, W. Schaffer, L. I. Unger, and A. Vaccarino, Phys. Rev. Lett. 65 (1990) 2491.
- [51] N. H. Christ, Nucl. Phys. A 544 (1992) 81c.
- [52] B. D. Serot and H. Uechi, Ann. Phys. (N.Y.) 179 (1987) 272.
- [53] H. A. Bethe, G. E. Brown, and J. Cooperstein, Nucl. Phys. A 462 (1987) 791.

FIGURE CAPTIONS

FIG. 1. Binding energy of symmetric and neutron matter.

FIG. 2. Equation of state of neutron matter.

FIG. 3. Neutron star masses for different nonlinear couplings ζ . Pure neutron matter is assumed.

FIG. 4. Density distributions of neutron stars as a function of the radius, calculated with different parameters ζ . The central mass density $\rho_c = 1.5 \times 10^{15}$ g/cm³ is the same for all curves. Part (a) shows the radial mass densities and part (b) the corresponding energy densities. The stars acquire most of their mass from the region $100 \lesssim \mathcal{E} \lesssim 500$ MeV/fm³.

FIG. 5. Energy difference $\Delta\mathcal{E} = [\mathcal{E}(\xi = 0) - \mathcal{E}(\xi)]/\mathcal{E}(\xi = 0)$ of nuclear matter as a function of the proton fraction y calculated at constant baryon density. In part (a) the density is fixed at its equilibrium value ρ_0 and part (b) shows the results at $5\rho_0$. Note the different vertical scales in (a) and (b).

FIG. 6. Neutron star mass for different values of ξ at fixed ζ . Pure neutron matter is assumed.

FIG. 7. Maximum neutron star mass as function of ζ and ξ . Results for pure neutron matter and for matter in β -equilibrium are displayed. The shaded areas show the mass range obtained when ξ is varied; the upper boundaries correspond to $\xi = 0$ and the lower boundaries to $\xi = 1.5$.

FIG. 8. Maximum neutron star mass as a function of the compression modulus K_0 . (All other nuclear matter inputs are held fixed.) The shaded area marks the covered range of masses. The upper boundary corresponds to $\zeta = 0, \xi = 0$ and the lower boundary to $\zeta = 0.06, \xi = 1.5$. For fixed values of the nonlinear couplings, the mass changes marginally with the compression modulus. This can be seen from the dashed line inside the shaded area, which corresponds to $\zeta = 0.02, \xi = 0.5$

FIG. 9. Neutron star masses for models with different nonlinear couplings for the neutral vector meson. The uppermost curve corresponds to the Walecka model, including cubic and quartic couplings for the scalar meson. Region *A* shows the range of masses obtained when the quartic vector coupling is turned on. Regions *A* and *B* correspond to models with up to sixth-order terms, and regions *A*, *B*, and *C* include an eighth-order term. The values of the nonlinear couplings are chosen within a natural range, as described in the text. The cross indicates the maximum mass ($1.58 M_\odot$) obtained for beta-stable matter in a calculation that includes the $\zeta, \zeta', \zeta'',$ and ξ couplings (see the text).

FIG. 10. Energy per baryon for neutron matter (solid) and quark matter (dashed). The quark matter results are calculated using $b = 120$ MeV/fm 3 and $\alpha_s = 0.4$ [52].

TABLES

TABLE I. Equilibrium Properties of Nuclear Matter

$(k_F)_0$	ρ_0	M_0^*/M	e_0	K_0	a_4
1.30 fm $^{-1}$	0.1484 fm $^{-3}$	0.60	-15.75 MeV	250 MeV	35 MeV

FIGURES

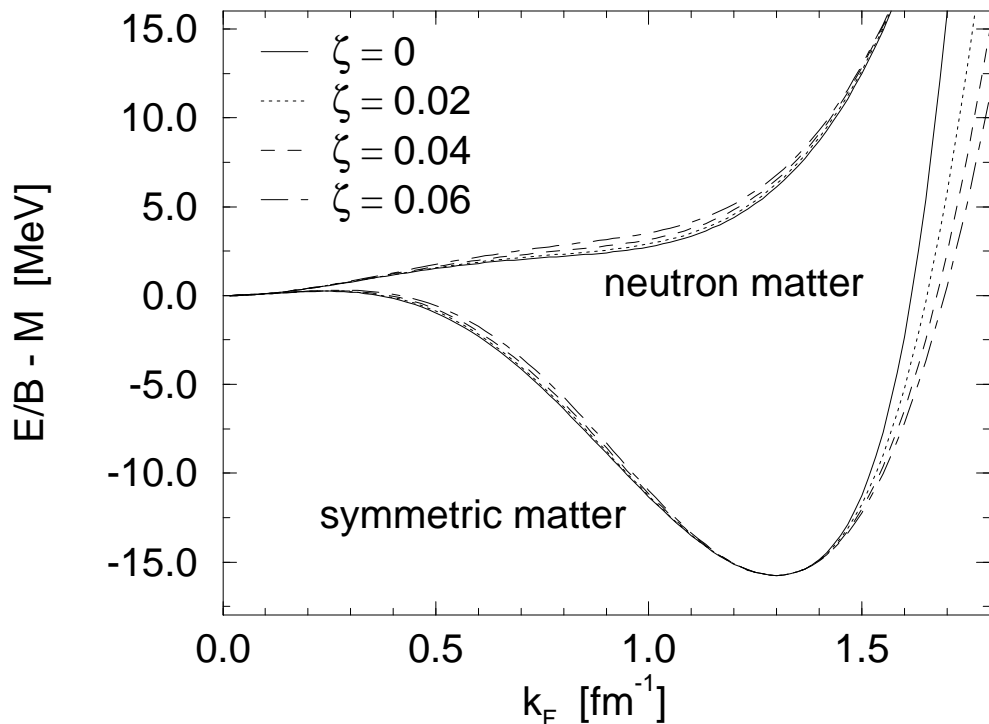


FIGURE 1

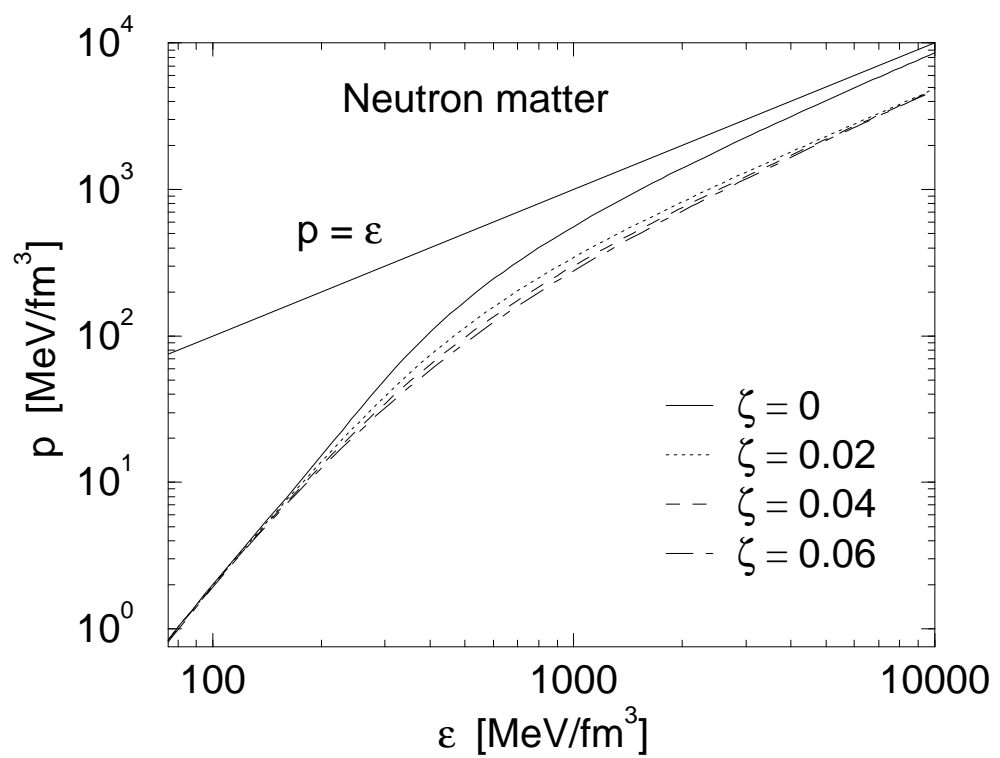


FIGURE 2

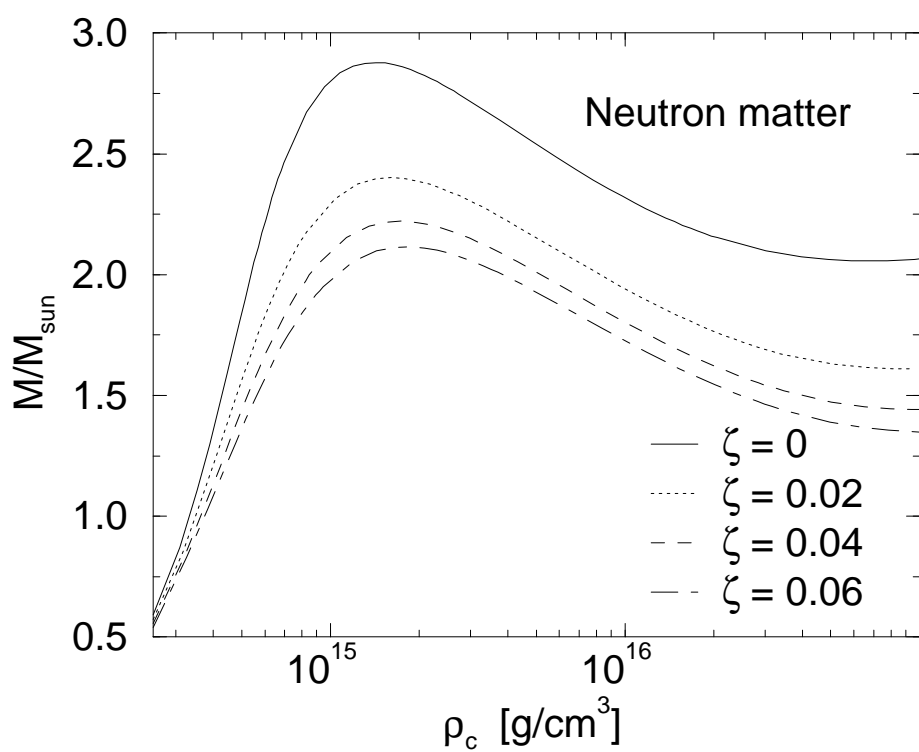


FIGURE 3

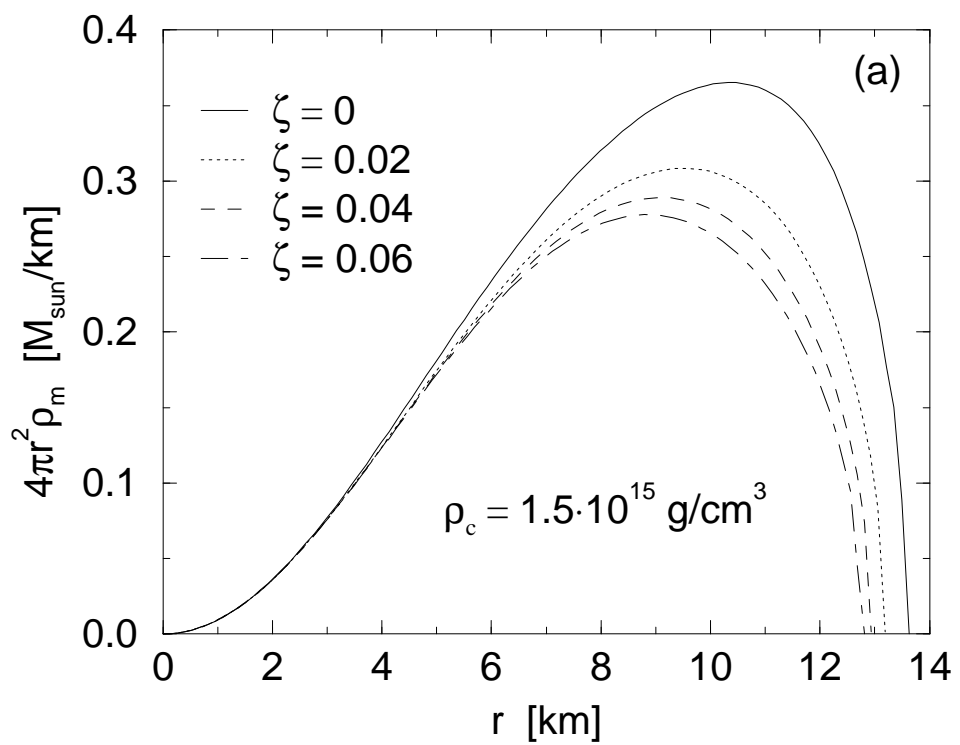


FIGURE 4(a)

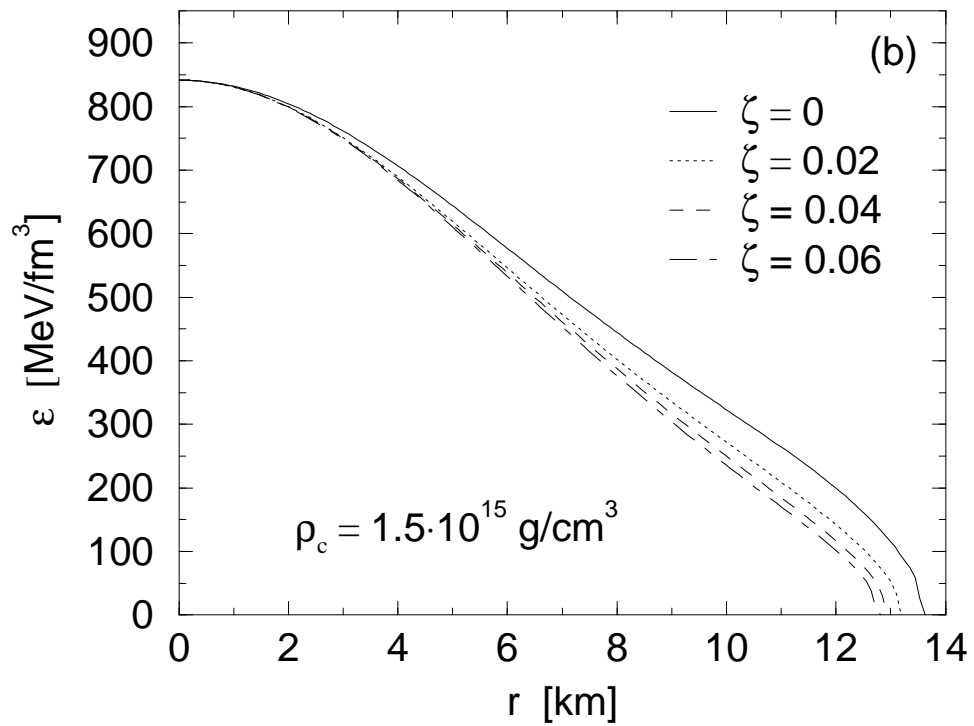


FIGURE 4(b)

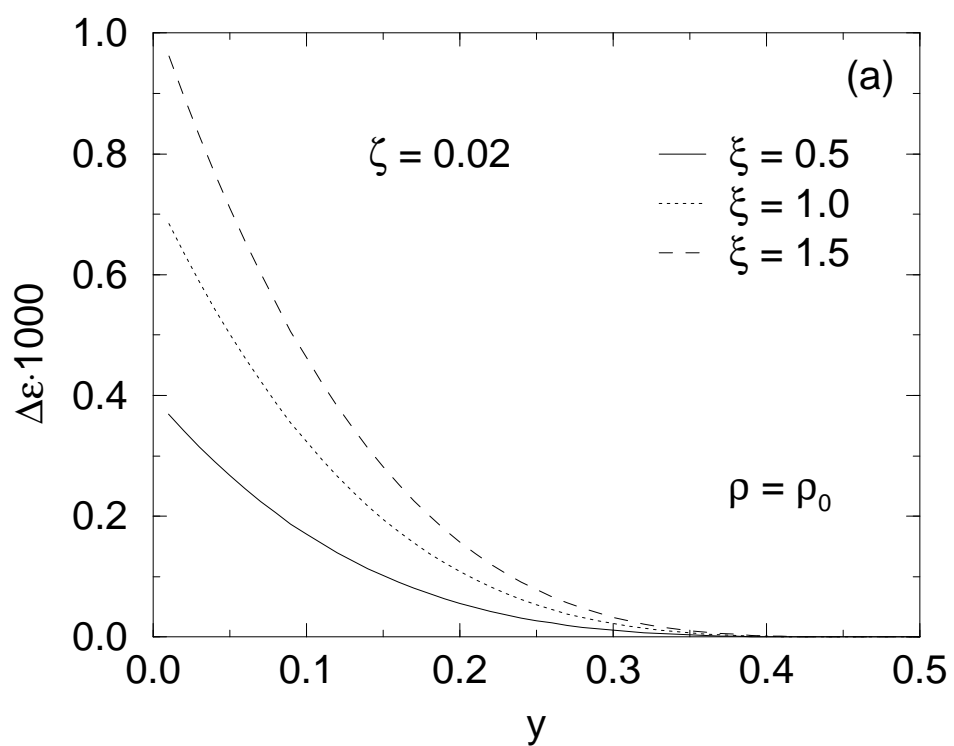


FIGURE 5(a)

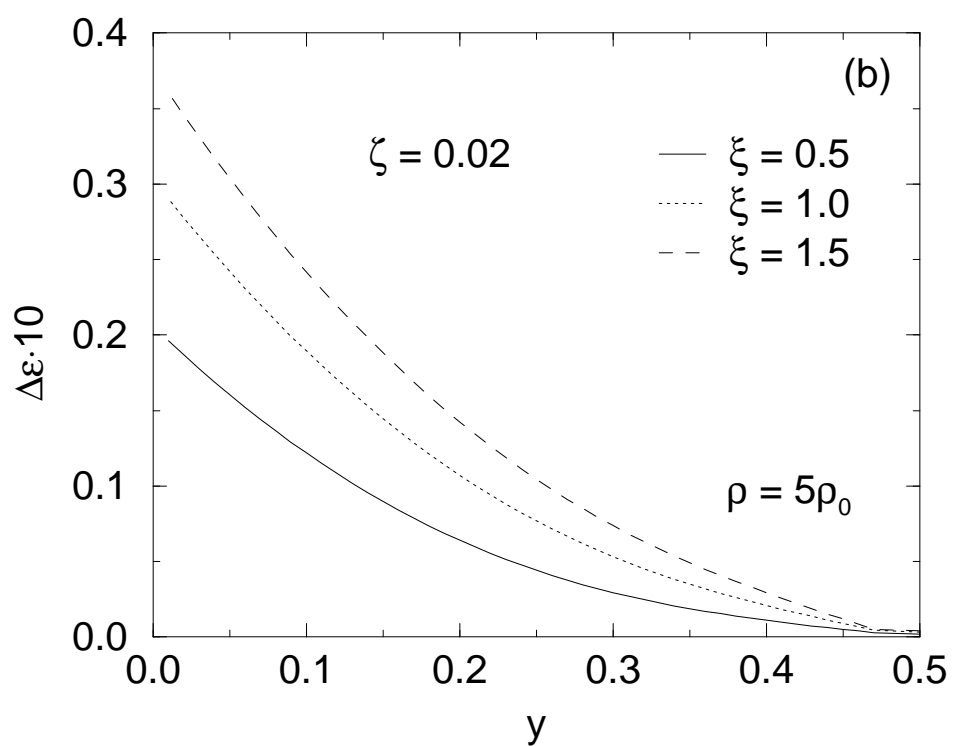


FIGURE 5(b)

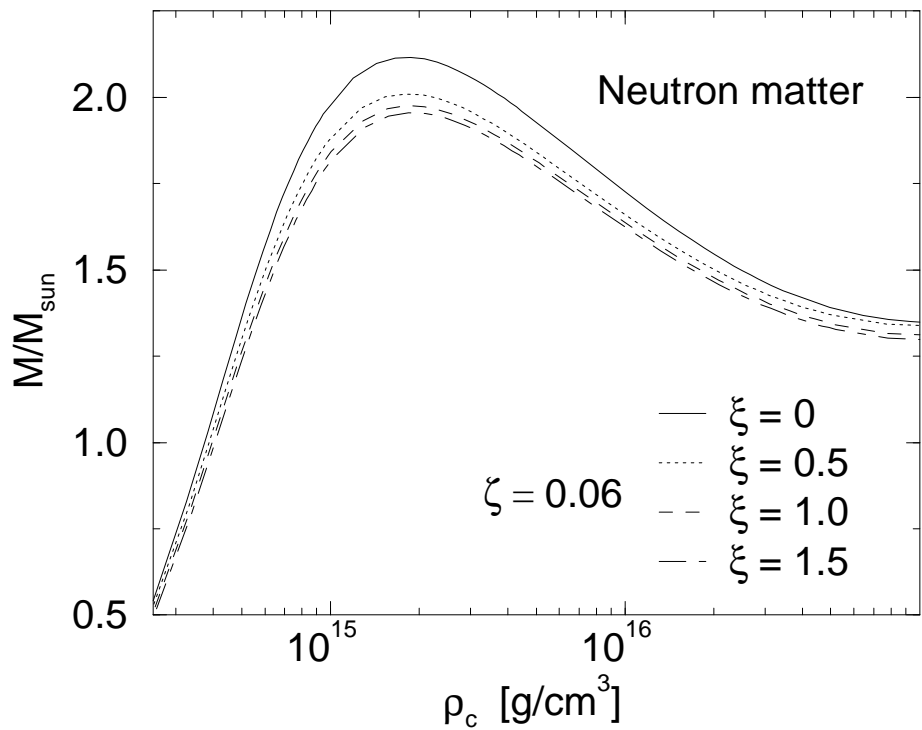


FIGURE 6

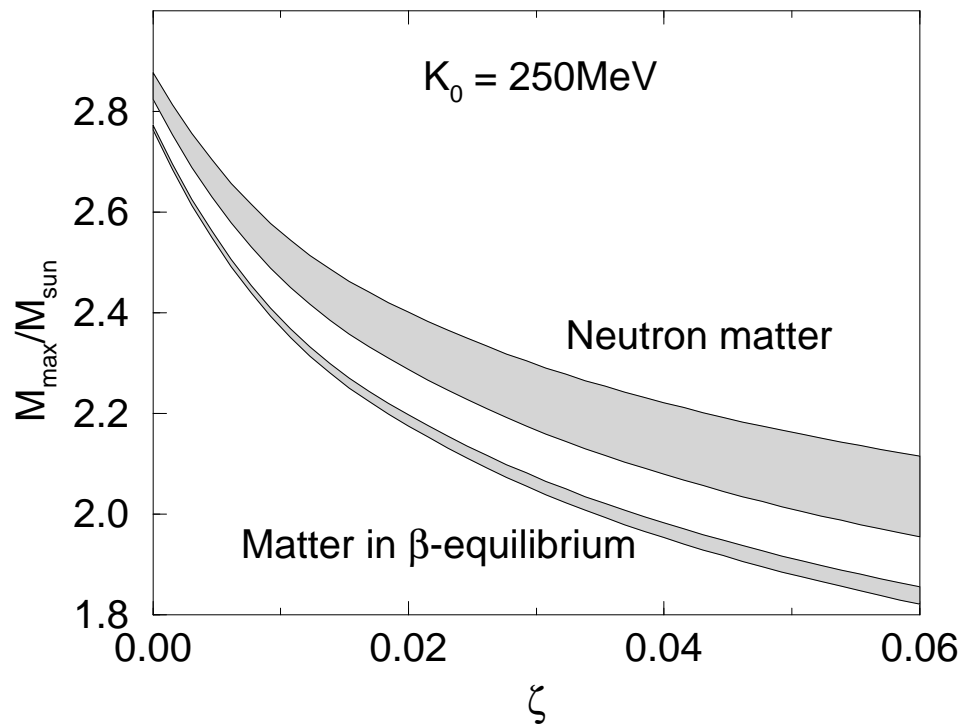


FIGURE 7

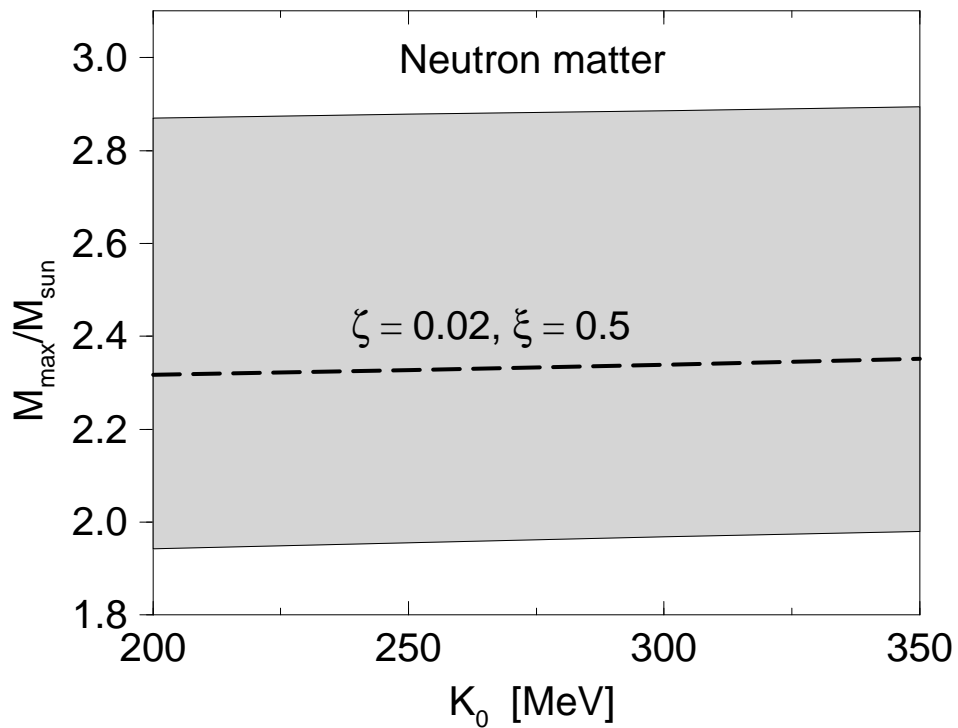


FIGURE 8

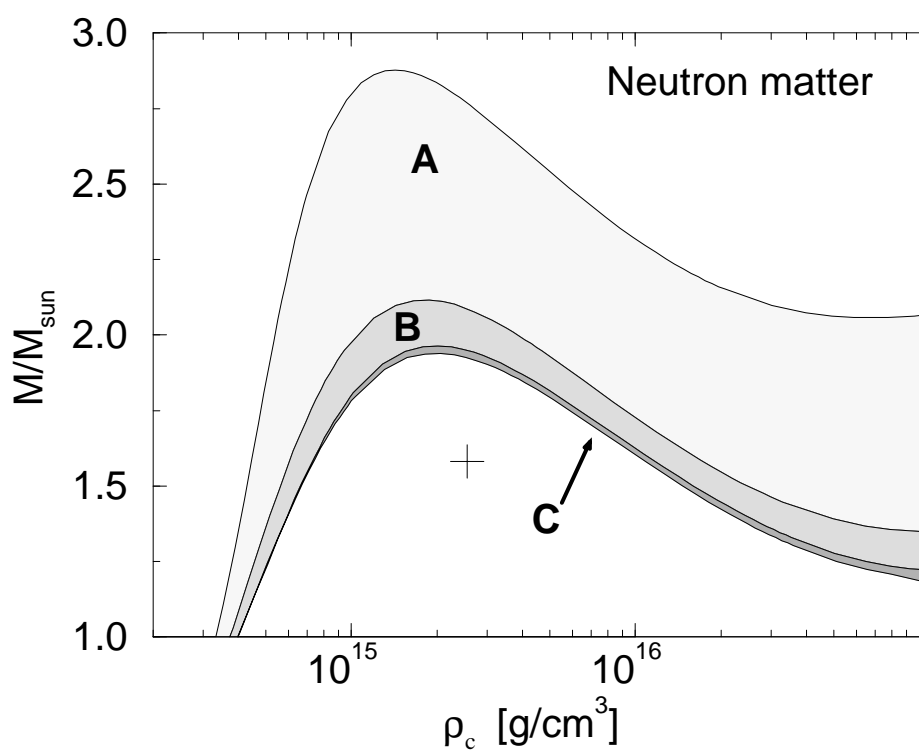


FIGURE 9

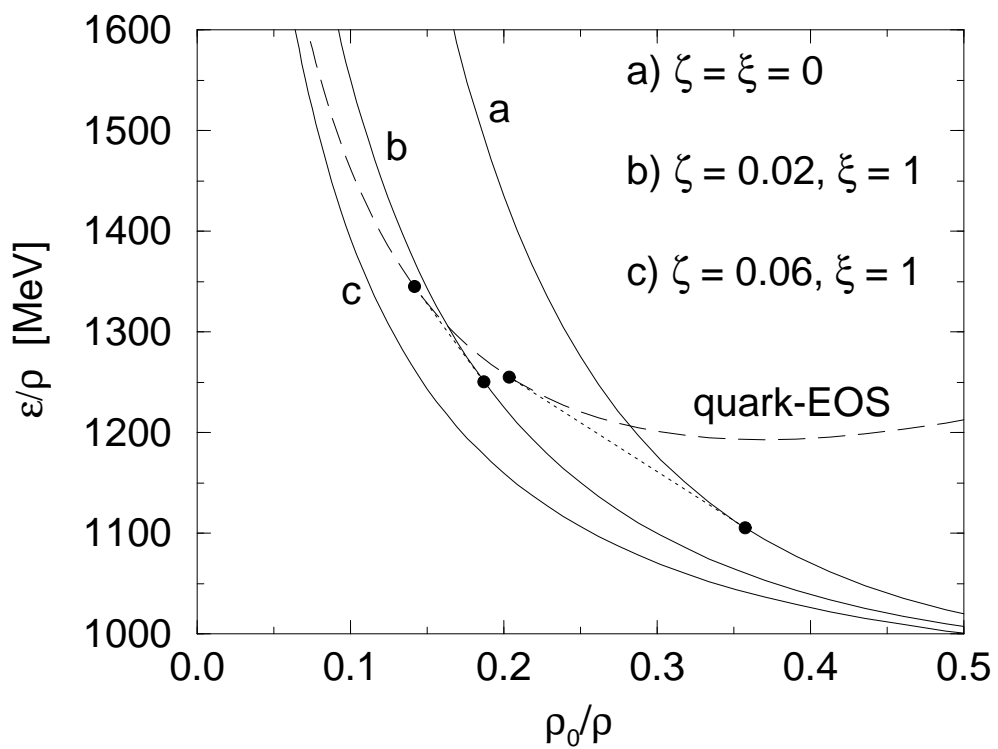


FIGURE 10

Neutron Star Structure and the Neutron Radius of ^{208}Pb

C. J. Horowitz*

Nuclear Theory Center and Department of Physics, Indiana University, Bloomington, Indiana 47405

J. Piekarewicz†

Department of Physics, Florida State University, Tallahassee, Florida 32306

(Received 2 October 2000)

We study relationships between the neutron-rich skin of a heavy nucleus and the properties of neutron-star crusts. Relativistic effective field theories with a thicker neutron skin in ^{208}Pb have a larger electron fraction and a lower liquid-to-solid transition density for neutron-rich matter. These properties are determined by the density dependence of the symmetry energy which we vary by adding nonlinear couplings between isoscalar and isovector mesons. An accurate measurement of the neutron radius in ^{208}Pb —via parity violating electron scattering—may have important implications for the structure of the crust of neutron stars.

DOI: 10.1103/PhysRevLett.86.5647

PACS numbers: 26.60.+c, 21.10.Gv

It is an extrapolation of 18 orders of magnitude from the neutron radius of a heavy nucleus—such as ^{208}Pb with $R_n \approx 5.5$ fm—to the approximately 10 km radius of a neutron star. Yet both radii depend on our incomplete knowledge of the equation of state of neutron-rich matter. Therefore, an accurate measurement of the neutron radius in ^{208}Pb may have important implications for some neutron-star properties.

Heavy nuclei are expected to have a neutron-rich skin. This important feature of nuclear structure arises because of the large neutron excess and because the Coulomb barrier reduces the proton density at the surface. The thickness of the neutron skin depends on the pressure of neutron-rich matter: the greater the pressure, the thicker the skin as neutrons are pushed out against surface tension. The same pressure supports a neutron star against gravity [1]. Thus models with thicker neutron skins often produce neutron stars with larger radii.

Neutron stars are expected to have a solid crust of nonuniform neutron-rich matter above a liquid mantle. The phase transition from solid to liquid depends on the properties of neutron-rich matter. Indeed, a high pressure implies a rapid rise of the energy with density making it energetically unfavorable to separate uniform matter into regions of high and low densities. Thus a high pressure typically implies a low transition density from a solid crust to a liquid mantle. This suggests an inverse relationship: the thicker the neutron-rich skin of a heavy nucleus, the thinner the solid crust of a neutron star.

In this Letter we study possible “data-to-data” relations between the neutron-rich skin of a heavy nucleus and the crust of a neutron star. These relations may impact neutron-star observables. Indeed, properties of the crust are important for models of glitches in the rotational period of pulsars [2,3], for the shape and gravitational radiation of nonspherical rotating stars [4] and for neutron-star cooling [5]. Note that the skin of a heavy nucleus and the

crust of a neutron star are composed of the same material: neutron-rich matter at similar densities.

The parity radius experiment (PREX) at the Jefferson Laboratory aims to measure the neutron radius in ^{208}Pb via parity violating electron scattering [6,7]. Parity violation is sensitive to the neutron density because the Z^0 boson couples primarily to neutrons. The result of this purely electroweak experiment could be both accurate and model independent. In contrast, all previous measurements of bulk neutron densities used hadronic probes that suffer from controversial uncertainties in the reaction mechanism (see, for example, Ref. [8]). PREX should provide a unique observational constraint on the thickness of the neutron skin in a heavy nucleus. In this Letter we explore some of the implications of this measurement on the structure of neutron stars.

Microscopic calculations of the energy of neutron matter constrain both the neutron skin in ^{208}Pb and the crust of a neutron star; see, for example, Ref. [9]. However, these calculations of infinite neutron matter are not directly tested by observable properties of finite nuclei such as their charge densities or binding energies. Moreover, non-relativistic calculations of symmetric nuclear matter have not succeeded in predicting the saturation density. It thus becomes necessary to fit some properties of a three-body force in order to reproduce nuclear saturation. Indeed, the properties of $A = 8$ pure neutron drops calculated in Ref. [10] may depend on the three-nucleon force used. Thus we feel that it is important to distinguish direct finite-nucleus measurements—such as PREX—from theoretical neutron-matter “observables” based solely on calculations. Indeed, PREX may provide an important test of these calculations [11].

We start with a relativistic effective field theory [12] that provides a simple description of finite nuclei and a Lorentz covariant extrapolation for the equation of state of dense neutron-rich matter. The theory has an isoscalar-scalar ϕ

(sigma) meson field and three vector fields: an isoscalar V (omega), an isovector b (rho), and the photon A . We now supplement the Lagrangian with new nonlinear sigma-rho and omega-rho couplings. These couplings allow us to

$$\begin{aligned} \mathcal{L}_{\text{int}} = & \bar{\psi} \left[g_s \phi - \left(g_v V_\mu + \frac{g_\rho}{2} \boldsymbol{\tau} \cdot \mathbf{b}_\mu + \frac{e}{2} (1 + \tau_3) A_\mu \right) \gamma^\mu \right] \psi - \frac{\kappa}{3!} (g_s \phi)^3 - \frac{\lambda}{4!} (g_s \phi)^4 + \frac{\zeta}{4!} g_v^4 (V_\mu V^\mu)^2 \\ & + \frac{\xi}{4!} g_\rho^4 (\mathbf{b}_\mu \cdot \mathbf{b}^\mu)^2 + g_\rho^2 \mathbf{b}_\mu \cdot \mathbf{b}^\mu [\Lambda_4 g_s^2 \phi^2 + \Lambda_v g_v^2 V_\mu V^\mu]. \end{aligned} \quad (1)$$

We consider a number of different parameter sets. First, we note that the nonlinear rho coupling ξ will modify the density dependence of the rho mean field, and this could change the neutron-skin thickness. However, unless ξ is made very large, this term was found to have a small effect [12]. Thus for simplicity, we set $\xi \equiv 0$ in all our parameter sets. Second, note that we could have added a cubic sigma-rho interaction of the form $\mathcal{L}_3 = M \Lambda_3 (g_s \phi) (g_\rho^2 \mathbf{b}_\mu \cdot \mathbf{b}^\mu)$. A nonzero Λ_3 does change the thickness of the neutron skin in ^{208}Pb —but at the expense of a change in the proton density. Therefore, we set $\Lambda_3 \equiv 0$ and focus exclusively on Λ_4 and Λ_v .

We start with the original NL3 parameter set of Lalazissis, König, and Ring [13]. (Note that a small adjustment of the $NN\rho$ coupling constant was needed to fit the symmetry energy of nuclear matter at a Fermi momentum of $k_F = 1.15 \text{ fm}^{-1}$; see text below.) The NL3 set has $\zeta = \Lambda_4 = \Lambda_v = 0$ and provides a good fit to the ground-state properties of many nuclei. In this model symmetric nuclear matter saturates at $k_F = 1.30 \text{ fm}^{-1}$ with a binding energy per nucleon of $E/A = -16.25 \text{ MeV}$ and an incompressibility of $K = 271 \text{ MeV}$. All other parameter sets considered here have been fixed to the same saturation properties.

We now add the new nonlinear couplings Λ_4 and/or Λ_v between the isoscalar and the isovector mesons. At the same time we adjust the strength of the $NN\rho$ coupling constant (g_ρ) from its NL3 value to maintain the symmetry energy of nuclear matter unchanged (see text below). Note that neither Λ_4 nor Λ_v affect the properties of symmetric nuclear matter since $\mathbf{b}_\mu \equiv 0$. Hence, the saturation properties remain unchanged. Our goal is to change the neutron density and the neutron-skin thickness in ^{208}Pb while making very small changes to the proton density which is well constrained by the measured charge density

change the density dependence of the symmetry energy which changes both the thickness of the neutron skin in ^{208}Pb and the neutron-star crust.

The interacting Lagrangian density is given by [12]

[14]. The two new couplings (Λ_4 and Λ_v) change the skin thickness in ^{208}Pb by similar amounts. Yet they have different high-density limits [12]. For $\Lambda_v = 0$ the symmetry energy is proportional to the baryon density ρ in the limit of very high density, while it only grows like $\rho^{1/3}$ for nonzero Λ_v . This can produce noticeable changes in neutron star radii.

Let us start with $\Lambda_4 = 0$. For a given omega-rho coupling Λ_v we readjust only the $NN\rho$ coupling constant g_ρ in order to keep an average symmetry energy fixed. The symmetry energy at saturation density is not well constrained by the binding energy of nuclei. However, some average of the symmetry energy at full density and the surface energy is constrained by binding energies. As a simple approximation we evaluate the symmetry energy not at full density $k_F \approx 1.30 \text{ fm}^{-1}$ but rather at an average density corresponding to $k_F = 1.15 \text{ fm}^{-1}$. Thus, all our parameter sets have a symmetry energy of 25.68 MeV at $k_F = 1.15 \text{ fm}^{-1}$. Note that the original NL3 parameter set predicts a symmetry energy of 37.4 MeV at full saturation density and close to 25.68 MeV at $k_F = 1.15 \text{ fm}^{-1}$ [13]. This simple procedure produces a nearly constant binding energy per nucleon for ^{208}Pb as Λ_v is changed, as can be seen in Table I. Moreover, Table I shows that increasing Λ_v reduces the neutron-skin thickness significantly—while maintaining the proton radius nearly constant. In the following we plot our results for a range of Λ_v values for which the proton radius is within 0.01 fm of its $\Lambda_v = 0$ value.

To study the solid crust of a neutron star we make a simple random-phase-approximation calculation of the transition density below which uniform neutron-rich matter becomes unstable against small amplitude density fluctuations. This provides a lower bound to the true transition

TABLE I. Results for the NL3 parameter set. B.E. is the binding energy per particle in ^{208}Pb , R_p is the proton, and $R_n - R_p$ is the difference between neutron and proton radii in Pb. (Note that we do not include center-of-mass corrections.) Finally, ρ_c is our estimate for the transition density of neutron-rich matter from a nonuniform to a uniform phase.

Λ_v	g_ρ^2	B.E. (MeV)	R_p (fm)	$R_n - R_p$ (fm)	ρ_c (fm^{-3})
0.0	79.6	7.85	5.460	0.280	0.052
0.005	84.9	7.86	5.461	0.265	0.056
0.01	90.9	7.87	5.462	0.251	0.061
0.015	97.9	7.88	5.463	0.237	0.067
0.02	106.0	7.88	5.466	0.223	0.075
0.025	115.6	7.89	5.469	0.209	0.081

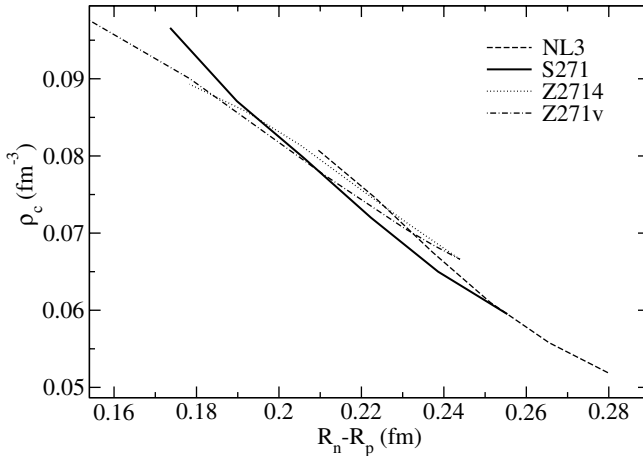


FIG. 1. Estimate of the transition density from nonuniform to uniform neutron-rich matter versus neutron-minus-proton radius in ^{208}Pb . The curves are for the four parameter sets described in the text.

density [15]. We start with the longitudinal dielectric function ϵ_L , as defined in Eq. (68) of Ref. [16], evaluated at an energy transfer $q_0 = 0$ and at an arbitrary momentum transfer q . That is,

$$\epsilon_L(q_0 = 0, q) = \det(1 - D_L \Pi_L). \quad (2)$$

Here Π_L is a longitudinal polarization matrix describing particle-hole excitations of a uniform system of protons, neutrons, and electrons in beta equilibrium, as given in Eq. (56) of Ref. [16]. The matrix D_L , describing meson and photon propagation, follows from Eq. (57) of Ref. [16]—but includes additional terms to account for the nonlinear nature of the meson self-couplings [17]. We estimate the transition density ρ_c by computing the largest density at which $\epsilon_L(0, q) < 0$ for any given q .

In Fig. 1 we display the transition density for various parameter sets (see Table II) as a function of the predicted difference in the root-mean-square neutron and proton radii $R_n - R_p$ in ^{208}Pb . The curves are parametrized by different values of Λ_v , as shown in Table I. The NL3 parameter set saturates nuclear matter with a relatively small value of the nucleon effective mass: $M^* \equiv M - g_s \phi = 0.59M$. The parameter set S271 saturates nuclear matter as NL3 but with $M^* = 0.70M$. This set also has $\zeta = 0$. The two remaining curves in the figure are for parameter sets having $\zeta = 0.06$ and both saturate nuclear matter with $M^* = 0.80M$. (Set Z271v has a nonzero Λ_v , while set Z2714 uses a nonzero Λ_4 .) Note that the scalar mass m_s for

parameter sets S271, Z271v, and Z2714 is adjusted to reproduce the proton radius in ^{208}Pb as computed with NL3. Figure 1 displays a clear inverse correlation between the transition density and the neutron-skin thickness $R_n - R_p$. The transition density expressed in fm^{-3} is about

$$\rho_c \approx 0.16 - 0.39(R_n - R_p), \quad (3)$$

with the skin thickness expressed in fm. Moreover, this correlation seems to be insensitive to M^* or to using Λ_4 or Λ_v to change $R_n - R_p$. These results suggest that a measurement of the neutron radius in ^{208}Pb will provide considerable information on the transition density.

Note that Fig. 1 shows only our results. Yet all other calculations that we are aware of also give consistent results. For example, the nonrelativistic microscopic equation of state of Friedman and Pandharipande has a transition density of $\rho_c = 0.096 \text{ fm}^{-3}$ according to Lorenz *et al.* [9]. For this equation of state Brown finds $R_n - R_p = 0.16 \pm 0.02 \text{ fm}$ [11]. These numbers are in excellent agreement with Eq. (3).

Brown also finds a linear relation between $R_n - R_p$ and the derivative of the energy of neutron matter versus density $dE/d\rho$ evaluated at $\rho = 0.1 \text{ fm}^{-3}$ [11]. He considers a large variety of nonrelativistic Skyrme interactions. Our results for $dE/d\rho$ versus $R_n - R_p$ are completely consistent. We expect these common $dE/d\rho$ values to give similar ρ_c values consistent with Eq. (3) for these Skyrme interactions. This is because $dE/d\rho$ is related to the pressure while ρ_c depends on the density dependence of the pressure.

Finally, for the relativistic interaction TM1 of Sugahara and Toki [18], we calculate from Eq. (2) $\rho_c \approx 0.059 \text{ fm}^{-3}$ and $R_n - R_p = 0.27 \text{ fm}$. The numbers are again in good agreement with Eq. (3).

In Fig. 2 we show the electron fraction per baryon Y_e versus density for uniform neutron-rich matter in beta equilibrium. We include results only for the S271 parameter set as all other sets yield similar results. The different curves are for different values of Λ_v which predict the indicated $R_n - R_p$ values. The curves start near the transition densities displayed in Fig. 1. The electron fraction Y_e is determined by the symmetry energy while $R_n - R_p$ is sensitive to the density dependence of the symmetry energy. Therefore a measurement of $R_n - R_p$ constrains the growth of Y_e with density. If $R_n - R_p$ is greater than about 0.24 fm, Y_e becomes large enough to allow the direct URCA process, of neutron followed by proton beta decays [19], to cool down a 1.4 solar mass neutron star.

TABLE II. Model parameters used in the calculations. The parameter κ and the scalar (m_s) and vector (m_v) masses are given in MeV. The nucleon and rho masses are kept fixed at $M = 939$ and $m_\rho = 763$ MeV, respectively.

Model	g_s^2	g_v^2	κ	λ	ζ	m_s	m_v
NL3	104.387	165.585	3.860	-0.015 91	0	508.194	782.5
S271	81.103	116.766	6.68	-0.015 78	0	505	783
Z271	49.440	70.669	6.17	0.156 34	0.06	465	783

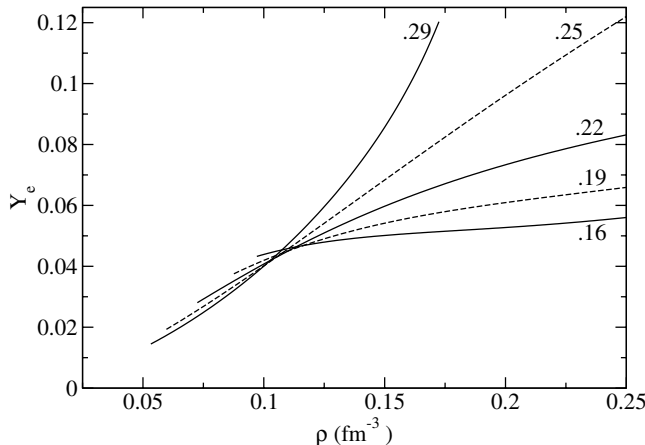


FIG. 2. Electron fraction Y_e versus baryon density for uniform neutron-rich matter in beta equilibrium using the S271 parameter set (other sets yield similar results). The curves are for different values of Λ_v that predict the indicated values of $R_n - R_p$ for ^{208}Pb , in fm.

The relationship between the radius of a 1.4 solar mass neutron star and $R_n - R_p$ will be discussed in future work.

We conclude the following:

(1) It is possible to fit nuclear observables—such as charge densities, binding energies, and single particle spectra—with effective field theories that predict a range of neutron-skin thicknesses. This can be done by adding nonlinear couplings between isoscalar and isovector meson fields or, in general, by adding interactions that modify the density dependence of the symmetry energy. We conclude that the neutron-skin thickness is not tightly constrained by these observables. Yet a measurement of the skin thickness will constrain the density dependence of the symmetry energy.

(2) The density dependence of the symmetry energy is adjustable in our relativistic effective field models while still reproducing nuclear-matter properties and other ground-state observables. Indeed, our models can provide a Lorentz-covariant extrapolation for the high-density equation of state with a symmetry energy that rises slower with density relative to earlier relativistic mean-field models.

(3) The electron fraction Y_e of neutron-rich matter in beta equilibrium is correlated with the neutron-skin thickness in ^{208}Pb . The thicker the neutron skin, the faster Y_e rises with density. In our models a neutron-skin thickness of the order of 0.24 fm or larger suggests that Y_e will become large enough to allow a direct URCA process to cool down a $1.4M_\odot$ neutron star.

(4) We have found an inverse correlation between the neutron-skin thickness and the density of a phase transition from nonuniform to uniform neutron-rich matter. In our models the transition density obeys the approximate relation: $\rho_c \approx 0.16 - 0.39(R_n - R_p)$, with $R_n - R_p$ in

fm and ρ_c in fm^{-3} . This suggests that a neutron skin measurement in ^{208}Pb can provide important information on the thickness and other properties of the crust of a neutron star.

(5) Microscopic calculations of the energy of neutron matter constrain the density dependence of the symmetry energy and hence the neutron-skin thickness in ^{208}Pb . Therefore a neutron-skin measurement may provide an important observational check on such calculations that is not provided by other observables. Moreover, a neutron-skin measurement may constrain three-body forces in neutron-rich matter.

We acknowledge useful discussions with A. Brown, R. Furnstahl, J. Lattimer, S. Reddy, and B. Serot. We thank A. Brown for sharing results prior to publication. This work was supported in part by DOE Grants No. DE-FG02-87ER40365 and No. DE-FG05-92ER40750.

*Email address: charlie@iucf.indiana.edu

[†]Email address: jorgep@scri.fsu.edu

- [1] J. M. Lattimer and M. Prakash, *Astrophys. J.* **550**, 426 (2001).
- [2] D. Pines and M. A. Alpar, *Nature (London)* **316**, 27 (1985).
- [3] B. Link, R. I. Epstein, and J. M. Lattimer, *Phys. Rev. Lett.* **83**, 3362 (1999).
- [4] G. Ushomirsky, L. Bildsten, and C. Cutler, Los Alamos Archive, astro-ph/0001129; L. Bildsten, *Astrophys. J.* **501**, L89 (1998).
- [5] See, for example, A. D. Kaminker *et al.*, *Astron. Astrophys.* **343**, 1009 (1999).
- [6] Jefferson Laboratory Experiment E-00-003, Spokespersons R. Michaels, P. A. Souder, and G. M. Urciuoli.
- [7] C. J. Horowitz, S. J. Pollock, P. A. Souder, and R. Michaels, *Phys. Rev. C* **63**, 025501 (2001).
- [8] L. Ray, G. W. Hoffmann, and W. R. Coker, *Phys. Rep.* **212**, 223 (1992).
- [9] B. Friedman and V. R. Pandharipande, *Nucl. Phys.* **A361**, 502 (1981); C. P. Lorenz, D. G. Ravenhall, and C. J. Pethick, *Phys. Rev. Lett.* **70**, 379 (1993).
- [10] B. S. Pudliner *et al.*, *Phys. Rev. Lett.* **76**, 2416 (1996).
- [11] B. Alex Brown, *Phys. Rev. Lett.* **85**, 5296 (2000).
- [12] H. Müller and B. D. Serot, *Nucl. Phys.* **A606**, 508 (1996).
- [13] G. A. Lalazissis, J. König, and P. Ring, *Phys. Rev. C* **55**, 540 (1997).
- [14] B. Frois *et al.*, *Phys. Rev. Lett.* **38**, 152 (1977).
- [15] C. J. Pethick, D. G. Ravenhall, and C. P. Lorenz, *Nucl. Phys.* **A584**, 675 (1995); F. Douchin and P. Haensel, *Phys. Lett. B* **485**, 107 (2000).
- [16] C. J. Horowitz and K. Wehrberger, *Nucl. Phys.* **A531**, 665 (1991).
- [17] C. J. Horowitz and J. Piekarewicz (to be published).
- [18] Y. Sugahara and H. Toki, *Nucl. Phys.* **A579**, 557 (1994).
- [19] C. J. Pethick and V. Thorsson, in *Lives of the Neutron Stars*, edited by A. Alpar *et al.*, NATO Advanced Study Institutes, Ser. C, Vol. 450 (Kluwer, Dordrecht, 1994).

LOW-MASS NEUTRON STARS AND THE EQUATION OF STATE OF DENSE MATTER

J. CARRIERE AND C. J. HOROWITZ

Nuclear Theory Center and Department of Physics, Indiana University, Bloomington, IN 47405;
jcarrier@indiana.edu, charlie@iucf.indiana.edu

AND

J. PIEKAREWICZ

Department of Physics, Florida State University, Tallahassee, FL 32306; jorgep@csit.fsu.edu

Received 2002 November 7; accepted 2003 April 22

ABSTRACT

Neutron star radii provide useful information about the equation of state of neutron-rich matter. Particularly interesting is the density dependence of the equation of state (EOS). For example, the softening of the EOS at high density, where the pressure rises slower than anticipated, could signal a transition to an exotic phase. However, extracting the density dependence of the EOS requires measuring the radii of neutron stars for a broad range of masses. A “normal” $1.4 M_{\odot}$ (M_{\odot} = solar mass) neutron star has a central density of a few times the nuclear-matter saturation density (ρ_0). In contrast, low-mass ($\simeq 0.5 M_{\odot}$) neutron stars have central densities near ρ_0 , so their radii provide information about the EOS at low density. Unfortunately, low-mass neutron stars are rare because they may be hard to form. Instead, a precision measurement of nuclear radii of atomic nuclei may contain similar information. Indeed, we find a strong correlation between the neutron radius of ^{208}Pb and the radius of a $0.5 M_{\odot}$ neutron star. Thus, the radius of a $0.5 M_{\odot}$ neutron star can be inferred from a measurement of the neutron radius of ^{208}Pb . Comparing this value to the measured radius of a $\simeq 1.4 M_{\odot}$ neutron star should provide the strongest constraint to date on the density dependence of the EOS.

Subject headings: dense matter — equation of state — stars: neutron

1. INTRODUCTION

The structure of neutron stars, particularly their masses and radii, depend critically on the equation of state (EOS) of dense matter (Lattimer & Prakash 2001). New measurements of masses and radii by state-of-the-art observatories should place important constraints on the EOS. Observing a rapid change of the EOS with density could signal a transition to an exotic phase of matter. Possibilities for new high-density phases include pion or kaon condensates (Pons et al. 2001), strange quark matter (Prakash 2002; Jaikumar & Prakash 2001), and/or a color superconductor (Heiselberg 2001; Alford 2001).¹ Measuring neutron star radii $R(M)$ for a large range of neutron star masses M is attractive, as it would allow one to directly deduce the EOS (Lindblom 1992), that is, the pressure as a function of the energy density $P(\epsilon)$.

While the masses of various neutron stars are accurately known (Thorsett & Chakrabarty 1999), precise measurements of their radii do not yet exist. Therefore, several groups are devoting considerable effort at measuring neutron star radii. Often one deduces the surface temperature T_{∞} and the luminosity L of the star from spectral and distance measurements, respectively. Assuming a blackbody spectrum, these measurements determine the surface area, and thus the effective radius R_{∞} , of the star from the Stefan-Boltzmann law

$$L = 4\pi\sigma R_{\infty}^2 T_{\infty}^4. \quad (1)$$

Opportunities for precision measurements on neutron star radii include the isolated neutron star RX J185635–3754 (Walter & Lattimer 2002; Drake et al. 2002; Pons et al. 2002) and quiescent neutron stars in globular clusters,

such as CXOU 132619.7–472910.8 (Brown, Bildsten, & Rutledge 1998; Rutledge et al. 2002), where distances are accurately known. Moreover, Sanwal and collaborators have recently detected absorption features in the radio-quiet neutron star 1E 1207.4–5209 (Sanwal et al. 2002) that may provide the mass-to-radius ratio of the star through the determination of the gravitational redshift of the spectral lines. These observations are being complemented by studies that aim at constraining the composition of the neutron star atmosphere (Hailey & Mori 2002). Finally, models of rotational glitches place a lower limit on the radius of the Vela pulsar at $R_{\infty} \gtrsim 12$ km (Link, Epstein, & Lattimer 1999).

While a determination of the mass-radius relation $R(M)$ for a variety of neutron stars would uniquely determine the equation of state, unfortunately, all accurately determined masses to date fall within a very small range. Indeed, a recent compilation by Thorsett and Chakrabarty of several radio binary pulsars place their masses in the narrow range of 1.25 – $1.44 M_{\odot}$ (Thorsett & Chakrabarty 1999). Note that several X-ray binaries appear to have larger masses, perhaps because of accretion. These include Cyg X-2 with a mass of $1.8 \pm 0.2 M_{\odot}$ (Orosz & Kuulkers 1999), Vela X-1 with $1.9 M_{\odot}$ (van Kerkwijk, van Paradijs, & Zuiderwijk 1995), and 4U 1700–37 (Heap & Corcoran 1992). If confirmed, they could provide additional information on the high-density EOS. However, these mass determinations are not without controversy (Stickland, Lloyd, & Radzuin-Woodham 1997; Brown, Weingartner, & Wijers 1996). On the other hand, it may be difficult to form low-mass neutron stars from the collapse of heavier, Chandrasekhar-mass objects. If so, information on the low-density EOS may not be directly available from neutron stars. Thus, it is important to make maximum use of any $R(M)$ measurements even if these are available for only a limited range of masses.

¹ Conference proceedings can be found at the eConf Web site: <http://www.slac.stanford.edu/econf/C010815/proceedings.html>.

Additional information on the low-density EOS can be obtained from precision measurements on atomic nuclei. For example, the neutron radius of a heavy nucleus, such as ^{208}Pb , is closely related to the pressure of neutron-rich matter (Brown 2000). Indeed, heavy nuclei develop a neutron-rich skin in response to this pressure. The higher the pressure, the further the neutrons are pushed out against surface tension, thereby generating a larger neutron radius. However, nuclear properties depend only on the EOS at normal (in the interior) and below (in the surface) nuclear-matter saturation density ($\rho_0 \approx 0.15$ nucleons fm $^{-3}$). This is in contrast to conventional $1.4 M_\odot$ neutron stars that, with central densities of several times ρ_0 , also depend on the high-density component of the EOS. This is not the case for low-mass neutron stars (with masses about $\frac{1}{2} M_\odot$). Reaching central densities near ρ_0 , *low-mass neutron stars probe the EOS at similar densities as atomic nuclei*. Therefore, one could infer the radius of low-mass neutron stars from detailed measurements of atomic nuclei. Inferring the radii of low-mass neutron stars from a nuclear measurement, combined with the measured radius of a $1.4 M_\odot$ star, may enable one to deduce the density dependence of the EOS. (For a recent discussion on the minimum stable mass of a neutron star, see Haensel, Zdunik, & Douchin 2002.) The parity radius experiment at Jefferson Laboratory (Michaels, Souder, & Urciuoli 2000) aims to measure accurately and model independently the rms neutron radius (R_n) of ^{208}Pb via parity violating elastic electron scattering (Horowitz et al. 2001). Such an experiment probes neutron densities because the weak vector charge of a neutron is much larger than that of a proton. The goal of the experiment is to measure R_n to a 1% accuracy (within $\approx \pm 0.05$ fm).

The outline of the paper is as follows. In § 2 we present a relativistic effective-field theory formalism to study relationships between the neutron radius of ^{208}Pb and the radii of neutron stars. Uncertainties in these relationships are estimated by considering a wide range of effective-field theory parameters, all of them constrained by known nuclear properties. This formalism has been used previously to study correlations between the neutron radius of ^{208}Pb and the properties of the neutron star crust (Horowitz & Piekarewicz 2001a), the radii of $1.4 M_\odot$ neutron stars (Horowitz & Piekarewicz 2001b), and the direct URCA cooling of neutron stars (Horowitz & Piekarewicz 2002). As the radius of low-mass neutron stars depends on the solid crust of nonuniform matter, a treatment of the crust is discussed in § 3. Our results, presented in § 4, show a strong correlation between the radius of a low-mass neutron star and the neutron radius R_n of ^{208}Pb that is essentially model independent. This is because the structure of both objects depends on the EOS at similar densities. In contrast, the radius of a $1.4 M_\odot$ neutron star shows a considerable model dependence. This is because a $1.4 M_\odot$ neutron star is also sensitive to the EOS at higher densities, and the high-density EOS is not constrained by nuclear observables. In § 5 we conclude that properties of low-mass neutron stars can be inferred from measuring properties of atomic nuclei. In particular, the radius of a $1/2 M_\odot$ neutron star can be deduced from a measurement of R_n in ^{208}Pb . One will then be able to directly compare this inferred radius to the measured radius of an $\approx 1.4 M_\odot$ neutron star to gain information on the density dependence of the EOS. Thus, even if a mass-radius measurement for a single ($\approx 1.4 M_\odot$) neutron star is available, one can use the atomic nucleus to gain information on

the density dependence of the EOS. This should provide the most precise determination of the density dependence of the EOS to date and should indicate whether a transition to a high-density exotic phase of matter is possible or not.

2. FORMALISM

Our starting point is the relativistic effective-field theory of Müller and Serot (Müller & Serot 1996) supplemented with new couplings between the isoscalar and the isovector mesons. This allows us to correlate nuclear observables, such as the neutron radius of ^{208}Pb , with neutron star properties. We will explore uncertainties in these correlations by considering a range of model parameters. The model has been introduced and discussed in detail in several earlier references (see Horowitz & Piekarewicz 2001a, 2001b, 2002), yet a brief summary is included here for completeness.

The interacting Lagrangian density is given by (Müller & Serot 1996; Horowitz & Piekarewicz 2001a)

$$\begin{aligned} \mathcal{L}_{\text{int}} = \bar{\psi} \Big\{ g_s \phi - \left[g_v V_\mu + \frac{g_\rho}{2} \boldsymbol{\tau} \cdot \mathbf{b}_\mu + \frac{e}{2} (1 + \tau_3) A_\mu \right] \gamma^\mu \Big\} \psi \\ - \frac{\kappa}{3!} (g_s \phi)^3 - \frac{\lambda}{4!} (g_s \phi)^4 + \frac{\zeta}{4!} g_v^4 (V_\mu V^\mu)^2 \\ + g_\rho^2 \mathbf{b}_\mu \cdot \mathbf{b}^\mu (\Lambda_s g_s^2 \phi^2 + \Lambda_v g_v^2 V_\mu V^\mu). \end{aligned} \quad (2)$$

The model contains an isodoublet nucleon field (ψ) interacting via the exchange of two isoscalar mesons, the scalar sigma (ϕ) and the vector omega (V^μ), one isovector meson, the rho (\mathbf{b}^μ), and the photon (A^μ). In addition to meson-nucleon interactions the Lagrangian density includes scalar and vector self-interactions. Omega-meson self-interactions ζ soften the equation of state at high density. Finally, the nonlinear couplings Λ_s and Λ_v are included to modify the density-dependence of the symmetry energy $a_{\text{sym}}(\rho)$. We employ equation (2) in a mean-field approximation where the meson fields are replaced by their ground-state expectation values. The coupling constants in equation (2) are fitted to nuclear matter and finite nuclei properties. All of the parameter sets considered here, namely, NL3 (Lalazissis, König, & Ring 1997), S271 (Horowitz & Piekarewicz 2001a), and Z271 (Horowitz & Piekarewicz 2001a) reproduce the following properties of symmetric nuclear matter: saturation at a Fermi momentum of $k_F = 1.30$ fm $^{-1}$ with a binding energy per nucleon of -16.24 MeV and an incompressibility of $K = 271$ MeV. The various parameter sets differ in their effective masses at saturation density, in their ω -meson self-interactions (which are included for Z271 and neglected for NL3 and S271) and in the nonlinear couplings Λ_s and Λ_v (see Table 1). Note that the NL3 parameterization has been used extensively to reproduce a variety of nuclear properties (Lalazissis et al. 1997).

The symmetry energy at saturation density is not well constrained experimentally. However, an average of the symmetry energy at saturation density and the surface symmetry energy is constrained by the binding energy of nuclei. Thus, the following prescription has been adopted: the value of the $NN\rho$ coupling constant is adjusted so that all parameter sets have a symmetry energy of 25.67 MeV at $k_F = 1.15$ fm $^{-1}$. This ensures accurate binding energies for heavy nuclei, such as ^{208}Pb . Following this prescription the symmetry energy at saturation density is predicted to be 37.3, 36.6, and 36.3 MeV for parameter sets NL3, S271, and

TABLE 1
MODEL PARAMETERS USED IN THE CALCULATIONS

Model	m_s (MeV)	g_s^2	g_v^2	κ (MeV)	λ	ζ
NL3	508.194	104.3871	165.5854	3.8599	-0.0159049	0
S271	505	81.1071	116.7655	6.68344	-0.01580	0
Z271	465	49.4401	70.6689	6.16960	+0.156341	0.06

NOTES.—The parameter κ and the scalar mass m_s are given in MeV. The nucleon, rho, and omega masses are kept fixed at $M = 939$, $m_\rho = 763$, and $m_\omega = 783$ MeV, respectively—except in the case of the NL3 model, where it is fixed at $m_\omega = 782.5$ MeV.

Z271, respectively (for $\Lambda_s = \Lambda_v = 0$). Changing Λ_s or Λ_v changes the density dependence of the symmetry energy by changing the effective ρ -meson mass. In general, increasing either Λ_s or Λ_v causes the symmetry energy to grow more slowly with density.

The neutron radius of ^{208}Pb depends on the density dependence of the symmetry energy. A large pressure for neutron matter pushes neutrons out against surface tension and leads to a large neutron radius. The pressure depends on the derivative of the energy of symmetric matter with respect to density (which is approximately known) and the derivative of the symmetry energy, $da_{\text{sym}}/d\rho$. Thus, parameter sets with a large $da_{\text{sym}}/d\rho$ yield a large neutron radius in ^{208}Pb . Note that all parameter sets approximately reproduce the observed proton radius and binding energy of ^{208}Pb . Therefore, changing Λ_s or Λ_v allows one to change the density dependence of the symmetry energy $da_{\text{sym}}/d\rho$ while keeping many other properties fixed. Once the model parameters have been fixed, it is a simple matter to calculate the EOS for uniform matter in beta equilibrium, where the chemical potentials of the neutrons μ_n , protons μ_p , electrons μ_e , and muons μ_μ satisfy

$$\mu_n - \mu_p = \mu_e = \mu_\mu . \quad (3)$$

Note that the high-density interior of a neutron star is assumed to be a uniform liquid; possible transitions to a quark- or meson-condensate phase are neglected.

3. BOUNDARY BETWEEN CRUST AND INTERIOR

Neutron stars are expected to have a solid inner crust of nonuniform neutron-rich matter above a liquid mantle. The phase transition from solid to liquid is thought to be weakly first-order and can be found by comparing a detailed model of the nonuniform crust to the liquid (Douchin & Haensel 2001). Yet in practice, model calculations yield very small density discontinuities at the transition. Therefore, a good approximation is to search for the density at which the uniform liquid first becomes unstable to small-amplitude density oscillations (see, for example, Douchin & Haensel 2000). This method would yield the exact transition density for a second-order phase transition.

The stability analysis of the uniform ground state is based on a relativistic random-phase approximation (RPA) for a system of electrons, protons, and neutrons (Horowitz & Wehrberger 1991). The approach is generalized here to accommodate the various nonlinear couplings among the meson fields. We start by considering a plane wave density fluctuation of momentum $q = |\mathbf{q}|$ and zero energy $q_0 = 0$. To describe small-amplitude particle-hole (or particle-

antiparticle) excitations of the fermions we compute the longitudinal polarization matrix that is defined as follows:

$$\Pi_L = \begin{pmatrix} \Pi_{00}^e & 0 & 0 & 0 \\ 0 & \Pi_s^n + \Pi_s^p & \Pi_m^p & \Pi_m^n \\ 0 & \Pi_m^p & \Pi_{00}^p & 0 \\ 0 & \Pi_m^n & 0 & \Pi_{00}^n \end{pmatrix} . \quad (4)$$

Here the one-one entry describes electrons, the two-two entry protons plus neutrons interacting via scalar mesons, the three-three entry protons interacting with vector mesons, and the four-four entry neutrons interacting with vector mesons. The individual polarization insertions are given by

$$i\Pi_s(q, q_0) = \int \frac{d^4 p}{(2\pi)^4} \text{Tr}[G(p)G(p+q)] , \quad (5a)$$

$$i\Pi_m(q, q_0) = \int \frac{d^4 p}{(2\pi)^4} \text{Tr}[G(p)\gamma_0 G(p+q)] , \quad (5b)$$

$$i\Pi_{00}(q, q_0) = \int \frac{d^4 p}{(2\pi)^4} \text{Tr}[G(p)\gamma_0 G(p+q)\gamma_0] , \quad (5c)$$

where Tr indicates a trace over Dirac indices. Note that the fermion Green's function has been defined as

$$G(p) = (p + M^*) \left[\frac{1}{p^{*2} - M^{*2}} + \frac{i\pi}{E_p^*} \delta(p_0^* - E_p^*) \theta(k_F - |\mathbf{p}|) \right] . \quad (6)$$

Here k_F is the Fermi momentum, $M^* = M - g_s \phi_0$ is the nucleon effective mass, $E_p^* = (p^2 + M^{*2})^{1/2}$, and $p_\mu^* = p_\mu - (g_v V_\mu \pm g_\rho b_\mu/2)$ (with the plus sign for protons and the minus sign for neutrons). Note that in the case of the electrons, $M^* = m_e$ and $p_\mu^* = p_\mu$. Explicit analytic formulas for Π_{00} , Π_s , and Π_m in the static limit ($q_0 = 0$) are given in the Appendix.

The lowest-order meson propagator D_L^0 is computed in (Horowitz & Wehrberger 1991) in the absence of nonlinear meson couplings. It is given by

$$D_L^0 = \begin{pmatrix} d_g & 0 & -d_g & 0 \\ 0 & -d_s^0 & 0 & 0 \\ -d_g & 0 & d_g + d_v^0 + d_\rho^0 & d_v^0 - d_\rho^0 \\ 0 & 0 & d_v^0 - d_\rho^0 & d_v^0 + d_\rho^0 \end{pmatrix} . \quad (7)$$

Expressions for the photon and for the various meson propagators in the limit of no nonlinear meson couplings

are given as follows:

$$d_g = \frac{e^2}{q^2} = \frac{4\pi\alpha}{q^2}, \quad (8a)$$

$$d_s^0 = \frac{g_s^2}{q^2 + m_s^2}, \quad (8b)$$

$$d_v^0 = \frac{g_v^2}{q^2 + m_v^2}, \quad (8c)$$

$$d_\rho^0 = \frac{g_\rho^2/4}{q^2 + m_\rho^2}. \quad (8d)$$

The appearance of a minus sign in the one-three element of D_L^0 relative to the one-one element is because electrons and protons have opposite electric charges.

The addition of nonlinear couplings in the Lagrangian leads to a modification of the meson masses. Effective meson masses are defined in terms of the quadratic fluctuations of the meson fields around their static, mean-field values (the linear fluctuations vanish by virtue of the mean-field equations). That is,

$$m_s^{*2} = -\frac{\partial^2 \mathcal{L}}{\partial \phi_0^2}, \quad m_v^{*2} = +\frac{\partial^2 \mathcal{L}}{\partial V_0^2}, \quad m_\rho^{*2} = +\frac{\partial^2 \mathcal{L}}{\partial b_0^2}. \quad (9)$$

This yields the following expressions for the effective meson masses in terms of the static meson fields and the coupling constants defined in the interacting Lagrangian of equation (2):

$$m_s^{*2} = m_s^2 + g_s^2 \left(\kappa \Phi_0 + \frac{\lambda}{2} \Phi_0^2 - 2\Lambda_s B_0^2 \right), \quad (10a)$$

$$m_v^{*2} = m_v^2 + g_v^2 \left(\frac{\zeta}{2} W_0^2 + 2\Lambda_v B_0^2 \right), \quad (10b)$$

$$m_\rho^{*2} = m_\rho^2 + g_\rho^2 (2\Lambda_s \Phi_0^2 + 2\Lambda_v W_0^2). \quad (10c)$$

Note that the following definitions have been introduced: $\Phi_0 \equiv g_s \phi_0$, $W_0 \equiv g_v V_0$, and $B_0 \equiv g_\rho b_0$.

Further, the new couplings between isoscalar and isovector mesons (Λ_s and Λ_v) lead to additional off-diagonal terms in the meson propagator. These arise because the quadratic fluctuations around the static solutions generate terms of the form

$$\frac{\partial^2 \mathcal{L}}{\partial \phi_0 \partial b_0} \neq 0 \quad \text{and} \quad \frac{\partial^2 \mathcal{L}}{\partial V_0 \partial b_0} \neq 0. \quad (11)$$

For simplicity we only consider here the following two cases: (1) $\Lambda_s \neq 0$ and $\Lambda_v = 0$ or (2) $\Lambda_s = 0$ and $\Lambda_v \neq 0$, and neglect the (slightly) more complicated case in which both coupling constants are nonzero.

For the first case of $\Lambda_s \neq 0$ and $\Lambda_v = 0$, the new components of the longitudinal meson propagator become

$$d_v = \frac{g_v^2}{q^2 + m_v^{*2}}, \quad (12a)$$

$$d_s = \frac{g_s^2 (q^2 + m_\rho^{*2})}{(q^2 + m_s^{*2})(q^2 + m_\rho^{*2}) + (4g_s g_\rho \Lambda_s \Phi_0 B_0)^2}, \quad (12b)$$

$$d_\rho = \frac{(g_\rho^2/4)(q^2 + m_s^{*2})}{(q^2 + m_s^{*2})(q^2 + m_\rho^{*2}) + (4g_s g_\rho \Lambda_s \Phi_0 B_0)^2}, \quad (12c)$$

$$d_{sp} = \frac{2g_s^2 g_\rho^2 \Lambda_s \Phi_0 B_0}{(q^2 + m_s^{*2})(q^2 + m_\rho^{*2}) + (4g_s g_\rho \Lambda_s \Phi_0 B_0)^2}. \quad (12d)$$

With these changes the modified longitudinal meson propagator now reads

$$D_L = \begin{pmatrix} d_g & 0 & -d_g & 0 \\ 0 & -d_s & d_{sp} & -d_{sp} \\ -d_g & d_{sp} & d_g + d_v + d_\rho & d_v - d_\rho \\ 0 & -d_{sp} & d_v - d_\rho & d_v + d_\rho \end{pmatrix}. \quad (13)$$

Alternatively, for the case of $\Lambda_s = 0$ and $\Lambda_v \neq 0$ we obtain

$$d_s = \frac{g_s^2}{q^2 + m_s^{*2}}, \quad (14a)$$

$$d_v = \frac{g_v^2 (q^2 + m_\rho^{*2})}{(q^2 + m_v^{*2})(q^2 + m_\rho^{*2}) - (4g_v g_\rho \Lambda_v W_0 B_0)^2}, \quad (14b)$$

$$d_\rho = \frac{(g_\rho^2/4)(q^2 + m_v^{*2})}{(q^2 + m_v^{*2})(q^2 + m_\rho^{*2}) - (4g_v g_\rho \Lambda_v W_0 B_0)^2}, \quad (14c)$$

$$d_{vp} = \frac{-2g_v^2 g_\rho^2 \Lambda_v W_0 B_0}{(q^2 + m_v^{*2})(q^2 + m_\rho^{*2}) - (4g_v g_\rho \Lambda_v W_0 B_0)^2}. \quad (14d)$$

With these changes the modified longitudinal meson propagator now reads

$$D_L = \begin{pmatrix} d_g & 0 & -d_g & 0 \\ 0 & -d_s & 0 & 0 \\ -d_g & 0 & d_g + d_v + d_\rho + 2d_{vp} & d_v - d_\rho \\ 0 & 0 & d_v - d_\rho & d_v + d_\rho - 2d_{vp} \end{pmatrix}. \quad (15)$$

The uniform system becomes unstable to small-amplitude density fluctuations of momentum transfer q when the following condition is satisfied:

$$\det [1 - D_L(q)\Pi_L(q, q_0 = 0)] \leq 0. \quad (16)$$

We estimate the transition density (ρ_c) between the inner crust and the liquid interior as the largest density for which equation (16) has a solution. Our results for ρ_c are listed in Tables 2–5 and also shown in Figure 1. We find a strong

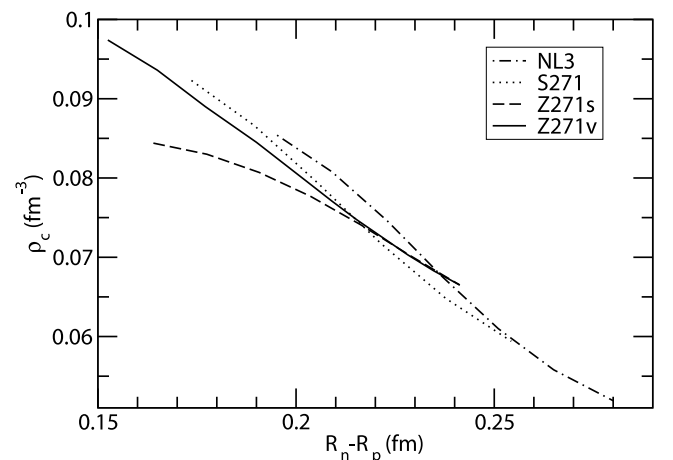


FIG. 1.—Transition density ρ_c at which uniform matter becomes unstable to density oscillations as a function of the neutron skin in ^{208}Pb . The solid curve is for the Z271 parameter set with $\Lambda_v \neq 0$ while the dashed curve uses Z271 with $\Lambda_s \neq 0$. The dotted curve is for the S271 set and the dot-dashed curve for NL3, both of these with $\Lambda_v \neq 0$.

TABLE 2
RESULTS FOR THE NL3 PARAMETER SET WITH $\Lambda_s = 0$

Λ_v	g_p^2	$R_n - R_p^{(208\text{Pb})}$ (fm)	$R(\frac{1}{3} M_\odot)$ (km)	$R(\frac{1}{2} M_\odot)$ (km)	$R(\frac{3}{4} M_\odot)$ (km)	$R(1.4 M_\odot)$ (km)	ρ_c (fm $^{-3}$)
0.030	127.0	0.1952	16.766	14.789	14.142	14.175	0.0854
0.025	115.6	0.209	18.37	15.59	14.60	14.38	0.0808
0.020	106.0	0.223	19.49	16.15	14.93	14.52	0.0746
0.015	97.9	0.237	19.73	16.39	15.10	14.61	0.0675
0.010	90.9	0.251	19.31	16.40	15.20	14.68	0.0610
0.005	84.9	0.265	18.70	16.35	15.31	14.81	0.0558
0.000	79.6	0.280	18.10	16.27	15.47	15.05	0.0519

NOTES.—The $NN\rho$ coupling constant g_p^2 and the neutron minus proton rms radius for ^{208}Pb are given along with the radii of $\frac{1}{3}, \frac{1}{2}, \frac{3}{4}$, and $1.4 M_\odot$ neutron stars. Last column gives the transition density ρ_c between the inner crust and liquid interior.

TABLE 3
RESULTS FOR THE S271 PARAMETER SET WITH $\Lambda_s = 0$

Λ_v	g_p^2	$R_n - R_p^{(208\text{Pb})}$ (fm)	$R(\frac{1}{3} M_\odot)$ (km)	$R(\frac{1}{2} M_\odot)$ (km)	$R(\frac{3}{4} M_\odot)$ (km)	$R(1.4 M_\odot)$ (km)	ρ_c (fm $^{-3}$)
0.05	127.8389	0.1736	15.88	14.06	13.43	13.25	0.0923
0.04	116.2950	0.1895	17.75	15.00	13.96	13.47	0.0866
0.03	106.6635	0.2054	19.25	15.77	14.42	13.65	0.0794
0.02	98.5051	0.2215	19.80	16.24	14.76	13.82	0.0717
0.01	91.5061	0.2378	19.54	16.46	15.08	14.07	0.0648
0.00	85.4357	0.2543	18.95	16.53	15.43	14.56	0.0594

NOTES.—The $NN\rho$ coupling constant g_p^2 and the neutron minus proton rms radius for ^{208}Pb are given along with the radii of $1/3, 1/2, 3/4$, and $1.4 M_\odot$ neutron stars. Last column gives the transition density ρ_c between the inner crust and liquid interior.

TABLE 4
RESULTS FOR THE Z271 PARAMETER SET WITH $\Lambda_s = 0$

Λ_v	g_p^2	$R_n - R_p^{(208\text{Pb})}$ (fm)	$R(\frac{1}{3} M_\odot)$ (km)	$R(\frac{1}{2} M_\odot)$ (km)	$R(\frac{3}{4} M_\odot)$ (km)	$R(1.4 M_\odot)$ (km)	ρ_c (fm $^{-3}$)
0.14	139.3368	0.1525	13.799	12.709	12.293	11.616	0.0974
0.12	129.2795	0.1650	15.012	13.379	12.688	11.748	0.0936
0.10	119.5245	0.1771	16.219	14.039	13.080	11.880	0.0890
0.08	112.9710	0.1900	17.405	14.696	13.481	12.016	0.0845
0.06	106.2682	0.2026	18.31	15.28	13.89	12.18	0.0796
0.05	103.2065	0.2090	18.61	15.53	14.09	12.29	0.0771
0.04	100.3162	0.2154	18.82	15.76	14.30	12.43	0.0747
0.03	97.5834	0.2218	18.95	15.96	14.53	12.62	0.0725
0.02	94.9956	0.2282	18.98	16.12	14.75	12.89	0.0703
0.01	92.5415	0.2347	18.94	16.25	14.98	13.27	0.0683
0.00	90.2110	0.2413	18.88	16.36	15.20	13.77	0.0665

NOTES.—The $NN\rho$ coupling constant g_p^2 and the neutron minus proton rms radius for ^{208}Pb are given along with the radii of $1/3, 1/2, 3/4$, and $1.4 M_\odot$ neutron stars. Last column gives the transition density ρ_c between the inner crust and liquid interior.

TABLE 5
RESULTS FOR THE Z271 PARAMETER SET WITH $\Lambda_v = 0$

Λ_s	g_p^2	$R_n - R_p^{(208\text{Pb})}$ (fm)	$R(\frac{1}{3} M_\odot)$ (km)	$R(\frac{1}{2} M_\odot)$ (km)	$R(\frac{3}{4} M_\odot)$ (km)	$R(1.4 M_\odot)$ (km)	ρ_c (fm $^{-3}$)
0.06	146.6988	0.1640	13.34	12.71	12.52	11.98	0.0844
0.05	132.8358	0.1775	14.63	13.48	13.01	12.19	0.0830
0.04	121.3666	0.1907	15.99	14.27	13.51	12.42	0.0807
0.03	111.7205	0.2036	17.28	15.02	14.00	12.68	0.0777
0.02	103.4949	0.2163	18.27	15.66	14.46	12.97	0.0741
0.01	96.3974	0.2288	18.79	16.10	14.86	13.32	0.0702
0.00	90.2110	0.2413	18.88	16.36	15.20	13.77	0.0665

NOTES.—The $NN\rho$ coupling constant g_p^2 and the neutron minus proton rms radius for ^{208}Pb are given along with the radii of $1/3, 1/2, 3/4$, and $1.4 M_\odot$ neutron stars. Last column gives the transition density ρ_c between the inner crust and liquid interior.

correlation between the neutron skin of ^{208}Pb and ρ_c , as originally discussed in (Horowitz & Piekarewicz 2001a).

At the lower densities of the inner crust the system is non-uniform and may have a very complex structure that may include spherical, cylindrical, and platelike nuclei, bubbles, rods, plates, etc. (Lorenz, Ravenhall, & Pethick 1993; Oyamatsu 1993). At present we do not have microscopic calculations of these structures in our models. Therefore, we adopt a simple interpolation formula to estimate the equation of state in the inner crust. That is, we assume a polytropic form for the EOS in which the pressure is approximately given by (Link et al. 1999)

$$P(\epsilon) = A + B\epsilon^{4/3}, \quad (17)$$

where ϵ is the mass-energy density. The two constants A and B in equation (17) are chosen so that the pressure is continuous at the boundary between the inner crust and the liquid interior (determined from the RPA analysis) and at the boundary between the inner and the outer crusts. For the low-density outer crust we assume the EOS of Baym, Pethick, & Sutherland (1971) up to a baryon density of $\rho_{\text{outer}} = 2.57 \times 10^{-4} \text{ fm}^{-3}$, which corresponds to an energy density of $\epsilon_{\text{outer}} = 4.30 \times 10^{11} \text{ g cm}^{-3}$ (or 0.24 MeV fm^{-3}) and a pressure of $P_{\text{outer}} = 4.87 \times 10^{-4} \text{ MeV fm}^{-3}$. Thus the two constants A and B of equation (17) are adjusted to reproduce P_{outer} at ϵ_{outer} and the pressure of the uniform liquid, calculated within the relativistic mean-field (RMF) approach, at ϵ_c which is the energy density corresponding to ρ_c . That is,

$$P(\epsilon) = \begin{cases} P_{\text{BPS}}(\epsilon) & \text{for } \epsilon_{\min} \leq \epsilon \leq \epsilon_{\text{outer}}, \\ A + B\epsilon^{4/3} & \text{for } \epsilon_{\text{outer}} < \epsilon \leq \epsilon_c, \\ P_{\text{RMF}}(\epsilon) & \text{for } \epsilon_c < \epsilon. \end{cases} \quad (18)$$

Note that $\epsilon_{\min} = 5.86 \times 10^{-9} \text{ MeV fm}^{-3}$ is the minimum value of the energy density included in the equation of state. This value corresponds to a minimum pressure of $P_{\min} = 6.08 \times 10^{-15} \text{ MeV fm}^{-3}$, which is the value at which we stop integrating the Tolman-Oppenheimer-Volkoff equations. That is, the radius R of a neutron star (see § 4) is defined by the expression $P(R) = P_{\min}$. For the relativistic mean-field interaction (TM1) of (Sugahara & Toki 1994), the relatively simple procedure presented here is a good approximation to the more complicated explicit calculation of the EOS in the inner crust (Shen et al. 1998).

4. RESULTS

Figures 2–5 and Tables 2–5 show the radii of neutron stars of mass $\frac{1}{3}, \frac{1}{2}, \frac{3}{4}$, and $1.4 M_\odot$ as a function of the neutron skin ($R_n - R_p$) of ^{208}Pb . One might expect a strong correlation between the radius of a neutron star and the neutron radius of ^{208}Pb , as the same pressure of neutron-rich matter that pushes neutrons out against surface tension in ^{208}Pb pushes neutrons out against gravity in a neutron star (Horowitz & Piekarewicz 2001b). However, the central density of a $1.4 M_\odot$ neutron star is a few times larger than normal nuclear-matter saturation density ρ_0 . Thus, $R(1.4 M_\odot)$ depends on the EOS at low and high densities while R_n only depends on the EOS for $\rho \leq \rho_0$. Softening the EOS (i.e., decreasing the pressure) at high densities will decrease $R(1.4 M_\odot)$ without changing R_n . Hence, while Figure 5 shows a definite correlation— $R(1.4 M_\odot)$

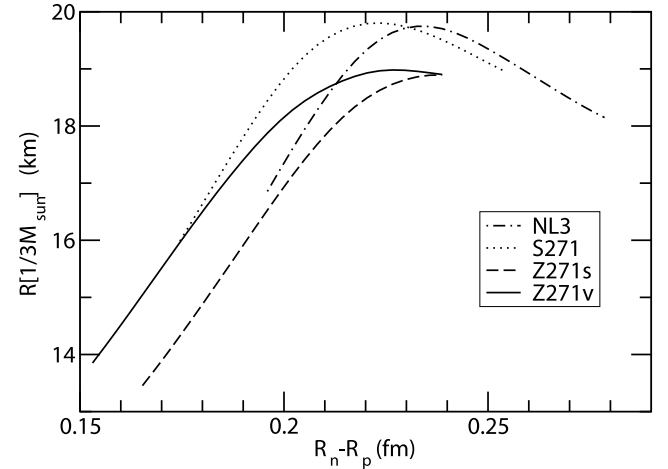


FIG. 2.—Radius of a neutron star of mass $\frac{1}{3} M_\odot$ as a function of the neutron skin in ^{208}Pb . The solid curve is for the Z271 parameter set with $\Lambda_v \neq 0$ while the dashed curve uses Z271 with $\Lambda_s \neq 0$. The dotted curve is for the S271 set and the dot-dashed curve for NL3, both of these with $\Lambda_v \neq 0$.

grows with increasing $R_n - R_p$ —there is a strong model dependence.

In contrast, the central density of a $\frac{1}{2} M_\odot$ star is of the order of ρ_0 , so $R(\frac{1}{2} M_\odot)$ and R_n depend on the EOS over a comparable density range. As a result, we find a strong correlation and weak model dependence in Figure 3. For example, if $R_n - R_p$ in ^{208}Pb is relatively large, e.g., $R_n - R_p \approx 0.25 \text{ fm}$, then $R(\frac{1}{2} M_\odot) \approx 16 \text{ km}$. Alternatively, if $R_n - R_p \approx 0.15 \text{ fm}$, then $R(\frac{1}{2} M_\odot) \lesssim 13 \text{ km}$. This is an important result. It suggests that even if observations of low-mass neutron stars are not feasible, one could still infer their radii from a single nuclear measurement. Note that the results for a $\frac{3}{4} M_\odot$ neutron star (Fig. 4) follow a similar trend.

A comment on the behavior of $\frac{1}{3} M_\odot$ neutron stars is now in order. Parameter sets that generate very large values for $R_n - R_p$ have large pressures near ρ_0 . This implies that the

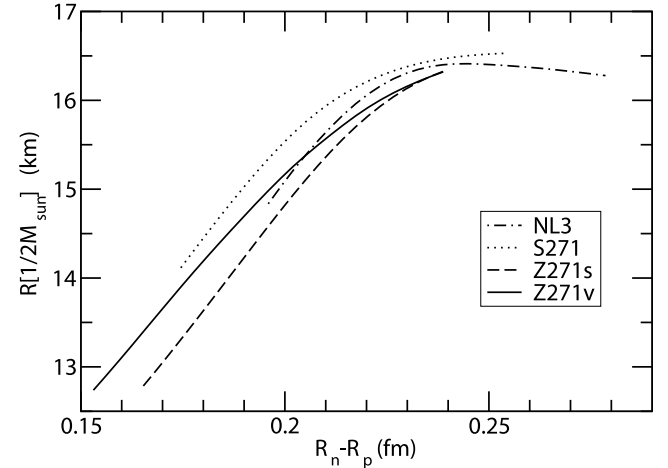


FIG. 3.—Radius of a neutron star of mass $\frac{1}{2} M_\odot$ as a function of the neutron skin in ^{208}Pb . The solid curve is for the Z271 parameter set with $\Lambda_v \neq 0$ while the dashed curve uses Z271 with $\Lambda_s \neq 0$. The dotted curve is for the S271 set and the dot-dashed curve for NL3, both of these with $\Lambda_v \neq 0$.

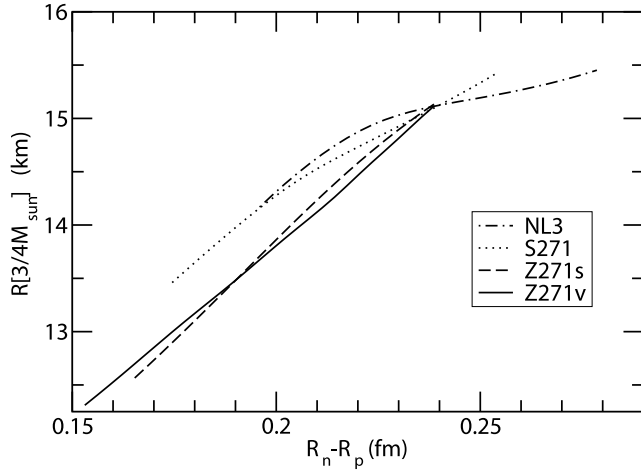


FIG. 4.—Radius of a neutron star of mass $\frac{3}{4} M_{\odot}$ as a function of the neutron skin in ^{208}Pb . The solid curve is for the Z271 parameter set with $\Lambda_v \neq 0$ while the dashed curve uses Z271 with $\Lambda_s \neq 0$. The dotted curve is for the S271 set and the dot-dashed curve for NL3, both of these with $\Lambda_v \neq 0$.

energy of neutron-rich matter rises rapidly with density. In turn, this leads (because all parameter sets are constrained to have the same symmetry energy at $\rho = 0.1 \text{ fm}^{-3}$) to lower energies and *lower pressures* at very low density than parameter sets with smaller values for $R_n - R_p$. This low-density region is important for low-mass neutron stars and could explain why $R(\frac{1}{3} M_{\odot})$ in Figure 2 actually decreases with increasing neutron skin for $R_n - R_p \gtrsim 0.23 \text{ fm}$.

We conclude this section with a rather speculative, yet insightful, comment on the impact of the above calculations on the equation of state of neutron-rich matter. As neutron star masses appear to lie in the very narrow range of $1.25\text{--}1.44 M_{\odot}$ (Thorsett & Chakrabarty 1999), the possibility of discovering very low mass neutron stars is remote; there may be no plausible mechanism for their formation. Our results suggest that there is no need to observe very low mass

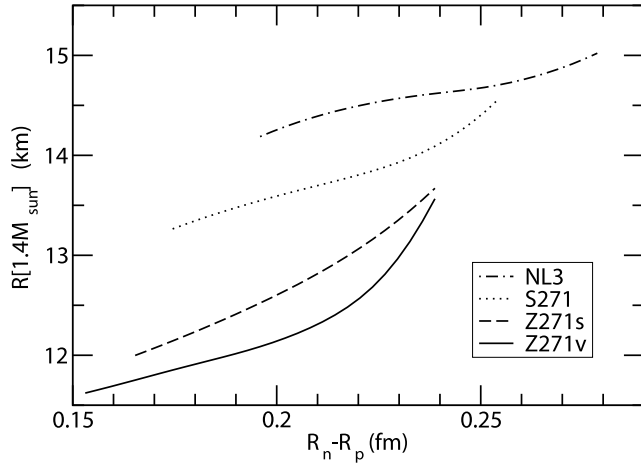


FIG. 5.—Radius of a neutron star of mass $1.4 M_{\odot}$ as a function of the neutron skin in ^{208}Pb . The solid curve is for the Z271 parameter set with $\Lambda_v \neq 0$ while the dashed curve uses Z271 with $\Lambda_s \neq 0$. The dotted curve is for the S271 set and the dot-dashed curve for NL3, both of these with $\Lambda_v \neq 0$.

neutron stars once the measurement of the neutron radius in ^{208}Pb becomes available. Indeed, the correlation between the neutron skin of ^{208}Pb and the radius of a low-mass star is sufficiently tight (as evinced in Fig. 3) that a useful limit on the radius of the star can be placed without ever having to observe it.

To illustrate this point we display in Figure 6 mass-radius relationships for a variety of equations of state as compiled by Lattimer & Prakash (2001); this is their Figure 2. To this figure we have superposed (as best as possible) observational limits obtained from RX J185635–3754 by Walter & Lattimer (2002); these limits are enclosed within the large rectangles. Now we speculate that the Jefferson Laboratory experiment reports a value for the neutron skin in ^{208}Pb of about 0.2 fm (there is no particular significance to this value other than it lies between relativistic and nonrelativistic predictions). Then, because of the tight correlation between the neutron skin of ^{208}Pb and the radius of low-mass neutron stars, we conclude that the radius of a $0.5 M_{\odot}$ neutron star should be about $14\text{--}15 \text{ km}$. By including this low-mass estimate into the figure (as small rectangles) a number of equations of state, previously allowed by the RX J185635–3754 limit, can now be ruled out. This, without the need for observing low-mass neutron stars or performing calculations of neutron skins in models not suitable for it (such as strange quark models). Thus, Figure 6 shows in one single figure constraints imposed on the EOS from both neutron skin and neutron star radii measurements.

5. DISCUSSION AND CONCLUSIONS

A number of relativistic effective-field theory parameter sets have been used to study correlations between the radii of neutron stars and the neutron radius R_n of ^{208}Pb . An RPA stability analysis was employed to find the transition density between the nonuniform inner crust and the uniform liquid interior. For the nonuniform outer crust we invoked the EOS of Baym et al. (1971). Then, a simple polytropic formula for the EOS, approximately valid for most of the crust (Link et al. 1999), was used to interpolate between the outer crust and the liquid interior. This simple, yet fairly accurate, procedure allows us to study the EOS for a variety of parameter sets that predict a wide range of values for the neutron radius of ^{208}Pb .

For a “normal” $1.4 M_{\odot}$ neutron star we find central densities of several times normal nuclear matter saturation density ($\rho_0 \approx 0.15 \text{ fm}^3$). Because the neutron radius of ^{208}Pb does not constrain the high-density component of the EOS, we find a strong model dependence between the radius of a $1.4 M_{\odot}$ neutron star and R_n . In contrast, the central density of a low-mass neutron star is close to ρ_0 . Therefore properties of the low-mass star are sensitive to the EOS over the same density range as R_n . As a result, we find a strong correlation and a weak model dependence between the radius of a $0.5 M_{\odot}$ neutron star and R_n (see Fig. 3). Thus, it should be possible to infer some properties of low-mass neutron stars from detailed measurements in atomic nuclei.

Understanding the density dependence of the equation of state is particularly interesting. A softening of the EOS at high density (where the pressure rises slower than expected) could signal the transition to an exotic phase, such as pion/kaon condensates, strange quark matter, and/or a color superconductor. Yet obtaining definitive results on the density dependence of the EOS may require measuring the

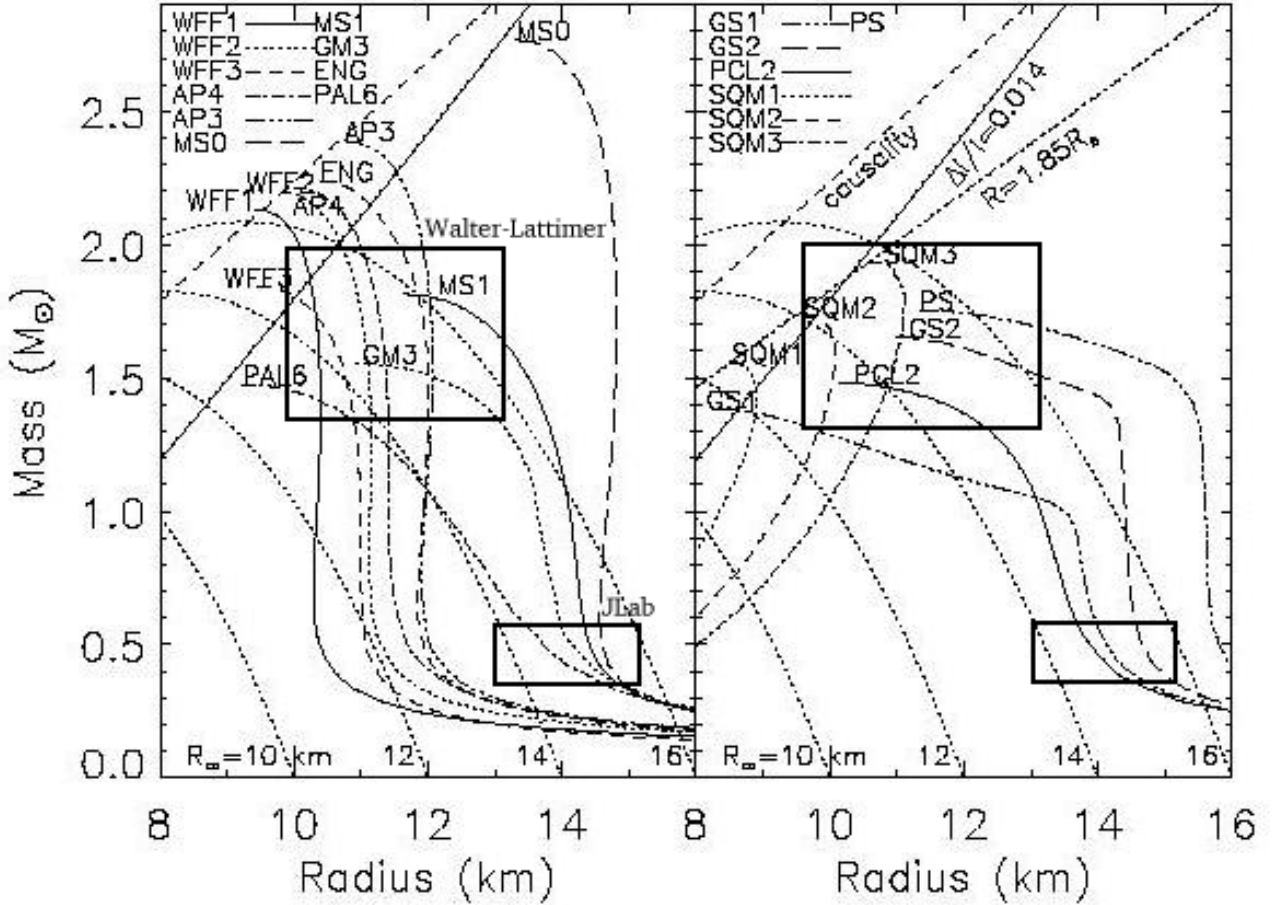


FIG. 6.—Mass-radius relationships for several EOS (Lattimer & Prakash 2001). Superposed on these, as big rectangles, are limits obtained from Walter & Lattimer (2002) and, as small rectangles, from an assumed neutron skin in ^{208}Pb of $R_n - R_p = 0.2 \text{ fm}$.

radius of neutron stars for a broad range of masses. This may be difficult as most compilations to date find neutron star masses in the very narrow range of $1.25\text{--}1.44 M_{\odot}$ (Thorsett & Chakrabarty 1999). Further, important ambiguities will remain if the radius of a $1.4 M_{\odot}$ neutron star proves to be moderately small. Would a small radius be an indication that the EOS is relatively soft at all densities and there is no phase transition, or is the EOS stiff at low density and undergoes an abrupt softening at high density from a phase transition?

Therefore, it is important to also make measurements that are exclusively sensitive to the low-density EOS. One obvious possibility is the radius of a low-mass ($\approx 0.5 M_{\odot}$) neutron star as its central density, close to ρ_0 , is much smaller

than that of a $1.4 M_{\odot}$ star. However, such low-mass stars may be very rare because they are hard to form. Notably, the neutron radius of a heavy nucleus, such as ^{208}Pb , contains similar information. Indeed, we find a strong correlation and a weak model dependence between the neutron radius of ^{208}Pb and the radius of a $0.5 M_{\odot}$ neutron star. This allows one to use nuclear information to infer the radius of a low-mass neutron star. Hence, comparing this inferred radius to the measured radius of a $\simeq 1.4 M_{\odot}$ neutron star, should provide the most complete information to date on the density dependence of the equation of state.

This work was supported in part by DOE grants DE-FG02-87ER40365 and DE-FG05-92ER40750.

APPENDIX

The polarizations are defined in equations (5a)–(5c) and describe particle-hole or particle-antiparticle excitations. In the static limit (energy transfer $q_0 = 0$) the scalar polarization for momentum transfer q is given by

$$\Pi_s(q, 0) = \frac{1}{2\pi^2} \left[k_F E_F - \left(3M^{*2} + \frac{q^2}{2} \right) \ln \frac{k_F + E_F}{M^*} + \frac{2E_F E^2}{q} \ln \left| \frac{2k_F - q}{2k_F + q} \right| \right] - \frac{1}{2\pi^2} \left(\frac{2E^3}{q} \ln \left| \frac{qE_F - 2k_F E}{qE_F + 2k_F E} \right| \right), \quad (\text{A1})$$

with Fermi momentum k_F , nucleon effective mass M^* , $E_F = (k_F^2 + M^{*2})^{1/2}$, and $E = (q^2/4 + M^{*2})^{1/2}$. Likewise, the

longitudinal polarization is given by

$$\Pi_{00}(q, 0) = -\frac{1}{\pi^2} \left[\frac{2}{3} k_F E_F - \frac{q^2}{6} \ln \frac{k_F + E_F}{M^*} - \frac{E_F}{3q} \left(M^{*2} + k_F^2 - \frac{3}{4} q^2 \right) \ln \left| \frac{2k_F - q}{2k_F + q} \right| \right] + \frac{1}{\pi^2} \left[\frac{E}{3q} \left(M^{*2} - \frac{q^2}{2} \right) \ln \left| \frac{qE_F - 2k_F E}{qE_F + 2k_F E} \right| \right], \quad (\text{A2})$$

while the mixed scalar-vector polarization becomes

$$\Pi_m(q, 0) = \frac{M^*}{2\pi^2} \left[k_F - \left(\frac{k_F^2}{q} - \frac{q}{4} \right) \ln \left| \frac{2k_F - q}{2k_F + q} \right| \right]. \quad (\text{A3})$$

REFERENCES

- Alford, M. 2001, in Proc. Conf. on Compact Stars in the QCD Phase Diagram, ed. R. Onyed & F. Sannino, eConf C010815, 137
- Baym, G., Pethick, C., & Sutherland, P. 1971, ApJ, 170, 299
- Brown, B. A. 2000, Phys. Rev. Lett., 85, 5296
- Brown, E. F., Bildsten, L., & Rutledge, R. E. 1998, ApJ, 504, L95
- Brown, G. E., Weingartner, J. C., & Wijers, R. A. M. J. 1996, ApJ, 463, 297
- Douchin, F., & Haensel, P. 2000, Phys. Lett. B., 485, 107
- . 2001, A&A, 380, 151
- Drake, J. J., et al. 2002, ApJ, 572, 996
- Haensel, P., Zdunik, J. L., & Douchin, F. 2002, A&A, 385, 301
- Hailey, C. J., & Mori, K. 2002, ApJ, 578, L133
- Heap, S. R., & Corcoran, M. F. 1992, ApJ, 387, 340
- Heiselberg, H. 2001, in Proc. Conf. on Compact Stars in the QCD Phase Diagram, ed. R. Onyed & F. Sannino, eConf C010815, 3
- Horowitz, C. J., & Piekarewicz, J. 2001a, Phys. Rev. Lett., 86, 5647
- . 2001b, Phys. Rev. C, 64, 062802
- . 2002, Phys. Rev. C, 66, 055803
- Horowitz, C. J., Pollock, S. J., Souder, P. A., & Michaels, R. 2001, Phys. Rev. C, 63, 025501
- Horowitz, C. J., & Wehrberger, K. 1991, Nucl. Phys. A, 531, 665
- Jaikumar, P., & Prakash, M. 2001, Phys. Lett. B, 516, 345
- Lalazissis, G. A., König, J., & Ring, P. 1997, Phys. Rev. C, 55, 540
- Lattimer, J. M., & Prakash, M. 2001, ApJ, 550, 426
- Lindblom, L. 1992, ApJ, 398, 569
- Link, B., Epstein, R. I., & Lattimer, J. M. 1999, Phys. Rev. Lett., 83, 3362
- Lorenz, C. P., Ravenhall, D. G., & Pethick, C. J. 1993, Phys. Rev. Lett., 70, 379
- Michaels, R., Souder, P. A., & Urciuoli, G. M. 2000, Jefferson Laboratory Experiment E-00-003 (Newport News: Jefferson Laboratory)
- Müller, H., & Serot, B. D. 1996, Nucl. Phys. A, 606, 508
- Orosz, J. A., & Kuulkers, E. 1999, MNRAS, 305, 132
- Oyamatsu, K. 1993, Nucl. Phys. A, 561, 431
- Pons, J. A., Miralles, J. A., Prakash, M., & Lattimer, J. M. 2001, ApJ, 553, 382
- Pons, J. A., Walter, F. M., Lattimer, J. M., Prakash, M., Neuhauser, R., & An, P. 2002, ApJ, 564, 981
- Prakash, M. 2002, Nucl. Phys. A, 698, 440
- Rutledge, R. E., Bildsten, L., Brown, E. F., Pavlov, G. G., & Zavlin, V. E. 2002, ApJ, 578, 405
- Sanwal, D., Pavlov, G. G., Zavlin, V. E., & Teter, M. A. 2002, ApJ, 574, L61
- Shen, H., Toki, H., Oyamatsu, K., & Sumiyoshi, K. 1998, Nucl. Phys. A, 637, 435
- Stickland, D., Lloyd, C., & Radzuin-Woodham, A. 1997, MNRAS, 286, L21
- Sugahara, Y., & Toki, H. 1994, Nucl. Phys. A, 579, 557
- Thorsett, S. E., & Chakrabarty, D. 1999, ApJ, 512, 288
- van Kerkwijk, J. H., van Paradijs, J., & Zuiderveld, E. J. 1995, A&A, 303, 497
- Walter, F. M., & Lattimer, J. M. 2002, ApJ, 576, L145

Relativistic models of the neutron-star matter equation of state

F. J. Fattoyev^{*} and J. Piekarewicz[†]

Department of Physics, Florida State University, Tallahassee, Florida 32306, USA

(Received 5 March 2010; published 17 August 2010)

Motivated by a recent astrophysical measurement of the pressure of cold matter above nuclear-matter saturation density, we compute the equation of state of neutron-star matter using accurately calibrated relativistic models. The uniform stellar core is assumed to consist of nucleons and leptons in beta equilibrium; no exotic degrees of freedom are included. We found the predictions of these models to be in fairly good agreement with the measured equation of state. Yet the *mass-versus-radius* relations predicted by these same models display radii that are consistently larger than the observations.

DOI: 10.1103/PhysRevC.82.025805

PACS number(s): 26.60.Kp, 21.60.Jz

I. INTRODUCTION

The quest for the Holy Grail of Nuclear Physics—the equation of state (EOS) of hadronic matter—remains an area of intense activity that cuts across a variety of disciplines. Indeed, the limits of nuclear existence, the dynamics of heavy-ion collisions, the structure of neutron stars, and the collapse of massive stellar cores all depend sensitively on the equation of state. With the advent and commissioning of sophisticated new radioactive beam facilities, powerful heavy-ion colliders, telescopes operating at a variety of wavelengths, and more sensitive gravitational wave detectors, one will be able to probe the nuclear dynamics over a wide range of nucleon asymmetries, temperatures, and densities. However, in the present contribution we focus on the dynamics of cold matter under extreme conditions of density (both small and large) and for this case neutron stars remain the tool of choice [1–4]. Being both very compact and extremely dense, neutron stars are unique laboratories for probing the equation of state of neutron-rich matter under conditions unattainable by terrestrial experiments.

Intimately connected to the equation of state of cold, neutron-rich matter is the *mass-versus-radius* (*M-R*) relationship of neutron stars. Indeed, an EOS is the sole ingredient that must be supplied to solve the equations of stellar structure (i.e., the Tolman-Oppenheimer-Volkoff equations). Conversely, knowledge of the *M-R* relation is sufficient to uniquely determine the equation of state of neutron-star matter [5]. As argued by Lindblom almost 20 years ago, the availability of such information—even from a single neutron star—will provide interesting information about the equation of state [5]. Viewed in this light, the recent report of combined mass-radius measurement for three neutron stars and the subsequent determination of the equation of state is significant [1]. In particular, the conclusion that the EOS so determined is softer than those containing only nucleonic degrees of freedom is both interesting and provocative.

In this contribution we compute the equation of state of neutron-star matter and the resulting *M-R* relation using

accurately calibrated relativistic mean-field models. These models have been calibrated to the properties of infinite nuclear matter at saturation density [6], to the ground-state properties of finite nuclei [7,8], or to both [9]. Unlike the former two, the latter parametrization predicts a significantly soft symmetry energy, a feature that appears consistent with the behavior of dilute neutron matter (see Ref. [10] and references therein). A detailed explanation of the role of the model parameters on the equation of state is given below. We note, however, that none of the models considered in this work include exotic degrees of freedom, such as hyperons, meson (condensates), or quarks. In this regard, our results are mixed when compared with the conclusions of Ref. [1]. On the one hand, the stellar radii predicted by the relativistic models are larger than observed, seemingly confirming that such equations of state are too stiff. On the other hand, the agreement between the predicted and observed EOS suggests the opposite.

The article has been organized as follows. In Sec. II we introduce the relativistic mean-field models that will be used to compute the equation of state of neutron-star matter. Special emphasis is placed on the various empirical parameters that may be tuned to soften the equation of state. In Sec. III we compare our results for the *M-R* relation and for the equation of state of neutron-star matter against the observational data presented in Ref. [1]. A few concluding remarks are provided in Sec. IV.

II. FORMALISM

The structure of neutron stars is sensitive to the equation of state of cold, fully catalyzed, neutron-rich matter over an enormous range of densities [2–4]. For the low-density outer crust we employ the equation of state of Baym *et al.* [11]. At densities of about a third to a half of nuclear-matter saturation density, uniformity in the system is restored and for this (liquid-core) region we use an EOS derived from a representative set of accurately calibrated relativistic mean-field models [6–9]. It was speculated that the region between the outer crust and the liquid core consists of complex and exotic structures, collectively known as *nuclear pasta* [12–14]. Whereas significant progress was made in simulating this exotic region [15–17], a detailed equation of state is still

*ff07@fsu.edu

†jpiekarewicz@fsu.edu

TABLE I. Parameter sets for the four models used in the text to generate the equation of state. The parameter κ and the meson masses m_s , m_v , and m_ρ are all given in MeV. The nucleon mass has been fixed at $M = 939$ MeV in all the models.

Model	m_s	m_v	m_ρ	g_s^2	g_v^2	g_ρ^2	κ	λ	ζ	Λ_v
NL3	508.194	782.501	763.000	104.387 1	165.585 4	79.600 0	3.859 9	-0.015 91	0.00	0.00
MS	485.000	782.500	763.000	111.042 8	216.899 8	70.594 1	0.508 2	+0.027 72	0.06	0.00
FSU	491.500	782.500	763.000	112.199 6	204.546 9	138.470 1	1.420 3	+0.023 76	0.06	0.03
XS	491.500	782.500	763.000	131.005 9	258.104 4	213.959 6	0.007 9	+0.043 39	0.09	0.04

missing. Hence, we resort to a fairly accurate polytropic EOS to interpolate between the solid crust and the uniform liquid interior [18,19]. To compute the transition density from the liquid core to the solid crust we employ a relativistic random-phase-approximation (RPA) analysis to search for the critical density at which the uniform system becomes unstable to small amplitude density oscillations [19].

Accounting for most of the stellar radius and practically all of its mass, the liquid core is structurally the most important component of the star. Matter in the liquid core is assumed to be composed of neutrons, protons, electrons, and muons in chemical equilibrium. We reiterate that no exotic degrees of freedom are included in the model. Both electrons and muons are treated as noninteracting relativistic Fermi gases. For the hadronic component, the equation of state is generated using accurately calibrated relativistic models. Details on the calibration procedure may be found in Refs. [20–23]. The model includes a nucleon field (ψ) interacting via standard Yukawa couplings to two isoscalar mesons (a scalar ϕ and a vector V^μ) and one vector-isovector meson (b^μ) [20,21]. Such an interacting Lagrangian density may be written as follows [6,20,21]:

$$\mathcal{L}_{\text{int}} = \bar{\psi} \left[g_s \phi - \left(g_v V_\mu + \frac{g_\rho}{2} \boldsymbol{\tau} \cdot \mathbf{b}_\mu \right) \gamma^\mu \right] \psi - U(\phi, V^\mu, \mathbf{b}^\mu). \quad (1)$$

In addition to the Yukawa couplings (g_s , g_v , and g_ρ), the model is supplemented by nonlinear meson interactions given by

$$U(\phi, V^\mu, \mathbf{b}^\mu) = \frac{\kappa}{3!} (g_s \phi)^3 + \frac{\lambda}{4!} (g_s \phi)^4 - \frac{\zeta}{4!} (g_v^2 V_\mu V^\mu)^2 - \Lambda_v (g_\rho^2 \mathbf{b}_\mu \cdot \mathbf{b}^\mu) (g_v^2 V_\mu V^\mu). \quad (2)$$

The inclusion of scalar cubic (κ) and quartic (λ) self-interactions dates back to the late seventies [24] and is instrumental for softening the incompressibility coefficient of symmetric nuclear matter, as required to explain the excitation of the nuclear *breathing mode* [25].

Of particular interest and of critical importance to the present study are the vector self-interaction (ζ) and the *isoscalar-isovector* mixing term Λ_v [9,22]. That both of these parameters are zero in the enormously successful NL3 model (see Table I) suggests that existing laboratory data are fairly insensitive to the physics encoded in these two parameters. Indeed, Müller and Serot found it was possible to build models with different values of ζ that reproduce the same observed properties at normal nuclear densities, yet produced maximum neutron-star masses that differ by almost one solar mass [6]. This result indicates that observational data on neutron

stars—rather than laboratory experiments—may provide the only meaningful constraint on the high-density component of the equation of state. Furthermore, it indicates that the empirical parameter ζ provides an efficient tool to control the high-density component of the equation of state.

The isoscalar-isovector coupling constant Λ_v was introduced in Ref. [22] to modify the poorly known density dependence of the symmetry energy. The symmetry energy represents the energy cost involved in changing protons into neutrons (and vice-versa). To a good approximation, it is given by the difference in energy between pure neutron matter and symmetric nuclear matter. With only one isovector parameter (g_ρ) to adjust, relativistic mean-field models have traditionally predicted a *stiff* symmetry energy. The addition of Λ_v provides a simple—yet efficient and reliable—method of softening the symmetry energy without compromising the success of the model in reproducing well-determined ground-state observables [9]. Indeed, whereas models with different values of Λ_v reproduce the same exact properties of symmetric nuclear matter, they yield vastly different predictions for both the neutron radii of heavy nuclei and for the radius of neutron stars [22,26]. Given that the neutron-star radius is believed to be primarily controlled by the symmetry pressure at intermediate densities [4], the upcoming Parity Radius Experiment (PREx) at the Jefferson Laboratory (with a start date of March, 2010) will provide a unique laboratory constraint on a fundamental neutron-star property [27,28].

In summary, the two empirical parameters ζ and Λ_v provide a highly economical and efficient control of the softness of the high-density component of equation of state and of the symmetry pressure at intermediate densities, respectively—with the former primarily controlling the maximum neutron-star mass and the latter the stellar radius. Parameter sets for all the models employed in this work are listed in Table I.

III. RESULTS

In Fig. 1 we compare observational results for three neutron-star masses and radii against the model predictions. These neutron stars are in the binaries 4U 1608-52 [29], EXO 1745-248 [30], and 4U 1820-30 [31]. The very stiff behavior of the NL3 equation of state is immediately evident. With both empirical parameters ζ and Λ_v set equal to zero, it is not surprising that the NL3 model predicts neutron-star masses as large as $2.8M_\odot$ with very large radii. As compared to the observational data, the NL3 model suggests a radius for a 1.7 solar-mass neutron star that is about 6 km too large. Moreover, the NL3 equation of state is so stiff that gravity in a $2.8M_\odot$

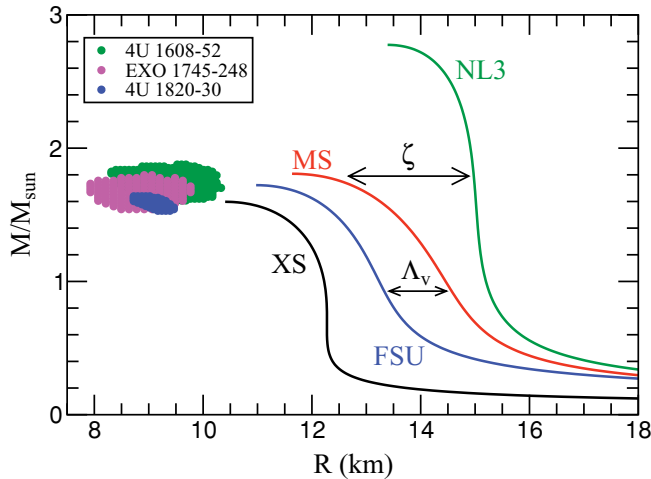


FIG. 1. (Color online) *Mass-versus-radius* relation predicted by the four relativistic mean-field models discussed in the text. The observational data represent 1σ confidence contours for the three neutron stars reported in Ref. [1].

neutron star can compress matter to only about four times normal nuclear density (see Table II). All these, even when the model provides an excellent description of many laboratory observables.

As first suggested by Müller and Serot [6], adding a vector self-interaction (with $\zeta = 0.06$) dramatically reduces the repulsion at high densities and ultimately the limiting neutron-star mass. As compared to the NL3 parameter set, the maximum neutron-star mass predicted by Müller and Serot (MS) is reduced by almost one solar mass (see Fig. 1 and Table II). Consistent with this softening is a significant increase in the compactness of the star. For example, for a neutron-star mass of $1.8M_{\odot}$, NL3 predicts a stellar radius that is more than 3 km larger than MS. Note, however, that the density dependence of the symmetry energy predicted by NL3 and MS is practically identical (see inset in Fig. 2). In particular, this is reflected in the identical prediction of 0.28 fm for the neutron-skin thickness of ^{208}Pb . This suggests that tuning the density dependence of the symmetry energy—via the addition of the isoscalar-isovector mixing term Λ_v —may yield a further reduction in neutron-star radii [26], as suggested by observation.

TABLE II. Predictions for the central baryon density, central pressure, mass, and radius of the limiting neutron star for the four models employed in the text. The last column lists predictions for the radius of a 1.4 solar-mass neutron star. The baryon density is given in fm^{-3} , the pressure in MeVfm^{-3} , the mass in solar masses, and the radii in kilometers.

Model	ρ	P	M	R	$R_{1.4}$
NL3	0.667	440.58	2.78	13.39	15.05
MS	1.040	311.92	1.81	11.64	13.78
FSU	1.153	345.78	1.72	10.97	12.66
XS	1.252	345.37	1.60	10.41	11.73

Incorporating information on nuclear collective modes in the calibration procedure of the FSUGold model favors a nonzero value for Λ_v [9]. Furthermore, it now seems that the resulting softening of the symmetry energy is consistent with the EOS of dilute neutron matter predicted by various microscopic approaches (see Refs. [10,32–34] and references therein). That the addition of Λ_v produces the intended effect can be appreciated in Fig. 1 and Table II; that is, although one has adopted the same value of ζ for both MS and FSUGold, their predictions for the radius of a “canonical” 1.4 solar-mass neutron star differ by more than 1 km. Related to this fact is the significantly smaller neutron-skin thickness of ^{208}Pb predicted by FSUGold (0.21 versus 0.28 fm). However, it appears that the combined softening of the EOS at high densities (through ζ) and of the symmetry pressure (through Λ_v) is insufficient to explain the observational data; the minimum stellar radius predicted by the FSUGold model is about 11 km, significantly larger than suggested by observation.

In an effort to describe the observational data, we have constructed an “extra soft” (XS) relativistic mean-field model constrained by the properties of symmetric nuclear matter at saturation density (i.e., equilibrium density, binding energy per nucleon, and incompressibility coefficient). In regards to these properties, the model is indistinguishable from FSUGold. The only additional constraint imposed on the model is that its limiting mass be no smaller than 1.6 solar masses. We feel that lowering this limiting value any further may start conflicting with the observational data. Although no exhaustive parameter search was conducted, we trust that the resulting *extra-soft* equation of state (as given in Table I) is representative of the softness that may be achieved with present-day relativistic mean-field models.

Note that the softening of the symmetry energy was implemented by simultaneously changing Λ_v and g_ρ ($NN\rho$ coupling constant) in such a way that the value of the symmetry energy remains fixed at a specific value of the baryon density. Given that nuclei have a low-density surface, the symmetry energy is best constrained not at nuclear matter saturation density, but at a slightly lower value [35]. Thus, all models considered in this contribution have a symmetry energy of ≈ 26 MeV at a density of $\approx 0.1 \text{ fm}^{-3}$ [22]. This procedure ensures that well-constrained observables (such as masses and charge radii) remain consistent with their experimental values. Moreover, as this procedure involves the tuning of only the isovector interaction, all properties of symmetric nuclear matter remain intact. Yet poorly constrained observables sensitive to the *slope* of the symmetry energy—such as the neutron skin thickness of neutron-rich nuclei and neutron-star radii—can be made to vary over a wide range of values [22,26]. Table III serves to illustrate this procedure for the case of ^{208}Pb , a doubly magic nucleus with a significant neutron excess. Note that whereas the binding energy per nucleon and the charge radius of ^{208}Pb are both within half of a percent of their experimental value, the unknown neutron skin of ^{208}Pb differs significantly (by more than 60%) among the various models. With a model as soft as XS, neutron-star radii get significantly reduced indeed (see Fig. 1). For example, the radius of a $1.4M_{\odot}$ neutron star is reduced by almost 1 km relative to the FSUGold prediction (see Table II) and by more

TABLE III. Experimental data for the binding energy per nucleon and charge radii for ^{208}Pb . Results are presented for three of the models employed in the text together with their predictions for the neutron skin thickness.

Nucleus	Observable	Experiment	NL3	FSU	XS
^{208}Pb	B/A (MeV)	7.87	7.88	7.89	7.90
	R_{ch} (fm)	5.50	5.51	5.52	5.50
	$R_n - R_p$ (fm)	—	0.28	0.21	0.17

than 1.5 km at its limiting mass of $1.6 M_\odot$. Still, the minimum neutron-star radius of $R = 10.41$ km predicted by the model remains outside the reported 1σ confidence contours [1].

Do we then conclude that the results presented in Fig. 1 are indicative of relativistic equations of state that are too stiff? Do the observational results unambiguously called for a softer equation of state, as would be produced by exotic states of matter, such as meson condensates and/or quark matter? To answer this question we compare in Fig. 2 the various equations of state used to generate Fig. 1 against the values extracted from the observational data [1]. The inset in the figure displays the symmetry pressure for the models under consideration. The observed softening of the symmetry pressure between models is entirely due Λ_v . Note, however, that unlike the neutron-skin thickness of neutron-rich nuclei, the radius of a neutron star is not uniquely constrained by the symmetry pressure at low to intermediate densities [26]. Thus, models with similar symmetry pressures may—and do—predict significantly different stellar radii. Contrary to the expectations generated by Fig. 1, most of the equations of state are not too stiff. Indeed, with the exception of NL3, the remaining equations of state appear, if anything, slightly too soft at the highest density. Based on these results—and these results alone—nucleonic equations of state do not seem to be in conflict with the observational data.

IV. CONCLUSIONS

In summary, the *mass-versus-radius* relation of neutron stars was computed using equations of state derived from relativistic mean-field models. Although the models are calibrated in the vicinity of nuclear-matter saturation density, it is possible to tune their high-density behavior in a highly efficient and economical manner. In this contribution we have used two parameters to control the maximum neutron-star

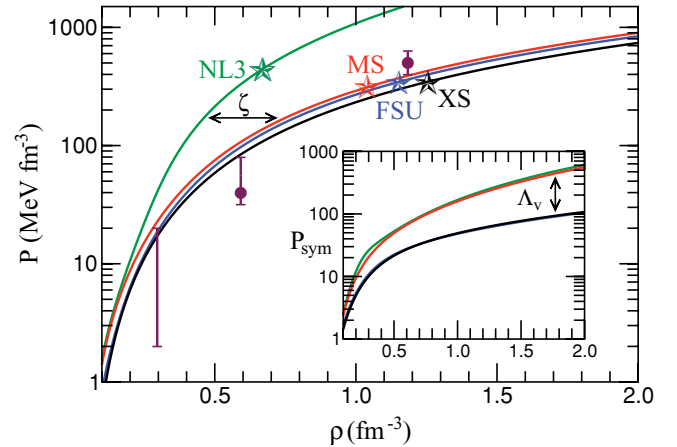


FIG. 2. (Color online) Equation of state (*pressure versus baryon density*) of neutron-star matter predicted by the four relativistic mean-field models discussed in the text. The three data points are from the observational extraction as described in Ref. [1]. The symbols (stars) indicate the central density and pressure for the maximum-mass neutron star. The inset shows the symmetry pressure, given as the pressure of pure neutron matter minus that of symmetric nuclear matter.

mass and the stellar radius. As we compared our predictions to the observational data a conflict emerged. Whereas one could generate equations of state that are in agreement with observation, the predicted stellar radii are too large. This result is particularly intriguing given that “*inversion*” methods exist for extracting the equation of state of stellar matter directly from masses and radii of neutron stars [5]. Thus, one would expect that if the M - R predictions do not match observation, neither would the equations of state. Clearly, to reconcile these facts much work remains to be done in both the observational and theoretical fronts. For now we must conclude—although the existence of exotic stars is very appealing—that the downfall of the purely nucleonic equations of state may be premature.

ACKNOWLEDGMENTS

The authors thank Prof. F. Özel for making available the observational data. This work was supported in part by a grant from the US Department of Energy (Grant No. DE-FD05-92ER40750).

-
- [1] F. Ozel, G. Baym, and T. Guver (2010) arXiv:1002.3153.
[2] J. M. Lattimer and M. Prakash, *Astrophys. J.* **550**, 426 (2001).
[3] J. M. Lattimer and M. Prakash, *Science* **304**, 536 (2004).
[4] J. M. Lattimer and M. Prakash, *Phys. Rep.* **442**, 109 (2007).
[5] L. Lindblom, *Astrophys. J.* **398**, 569 (1992).
[6] H. Mueller and B. D. Serot, *Nucl. Phys. A* **606**, 508 (1996).
[7] G. A. Lalazissis, J. Konig, and P. Ring, *Phys. Rev. C* **55**, 540 (1997).
[8] G. A. Lalazissis, S. Raman, and P. Ring, *At. Data Nucl. Data Tables* **71**, 1 (1999).
[9] B. G. Todd-Rutel and J. Piekarewicz, *Phys. Rev. Lett.* **95**, 122501 (2005).
[10] J. Piekarewicz, *J. Phys. G* **37**, 064038 (2010).
[11] G. Baym, C. Pethick, and P. Sutherland, *Astrophys. J.* **170**, 299 (1971).
[12] D. G. Ravenhall, C. J. Pethick, and J. R. Wilson, *Phys. Rev. Lett.* **50**, 2066 (1983).

- [13] M. Hashimoto, H. Seki, and M. Yamada, *Prog. Theor. Phys.* **71**, 320 (1984).
- [14] C. P. Lorenz, D. G. Ravenhall, and C. J. Pethick, *Phys. Rev. Lett.* **70**, 379 (1993).
- [15] C. J. Horowitz, M. A. Perez-Garcia, and J. Piekarewicz, *Phys. Rev. C* **69**, 045804 (2004).
- [16] C. J. Horowitz, M. A. Perez-Garcia, J. Carriere, D. K. Berry, and J. Piekarewicz, *Phys. Rev. C* **70**, 065806 (2004).
- [17] C. J. Horowitz, M. A. Perez-Garcia, D. K. Berry, and J. Piekarewicz, *Phys. Rev. C* **72**, 035801 (2005).
- [18] B. Link, R. I. Epstein, and J. M. Lattimer, *Phys. Rev. Lett.* **83**, 3362 (1999).
- [19] J. Carriere, C. J. Horowitz, and J. Piekarewicz, *Astrophys. J.* **593**, 463 (2003).
- [20] B. D. Serot and J. D. Walecka, *Adv. Nucl. Phys.* **16**, 1 (1986).
- [21] B. D. Serot and J. D. Walecka, *Int. J. Mod. Phys. E* **6**, 515 (1997).
- [22] C. J. Horowitz and J. Piekarewicz, *Phys. Rev. Lett.* **86**, 5647 (2001).
- [23] B. G. Todd and J. Piekarewicz, *Phys. Rev. C* **67**, 044317 (2003).
- [24] J. Boguta and A. R. Bodmer, *Nucl. Phys. A* **292**, 413 (1977).
- [25] D. H. Youngblood, H. L. Clark, and Y.-W. Lui, *Phys. Rev. Lett.* **82**, 691 (1999).
- [26] C. J. Horowitz and J. Piekarewicz, *Phys. Rev. C* **64**, 062802 (2001).
- [27] C. J. Horowitz, S. J. Pollock, P. A. Souder, and R. Michaels, *Phys. Rev. C* **63**, 025501 (2001).
- [28] K. Kumar, R. Michaels, P. A. Souder, and G. M. Urciuoli (2005), [<http://hallaweb.jlab.org/parity/prex>].
- [29] T. Guver, F. Ozel, A. Cabrera-Lavers, and P. Wroblewski (2008) [arXiv:0811.3979](https://arxiv.org/abs/0811.3979).
- [30] F. Ozel, T. Guver, and D. Psaltis, *Astrophys. J.* **693**, 1775 (2009).
- [31] T. Guver, P. Wroblewski, L. Camarota, and F. Ozel (2010) [arXiv:1002.3825](https://arxiv.org/abs/1002.3825).
- [32] A. Schwenk and C. J. Pethick, *Phys. Rev. Lett.* **95**, 160401 (2005).
- [33] A. Gezerlis and J. Carlson, *Phys. Rev. C* **81**, 025803 (2010).
- [34] J. Piekarewicz, *Phys. Rev. C* **76**, 064310 (2007).
- [35] R. J. Furnstahl, *Nucl. Phys. A* **706**, 85 (2002).

Neutron star properties and the symmetry energy

Rafael Cavagnoli,^{1,2} Debora P. Menezes,¹ and Constança Providência²

¹Departamento de Física - CFM - Universidade Federal de Santa Catarina, Florianópolis-SC-CP. 476-CEP 88.040-900 - Brazil

²Centro de Física Computacional, Department of Physics, University of Coimbra, P 3004-516 Coimbra, Portugal

(Received 8 August 2011; published 27 December 2011)

The effect of the symmetry energy on the properties of compact stars is discussed. It is shown that, for stars with masses above $1M_\odot$, the radius of the star varies linearly with the symmetry energy slope L . We also analyze the dependence of the hyperon content and onset density of the direct Urca process on the symmetry energy and meson coupling parametrization.

DOI: 10.1103/PhysRevC.84.065810

PACS number(s): 21.65.-f, 25.75.Nq, 05.70.Fh, 12.38.Mh

I. INTRODUCTION

Constraining the high-density equation of state (EOS) of neutron-rich matter is essential to understand the physics of compact stars [1].

There have been recent attempts to set constraints on the high-density EOS using observational data obtained from compact stars [2,3], or microscopic calculations [4]. In particular, in Ref. [3] an empirical dense equation of state obtained from a heterogeneous set of six neutron stars with well-determined distances was proposed.

Phenomenological nuclear models are generally fit to the ground-state properties of nuclei and, frequently, also to the collective response of these systems [5–7], or nuclear matter saturation properties [8]. However, these constraints generally only determine quite uniquely the EOS close to saturation density and for an isospin asymmetry smaller than 0.2 [9,10]. Extrapolation to high densities and/or high isospin asymmetries is kept unconstrained and different models predict quite different neutron star properties.

In Ref. [11] it was proposed that the parametrization of the nuclear EOS could also be constrained by the collective response of nuclei to the isoscalar monopole giant resonance (ISGMR) and the isovector dipole giant resonance (IVGDR). The author of [11] has proposed that the ISGMR and IVGDR of ^{208}Pb were sensitive both to the incompressibility K and the symmetry energy ϵ_{sym} , due to its isospin asymmetry. Therefore, the ISGMR data from a nucleus with a well-developed breathing mode but a small neutron-proton asymmetry such as ^{90}Zr should be used to fix the incompressibility at saturation instead of a nucleus with a nonnegligible isospin asymmetry like ^{208}Pb . Once the incompressibility at saturation is fixed, the IVGDR ^{208}Pb may be used to constrain the symmetry energy.

This information together with the ground-state properties of nuclei has been used to define the Florida State University (FSU) parametrization proposed in Ref. [6]. However, since the high-density EOS is not constrained, FSU presents an EOS that is too soft at high densities and does not predict a star with a mass larger than $1.72M_\odot$, which is $0.25M_\odot$ below the mass $1.97 \pm 0.04 M_\odot$ of the recent mass measurement of the binary millisecond pulsar PSR J16142230 [12]. In order to overcome this drawback, the parametrization [7] was built in a way close to FSU but including an extra constraint: the EOS is compatible with the empirical equa-

tion of state determined in Ref. [3]. As a result the new parametrization predicts stars with larger masses and smaller radii [7].

In the present work we want to understand how sensitive is the mass or radius curve of a family of stars to the symmetry energy and its slope at saturation. We study not only maximum-mass configurations but also stars with a mass in the range $1.0M_\odot < M < 1.4M_\odot$. These stars have a central density that goes from $1.5\rho_0$ to $2-3\rho_0$, and therefore we will be testing the equation of state at suprasaturation densities.

At high density the formation of hyperons is energetically favorable and therefore we also study the effect of the symmetry energy on the appearance of these exotic degrees of freedom [8,13]. We consider two different hyperon-meson parametrizations: a first one proposed in Ref. [8] and a second one that takes into account the different binding energies of the hyperons [14,15].

In Sec. II we present the formalism used in the present work, in Sec. III the results are presented and discussed, and in the last section conclusions are drawn.

II. THE FORMALISM

In the present section we present the hadronic equations of state (EOS) used in this work. We describe hadronic matter within the framework of the relativistic nonlinear Walecka model (NLWM) [16]. In this model the nucleons are coupled to neutral scalar σ , isoscalar-vector ω_μ , and isovector-vector $\vec{\rho}_\mu$ meson fields. We include a $\rho\omega$ meson coupling term as in Refs. [6,7,17] in order to study the effect of the symmetry energy on the star properties while leaving the isoscalar channel fixed.

The Lagrangian density reads

$$\begin{aligned} \mathcal{L} = & \sum_{j=1}^8 \bar{\psi}_j [\gamma_\mu (i\partial^\mu - g_{\omega j}\omega^\mu - g_{\rho j}\vec{\tau}_j \cdot \vec{\rho}^\mu) - m_j^*] \psi_j \\ & + \sum_{l=1}^2 \bar{\psi}_l (i\gamma_\mu \partial^\mu - M_l) \psi_l + \frac{1}{2} \partial_\mu \sigma \partial^\mu \sigma - \frac{1}{2} m_\sigma^2 \sigma^2 \\ & - \frac{1}{3!} k \sigma^3 - \frac{1}{4!} \lambda \sigma^4 - \frac{1}{4} \Omega_{\mu\nu} \Omega^{\mu\nu} + \frac{1}{2} m_\omega^2 \omega_\mu \omega^\mu \end{aligned}$$

TABLE I. The σ and ω meson potentials for symmetric nuclear matter at saturation.

	NL3	GM1	GM3	NL ρ	FSU	IU-FSU
V_σ (MeV)	377.15	281.34	206.28	234.68	358.94	359.15
V_ω (MeV)	305.46	215.71	145.45	171.10	282.42	276.84

$$+ \frac{1}{4!} \xi g_\omega^4 (\omega_\mu \omega^\mu)^2 - \frac{1}{4} \vec{R}_{\mu\nu} \cdot \vec{R}^{\mu\nu} + \frac{1}{2} m_\rho^2 \vec{\rho}_\mu \cdot \vec{\rho}^\mu \\ + \Lambda_v (g_\rho^2 \vec{\rho}_\mu \cdot \vec{\rho}^\mu) (g_\omega^2 \omega_\mu \omega^\mu), \quad (1)$$

where $m_j^* = m_j - g_{\sigma j} \sigma$ is the baryon effective mass, $\Omega_{\mu\nu} = \partial_\mu \omega_\nu - \partial_\nu \omega_\mu$, $\vec{R}_{\mu\nu} = \partial_\mu \vec{\rho}_\nu - \partial_\nu \vec{\rho}_\mu - g_\rho (\vec{\rho}_\mu \times \vec{\rho}_\nu)$, g_{ij} are the coupling constants of mesons $i = \sigma, \omega, \rho$ with baryon j , m_i is the mass of meson i , and l represents the leptons e^- and μ^- . The couplings k ($k = 2M_N g_\sigma^3 b$) and λ ($\lambda = 6g_\sigma^4 c$) are the weights of the nonlinear scalar terms and $\vec{\tau}$ is the isospin operator. The sum over j in Eq. (1) extends over the octet of lightest baryons $\{n, p, \Lambda, \Sigma^-, \Sigma^0, \Sigma^+, \Xi^-, \Xi^0\}$.

We consider two different sets of hyperon-meson couplings. For the coupling set A the ω and ρ meson-hyperon coupling constants are obtained using SU(6) symmetry:

$$\frac{1}{2} g_{\omega\Lambda} = \frac{1}{2} g_{\omega\Sigma} = g_{\omega\Xi} = \frac{1}{3} g_{\omega N}, \quad (2)$$

$$\frac{1}{2} g_{\rho\Sigma} = g_{\rho\Xi} = g_{\rho N}, \quad g_{\rho\Lambda} = 0, \quad (3)$$

where N means “nucleon” ($g_{iN} \equiv g_i$). The coupling constants $\{g_{\sigma j}\}_{j=\Lambda, \Sigma, \Xi}$ of the hyperons with the scalar meson σ are constrained by the hypernuclear potentials in nuclear matter to be consistent with hypernuclear data [14]. The hypernuclear potentials were constructed as

$$V_j = x_{\omega j} V_\omega - x_{\sigma j} V_\sigma, \quad (4)$$

where $x_{ij} \equiv g_{ij}/g_i$, $V_\omega \equiv g_\omega \omega_0$ and $V_\sigma \equiv g_\sigma \sigma_0$ are the nuclear potentials for symmetric nuclear matter at saturation with the parameters of Table I. Following Ref. [14], we use

$$V_\Lambda = -28 \text{ MeV}, \quad V_\Sigma = 30 \text{ MeV}, \quad V_\Xi = -18 \text{ MeV}. \quad (5)$$

All hyperon coupling ratios $\{g_{\sigma j}, g_{\omega j}, g_{\rho j}\}_{j=\Lambda, \Sigma, \Xi}$ are now known once the coupling constants $\{g_\sigma, g_\omega, g_\rho\}$ of the nucleon sector are given.

However, while the binding of the Λ to symmetric nuclear matter is well settled experimentally [18], the binding values of the Σ^- and Ξ^- have still a lot of uncertainties. Experiments involving kaons and pions [19] and related Distorted Wave Impulse Approximation (DWIA) analyses [20] suggest that the Σ nuclear potential is repulsive (see also [21] for a recent review). Experimental data for the isoscalar Σ potential seem to be compatible with $+30 \pm 20$ MeV [21]. There is not much experimental information on the interaction of Ξ with nuclear matter. Measurements from the production of Ξ in the $^{12}\text{C}(K^-, K^+)^{12}\text{Be}$ are compatible with a shallow attractive potential $V_\Xi \sim -14$ MeV [22]. Taking for the Ξ a less attractive potential or for the Σ an even more repulsive potential would reduce the fraction of hyperons in stellar matter.

Therefore, in order to show how results are sensitive to the hyperon couplings we consider set B defined as proposed

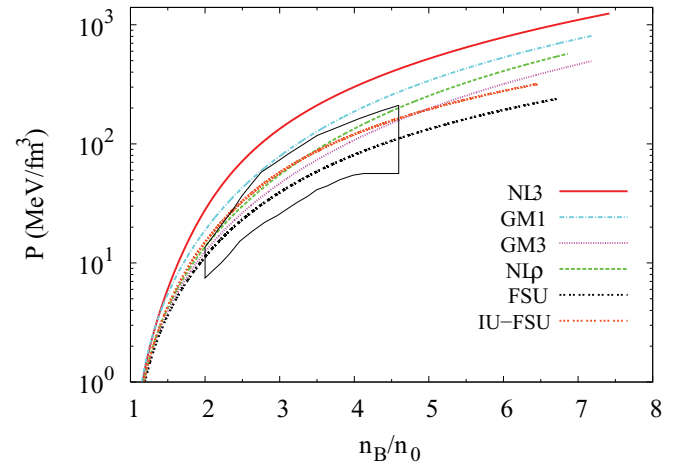


FIG. 1. (Color online) EOS for symmetric matter and different models: pressure as a function of the baryon number density. The enclosed area represents experimental data according to Danielewicz *et al.* [25].

in Ref. [8] with $x_\sigma = 0.8$ and equal for all the hyperons. We obtain the fraction x_ω from Eq. (4) with $V_j = V_\Lambda = -28$ MeV, and take the same value for all the hyperons. For the hyperon- ρ -meson coupling we consider $x_\rho = x_\sigma$. This choice of coefficients has been shown to give high maximum-mass configurations [23] which could describe the millisecond pulsar J1614-2230 mass [12].

In Table II we give the symmetric nuclear matter properties at saturation density as well as the parameters of the models used in the present work.

The equations of state (EOS) are the standard relativistic mean-field equations known in the literature. In case of Eq. (1), the EOS are the same as presented in Ref. [9] for the hadronic case. The baryon number density is

$$n_B = \sum_{j=1}^8 n_j, \quad (6)$$

where n_j is the baryon number density of baryon j at zero temperature,

$$n_j = \frac{1}{3\pi^2} k_{Fj}^3, \quad (7)$$

and k_{Fj} is the Fermi momentum of baryon j . For the sake of comparisons with symmetric nuclear matter ($n_B = n_p + n_n$), the symmetry energy is defined as

$$\mathcal{E}_{\text{sym}} = \frac{1}{2} \left[\frac{\partial^2 (\mathcal{E}/n_B)}{\partial \alpha^2} \right]_{\alpha=0} = \frac{k_F^2}{6E_F} + \frac{g_\rho^2}{4m_\rho^{*2}} n_B, \quad (8)$$

where \mathcal{E} is the energy density obtained from Eq. (1) for $j = 1, 2$ and with no leptons, α is the asymmetry parameter $\alpha = (N - Z)/A = (n_n - n_p)/n_B$, $E_F = (k_F^2 + m^{*2})^{1/2}$ with $k_F = (3\pi^2 n_B/2)^{1/3}$, $m_\rho^{*2} = m_\rho^2 + 2\Lambda_v g_\omega^2 g_\rho^2 \omega_0^2$, and the slope of the symmetry energy is

$$L = \left[3n_B \frac{\partial \mathcal{E}_{\text{sym}}}{\partial n_B} \right]_{n_B=n_0}. \quad (9)$$

TABLE II. Parameter sets used in this work and corresponding saturation properties.

	FSU [6]	IU-FSU [7]	NL ρ [24]	NL3 [5]	GM1 [8]	GM3 [8]
n_0 (fm $^{-3}$)	0.148	0.155	0.160	0.148	0.153	0.153
K (MeV)	230	231.2	240	271.76	300	240
m^*/m	0.62	0.62	0.75	0.60	0.70	0.78
m (MeV)	939	939	939	939	938	938
$-B/A$ (MeV)	16.3	16.4	16.0	16.299	16.3	16.3
\mathcal{E}_{sym} (MeV)	32.6	31.3	30.5	37.4	32.5	32.5
L (MeV)	61	47.2	85	118	94	90
m_σ (MeV)	491.5	491.5	512	508.194	512	512
m_ω (MeV)	782.5	782.5	783	783	783	783
m_ρ (MeV)	763	763	763	763	770	770
g_σ	10.592	9.971	8.340	10.217	8.910	8.175
g_ω	14.302	13.032	9.238	12.868	10.610	8.712
g_ρ	11.767	13.590	7.538	8.948	8.196	8.259
b	0.000756	0.001800	0.006935	0.002052	0.002947	0.008659
c	0.003960	0.000049	-0.004800	-0.002651	-0.001070	-0.002421
ξ	0.06	0.03	0	0	0	0
Λ_v	0.03	0.046	0	0	0	0

When the hyperons are present we define the strangeness fraction

$$f_s = \frac{1}{3} \frac{\sum_j |s_j| n_j}{n_B}, \quad (10)$$

where s_j is the strangeness of baryon j and n_B in this case is given by Eq. (6).

III. RESULTS

In Figs. 1 and 2(a), the pressure of symmetric nuclear matter and the symmetry energy, respectively, are plotted for a large range of densities. In Fig. 1 we also include the experimental constraints obtained from collective flow data in heavy-ion collisions [25]. We have considered a wide range of models frequently used to study stellar matter or finite nuclei with quite different behaviors at high densities. Even though some of the models do not satisfy the constraints determined in Ref. [25],

as a whole this set of models allows us to understand the influence of a hard or soft equation of state (EOS) and a hard or soft symmetry energy on the star properties.

We have considered the following parametrizations: NL3 [5], with a quite large symmetry energy and incompressibility at saturation and which was fit in order to reproduce the ground state properties of both stable and unstable nuclei. FSU [6], which was accurately calibrated to simultaneously describe the GMR in ^{90}Zr and ^{208}Pb and the IVGDR in ^{208}Pb and still reproduce ground-state observables of stable and unstable nuclei. FSU is very soft at high densities, therefore the authors of [7] have proposed a parametrization with similar properties, which they call Indiana University-FSU (IU-FSU), having a harder behavior at high densities. GM1 and GM3 [8] are generally used to describe stellar matter, with a symmetry energy not so hard as the one of NL3, and NL ρ [24], which has been used to discuss the hadron-matter-quark-matter transition

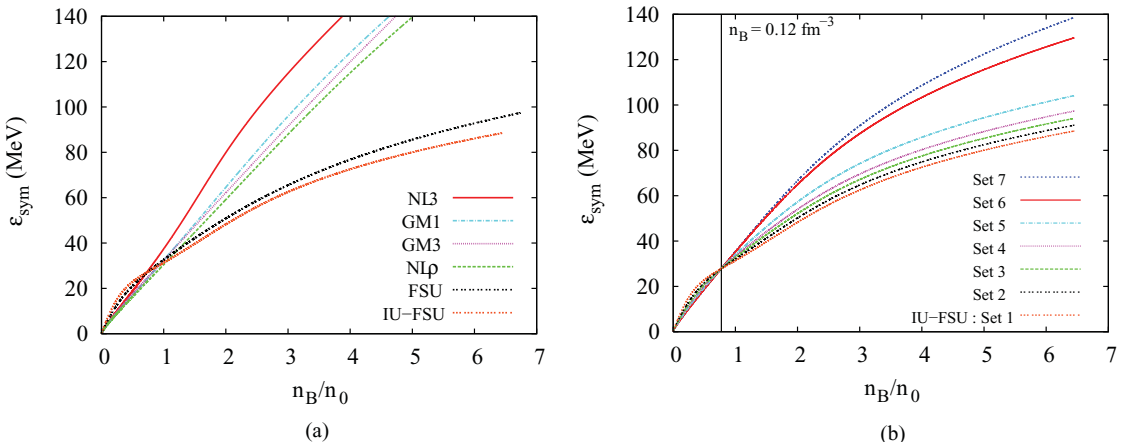


FIG. 2. (Color online) Symmetry energy as a function of the baryon number density (a) for different models and (b) for modified IU-FSU.

TABLE III. Parameter sets generated from the IU-FSU model (set 1) that differ in their value of the symmetry energy \mathcal{E}_{sym} and corresponding slope L at saturation but have the same isoscalar properties.

	Set 1	Set 2	Set 3	Set 4	Set 5	Set 6	Set 7
g_ρ	13.590	11.750	10.750	10.150	9.500	8.750	8.650
Λ_v	0.0406	0.03643	0.02905	0.02354	0.01635	0.00598	0.00439
\mathcal{E}_{sym} (MeV)	31.34	32.09	32.74	33.26	34.00	35.21	35.41
L (MeV)	47.20	55.09	62.38	68.73	78.45	96.02	99.17

in Ref. [26], and that has, at high densities, a behavior between GM1 and GM3.

In order to study the effect of the isovector channel in the star properties we also consider a modified version of the IU-FSU parametrization: we keep the isoscalar channel and change g_ρ and Λ_v keeping the symmetry energy fixed at the density 0.12 fm^{-3} . It has been shown in Ref. [10] that phenomenological models fit to the properties of nuclei and nuclear matter have similar values of symmetry energy for this density. We generate a set of models that differ in their symmetry energy and corresponding slope at saturation, as indicated in Table III, but have the same isoscalar properties. In Fig. 2(b) we show the symmetry energy density dependence of this set of models. Set 1 is the parametrization IU-FSU. The other parametrizations have a larger symmetry energy and a larger slope L at saturation. The maximum value of L we considered is within the experimental values obtained from isospin diffusion in heavy-ion reactions [27]. The range of values considered for L span all the interval obtained for L from different analysis of experimental measurements [28] and a microscopic Brueckner Hartree-Fock calculation [29]. Smaller values of L would give unacceptable EOS because they would predict that neutron matter is bound.

The effect of the symmetry energy on the strangeness fraction is seen in Figs. 3 and 4. It is clear from these figures that the strangeness content is sensitive to the model and the meson-hyperon couplings. In general, the softer the EOS the larger the strangeness onset density and the smaller the strangeness content. From Fig. 4, we conclude that the smaller the symmetry energy the smaller the hyperon content. A large

meson-hyperon vector coupling, as occurs in set *B*, hinders the formation of hyperons.

However, we should point out that, when comparing different models, we are comparing not only the effect of the density dependence of the symmetry energy but also the density dependence of the isoscalar channel (i.e., the incompressibility and effective mass). This explains why FSU, a softer EOS with a smaller incompressibility, has a smaller strangeness content than IU-FSU, a model with softer symmetry energy than FSU above the saturation density.

The EOS of the IU-FSU EOS becomes softer than GM3 ($NL\rho$) for densities above $\sim 5n_0$ ($\sim 3.5n_0$); see Fig. 1. This explains why IU-FSU has a smaller hyperon content with respect to GM3 (set *A*) or GM3 and $NL\rho$ (set *B*) at high densities but not at intermediate densities. On the other hand, FSU is always softer than all the other EOSs and, for set *B* below $3n_0$ and $5n_0$, its strangeness fraction is larger than the corresponding fraction in the $NL\rho$ and GM3 models, respectively. This behavior is defined by the effective masses: $NL\rho$ and GM3 have larger effective masses (i.e., smaller g_s couplings) and, therefore, the chemical potential of the hyperons decreases slower with density and the onset occurs at larger densities. At large densities the sigma field saturates and the behavior of the system is defined by the vector meson.

We also comment on the behavior of NL3 with set *B*: NL3 is a model that breaks down at quite low densities when hyperons are included because the effective mass of the nucleons goes to zero ($n_B \sim 4n_0$); see Ref. [30]. This explains why the NL3 curve in Fig. 3(b) stops below $4n_0$.

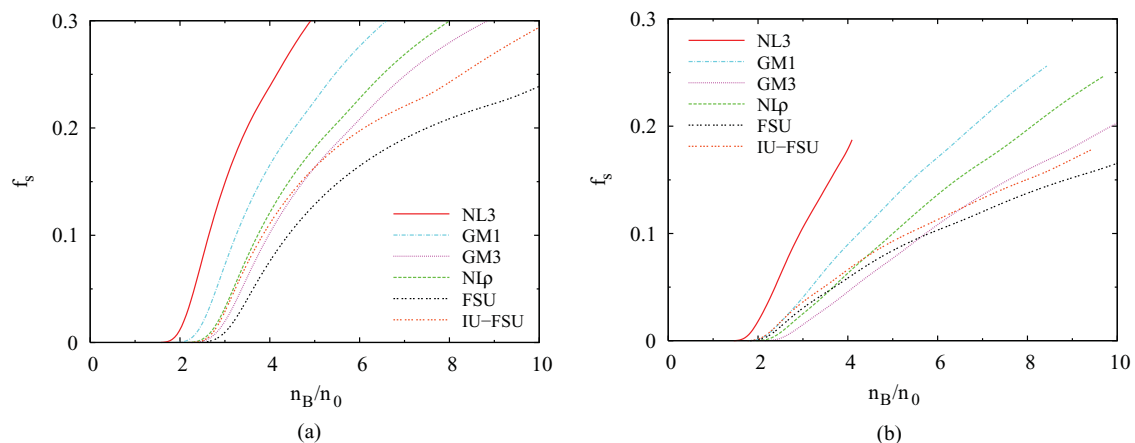


FIG. 3. (Color online) Strangeness fraction when hyperons are present for (a) set *A* and (b) set *B*.

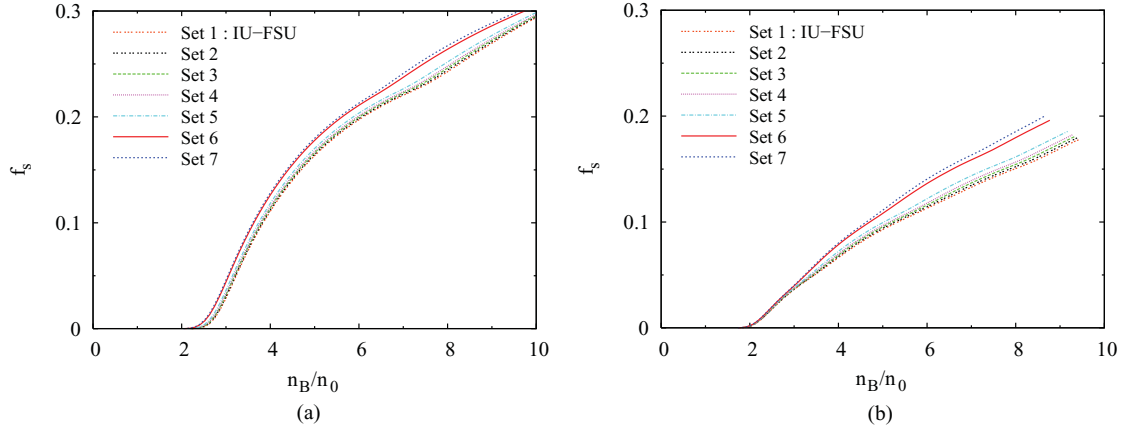


FIG. 4. (Color online) Strangeness fraction for IU-FSU and related parametrizations with (a) meson-hyperon coupling set *A* and (b) meson-hyperon coupling set *B*.

When comparing results with the modified versions of the IU-FSU model we are not changing the isoscalar channel. FSU has a softer EOS than IU-FSU (i.e., a smaller incompressibility at high densities). As a result, the formation of hyperons is hindered in FSU with respect to IU-FSU. The explanation is the difference on the isoscalar channel of these two models.

The symmetry energy is directly affecting the isovector chemical potential and, therefore, the chemical equilibrium. In Fig. 5, the chemical potential for neutral, positively charged, and negatively charged baryons in β equilibrium are represented. It is seen that the neutron chemical potential becomes slightly smaller for a softer symmetry energy, because the ρ -meson field is weaker. However, the density dependence of the symmetry energy has a stronger effect on the electron chemical potential: a smaller L corresponds to a smaller proton fraction and, therefore, electron fraction, so that the electron chemical potential decreases when L decreases. As a result, the sum $\mu_n + \mu_e$, which defines the chemical potential of single negatively charged baryons, feels a much stronger reduction than the neutron chemical potential, and the difference $\mu_n - \mu_e$, which defines the chemical potential of

single positively charged baryons, increases above saturation density when L decreases.

As a consequence, a soft symmetry energy shifts the hyperon onset to larger densities, if Λ , a neutral hyperon with isospin zero, is the first hyperon to appear. This is the case of set *A* (see the left panel of Fig. 6). However, the onset of hyperons is not affected by L when a negatively charged hyperon such as Σ^- is the first hyperon to appear, such as, for instance, in set *B* (see the right panel of Fig. 6). Although the sum $\mu_n + \mu_e$ decreases, the same happens with the Σ^- chemical potential and the net result is that the onset of the hyperon Σ^- is almost independent of L . As soon as Λ appears, the different parametrizations of the modified IU-FSU start to differ.

In Tables IV–IX, we give the direct Urca onset density, mass and radius of maximum-mass stars, the radius of stars with $M = 1.0M_\odot$ and $1.4M_\odot$, the symmetry energy \mathcal{E}_{sym} , and the symmetry energy slope L . Tables IV and V give this information for stars without hyperons. Tables VI and VIII give this information for stars with hyperons that couple to mesons through set *A*. Tables VII and IX give this information for stars with hyperons that couple to mesons through set *B*.

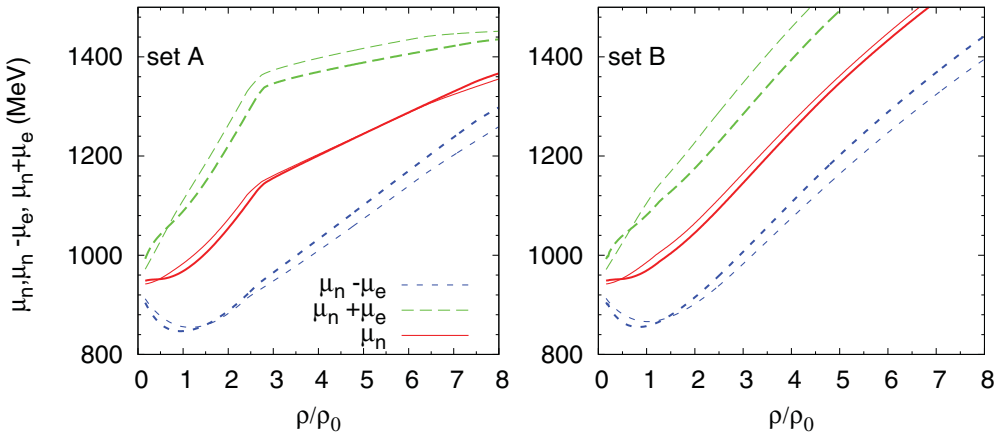


FIG. 5. (Color online) Chemical potential for neutral (full lines), positively charged (dotted lines), and negatively charged (dashed lines) baryons in β equilibrium: hyperon set *A* (left panel) and hyperon set *B* (right panel). The thick lines are for IU-FSU (set 1) and the thin lines are for set 7 of the modified IU-FSU.

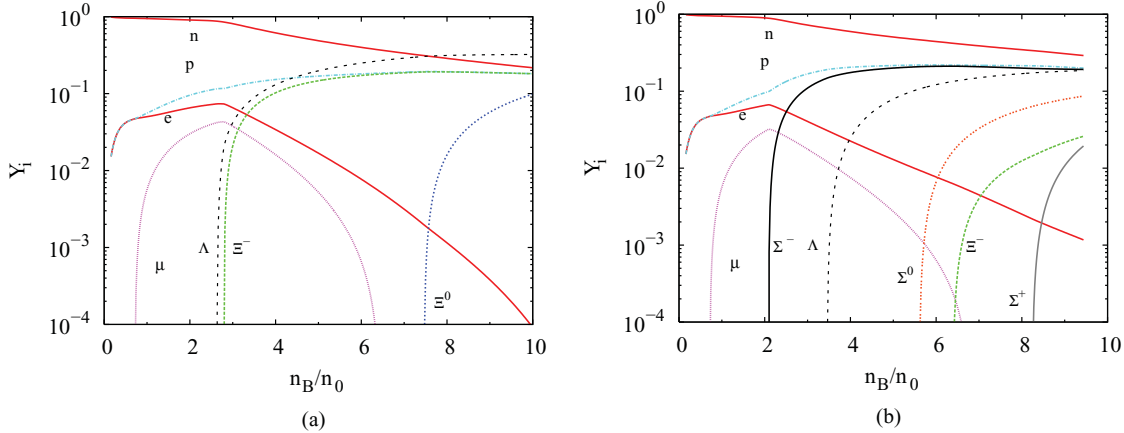


FIG. 6. (Color online) Particle fractions, IU-FSU for (a) set A and (b) set B.

The properties of stars obtained with models NL3, GM1, GM3, NL ρ , FSU, and IU-FSU are given in Tables IV, VI, and VII, respectively, and the properties of stars from a set of EOS obtained from IU-FSU by changing the isovector channel are presented in Tables V, VIII, and IX.

Cooling of the star by neutrino emission can occur relatively fast if the direct Urca process, $n \rightarrow p + e^- + \bar{\nu}_e$, is allowed [31]. The direct Urca (DU) process takes place when the proton fraction exceeds a critical value x_{DU} [31], which can be evaluated in terms of the leptonic fraction as [32]

$$x_{\text{DU}} = \frac{1}{1 + (1 + x_e^{1/3})^3}. \quad (11)$$

where $x_e = n_e / (n_e + n_\mu)$ is the electron leptonic fraction, n_e is the number density of electrons, and n_μ is the number density of muons. Cooling rates of neutron stars seem to indicate that this fast cooling process does not occur and, therefore, a constraint is set imposing that the direct Urca process is only allowed in stars with a mass larger than $1.5M_\odot$, or a less restrictive limit, $1.35M_\odot$ [32]. Since the onset of the direct Urca process is closely related with the density dependence of the symmetry energy, this constraint gives information on the isovector channel of the EOS. In stellar matter with hyperons, the direct Urca process may also occur for the hyperons. As discussed in Ref. [33], although the neutrino luminosities

TABLE IV. Symmetry energy and no-hyperon star properties for NL3, GM1, GM3, FSU, and IU-FSU EOS. The onset density of the direct Urca process, symmetry energy slope and symmetry energy at saturation, mass and radius of the maximum-mass configuration, and radius of $1.4M_\odot$ and $1.0M_\odot$ stars are given.

Set	n_{urca}/n_0	L (MeV)	\mathcal{E}_{sym} (MeV)	M_{max}/M_\odot	$R_{M_{\text{max}}}$ (km)	$R_{1.4M_\odot}$ (km)	$R_{1.0M_\odot}$ (km)
NL3	1.38	118.0	37.4	2.81	13.38	14.71	14.65
GM1	1.81	94.0	32.5	2.39	11.99	13.81	13.76
GM3	2.04	90.0	32.5	2.04	10.94	13.12	13.38
NL ρ	2.14	85.0	30.5	2.11	10.88	12.92	13.08
FSU	3.16	61.0	32.6	1.73	10.87	12.41	12.78
IU-FSU	3.95	47.2	31.3	1.95	11.23	12.55	12.51

in these processes are much less than the ones obtained in the nucleon direct Urca process, they will play an important role if they occur at densities below the nucleon direct Urca process. In particular, the process $\Lambda \rightarrow p + e + \bar{\nu}$ may occur at densities below the nucleon DU onset.

In Fig. 7 the proton fractions for β -equilibrium matter are plotted for NL3, GM1, GM3, FSU, and IU-FSU. The black region defines the proton fraction at the onset of the direct Urca process.

The effect of the symmetry energy and the hyperon content on the onset density of the nucleon direct Urca process is seen in Fig. 8 as function of the slope L for the IU-FSU and modified versions in the left panel and for the NL3, GM1, GM3, NL ρ , FSU, and IU-FSU models in the right panel. We first analyze the effect of the symmetry energy slope on this quantity. We conclude that: (a) for matter without hyperons the larger the L the smaller the neutron-proton asymmetry above the saturation density and, therefore, the smaller the direct Urca onset density; (b) the larger the slope the smaller the onset density because a larger L corresponds to a harder symmetry energy and, therefore, larger fractions of protons are favored; (c) for a low value of L the presence of hyperons decreases the onset density. The effect of the inclusion of hyperons depends on the hyperon-meson coupling. With set A, Λ is the first

TABLE V. Symmetry energy and no-hyperon star properties for IU-FSU modified EOS. The onset density of the direct Urca process, symmetry energy slope and symmetry energy at saturation, mass and radius of the maximum-mass configuration, and radius of $1.4M_\odot$ and $1.0M_\odot$ stars are given.

Set	n_{urca}/n_0	L (MeV)	\mathcal{E}_{sym} (MeV)	M_{max}/M_\odot	$R_{M_{\text{max}}}$ (km)	$R_{1.4M_\odot}$ (km)	$R_{1.0M_\odot}$ (km)
1	3.95	47.20	31.34	1.95	11.23	12.55	12.51
2	3.42	55.09	32.09	1.95	11.27	12.68	12.72
3	2.99	62.38	32.74	1.95	11.31	12.78	12.88
4	2.66	68.73	33.26	1.95	11.35	12.86	13.00
5	2.24	78.45	34.00	1.95	11.41	13.00	13.20
6	1.74	96.02	35.21	1.97	11.57	13.33	13.60
7	1.68	99.17	35.41	1.98	11.63	13.41	13.70

TABLE VI. Symmetry energy and star properties for NL3, GM1, GM3, FSU, and IU-FSU EOS and set *A* for the meson-hyperon couplings. The onset density of the direct Urca process, symmetry energy slope and symmetry energy at saturation, mass and radius of the maximum-mass configuration, and radius of $1.4M_{\odot}$ and $1.M_{\odot}$ stars are given.

Set	n_{urca}/n_0	L (MeV)	\mathcal{E}_{sym} (MeV)	M_{max}/M_{\odot}	$R_{M_{\text{max}}}$ (km)	$R_{1.4M_{\odot}}$ (km)	$R_{1.0M_{\odot}}$ (km)
NL3	1.38	118.0	37.4	2.00	13.51	14.71	14.65
GM1	1.81	94.0	32.5	1.82	12.83	13.80	13.75
GM3	2.04	90.0	32.5	1.595	12.20	13.12	13.37
NL ρ	2.14	85.0	30.5	1.594	11.94	12.91	13.08
FSU	3.51	61.0	32.6	1.375	11.95	—	12.79
IU-FSU	3.28	47.2	31.3	1.55	11.92	12.54	12.50

hyperon to appear, as can be seen in Fig. 6(a). With the onset of Λ , the neutron fraction decreases as well as the proton fraction. The behavior of the onset density for the DU depends on the balance between these two effects. In general the DU process is favored but, for a small range of L ($65 < L < 80$ MeV), the DU process may occur at densities larger than the values obtained for nucleonic matter. (d) The hyperon direct Urca may occur at densities below the onset of the nucleon direct Urca for set *A* if L is low enough ($L < 68$ MeV), as shown in the left panel of Fig. 8, where the green dots define the onset density of the process $\Lambda \rightarrow p + e + \bar{\nu}$.

For set *B*, Σ^- is the first hyperon to appear according to Fig. 6(b). With the onset of a negatively charged hyperon, Σ^- or Ξ^- , there is an increase of the proton fraction due to electrical neutrality as well as a decrease of the neutron fraction: both effects favor the DU onset.

In Figs. 9–11, the mass radius for the families of stars obtained, respectively, from the EOS without hyperons and from the EOS with the meson-hyperon sets *A* and *B* are shown. In the three figures, we show on the left panel the curves obtained with models NL3, GM1, GM3, NL ρ , FSU, and IU-FSU, and in the right panel we show the curves for IU-FSU and the modified IU-FSU models. We also include the constrains obtained by [3] and the mass of the millisecond binary pulsar J1614-2230 [12]. For the crust of the star we have joined our

TABLE VII. Symmetry energy and star properties for NL3, GM1, GM3, FSU, and IU-FSU EOS and set *B* for the meson-hyperon couplings. The onset density of the direct Urca process, symmetry energy slope and symmetry energy at saturation, mass and radius of the maximum-mass configuration, and radius of $1.4M_{\odot}$ and $1.M_{\odot}$ stars are given.

Set	n_{urca}/n_0	L (MeV)	\mathcal{E}_{sym} (MeV)	M_{max}/M_{\odot}	$R_{M_{\text{max}}}$ (km)	$R_{1.4M_{\odot}}$ (km)	$R_{1.0M_{\odot}}$ (km)
NL3	1.3827	118.0	37.4	2.43	13.51	14.71	14.65
GM1	1.8121	94.0	32.5	2.18	11.81	13.81	13.75
GM3	2.0370	90.0	32.5	1.88	11.05	13.12	13.38
NL ρ	2.1389	85.0	30.5	1.91	10.92	12.89	13.09
FSU	2.4346	61.0	32.6	1.42	10.76	11.32	12.77
IU-FSU	2.4585	47.2	31.3	1.69	11.14	12.37	12.50

TABLE VIII. Symmetry energy and star properties for IU-FSU modified EOS and set *A* for the meson-hyperon couplings. The onset density of the direct Urca process, symmetry energy slope and symmetry energy at saturation, mass and radius of the maximum-mass configuration, and radius of $1.4M_{\odot}$ and $1.M_{\odot}$ stars are given.

Set	n_{urca}/n_0	L (MeV)	\mathcal{E}_{sym} (MeV)	M_{max}/M_{\odot}	$R_{M_{\text{max}}}$ (km)	$R_{1.4M_{\odot}}$ (km)	$R_{1.0M_{\odot}}$ (km)
1	3.28	47.20	31.34	1.55	11.92	12.54	12.50
2	3.17	55.09	32.09	1.54	12.01	12.67	12.72
3	3.02	62.38	32.74	1.54	12.08	12.77	12.88
4	2.88	68.73	33.26	1.53	12.15	12.86	13.01
5	2.24	78.45	34.00	1.53	12.28	12.99	13.20
6	1.72	96.02	35.21	1.54	12.60	13.32	13.61
7	1.68	99.17	35.41	1.54	12.66	13.41	13.70

EOS with the Negele and Vautherin EOS [34] for the inner crust and the Baym-Pethick-Sutherland (BPS) EOS [35] for the outer crust.

We discuss first the results without hyperons (Fig. 9). All the models except FSU are able to describe the pulsar J1614-2230. However, only IU-FSU and FSU satisfy the constrains on [3]. The set of relativistic mean-field (RMF) models chosen has quite different properties and is reflected in the differences between the models: the harder models like NL3 and GM1 predict larger masses and radii, the softer EOS, FSU, the smallest mass, the smaller the L the smaller the radius. This last property is clearly seen in the left panel of Fig. 12 were the radius of maximum-mass stars (squares), $1.4M_{\odot}$ stars (circles), and $1.0M_{\odot}$ stars (triangles) are plotted as a function of the symmetry energy slope for nucleonic stars. The full symbols are for the modified IU-FSU models and the empty symbols are for the NL3, GM1, GM3, NL ρ , and FSU models. The modified IU-FSU models show that, if the isoscalar channel is left unchanged, the radius decreases if L decreases. This reduction is larger for $1.0M_{\odot}$ stars (more than 1 km for $45 < L < 100$ MeV) but even for the maximum-mass configurations there is still a 0.5 km difference. The set of RMF models chosen also show the same trend. However, since the isoscalar properties differ among the models, and they also affect the radius, the linear behavior is not present.

TABLE IX. Symmetry energy and star properties for IU-FSU modified EOS and set *B* for the meson-hyperon couplings. The onset density of the direct Urca process, symmetry energy slope and symmetry energy at saturation, mass and radius of the maximum-mass configuration, and radius of $1.4M_{\odot}$ and $1.M_{\odot}$ stars are given.

Set	n_{urca}/n_0	L (MeV)	\mathcal{E}_{sym} (MeV)	M_{max}/M_{\odot}	$R_{M_{\text{max}}}$ (km)	$R_{1.4M_{\odot}}$ (km)	$R_{1.0M_{\odot}}$ (km)
1	2.4585	47.20	31.34	1.69	11.14	12.37	12.50
2	2.3916	55.09	32.09	1.69	11.20	12.46	12.71
3	2.3246	62.38	32.74	1.68	11.25	12.56	12.88
4	2.2577	68.73	33.26	1.68	11.29	12.64	13.01
5	2.1239	78.45	34.00	1.68	11.36	12.80	13.20
6	1.7225	96.02	35.21	1.69	11.57	13.18	13.63
7	1.6779	99.17	35.41	1.69	11.62	13.27	13.70

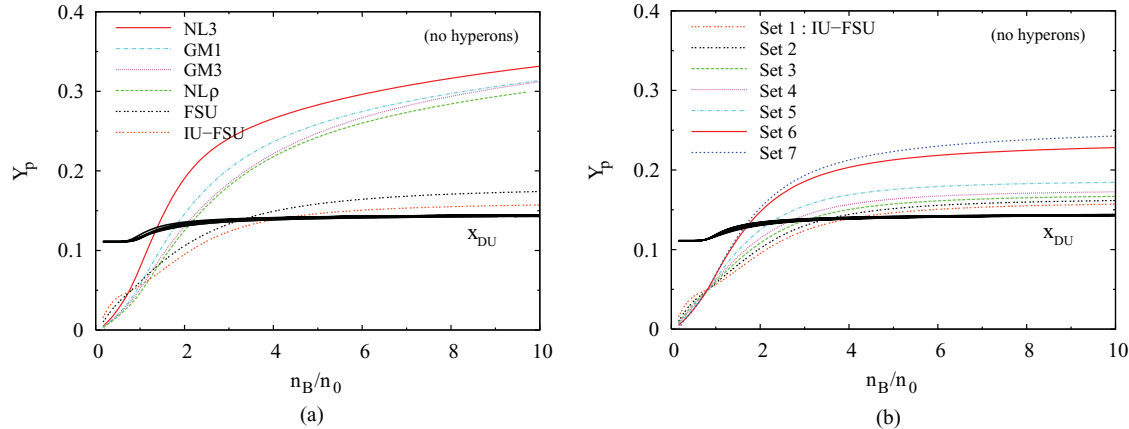


FIG. 7. (Color online) Onset of direct Urca process in stellar matter without hyperons: proton fraction for β -equilibrium matter and proton fraction at the onset of the direct Urca process (black region) (a) for NL3, GM1, GM3, NL ρ , FSU, IU-F and (b) for modified IU-FSU.

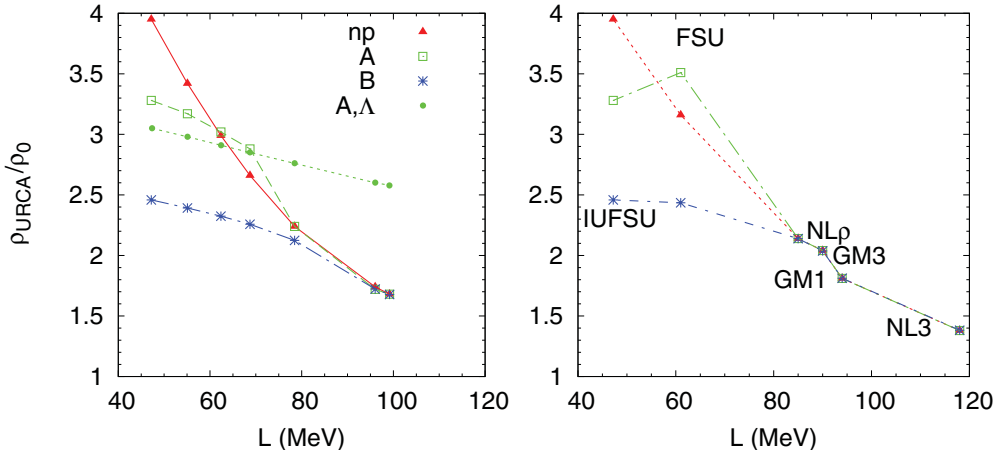


FIG. 8. (Color online) Onset of direct Urca process in stellar matter. Left panel corresponds to modified IU-FSU model and right panel corresponds to NL3, GM1, GM3, NL ρ , FSU, and IU-FSU, for no-hyperon matter (red triangles), hyperon coupling set A (green squares) and hyperon coupling set B (blue stars). In the left panel the direct Urca process involving Λ is also shown (full dots). All the other data refer to the direct Urca process for protons and neutrons.

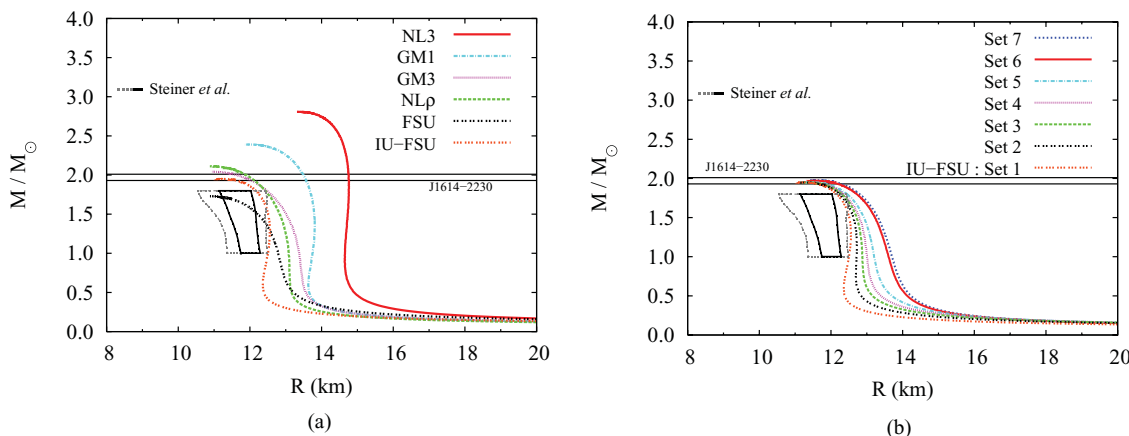


FIG. 9. (Color online) Mass-radius curves obtained for no-hyperon stellar matter EOS for (a) NL3, GM1, GM3, NL ρ , FSU, and IU-FSU and for (b) IU-FSU and modified IU-FSU. The areas limited by the dotted gray and solid black curves are given by [3].

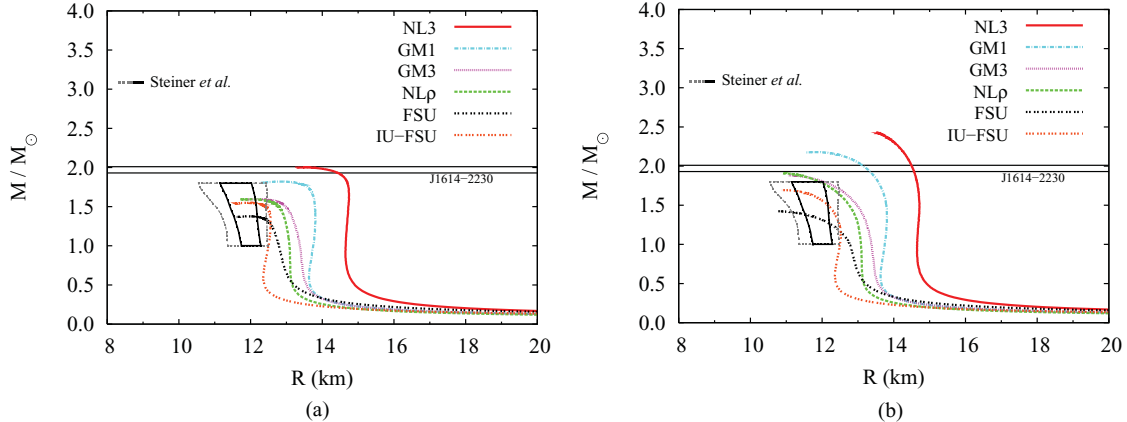


FIG. 10. (Color online) Mass-radius relations obtained for NL3, GM1, GM3, NL ρ , FSU, and IU-FSU with the hyperon-meson coupling (a) set A and (b) set B.

Including hyperons in the EOS makes the EOS softer at large densities and the mass of the maximum-mass stars is smaller [36]. This is seen in Fig. 10 where the mass-radius curves obtained with hyperon-meson coupling sets A and B are plotted in the left and right panels, respectively. We conclude that it is important to have correct couplings since the star masses are sensitive to the hyperon couplings. For set A only the NL3 model is able to describe the PSR J1316-2230, while within set B NL3, GM1, GM3, and NL ρ are able to describe a star with a mass $(1.97 \pm 0.4)M_\odot$. The trend discussed above between the star radius and L is still present in these stars; see the empty symbols in the middle and right panels of Fig. 12. This trend is confirmed by the modified IU-FSU models; see full symbols in the middle and right panels of Fig. 12. Stars with $1.0M_\odot$ and $1.4M_\odot$ contain no hyperons, or only a small fraction, and therefore their radii do not differ from the results obtained for np matter. Maximum-mass stars, however, do have hyperons and their radii depend on the hyperon couplings chosen: for set A radius is larger and the maximum mass is smaller than the corresponding quantities predicted by set B. None of the models are able to describe PSR J1614-2230. We also conclude

that the mass of the maximum-mass configuration is quite insensitive to the symmetry energy slope.

IV. CONCLUSIONS

In the present work we studied the effect of the density dependence of the symmetry energy on the star properties, namely, the hyperon content, DU, radius, and mass.

The study was performed within the RMF framework. We considered parametrizations which have been fit to the equilibrium properties of stable and unstable nuclei and/or dynamical response of nuclei, or to the saturation properties of symmetric nuclear matter. In order to test the density dependence of the symmetry energy we considered the IU-FSU parametrization. Keeping the isoscalar channel fixed, we changed the isovector channel in order to reproduce the values of the symmetry energy slope that were obtained from experimental measurements, $40 < L < 110$ MeV [27,28].

For the hadronic EOS, we considered two different parametrizations of the meson-hyperon couplings: in set A we considered the couplings that reproduce the binding energy of

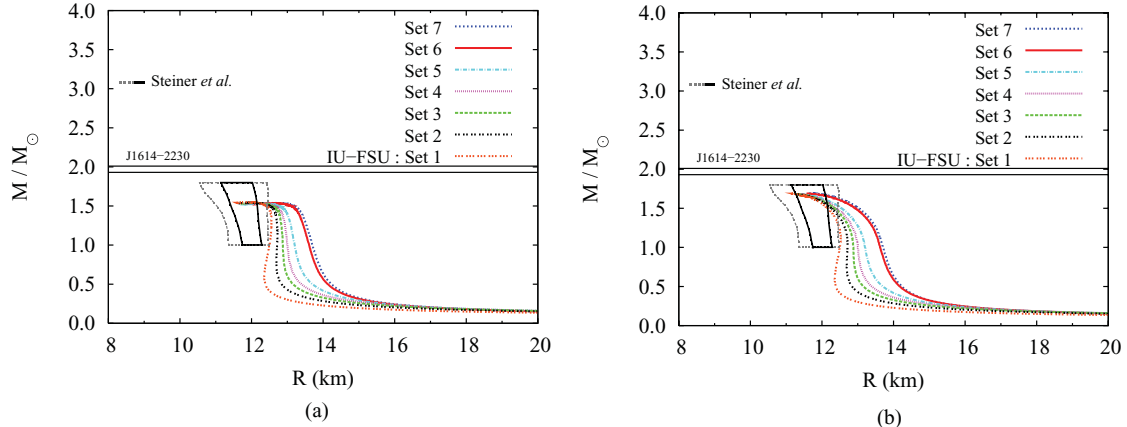


FIG. 11. (Color online) Mass-radius relations obtained with the modified IU-FSU and with the meson-hyperon coupling for (a) set A and for (b) set B.

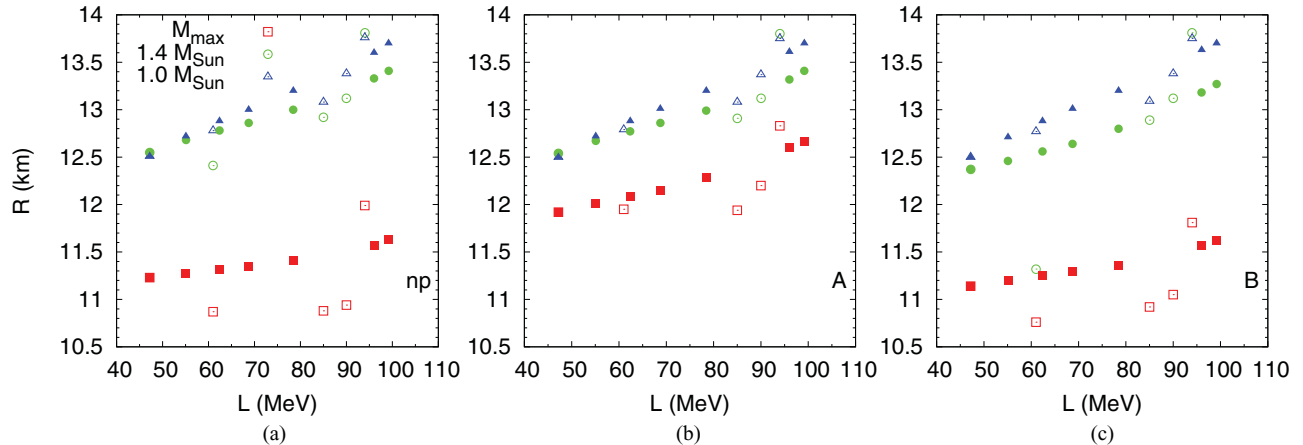


FIG. 12. (Color online) Star-radius dependence on the slope of the symmetry energy for stars with maximum mass (squares), $1.4M_{\odot}$ (circles), and $1M_{\odot}$ (triangles). The empty symbols are for the set of different models considered with hyperon coupling A. The full symbols are for the modified IU-FSU (a) with no hyperons, (b) with hyperons and for coupling A, and (c) with hyperons and for coupling B.

hyperons to symmetric nuclear matter; however, since only the binding energy of the Λ is well determined, we have also considered set B, which corresponds to the couplings proposed in Ref. [8] with $x_s = 0.8$. With set B and the GM1 parametrization of the RMF for the nuclear EOS, the authors of [23] could obtain a maximum-mass-star configuration of the order of the one recently measured by Demorest *et al.* [12].

We analyzed the effect of L on the radius of stars with $1M_{\odot}$, $1.4M_{\odot}$ and maximum-mass configurations. The first two cases correspond to stars that have a central baryonic density in the range $1.5\rho_0$ to $3\rho_0$ and therefore give information on the EOS just above the saturation densities. These densities will be probed at the GSI Facility for Antiproton and Ion Research (FAIR) [37].

We have concluded that the radius of the star is sensitive to the slope L , and, in particular, the smaller the value of the slope, the smaller the radius of the star. It was also shown that the density dependence of the symmetry energy affects the onset density of the direct Urca process: the smaller L , the larger the density. This can be understood because a smaller L at saturation corresponds to a softer symmetry energy at high densities, and, therefore, a smaller proton fraction. However, the DU onset also depends on the hyperon content and the hyperon-meson couplings. If Λ is the first hyperon to appear, the DU may be hindered or favored according to a balance between the neutron and proton reductions. However, if a negatively charged hyperon such as the Σ^- is the first hyperon to appear, there is a decrease of the neutron fraction and an increase of the proton fraction: both effects favor the DU onset.

It was also shown that the larger L , the larger the hyperon content because a larger L makes the EOS harder and, therefore, it is energetically favorable to have a larger hyperon fraction. However, this only occurs if the first hyperon to appear is the Λ . A delicate balance between the increase suffered by the chemical potential of the Σ^- and the neutron plus electron chemical potential may make the hyperon onset independent of L .

We also conclude that the total strangeness content is sensitive to the meson-hyperon couplings and stronger constraints on the determination of these constants are required. For larger hyperon-vector meson couplings we have obtained a smaller strangeness content.

According to recent estimates based on a microscopic non-relativistic approach, including hyperon degrees of freedom seems to make the EOS too soft even including three-body forces [38], so that at most star masses of $1.6M_{\odot}$ are attained, far from the very precise mass value recently measured [12]. More data on hypernuclei are required in order to clarify this point.

ACKNOWLEDGMENTS

This work was partially supported by CNPq (Brazil) and CAPES (Brazil)/FCT (Portugal) under project 232/09, by FCT (Portugal) under the Grants No. PTDC/FIS/113292/2009 and No. CERN/FP/109316/2009. R.C. is grateful for the warm hospitality at Centro de Física Computacional/FCTUC.

-
- [1] James M. Lattimer and Madappa Prakash, *Phys. Rep.* **442**, 109 (2007).
 - [2] F. Özel, T. Güver, and D. Psaltis, *Astrophys. J.* **693**, 1775 (2009); F. Özel, G. Baym, and T. Guver, *Phys. Rev. D* **82**, 101301 (2010).
 - [3] A. W. Steiner, J. M. Lattimer, and E. F. Brown, *Astrophys. J.* **722**, 33 (2010).
 - [4] K. Hebeler, J. M. Lattimer, C. J. Pethick, and A. Schwenk, *Phys. Rev. Lett.* **105**, 161102 (2010).
 - [5] G. A. Lalazissis, J. König, and P. Ring, *Phys. Rev. C* **55**, 540 (1997).
 - [6] B. G. Todd-Rutel and J. Piekarewicz, *Phys. Rev. Lett.* **95**, 122501 (2005); F. J. Fattoyev and J. Piekarewicz, *Phys. Rev. C* **82**, 025805 (2010).

- [7] F. J. Fattoyev, C. J. Horowitz, J. Piekarewicz, and G. Shen, *Phys. Rev. C* **82**, 055803 (2010).
- [8] N. K. Glendenning and S. A. Moszkowski, *Phys. Rev. Lett.* **67**, 02414 (1991).
- [9] Rafael Cavagnoli, Constança Providênciac, and Debora P. Menezes, *Phys. Rev. C* **83**, 045201 (2011).
- [10] Camille Ducoin, Jérôme Margueron, Constança Providênciac, and Isaac Vidaña, *Phys. Rev. C* **83**, 045810 (2011).
- [11] J. Piekarewicz, *Phys. Rev. C* **66**, 034305 (2002); **69**, 041301 (2004).
- [12] Paul Demorest, Tim Pennucci, Scott Ransom, Mallory Roberts, and Jason Hessels, *Nature (London)* **467**, 1081 (2010).
- [13] N. K. Glendenning, *Compact Stars* (Springer-Verlag, New York, 2000).
- [14] J. Schaffner-Bielich and A. Gal, *Phys. Rev. C* **62**, 034311 (2000); J. Schaffner-Bielich, M. Hanauske, H. Stocker, and W. Greiner, *Phys. Rev. Lett.* **89**, 171101 (2002); E. Friedman and A. Gal, *Phys. Rep.* **452**, 89 (2007).
- [15] M. Chiapparini, M. E. Bracco, A. Delfino, M. Malheiro, D. P. Menezes, and C. Providencia, *Nucl. Phys. A* **826**, 178 (2009).
- [16] B. D. Serot and J. D. Walecka, *Adv. Nucl. Phys.* **16**, 1 (1986); J. Boguta and A. R. Bodmer, *Nucl. Phys. A* **292**, 413 (1977).
- [17] C. J. Horowitz and J. Piekarewicz, *Phys. Rev. Lett.* **86**, 5647 (2001).
- [18] D. J. Millerner, C. B. Dover, and A. Gal, *Phys. Rev. C* **64**, 044302 (2001); Y. Yamamoto, H. Bando, and J. Zofka, *Prog. Theor. Phys.* **80**, 757 (1998).
- [19] S. Bart *et al.*, *Phys. Rev. Lett.* **83**, 5238 (1999); H. Noumi *et al.*, *ibid.* **89**, 072301 (2002); **90**, 024002 (2003); P. K. Saha *et al.*, *Phys. Rev. C* **70**, 044613 (2004).
- [20] M. Kohno, Y. Fujiwara, Y. Watanabe, K. Ogata, and M. Kawai, *Prog. Theor. Phys.* **112**, 895 (2004); *Phys. Rev. C* **74**, 064613 (2006); T. Harada and Y. Hirabayashi, *Nucl. Phys. A* **759**, 143 (2005); **767**, 206 (2006).
- [21] Avraham Gal, *Prog. Theor. Phys. Suppl.* **186**, 270 (2010).
- [22] T. Fukuda *et al.*, *Phys. Rev. C* **58**, 1306 (1998); P. Khaustov *et al.*, *ibid.* **61**, 054603 (2000).
- [23] I. Bombaci, P. K. Panda, C. Providênciac, and I. Vidana, *Phys. Rev. D* **77**, 083002 (2008).
- [24] B. Liu, V. Greco, V. Baran, M. Colonna, and M. Di Toro, *Phys. Rev. C* **65**, 045201 (2002).
- [25] P. Danielewicz, R. Lacey, and W. G. Lynch, *Science* **298**, 1592 (2002).
- [26] M. Di Toro, B. Liu, V. Greco, V. Baran, M. Colonna, and S. Plumari, *Phys. Rev. C* **83**, 014911, (2011).
- [27] L. W. Chen, C. M. Ko, and B. A. Li, *Phys. Rev. Lett.* **94**, 032701 (2005).
- [28] A. Klimkiewicz *et al.*, *Phys. Rev. C* **76**, 051603 (2007); D. V. Shetty, S. J. Yennello, and G. A. Soulis, *ibid.* **76**, 024606 (2007); M. B. Tsang, Y. Zhang, P. Danielewicz, M. Famiano, Z. Li, W. G. Lynch, and A. W. Steiner, *Phys. Rev. Lett.* **102**, 122701 (2009); M. Centelles, X. Roca-Maza, X. Viñas, and M. Warda, *ibid.* **102**, 122502 (2009); M. Warda, X. Viñas, X. Roca-Maza, and M. Centelles, *Phys. Rev. C* **80**, 024316 (2009); Andrea Carbone, Gianluca Colò, Angela Bracco, Li-Gang Cao, Pier Francesco Bortignon, Franco Camera, and Oliver Wieland, *ibid.* **81**, 041301(R) (2010).
- [29] Isaac Vidaña, Constança Providênciac, Artur Polls, and Arnau Rios, *Phys. Rev. C* **80**, 045806 (2009).
- [30] A. M. S. Santos and D. P. Menezes, *Phys. Rev. C* **69**, 045803 (2004).
- [31] J. M. Lattimer, C. J. Pethick, M. Prakash, and P. Haensel, *Phys. Rev. Lett.* **66**, 2701 (1991).
- [32] T. Klähn *et al.*, *Phys. Rev. C* **74**, 035802 (2006).
- [33] M. Prakash, M. Prakash, J. M. Lattimer, and C. J. Pethick, *Astrophys. J.* **390**, L77 (1992).
- [34] J. W. Negele and D. Vautherin, *Nucl. Phys. A* **207**, 298 (1973).
- [35] G. Baym, C. Pethick, and D. Sutherland, *Astrophys. J.* **170**, 299 (1971).
- [36] M. Prakash, I. Bombaci, M. Prakash, P. J. Ellis, J. M. Lattimer, and R. Knorren, *Phys. Rep.* **280**, 1 (1997).
- [37] S. ChattoPadhyay, *J. Phys. G* **35**, 104027 (2008); P. Senger *et al.*, *ibid.* **36**, 064037 (2009); CBM Collaboration, Johann M. Heuser, *Nucl. Phys. A* **830**, 563c (2009) [<http://www.gsi.de/fair>].
- [38] I. Vidaña, D. Logoteta, C. Providênciac, A. Polls, and I. Bombaci, *Europhys. Lett.* **94**, 11002 (2011).